

## ABSTRACT

### Structural Characterization of Peptides and Peptide Fragment Ions Using High Resolution Mass Spectrometry and Ion Mobility Spectrometry

Mahsan Miladi, B.S., M.S.

Mentor: Touradj Solouki, Ph.D.

Modern mass spectrometers are among the most sensitive and suitable analytical tools for high-throughput protein characterization in proteomics. However, fragment ion rearrangements during gas-phase dissociation processes can limit the success of mass spectrometry (MS) based proteomics approaches. State-of-the-art MS and ion mobility (IM) spectrometry techniques were utilized to further our understanding of gas-phase peptide fragment ion rearrangements.

Gas-phase hydrogen/deuterium exchange (HDX) and IM-MS were used to assess the influence of basic histidine residue position and fragment ion size on the observed structural rearrangements. A systematic study of HDX patterns and reaction kinetics for fragments from seven isomeric (Histidine)(Alanine)<sub>6</sub>-NH<sub>2</sub> heptapeptides suggested the presence of at least two ion population types for b<sub>n</sub> ions (fragment ions formed by peptide amide bond cleavages where charge is kept on the n-terminus side), regardless of the histidine position. Furthermore, IM-MS measurements confirmed the presence of more than one b<sub>n</sub> isomers for (Histidine)(Alanine)<sub>6</sub>-NH<sub>2</sub> fragment ions.

Tandem MS and isotope labelings were utilized to investigate possible pathways for generation of structural isomers of  $b_n^+$  fragments. Results from tandem MS of an isotopically labeled (Histidine)(Alanine)<sub>6</sub>-NH<sub>2</sub> peptide revealed the first experimental evidence for generation of sequence-scrambled fragments from y-type ions (where charge remains on the c-terminus side fragment). Thorough analysis of thirty-two additional y-type fragment ions with different charge states (+1 to +3) and sizes (3 to 12 amino acids) confirmed our initial observation of sequence-scrambling from y-type ions (16 out of 32 or ~50 %).

Although gas-phase HDX reactions provide valuable structural information, competing reaction channels such as HDX reagent adduct formation can complicate the interpretation of HDX data. We used *ab initio* calculations combined with HDX, IM-MS, and isotope labeling to identify potential peptide functional groups involved in gas-phase HDX adduct formation. We used benzyloxycarbonyl (Z)-capped dipeptide containing glycine (G) and proline (P) (Z-PG) as a model and studied the influence of protonation and metal ion (Na<sup>+</sup>, K<sup>+</sup>, and Cs<sup>+</sup>) complexation on gas-phase ND<sub>3</sub> adduct formation. Both experimental and theoretical findings indicated that simultaneous availability of carbonyl groups from glycine, proline, and Z were necessary for ND<sub>3</sub> adduct formation with Z-PG.

Structural Characterization of Peptides and Peptide Fragment Ions Using High Resolution  
Mass Spectrometry and Ion Mobility Spectrometry

by

Mahsan Miladi, B.S., M.S.

A Dissertation

Approved by the Department of Chemistry and Biochemistry

---

Patrick J. Farmer, Ph.D., Chairperson

Submitted to the Graduate Faculty of  
Baylor University in Partial Fulfillment of the  
Requirements for the Degree  
of  
Doctor of Philosophy

Approved by the Dissertation Committee

---

Touradj Solouki, Ph.D., Chairperson

---

C. Kevin Chambliss, Ph.D.

---

Sascha Usenko, Ph.D.

---

Charles M. Garner, Ph.D.

---

Stephen L. Gipson, Ph.D.

---

Christopher M. Kearney, Ph.D.

Accepted by the Graduate School

May, 2014

---

J. Larry Lyon, Ph.D., Dean

Copyright © 2014 by Mahsan Miladi

All rights reserved

## TABLE OF CONTENTS

LIST OF FIGURES .....	vii
LIST OF SCHEMES.....	xiv
LIST OF TABLES .....	xv
ABBREVIATIONS .....	xvii
ACKNOWLEDGMENTS.....	xx
DEDICATION.....	xxii
CHAPTER ONE .....	1
Introduction .....	1
1.1. Biological Mass Spectrometry.....	1
1.2. Mass Spectrometers.....	2
1.2.1. Ionization Sources.....	3
1.2.1.1. Electrospray Ionization .....	3
1.2.2. Mass Analyzers.....	5
1.2.2.1. Fourier Transform-Ion Cyclotron Resonance (FT-ICR) Mass Analyzer.....	6
1.2.2.2. Orbitrap Mass Analyzer.....	11
1.2.2.3. Time of Flight (TOF) Mass Analyzer.....	13
1.3. Gas-Phase Ion Fragmentation Techniques in Proteomics.....	14
1.4. Gas-phase MS Techniques for Conformational Analysis of Proteins/Peptides.....	15
1.4.1. Gas Phase Hydrogen/Deuterium Exchange (HDX) Reaction.....	16
1.4.2. Ion Mobility-Mass Spectrometry (IM-MS).....	19
CHAPTER TWO .....	23
Protein and Peptide Amino Acid Sequencing Using Mass Spectrometry.....	23
2.1. Mass Spectrometry-based Proteomics Strategies .....	23
2.2. Nomenclature for Protein and Peptide Fragments in Mass Spectrometry.....	25
2.3. Challenges Associated with Search Engines and Strategies in Peptide Sequencing.....	26
2.4. Peptides' Amino Acid Sequence Rearrangement during Gas-phase Fragmentation.....	29
2.5. Gas-phase Structural Analysis of Peptide Fragment Ions.....	33

2.6. Structures of b-type Fragment Ions .....	34
2.7. Justification of the Research Presented in this Dissertation.....	40
CHAPTER THREE .....	42
A Systematic Study on the Effect of Histidine Position and Fragment Ion Size in the Formation of b <sub>n</sub> Ions.....	42
Abstract .....	42
3.1. Introduction.....	43
3.2. Experimental.....	46
3.2.1. Sample Preparation.....	46
3.2.2. Mass Spectrometry.....	47
3.2.3. Ion Mobility-Mass Spectrometry.....	48
3.2.4. Data Analysis.....	49
3.3. Results and Discussions.....	50
3.3.1. Gas-Phase H/D Exchange Reactions.....	51
3.3.2. Fragment Ion Scrambling in P1-P7 Peptides.....	51
3.3.3. H/D Exchange Reaction Patterns.....	53
3.3.4. Kinetics of the H/D Exchange Reactions.....	58
3.3.5. Ion Mobility (IM) Profiles.....	65
3.4. Conclusion.....	71
Acknowledgment.....	72
CHAPTER FOUR .....	73
Evidence for Sequence Scrambling in Collision-Induced Dissociation of y-Type Fragment Ions.....	73
Abstract .....	73
4.1. Introduction.....	74
4.2. Experimental.....	77
4.2.1. Sample Preparation.....	77
4.2.2. Instrumentation.....	77
4.2.3. Nomenclature for labeling CID Products from y-Type Ions....	78
4.3. Results and Discussions.....	79
4.3.1. CID of y <sub>6</sub> <sup>+</sup> from AAAAHAA.....	79
4.3.2. CID of y Fragment Ions from Des-Acetylated- $\alpha$ -Melanocyte.....	84
4.3.3. CID of y Fragment Ions from Angiotensin II Antipeptide....	89
4.3.4. CID of y Fragment Ions from Glu-fibrinopeptide b.....	95
4.4. Conclusion.....	96
Acknowledgment.....	97
CHAPTER FIVE .....	98
Structural Dependent Competition between Gas-Phase H/D Exchange and Adduct Formation Reactions.....	98
Abstract .....	98
5.1. Introduction.....	99
5.2. Experimental and Theoretical.....	101

5.2.1. Sample Preparation.....	101
5.2.2. FT-ICR MS.....	102
5.2.3. IM-MS.....	103
5.2.4. Molecular Modeling .....	104
5.2.5. Theoretical CCS Calculations.....	105
5.3. Results and Discussions.....	106
5.3.1. HDX of $[Z-PG + H]^+$ and $[Z-PG + metal]^+$ .....	106
5.3.2. Theoretically Optimized Geometries of $[Z-PG + H]^+$ and $[Z-PG + metal]^+$ .....	109
5.3.3. IM-MS of $[Z-PG + H]^+$ and $[Z-PG + metal]^+$ .....	112
5.3.4. HDX and IM-MS of $[Z-PG + H - CO_2]^+$ .....	115
5.3.4. HDX of $[Z-PG-OCH_3 + H]^+$ .....	118
5.4. Conclusion.....	119
Acknowledgment.....	120
CHAPTER SIX .....	121
Conclusions and Future Directions.....	121
Dissertation Overview and Future Directions.....	122
APPENDICES .....	127
APPENDIX A.....	128
APPENDIX B.....	138
APPENDIX C.....	146
REFERENCES .....	149

## LIST OF FIGURES

Figure 1.1. Schematic representation of positive-ion mode ESI setup.....	4
Figure 1.2. An ion immersed in the magnetic field of “ <b>B</b> ” experiences both magnetic Lorentz and centrifugal forces.....	7
Figure 1.3. Illustration of the basic components of IonSpec ESI/FT-ICR mass spectrometer equipped with an open-ended cylindrical Penning trap and a 9.4 tesla superconducting magnet.....	9
Figure 1.4. Schematic representation of ion signal detection events in FT-ICR MS.....	10
Figure 1.5. Pictorial representation of the cross sectional view of an Orbitrap mass analyzer.....	12
Figure 1.6. Schematic representation of a home-built pulsed-leak valve setup for controlled release of deuterium reagent into the ICR cell. Sample pulse valve is used to introduce the reagent gas into the “T-section” assembly behind a leak valve. Then, the neutral reagent molecules are leaked into the vacuum chamber under a precise control and using the leak valve. The exhaust pulse valve is connected to a mechanical pump and used to pump the residual gas in T-section space at the end of the ion-molecule reaction event.....	17
Figure 1.7. Onium ion mechanism for gas-phase HDX reactions of peptides.....	19
Figure 1.8. Schematic representation of Waters Synpat G2 TWIMS system.....	21
Figure 1.9. Traveling wave voltage pulse propels ions along the stacked ring ion guide (SRIG) and in the presence of background gas.....	22
Figure 2.1. Schematic representation of “bottom-up” and “top-down” MS-based protein/peptide amino acid sequence identification.....	24
Figure 2.2. Roepstorff” nomenclature system for product ions produced from backbone cleavage of proteins/peptides during gas-phase fragmentation. Red circles indicate positions of all alpha carbons (C $\alpha$ with respect to carbonyl groups) in the amino acid sequence.....	26
Figure 2.3. Percentages of known (identified) and unknown fragment ions from CID of different charge states ( <i>i.e.</i> , +1, +2, and +3) of tryptic	

digested peptides (52 peptides) from bovine serum albumin (BSA). Plots were generated by calculating the percentage of unknown ions from CID MS data taken from NIST peptide tandem MS library.....	28
Figure 2.4. Schematic representation of amino acid sequence scrambling during gas-phase fragmentation process of a peptide ion. Each circle denotes an amino acid and each number inside a circle denotes the amino acid residue position in peptide sequence.....	30
Figure 2.5. CID mass spectrum of a singly-charged protonated peptide (amino acid sequence: GVVVHPV). Observed b- and y-type fragment ions are labeled. Peaks with red labels denote sequence-scrambled fragment ions.....	32
Figure 2.6. Reaction mechanism for the formation of a $b_2^+$ with acylium-type structure followed by immonium ion formation.....	35
Figure 2.7. Reaction mechanism for the formation of a $b_2^+$ with oxazolone-type structure.....	36
Figure 2.8. Reaction mechanism for the formation of a $b_2^+$ with diketopiperazine-type structure.....	37
Figure 2.9. Reaction mechanism for the formation of a macrocyclic-type structure for a $b_5^+$ fragment.....	38
Figure 2.10. Reaction mechanism for the formation of a macrocyclic-type structure for a $a_5^+$ fragment.....	39
Figure 3.1. ESI/FT-ICR mass spectra of SWIFT-isolated $^{12}C_{all}$ peak at 0 s (top panel), 100 s (middle panel), and 500 s (bottom panel) reaction times with $ND_3$ (at $PND_3 \approx 4.2 \times 10^{-8}$ Torr) for (a) molecular ion ( <i>i.e.</i> , $[M + H]^+$ ) and (b) $b_7^+$ fragment of A(His)AAAAA-NH <sub>2</sub> (P2 peptide)...	54
Figure 3.2. ESI/FT-ICR mass spectra of SWIFT-isolated $^{12}C_{all}$ peak at 0 s (top panel), 100 s (middle panel), and 500 s (bottom panel) reaction times with $ND_3$ (at $PND_3 \approx 4.2 \times 10^{-8}$ Torr) for (a) $b_4^+$ , (b) $b_5^+$ , and (c) $b_6^+$ fragments of A(His)AAAAA-NH <sub>2</sub> (P2 peptide) .....	57
Figure 3.3. Temporal plots of normalized ion abundance versus H/D exchange reaction time for disappearance of the $^{12}C_{all}$ peak (or $D_0$ ) for (a) $[M + H]^+$ and (b) $b_7^+$ fragment of A(His)AAAAA-NH <sub>2</sub> . The fitted single exponential decay equations for each fragment ions are shown in the corresponding plots. The insets show semi-log plots of $\ln(I_{D0} / I_{Dm})$ vs. H/D exchange reaction time of each b fragment ion. The empty circles (○) and triangles (Δ) in the semilog plots show the segments corresponding	

to “fast” + “slow” and “slow” H/D-exchanging populations, respectively. The fitted linear equations for each segment are shown in the plots. The filled squares (■) in the semi-log plots correspond to H/D exchange data which were not used for linear fitting.....59

Figure 3.4. Semi-log plots of  $\ln(I_{D0} / I_{Dm})$  vs. H/D exchange reaction time for (a)  $b_4^+$ , (b)  $b_5^+$ , and (c)  $b_6^+$  fragment ions of A(His)AAAAA-NH<sub>2</sub>. The empty circles (○) and triangles (Δ) in the semi-log plots show the segments corresponding to “fast” + “slow” and “slow” H/D-exchanging populations, respectively. The fitted linear equations for each segment are shown in the plots. The filled squares (■) in the semi-log plots correspond to H/D exchange data which were not used for linear fitting.....61

Figure 3.5. Plot of ion mobility peak widths (FWHH) versus arrival time values for standard sodium adduct polypropylene glycol (PPG) ions {empty squares (□)} and  $b_n^+$  (n = 4-7) and  $[M + H]^+$  of P3 {empty circles (○)}. The  $m/z$ s of the sodium adduct PPG species and the number of propylene glycol units (*i.e.*, “m”) in  $[PPG(m) + Na]^+$  (m = 6-10) are labeled. The equation obtained from the linear fitting (dash-line) to the sodium adduct PPG ions data is also shown in the top portion of plot. Each data point is the average of six experimental trials performed in two different days and errors (95 % confidence level) for both arrival time (<0.7 %) and FWHH (<2 %) values are shown as error bars.....69

Figure 4.1. Collision-induced dissociation (CID) mass spectra of  $m/z$ -isolated (a)  $[y_6]^+$  ( $m/z$  511) (generated from in-source fragmentation of AAAAHAA-NH<sub>2</sub>) and (b)  $[y_6 - (NH_3)]^+$  ( $m/z$  494) (generated from CID of  $[y_6]^+$ ) at 20 % normalized collision energy. Insets in panels (a) and (b) show the expanded views of  $m/z$  range of 421 to 424 corresponding to  $[y_6 - (NH_3 + A)]^+$  and  $[y_6 - (NH_3 + A)]^+$  fragment ions.....80

Figure 4.2. Collision induced dissociation (CID) mass spectra of  $m/z$ -isolated (a)  $[y_7]^{2+}$  ( $m/z$  444) (generated from CID of  $[M + 3H]^{3+}$  of des-acetylated- $\alpha$ -melanocyte [SYSMEHFRWGKPV-NH<sub>2</sub>]) and (b)  $[y_7 - (NH_3)]^{2+}$  ( $m/z$  436) (generated from CID of  $[y_7]^{2+}$ ) at 15 % normalized collision energy. A list of assigned fragments is included in the appendix materials (Tables B1 and B2). Peaks corresponding to electronic noise are marked with asterisk (\*) symbols.....86

Figure 4.3. Collision induced dissociation (CID) mass spectra of  $m/z$ -isolated (a)  $[y_7]^+$  ( $m/z$  770) (generated from in-source fragmentation of angiotensin II antipeptide (EGVYVHPV)) and (b)  $[y_7 - (H_2O + PV)]^+$  ( $m/z$  556) (generated from CID of  $[y_7]^+$ ) at 30 % normalized collision energy. A list of the assigned fragments is included in the appendix materials (Tables B3 and B4).....92

Figure 5.1. (Top) ESI/FT-ICR mass spectrum of a *Z-PG* sample containing  $\text{Na}^+$ ,  $\text{K}^+$ , and  $\text{Cs}^+$  after SWIFT-isolation ( $D_0$ ) of  $[\text{Z-PG} + \text{H}]^+$ ,  $[\text{Z-PG} + \text{Na}]^+$ ,  $[\text{Z-PG} + \text{K}]^+$ , and  $[\text{Z-PG} + \text{Cs}]^+$ . Expanded view ESI/FT-ICR mass spectra of  $m/z$ -isolated *Z-PG* species after (middle) 5 s and (bottom) 600 s HDX reaction time with  $\text{ND}_3$  (at  $P(\text{ND}_3) \approx 4.4 \times 10^{-8}$  Torr).  $D_n$  ( $n = 0$  to 3) denotes the number of deuterium atom(s) incorporated in each of the *Z-PG* species. Roman numbers on top of the peaks in panel a designate the identities of  $\text{ND}_3$  adduct species of  $[\text{Z-PG} + \text{H}]^+$ : I  $\equiv [\text{D}_0 + \text{ND}_2\text{H}]^+$  ( $m/z$  326); II  $\equiv [\text{D}_0 + \text{ND}_3]^+$  ( $m/z$  327); III  $\equiv [\text{D}_1 + \text{ND}_3]^+$  ( $m/z$  328); IV  $\equiv [\text{D}_2 + \text{ND}_3]^+$  ( $m/z$  329); V  $\equiv [\text{D}_3 + \text{ND}_3]^+$  ( $m/z$  330). Arrow heads pointing down in (c) and (d) point to the expected  $m/z$  values of  $\text{ND}_3$  adducts of  $[\text{Z-PG} + \text{Na}]^+$  (panel c),  $[\text{Z-PG} + \text{K}]^+$  (panel c), and  $[\text{Z-PG} + \text{Cs}]^+$  (panel d).....107

Figure 5.2. Optimized geometries of (a)  $[\text{Z-PG} + \text{H}]^+$ , (b)  $[\text{Z-PG} + \text{Na}]^+$ , and (c)  $[\text{Z-PG} + \text{K}]^+$ , and (d)  $[\text{Z-PG} + \text{Cs}]^+$ . Carbon and hydrogen atoms are shown in dark gray and light gray colors, respectively. Nitrogen and oxygen atoms are labeled as “N” and “O”, respectively. Total energy ( $E_{\text{tot}}$ ) (in Hartree (h)) for each structure is given.....110

Figure 5.3. Optimized geometry for  $[\text{Z-PG} + \text{H} + \text{ND}_3]^+$  (at B3LYP/6-31+G(d,p) level of theory). Carbon and hydrogen atoms are shown in dark gray and light gray colors, respectively. Nitrogen and oxygen atoms are labeled as “O” and “N”, respectively. Total energy ( $E_{\text{tot}}$ ) (in Hartree (h)) is given.....112

Figure 5.4. IM profiles of (a)  $[\text{Z-PG} + \text{H}]^+$ , (b)  $[\text{Z-PG} + \text{Na}]^+$ , (c)  $[\text{Z-PG} + \text{K}]^+$ , and (d)  $[\text{Z-PG} + \text{Cs}]^+$ .....113

Figure 5.5. (a) ESI/FT-ICR mass spectrum of  $[\text{Z-PG} + \text{H} - \text{CO}_2]^+$  after 600 s HDX reaction time with  $\text{ND}_3$  (at  $P(\text{ND}_3) \approx 4.4 \times 10^{-8}$  Torr).  $D_n$  ( $n = 1$  and 2) denotes the number of deuterium atom(s) incorporated in  $[\text{Z-PG} + \text{H} - \text{CO}_2]^+$ . (b) IM profile of  $[\text{Z-PG} + \text{H} - \text{CO}_2]^+$ . The two vertical dash lines in panel b are guides showing the position of peak ATs of the two  $[\text{Z-PG} + \text{H} - \text{CO}_2]^+$  conformers.....115

Figure 5.6. (a) CID mass spectrum of  $m/z$ -isolated  $[\text{Z-PG} + \text{H}]^+$  ( $m/z$  310) and (b) profile of  $[\text{Z-PG} + \text{H} - \text{CO}_2]^+$ . “G” in *Z-PG* contains two labeled carbon thirteen ( $^{13}\text{C}_2$ ) isotopes and one labeled nitrogen fifteen ( $^{15}\text{N}_1$ ) isotope. Inset in panel a shows the expanded view of  $m/z$  range between 262 to 268 corresponding to loss of carbon dioxide from  $[\text{Z-PG} + \text{H}]^+$ .....117

Figure 5.7. ESI/FT-ICR mass spectra of  $m/z$ -isolated ( $D_0$ ) (left)  $[\text{Z-PG-OMe} + \text{H}]^+$ , (middle)  $[\text{Z-PG-OMe} + \text{Na}]^+$ , (middle)  $[\text{Z-PG-OMe} + \text{K}]^+$ , and (right)  $[\text{Z-PG-OMe} + \text{Cs}]^+$

after 600 s reaction time with ND<sub>3</sub> (at P(ND<sub>3</sub>) ≈ 4.4 × 10<sup>-8</sup> Torr).  
 I ≡ [D<sub>0</sub> + ND<sub>2</sub>H]<sup>+</sup> (*m/z* 340); II ≡ [D<sub>0</sub> + ND<sub>3</sub>]<sup>+</sup> (*m/z* 341);  
 III ≡ [D<sub>1</sub> + ND<sub>3</sub>]<sup>+</sup> (*m/z* 342); IV ≡ [D<sub>2</sub> + ND<sub>3</sub>]<sup>+</sup> (*m/z* 343) .....118

Figure A.1. Sustained off-resonance irradiation-collision induced dissociation (SORI- CID) FT-ICR mass spectrum of protonated AHAAAAA-NH<sub>2</sub>. SORI-CID parameters: Δ*f* = ~- 500 Hz, RF Amplitude = 12 V<sub>base-to-peak</sub>, duration = 262 ms (N<sub>2</sub> was used as collision gas).....129

Figure A.2. Sustained off-resonance irradiation-collision induced dissociation (SORI- CID) FT-ICR mass spectrum of protonated AAA(His)AAA-NH<sub>2</sub>. SORI-CID parameters: Δ*f* = ~- 500 Hz, RF Amplitude = 12 V<sub>base-to-peak</sub>, duration = 262 ms (N<sub>2</sub> was used as collision gas).....131

Figure A.3. Sustained off-resonance irradiation-collision induced dissociation (SORI- CID) FT-ICR mass spectrum of protonated AAAAAA(His)-NH<sub>2</sub>. SORI-CID parameters: Δ*f* = ~- 500 Hz, RF Amplitude = 12 V<sub>base-to-peak</sub>, duration = 262 ms (N<sub>2</sub> was used as collision gas). .....133

Figure A.4. Semi-log plots of ln(D<sub>0</sub>/D<sub>m</sub>) vs. H/D exchange reaction time for (a) b<sub>4</sub><sup>+</sup>, (b) b<sub>5</sub><sup>+</sup> fragment ions of pentaalanine (A<sub>5</sub>). The empty circles (○) and triangles (Δ) in the semi-log plots show the segments corresponding to “fast” + “slow” and “slow” H/D-exchanging populations, respectively. The fitted linear equations for each segment are shown in the plots. The filled square (■) in the semi-log plot in panel (a) corresponds to H/D exchange data which were not used for linear fitting. The mass spectra in panels (c) and (d) are the H/D exchange isotopic patterns (after 100 ms reaction time) of mass isolated <sup>12</sup>C<sub>12</sub> ion populations of b<sub>4</sub><sup>+</sup> and b<sub>5</sub><sup>+</sup>, respectively. CH<sub>3</sub>OD (at pressure of 3.5 × 10<sup>-5</sup> Torr) was used as deuterating reagent. ....135

Figure A.5. Ion mobility arrival time distributions (ATDs) acquired for molecular ions (*i.e.*, [M + H]<sup>+</sup>) and the histidine-containing b<sub>n</sub><sup>+</sup> (n = 4-7) fragment ions of (a) AA(His)AAAA-NH<sub>2</sub> (P3), (b) AAA(His)AAA-NH<sub>2</sub> (P4), and (c) AAAAAA(His)-NH<sub>2</sub> (P7) .....136

Figure A.6. Semi-log plots of ln(D<sub>0</sub>/D<sub>m</sub>) vs. H/D exchange reaction time for b<sub>5</sub><sup>+</sup> fragment ions of AA(His)AAAA-NH<sub>2</sub>. The empty circles (○) and triangles (Δ) in the semi-log plots show the segments corresponding to “fast” + “slow” and “slow” H/D-exchanging populations, respectively. The fitted linear equations for each segment are shown in the plots. The filled squares (■) in the semi-log plots correspond to H/D exchange data which were not used for linear fitting. ND<sub>3</sub> (at pressure of ~4.0 × 10<sup>-8</sup> Torr) was used as deuterating reagent.....137

Figure B.1. Collision-induced dissociation (CID) mass spectra of the *m/z*-isolated

(a)  $[y_6]^+$  ( $m/z$  511) (generated from CID of doubly charged AAAAHAA-NH<sub>2</sub>) and (b)  $[y_6 - (NH_3)]^+$  ( $m/z$  494) (generated from CID of  $[y_6]^+$ ) at 20 % normalized collision energy. Insets in panels (a) and (b) show the expanded views of  $m/z$  range of 422.1 to 422.3 corresponding to identified sequence scrambled fragment ion (*i.e.*,  $[y_6 - (NH_3 + \underline{A})]^+$ ) with mass measurement errors of 4.2 and 0.5 ppm, respectively.....139

Figure B.2. Collision-induced dissociation (CID) mass spectra of the  $m/z$ -isolated (a)  $[y_5]^+$  ( $m/z$  440) (generated from CID of doubly charged AAAAHAA-NH<sub>2</sub>) and (b)  $[y_5 - (NH_3)]^+$  ( $m/z$  423) (generated from CID of  $[y_6]^+$ ) at 20 % normalized collision energy. Insets in panels (a) and (b) show the expanded views of  $m/z$  range of 351.0 to 351.3 corresponding to identified sequence scrambled fragment ion (*i.e.*,  $[y_5 - (NH_3 + \underline{A})]^+$ ) with mass measurement errors ~ 3.3 and 0.1 ppm respectively.....140

Figure B.3. Collision-induced dissociation (CID) mass spectra of the  $m/z$ -isolated (a)  $[y_4]^+$  ( $m/z$  440) (generated from CID of doubly charged AAAAHAA-NH<sub>2</sub>) and (b)  $[y_4 - (NH_3)]^+$  ( $m/z$  423) (generated from CID of  $[y_4]^+$ ) at 20 % normalized collision energy. Insets in panels (a) and (b) show the expanded views of  $m/z$  range of 351.0 to 351.3 corresponding to identified sequence scrambled fragment ion (*i.e.*,  $[y_4 - (NH_3 + \underline{A})]^+$ ) with mass measurement accuracy of 0.5 and 0.4 ppm respectively.....141

Figure C.1. Overlaid IM profiles of  $[Z-PG + Ca - H]^+$  (dash curve) and  $[Z-PG + K]^+$  (solid curve).....147

Figure C.2. (a) Post-IM/CID MS profile of  $m/z$ -isolated  $[Z-PG + H - CO_2]^+$ . (b) Deconvoluted IM profiles of “Compact” (solid curve) and “Elongated” (dash curve) conformers of  $[Z-PG + H - CO_2]^+$ . Insets show the deconvoluted CID mass spectra of “Compact” (left) and “Elongated” (right) conformers of  $[Z-PG + H - CO_2]^+$ . A previously reported IM deconvolution technique (*J. Am. Soc. Mass Spectrom.* 2012, 23, 1873-1884) was used to extract pure IM and CID mass spectra of the two  $[Z-PG + H - CO_2]^+$  conformers. Post-IM/CID MS experiment was performed by setting the potential difference between IM cell exit and transfer cell entrance to 28 V. All other parameters are given in experimental section.....148

## LIST OF SCHEMES

Scheme 4.1. Possible pathways for formation of fragment ions at $m/z$ 422 and 423 generated from CID of $[y_6]^+$ from AAAAH <u>A</u> ANH <sub>2</sub> .....	83
Scheme 4.2. Proposed mechanism for generation of sequence-scrambled fragment ions from CID of $[y_7]^{2+}$ from des-acetylated- $\alpha$ -melanocyte.....	88
Scheme 4.3. Proposed mechanism for generation of sequence-scrambled fragment ions from CID of $[y_7]^+$ from angiotensin II anti-peptide.....	94
Scheme 5.1. Benzyloxycarbonyl (Z)-proline (P) glycine (G) .....	100

## LIST OF TABLES

Table 3.1. Experimental rate constants for $b_4^+$ - $b_7^+$ fragment ions of all seven (His)(A) <sub>6</sub> -NH <sub>2</sub> type model heptapeptides. Rate constants are in $\times 10^{-11}$ cm <sup>3</sup> molecule <sup>-1</sup> s <sup>-1</sup> and an average of three experimental trials, with standard deviations (n = 3) included within parentheses.....	63
Table 3.2. Ion mobility peak arrival time, full width at half height (FWHH), and R <sup>2</sup> obtained from Gaussian curve fitting for [M + H] <sup>+</sup> and histidine-containing $b_4^+$ - $b_7^+$ fragment ions of seven (P1-P7) studied heptapeptides.....	67
Table 4.1. Summary of the total number of observed fragments, number of scrambled fragments, and the identities of the scrambled fragment ions generated from CID of y fragment ions from des-acetylated- $\alpha$ -melanocyte, angiotensin II antipeptide, and glu-fibrinopeptide b.....	90
Table 5.1. Experimental and theoretical collision cross sections ( $\Omega$ ) of Z-PG and Z-GP species. Errors at 95 % confidence level (n = 15 for experimental and n = 40 for theoretical) are included in parentheses.....	114
Table A1. Amino acid composition of the observed SORI-CID fragment ions, their theoretical $m/z$ , experimental $m/z$ , and MMA errors for protonated A(His)AAAAA-NH <sub>2</sub> (signal-to-noise threshold for the assigned fragments is higher than ~4). The fragment ion that could exclusively be assigned as scrambled ion is shown in italic font.....	130
Table A2. Amino acid composition of the observed SORI-CID fragment ions, their theoretical $m/z$ , experimental $m/z$ , and MMA errors for protonated AAA(His)AAA-NH <sub>2</sub> (signal-to-noise threshold for the assigned fragments is higher than ~4). The two fragment ions that could exclusively be assigned as scrambled ions are shown in italic font.....	132
Table A3. Amino acid composition of the observed SORI-CID fragment ions, their theoretical $m/z$ , experimental $m/z$ , and MMA errors for protonated AAAAAA(His)-NH <sub>2</sub> (signal-to-noise threshold for the assigned fragments is higher than ~4) .....	134
Table B1. Fragment ion identity, theoretically calculated $m/z$ values, experimentally observed $m/z$ values, and error (ppm) of the assigned fragment ions observed in CID mass spectrum of	

$[y_7]^{+2}$  (FRWGKPV-NH<sub>2</sub>) from des-acetylated- $\alpha$ -melanocyte. The sequence-scrambled fragment ions are shown in italic font.....142

Table B2. Fragment ion identity, theoretically calculated  $m/z$  values, experimentally observed  $m/z$  values, and error (ppm) of the assigned fragment ions observed in CID mass spectrum of  $[y_7 - (NH_3)]^{+2}$  from des-acetylated- $\alpha$ -melanocyte. The sequence-scrambled fragment ion is shown in italic font.....143

Table B3. Fragment ion identity, theoretically calculated  $m/z$  values, experimentally observed  $m/z$  values, and error (ppm) of the assigned fragment ions observed in CID mass spectrum of  $[y_7]^+$  [GVYVHPV] from angiotensin II anti-peptide. The sequence-scrambled fragment ions are shown in italic font.....144

Table B4. Fragment identity, theoretically calculated  $m/z$  values, experimentally observed  $m/z$  values, and error (ppm) of assigned fragment ions observed in CID spectrum of  $[y_7 - (H_2O + PV)]^+$  from angiotensin II anti-peptide. The fragment ions that could be assigned as scrambled ions are shown in italic font.....145

## ABBREVIATIONS

<i>Abbreviation</i>	<i>Description</i>
AE	Appearance Energy
ATDs	Arrival Time Distributions
BIRD	Blackbody Infrared Radiative Dissociation
B3LYP	Becke 3-Parameter Lee-Yang-Parr Functional
BSA	Bovine Serum Albumin
CID	Collision-Induced Dissociation
CCS or $\Omega$	Collision Cross Section
DC	Direct Current
DFT	Density Functional Theory
DT	Drift Tube
e	Electron
ECD	Electron Capture Dissociation
EI	Electron Ionization
ESI	Electrospray Ionization
nESI	Nano-Electrospray Ionization
ETD	Electron Transfer Dissociation
FAB	Fast Atom Bombardment
FAIMS	Field Asymmetric Waveform Ion Mobility Spectrometry
FT	Fourier Transform
FT-ICR	Fourier Transform-Ion Cyclotron Resonance
FWHHs	Full-Width Half-Heights
GB	Gas-Phase Basicity
GPMDB	Global Proteome Machine Database
HDMS	High Definition Mass Spectrometry
HDX	Hydrogen/Deuterium Exchange
HPLC	High-Performance Liquid Chromatography
ICR	Ion Cyclotron Resonance
IM-MS	Ion Mobility-Mass Spectrometry
IMS	Ion Mobility Spectrometry
IRMPD	Infrared Multiphoton Dissociation
LC	Liquid Chromatography
LD	Laser Desorption
LTQ	Linear Trap Quadrupole

## ABBREVIATIONS

<i>Abbreviation</i>	<i>Description</i>
MALDI	Matrix Assisted Laser Desorption Ionization
MMA	Mass Measurement Accuracy
MPD	Multiphoton Dissociation
MRP	Mass Resolving Power
MS	Mass Spectrometry
MW	Molecular Weight
<i>m/z</i>	Mass-to-Charge Ratio
NIST	National Institute Of Standards And Technology
NMR	Nuclear Magnetic Resonance
PA	Proton Affinity
PD	Plasma Desorption
PPG	Polypropylene Glycol
PTM	Post-Translational Modification
PW	Peak Width
Q	Quadrupole
QIT	Quadrupole Ion Trap
RF	Radio Frequency
SID	Surface-Induced Dissociation
SIMS	Secondary Ion Mass Spectrometry
SRIG	Stacked Ring Ion Guide
SORI	Sustained Off Resonance Irradiation
SWIFT	Stored Waveform Inverse Fourier Transform
S/N	Signal-To-Noise Ratio
TIC	Total Ion Chromatogram
TOF	Time-Of-Flight
T-Wave	Travelling Wave
TWIG	Travelling Wave Ion Guide
TWIMS	Travelling Wave Ion Mobility Spectrometry
UHV	Ultra High Vacuum
VOC	Volatile Organic Compound
Z	Benzyloxycarbonyl

## AMINO ACID ABBREVIATIONS

<i>One Letter Abbreviation</i>	<i>Three Letter Abbreviation</i>	<i>Amino Acid</i>
A	Ala	Alanine
D	Asp	Aspartic Acid
C	Cys	Cysteine
E	Glu	Glutamic Acid
F	Phe	Phenylalanine
G	Gly	Glycine
H	His	Histidine
I	Ile	Isoleucine
K	Lys	Lysine
L	Leu	Leucine
M	Met	Methionine
N	Asn	Asparagine
P	Pro	Proline
Q	Gln	Glutamine
R	Arg	Arginine
S	Ser	Serine
T	Thr	Threonine
V	Val	Valine
W	Trp	Tryptophan
Y	Tyr	Tyrosine

## ACKNOWLEDGMENTS

First and foremost, I would like to express my deepest gratitude to my advisor, Dr. Touradj Solouki, for his guidance, support, and patience throughout my graduate degree. He provided expert direction, a state-of-art research environment, and the ability to work with distinguished collaborators. He supported me to present my research at national conferences and introduced me to others who are engaged in cutting-edge research in sciences. He also gave me opportunities to improve myself in many areas including scientific reasoning, oral presentation of my research, and written communication.

My thanks are also extended to my committee members, Dr. C. Kevin Chambliss, Dr. Charles Garner, Dr. Chris Kearney, and Dr. Sascha Usenko for taking time to review my dissertation, offer helpful suggestions through valuable discussions, and for their accessibility. I also appreciate support and instrumental training from Dr. Alejandro Ramirez, director of MS facility in chemistry and biochemistry department. Furthermore, I would like to acknowledge Dr. Becker and Dr. Munisamy from Dr. Chambliss's research group for helpful discussions and training on ion mobility mass spectrometry instruments.

I would also like to thank Dr. Kevin L. Shuford for his assistance and discussions for performing molecular modeling in the work presented in this dissertation. I gratefully acknowledge all the people with whom we collaborated including Dr. Arpad Somogyi (University of Arizona), and Dr. Talat Yalcin (Izmir Institute of Technology, Department of Chemistry, Turkey). Additional thanks must also be given to the faculty, staff, and

graduate students of chemistry and biochemistry department at Baylor University for making my graduate time at Baylor University a great experience.

My great thanks also go to current and past members of Dr. Solouki's research group (Dr. Szulejko, Abdullah, Brett, Daniel, Ting, Jackie, Elizabeth) for giving me the opportunity to work in such a friendly and helpful laboratory environment. You are my family here and you have made the graduate time a great memory that I will cherish forever in my life. I wish you all the best for the future.

Finally, affectionate thankfulness is given to my husband, Behrooz Zekavat, for all of his support, encouragement, patience, and love during the past five years of my life and to my parents and my brothers, for their faith in me and unending encouragements.

## DEDICATION

To my husband, Behrooz, for his love, patience, and support.

To my parents, Malektaj and Masoud, for their endless love and encouragement.

## CHAPTER ONE

### *Introduction*

#### *1.1. Biological Mass Spectrometry*

A major portion of current efforts in biological sciences is focused on the understanding of “systems biology” of living organisms.<sup>1, 2</sup> The term “systems biology” refers to comprehensive study of “x-omics” (*i.e.*, genomics, metabolomics, proteomics, and transcriptomics) of living organisms.<sup>3</sup> The ultimate goal in “systems biology” research is to understand the connections between complex networks of biological events that can result in either diseased or healthy states of living systems.<sup>4</sup> Analyses of complex biological networks/samples requires the use of highly sensitive state-of-the-art instrument that can (i) resolve different components of a mixture, (ii) provide individual molecular identities, (iii) yield relative abundance or concentration information, and (iv) illustrate potential interactions among various sample constituents at a high level of confidence.<sup>5</sup>

To address these challenging analytical requirements in emerging areas of science, performance characteristics of modern instruments are continuously improved.<sup>6, 7</sup> Because of the minimal sample requirements<sup>8, 9</sup> and potential for rapid sample analyses<sup>10, 11</sup> mass spectrometry (MS) (and in particular MS-based proteomics) has played a significant role in systems biology research.<sup>12, 13</sup> Recent developments in instrumentation and bioinformatics have made MS-based proteomics an essential analytical tool for characterization of living cells and organisms at the molecular level. In MS-based

proteomic measurements/studies, either digested or intact proteins are subjected to gas-phase fragmentation and MS analyses. The resulting fragment ions are then utilized to determine sequences of peptides and/or proteins from which the digested peptides and/or fragment ions are originated.

Results from structural mass spectrometry and gas-phase protein sequencing are most reliable when gas-phase ion rearrangements either do not occur or are very minor reaction channels. However, ion rearrangements impose tangible limitations for modern tandem and biological mass spectrometry. The focus of this dissertation is to investigate prevalence and mechanism(s) of gas-phase ion rearrangements and their importance in the application and use of MS and tandem MS techniques for structural characterization of peptides and peptide fragment ions. To streamline the description of dissertation objectives, this chapter provides an introduction to some important MS techniques, concepts, and terminologies but more detailed description of MS-based proteomics is given in Chapter two.

## *1.2. Mass Spectrometers*

All mass spectrometers are consisted of three primary components: (i) an ionization source, (ii) a mass analyzer, (iii) and a detector. Depending on the mechanisms of ion detection and types of mass analyzers, all mass spectrometers operate under high ( $\sim 10^{-7}$  Torr) or ultrahigh ( $\sim 10^{-10}$  Torr) vacuum to avoid unwanted chemical reactions,<sup>14, 15</sup> ion-molecule collisions,<sup>16</sup> neutralization of ions,<sup>17</sup> and ion scattering.<sup>18</sup> Following sections provide additional instrumental details about the specific mass spectrometers that were used in this research.

### 1.2.1. Ionization Sources

The first step in MS analysis is to convert analyte of interest into gas-phase ions. Selection of the “hard” (*e.g.*, electron impact (EI)<sup>19</sup> and laser desorption (LD)<sup>20</sup>) or “soft” (*e.g.*, chemical ionization (CI),<sup>21</sup> electrospray ionization (ESI)<sup>22-24</sup>, matrix-assisted laser desorption ionization (MALDI)<sup>20, 25, 26</sup>) ionization types normally depends on the state (*viz.*, gas-, liquid-, or solid-phase) and classes of compounds under the study. For example, biological samples have relatively high molecular weight (MW) compounds, such as proteins and peptides, with high polarities. High MWs and polarities of proteins and peptides limit their volatilities and subsequent ionizations by EI.

Ionization of large labile molecules (polar non-volatile compounds) such as proteins was initially reported by using plasma desorption (PD).<sup>27</sup> This invention was followed by introduction of various other ionization techniques (*e.g.*, fast atom bombardment (FAB)<sup>28</sup> and secondary ionization MS (SIMS)<sup>29</sup>), including two of the very important ionization techniques in biological MS, namely, MALDI<sup>20, 25, 26</sup> and ESI<sup>22-24</sup> that changed the field of modern MS-based proteomics. Each of the latter ionization techniques resulted in recent Nobel Prizes devoted to MS-related topics. In the following section, a brief description of ESI method is presented.<sup>30</sup>

#### 1.2.1.1. Electrospray Ionization

Ionization in ESI is achieved under atmospheric pressure and by applying a high electric field to a sample in liquid phase passing through a metal nano/micro capillary tip (Figure 1.1). A high electric field is established by setting a voltage difference ( $\sim +2$  kV to  $\sim +5$  kV for positive-ion mode ESI) between the metal nano/micro capillary and mass spectrometer inlet. Ion generation process in ESI includes three major steps<sup>31</sup>: (i) droplet

generation and charging at ES capillary tip, (ii) droplet shrinkage and evaporation, and (3) gaseous ion formation.<sup>32</sup> The applied high electric field on metal capillary tip generates ions inside the solution, and causes positive ions to be drawn near the surface of capillary and meniscus of the liquid. The liquid meniscus is then destabilized (when enriched with positive ions) and forms charged droplets.

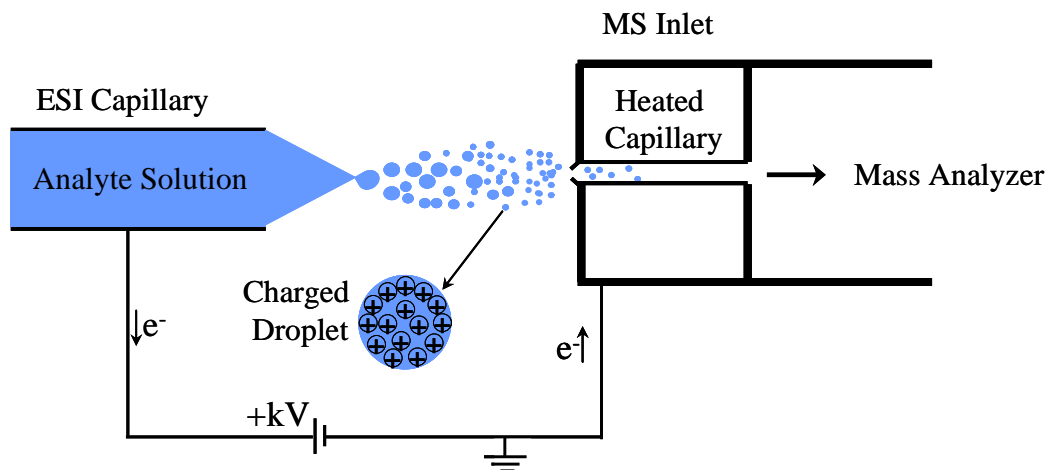


Figure 1.1. Schematic representation of positive-ion mode ESI setup.

To evaporate solvent molecules from the generated charged droplets, either a heated metal capillary or hot inert gas (*e.g.*, heated  $N_2$ ) is used. Upon solvent evaporation, the sizes of charged droplet become smaller and the highly charged droplets start to shrink and break/divide into smaller droplets. This phenomenon occurs because the number of charge particles per unit volume of a droplet increases and reaches the Coulombic repulsion or “Rayleigh stability limit”.<sup>33</sup>

Two models, including “charge residue” and “ion evaporation”, have been proposed for generation of gas-phase ions from charged droplets.<sup>34</sup> The charge residue

model suggests that large charged droplets shrink and form smaller droplets. The charged droplet shrinkage process is repeated until each droplet contains only one charged particle (molecular ion). The remaining single molecular ion in the droplet is then released into gas phase after solvent is completely evaporated.

The ion evaporation model suggests that a large charged droplet shrinks upon solvent evaporation until droplet surface charge density is sufficiently high to eject the charged particles/molecular ions directly into the gas phase from the droplet.<sup>34</sup> Once the analytes of interest are ionized they can be guided into a mass analyzer and then a detector for mass-to-charge ratio ( $m/z$ ) measurements/analyses.<sup>35</sup>

### 1.2.2. Mass Analyzers

Mass analyzers in mass spectrometers are used to separate ions according to their mass-to-charge ( $m/z$ ) ratios. Generally, it is the mass analyzer type that plays a key role in establishing achievable mass resolving power ( $m/\Delta m_{50\%}$ ) for a mass spectrometer. All currently utilized mass analyzers separate or measure ions based on known ion physics or theories that relate charge of an ion ( $q = e \cdot z$ ) to its motion in magnetic (**B**) and/or electric (**E**) fields; each analyzer has its own merits and limitations.<sup>36</sup>

Mass analyzers can be selected based on their applications, resolving powers, costs, and desired performances. Some commonly used mass analyzers include ion traps<sup>37</sup> with different configurations (*e.g.*, ion cyclotron resonance (ICR) cell,<sup>38</sup> Orbitrap,<sup>39</sup> *etc.*), linear quadrupoles,<sup>40</sup> and time-of-flight (TOF).<sup>41</sup> Following sections contain additional detailed descriptions about principles of mass analysis with two Fourier transform (FT)-based, FT-ICR and Orbitrap, and TOF mass analyzers.

### 1.2.2.1. Fourier Transform-Ion Cyclotron Resonance (FT-ICR) Mass Analyzer

Lawrence and Edlefsen, two nuclear physicists, introduced the ICR phenomenon in 1930 by invention of a circular particle accelerator.<sup>42</sup> Lawrence *et al.* demonstrated that cyclotron radius of an ion can be increased by applying an alternating electric field of the same frequency as the ion's natural cyclotron frequency.<sup>43</sup> Introduction of cyclotron resonance phenomenon resulted in the invention of the first ICR-based mass spectrometer for measuring the Faraday constant and  $m/z$  of EI-generated hydrogen ions with a mass resolving power (MRP) of  $m/\Delta m_{50\%} \sim 3,500$  (at a constant magnetic field of 4,700 gauss).<sup>44</sup> The first commercial ICR instrument, known as ICR-9, was introduced by Varian Associates and Stanford University (SU) in 1966.<sup>45, 46</sup>

The Varian-SU ICR system was designed for gas-phase ion-molecule reaction studies. In 1970, McIver introduced an analyzer cell for ion trappings of up to 0.1 s.<sup>38</sup> McIver's ICR cell had two end trapping plates for application of electrostatic trapping voltages and trapping ions in the direction of magnetic field. Later, in 1974, Marshall and Comisarow utilized FT techniques in ICR mass spectrometry and introduced the concept of FT-ICR MS in which multiple ions could be trapped and analyze simultaneously.<sup>47</sup>

Among all currently available mass analyzers, FT-ICR offers the highest mass measurement accuracy (MMA)<sup>48</sup> and mass resolving power (MRP)<sup>49, 50</sup> for analysis of gas-phase ions.<sup>51</sup> In addition to superb sensitivity advantage,<sup>52-54</sup> FT-ICR MS is the technique of choice for conducting ion-molecule reactions and measuring accurate gas-phase reaction rate constants.<sup>55</sup> The basic principle of  $m/z$  analysis in ICR relies on physics of moving charged particles in uniform magnetic fields. Figure 1.2 shows an ion moving perpendicular to a constant magnetic field (**B**); this ion is subjected to two forces

that are known as Lorentz force ( $\mathbf{F}_L$ ) and centrifugal force ( $\mathbf{F}_C$ ) (bold letters indicate vector quantities)<sup>56, 57</sup>:

$$\mathbf{F}_L = m (d\mathbf{v} / dt) = q (\mathbf{v} \times \mathbf{B}) \quad (\text{Equation 1.1})$$

In equation (1.1), “m”, “v”, and “q” denote the mass, velocity, and charge of an ion, respectively, and “t” denotes time. The ion’s velocity component(s), which is perpendicular to  $\mathbf{B}$ , brings the ion into a cyclotron motion (Figure 1.2). Assuming that the direction of magnetic field lines is in the Z direction (in/out of page in Figure 1.2), ions rotate around the Z coordinate and in the X-Y plane.

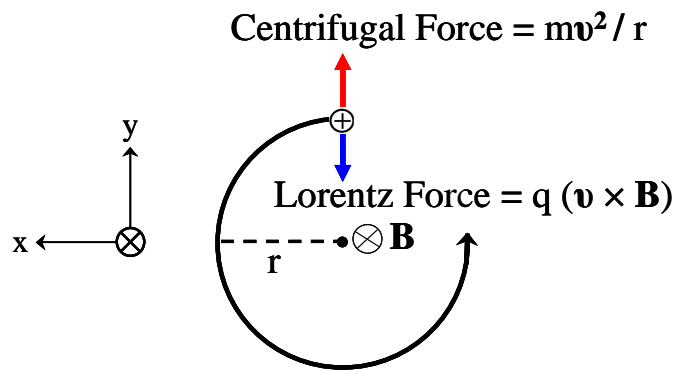


Figure 1.2. An ion immersed in the magnetic field of “ $\mathbf{B}$ ” experiences both magnetic Lorentz and centrifugal forces.

The magnitude of two forces ( $\mathbf{F}_L$  &  $\mathbf{F}_C$ ) on the ion with cyclotron radius of “r” is:

$$q \times v_{xy} \times B = m \times (v_{xy}^2 / r) \quad (\text{Equation 1.2})$$

where “ $v_{xy}$ ” is ion’s velocity in X-Y plane and is calculated from:

$$v_{xy} = [(v_x^2 + v_y^2)]^{0.5} \quad (\text{Equation 1.3})$$

Equation (1.2) can be simplified to yield the following equation:

$$q \times B / m = v_{xy} / r \quad (\text{Equation 1.4})$$

Also, angular velocity (“ $\omega$ ” in rad/s) is defined as:

$$\omega = v_{xy} / r = 2\pi \times f \quad (\text{Equation 1.5})$$

From equations (1.4) and (1.5), the natural ICR angular frequency of ions can be calculated:

$$\omega = 2\pi \times f = q \times (B / m) \quad (\text{Equation 1.6})$$

In conventional FT-ICR MS, ions can be produced inside or outside of the ICR cell. In external ion source FT-ICR MS,<sup>58, 59</sup> ions, after their generation in external ionization sources, are transferred into the ICR cell using a series of ion focusing lenses and radio frequency (RF)-only ion guides<sup>60</sup> such as quadrupoles, hexapoles, or octapoles. Figure 1.3 shows the configuration of an IonSpec (former IonSpec Corp.-now a division of Agilent Technologies, Inc., Santa Clara, CA, USA) FT-ICR mass spectrometer equipped with an external ESI source, quadrupole ion guide, and a 9.4 T superconducting magnet (used for conducting experiments reported in this dissertation). Ultrahigh vacuum (pressure < 10<sup>-9</sup> Torr) is maintained by using three turbo-pumps (denoted as TP in Figure 1.3). The system is also equipped with a hexapole assembly for ion accumulation prior to FT-ICR MS detection and enhanced analytical sensitivity.<sup>61</sup>

Major steps/events involved in FT-ICR MS signal detection and mass spectrum acquisition include: (a) ion quenching, (b) ion trapping, (c) reaction delay, (d) ion excitation, and (e) ion detection event. During ion quenching event, the ICR cell is cleaned from any existing ions that may have been left from a previous experiment. Ion quenching is achieved by applying a direct current (DC) positive (or negative) voltage to one ICR cell end trapping plate and a DC negative voltage (or opposite polarity with respect) to the opposite end trapping plate. In an “ion trapping” event, the transferred ions

from an external ionization source or internally generated ions (*i.e.*, within the cell) are trapped inside the ICR cell.

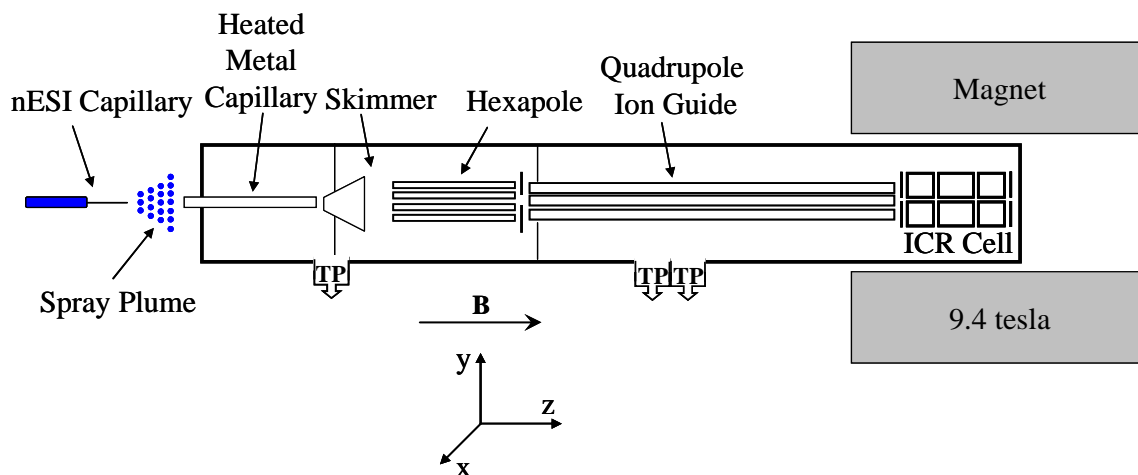


Figure 1.3. Illustration of the basic components of IonSpec ESI/FT-ICR mass spectrometer equipped with an open-ended cylindrical Penning trap and a 9.4 tesla superconducting magnet.

Ion trapping is achieved by applying a symmetric DC voltage to the two ICR cell trapping plates to restrict the motion of ions in the Z direction (parallel to the magnetic field lines). The translational energy of trapped ions may be collisionally reduced or “cooled” *via* ion-neutral collisions.<sup>62</sup> Generally, an inert neutral gas (*e.g.*, N<sub>2</sub>) is used for “ion cooling” in the ICR cell. If desired, trapped ions can be reacted with a neutral reagent gas (*e.g.*, hydrogen/deuterium (H/D) exchange and proton transfer reagents) to conduct gas-phase ion-molecule reactions.<sup>63</sup>

After the introduction of ion cooling inert gas and/or ion-molecule reaction reagent(s), quite often, “reaction delay” events are used to reach to UHV conditions. Pressure reductions inside the ICR cell (or acceptable UHV conditions) are desirable for

subsequent FT-ICR MS excitation and successful ion detection. To detect signals from trapped ions in ICR cells, ions should form monopoles<sup>64</sup> and their ICR radii should be sufficiently large to induce an image current on the detection plates. To achieve the aforementioned outcome (*i.e.*, to generate detectable monopole ion packets), in the excitation event, a combination of alternating electrical fields with varied frequencies (known as “chirp” or frequency sweep excitation)<sup>65</sup> is applied on excitation plates of the ICR cell. The ion detection event is represented pictorially in Figure 1.4. Immediately after the excitation event, induced ion current on detection plates of the ICR cell are recorded as a function of time (time-domain signal). The ICR frequencies ( $f$ ) of the detected ions are subsequently extracted by performing Fourier transform (FT) on the detected ion image signal (*i.e.*, FT of time domain transient signal to frequency domain).<sup>66</sup> The experimentally observed ions’ frequencies are then converted to  $m/z$  values by incorporating the magnetic field strength ( $B$ ) and using equation (1.6) and a calibration file.<sup>67</sup> Lastly, the ions’ intensities are plotted as a function  $m/z$  to obtain an FT-ICR mass spectrum.

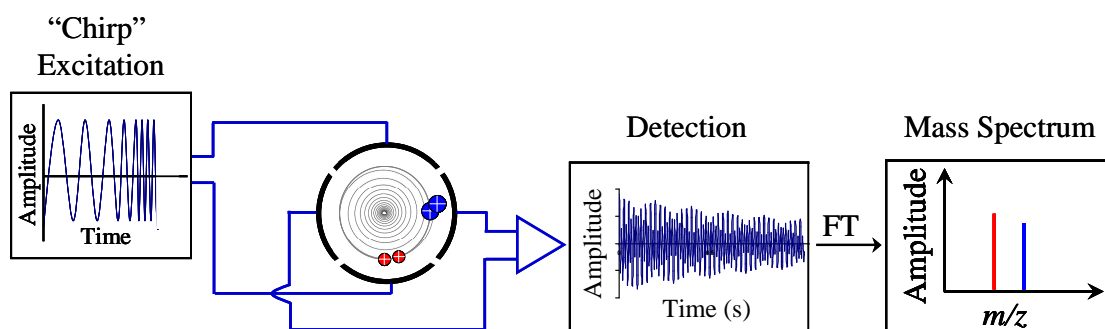


Figure 1.4. Schematic representation of an ion detection event in FT-ICR MS.

The mass resolving power (MRP) of mass spectral peaks in FT-ICR mass spectra depends on the number of data points and acquisition duration of time-domain signals.<sup>56</sup> Generally, the MRP of FT mass spectra increases with time-domain signals' duration. Time-domain signals are multiplied by special “window” functions prior to Fourier transformation.<sup>68</sup> This process is called “windowing” in time domain and “apodization” in frequency domain.<sup>68</sup> Windowing and apodization reduce the spectral skirts (known as “leakage”<sup>68</sup>) and narrow the peak widths at the base. Two most commonly used window functions include Blackman-Harris and Hamming functions.<sup>68</sup>

#### *1.2.2.2. Orbitrap Mass Analyzer*

Another FT-based ion trap mass analyzer that has rapidly become a popular tool for “x-omics” analyses is the Orbitrap.<sup>66, 69</sup> An Orbitrap consists of an electrostatic ion trap device, and its principle is based on an earlier ion storage device, the Kingdon trap.<sup>70</sup> The Orbitrap mass analyzer was originally introduced by Makarov<sup>71</sup> in 2000 and it was commercialized in the form of a hybrid linear ion trap/Orbitrap mass spectrometer in 2005.<sup>72</sup> It should be noted that Orbitrap-like ion trajectories and detections were reported earlier in FT-ICR MS experiments.<sup>73, 74</sup> Figure 1.5 shows a cross sectional view of a typical Orbitrap cell. An Orbitrap cell consists of a spindle-like central electrode and a barrel-like outer electrode (Figure 1.5).

Ions enter the Orbitrap cell through a narrow ion injection port tangentially to the outer electrode. Subsequently, ions are trapped by keeping the outer detection electrodes at ground potential and application of a high voltage (kV range) to the central electrode.<sup>69,</sup>  
<sup>75</sup> The resulting quadrologarithmic electrostatic potential (combination of quadrupole

field of the ion trap and a logarithmic field of a cylindrical capacitor) brings the trapped ions into a spiral oscillation motion around the central electrode (Figure 1.5).<sup>71</sup>

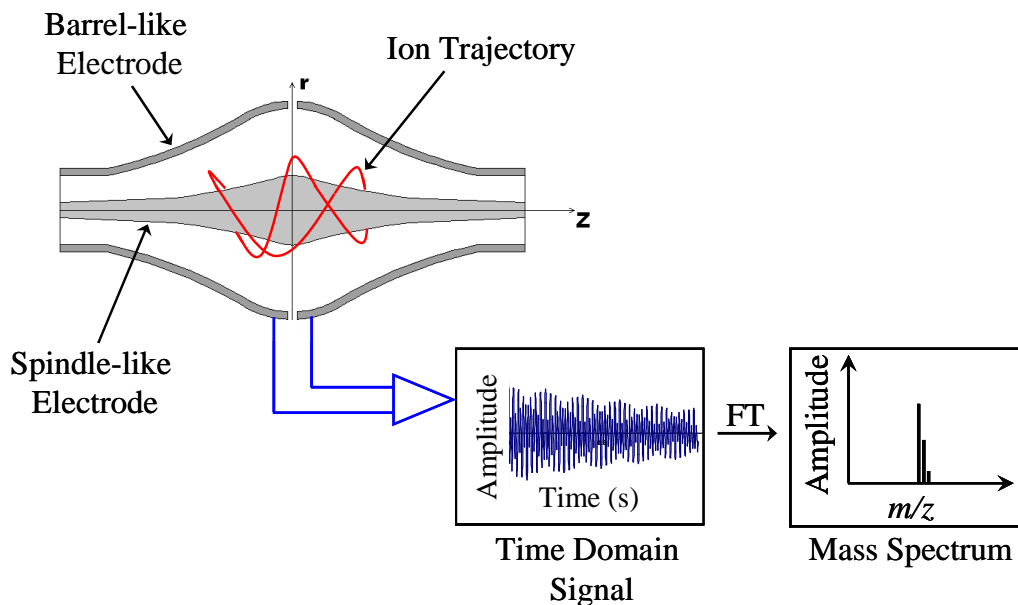


Figure 1.5. Pictorial representation of the cross sectional view of an Orbitrap mass analyzer.

The oscillating ions in Orbitrap induce an image current (time-domain signal) on the outer electrodes. Ion signal detection is followed by FT of the recorded image current to convert the time-domain signal into the axial (along the Z axis in Figure 1.5) frequencies of the trapped ions.

The axial frequency of an oscillating ion in Orbitrap is inversely proportional to the square root of the ion's  $m/z$  value according to equation (1.7)<sup>71</sup>:

$$\omega = [(q / m) \times k]^{0.5} \quad \text{(Equation 1.7)}$$

where “q” and “m” denote the mass and charge of the ion. “k” is a constant that depends on the precise geometrical shape of the Orbitrap cell electrodes and applied potential.

### 1.2.2.3. Time of Flight (TOF) Mass Analyzer

The concept of time-of-flight (TOF) mass analyzer was described by Stephens in 1946.<sup>76</sup> Later, Wiley and McLaren demonstrated the first design of a commercial TOF MS instrument in 1955.<sup>77</sup> The principle of ion analysis in TOF mass analyzers is based on gas-phase separation of accelerated ions in a field-free region of a flight tube. TOF consists of an ion acceleration source and a long flight tube (generally ~1 m to 2 m in length) in which ions can fly under zero electric field condition. Flight times of ions (after departing the ion acceleration region) that have different  $m/z$  values will be different in a field-free flight tube. This  $m/z$ -dependent flight time is the basis of mass analysis in TOF MS instruments.

In a typical TOF MS analysis, ion packets (from ion sources) are accelerated into the TOF drift tube. To maintain the same starting time (time zero) for all ions, acceleration event is pulsed either by pulsing the acceleration voltage or ionization event itself (for example, by using a short laser pulse).<sup>78</sup> Once ions are accelerated in the same electric field (or acceleration field  $\mathbf{E}$ ), all departing ions that have same electrical charges will possess the same kinetic energy (*i.e.*,  $KE = \mathbf{E} \cdot q = \frac{1}{2} mv^2$ ) when they enter a field-free tube. However, lighter ions (with small  $m$ ) will have higher velocities ( $v$ ) and thus reach the TOF detector first (while heavier ions will arrive at the detector at longer times). In a conventional linear TOF instrument, a detector is positioned at the end of the TOF analyzer to measure the arrival time of each ion. By knowing the flight time of each ion ( $t$ ), the  $m/z$  of the ion can be determined according to equation (1.8)<sup>41</sup>:

$$m/z = 2 \times e \times V \times (t^2 / L^2) \quad (\text{Equation 1.8})$$

where “*m*” denotes mass of an ion, “*z*” denotes the charge state of the ion, “*e*” denotes electron charge, “*V*” denotes acceleration voltage, “*t*” denotes ion’s flight time, and “*L*” denotes the length of flight tube.

### *1.3. Gas-Phase Ion Fragmentation Techniques in Proteomics*

Development of various ion fragmentation techniques has increased the protein/peptide sequence coverage/information and revolutionized the field of proteomics.<sup>79</sup> Several different types of ion dissociation techniques are utilized in MS-based proteomics studies. These ion fragmentation techniques can be classified into two general categories: (a) activational and (b) non-activational dissociation techniques. Examples of activational dissociation techniques include collision induced dissociation (CID),<sup>80</sup> sustained off-resonance irradiation collision induced dissociation (SORICID),<sup>81</sup> multiphoton dissociation (MPD),<sup>82, 83, 84</sup> surface induced dissociation (SID),<sup>85, 86</sup> and blackbody infrared radiative dissociation (BIRD).<sup>87</sup> The two most important non-activational fragmentation techniques are electron capture dissociation (ECD),<sup>88</sup> electron transfer dissociation (ETD).<sup>89</sup>

In activational techniques, vibrational or electronic energy of an ion is increased stepwise (*e.g.*, by multiple collisions in CID or absorption of photons in MPD) until the accumulated vibronic energy surpasses the fragment ion “appearance energy”<sup>90, 91</sup> and becomes sufficient to cleave the weakest bond.<sup>92</sup> Also, acquired energy by the ion in activational fragmentation methods can be randomized throughout different chemical bonds in the ion.<sup>93, 94</sup> However, in non-activational, or ergotic techniques there is a low chance for an ion to distribute its acquired internal energy to different chemical bonds.<sup>95</sup> Among gas-phase activational dissociation techniques, CID is the most commonly used

fragmentation method in MS-based proteomics.<sup>96, 97</sup> In CID experiments, precursor ions are accelerated and forced to collide with neutral gas molecules (*e.g.*, nitrogen (N<sub>2</sub>) or argon (Ar)) in the source region or collision cell (*e.g.*, ion trap cell) of mass spectrometers. In inelastic collision between a precursor ion and neutral gas molecule, a portion of kinetic energy of precursor ion is converted into internal energy and results in fragmentation of precursor ions.<sup>92</sup>

Among non-activational techniques, ECD is widely used for identification of proteins' post-translational modifications (PTMs) in proteomics.<sup>98, 99</sup> There is a high probability for loss of labile PTMs on proteins/peptides backbones during dissociation when PTM-containing proteins/peptides are subjected to fragmentation using activational techniques. PTM loss can make it difficult, or impossible, to localize the site of modifications in proteins/peptides. In ECD a multiply charged ion (*e.g.*, of a protein) is trapped inside the MS ion trap cell (*e.g.*, ICR) and irradiated by low energy (< 1eV) electrons. Electron capture by proteins/peptides generates radical species that rapidly undergo chemical bond cleavage.<sup>99</sup> Although implementation of CID is straightforward, ECD and CID can each provide unique operational advantages and used as a standalone or combined ion fragmentation technique.<sup>100, 101</sup>

More details about various gas-phase fragmentation techniques can be found in references<sup>92, 102, 103</sup>.

#### *1.4. Gas-phase MS Techniques for Conformational Analysis of Proteins/Peptides*

The ability to analyze the tertiary structures of proteins remains as a driving force for development of analytical tools capable of providing detailed structural/conformational information. Predominantly utilized techniques for determining

atomic-resolution structures of biomolecules are X-ray crystallography<sup>104</sup> and nuclear magnetic resonance (NMR) spectroscopy.<sup>105</sup> However, there are challenges associated with using these spectroscopy techniques for structural analysis of proteins. For example, X-ray crystallography provides static snapshots of proteins/peptides. However, proteins/peptides are not static objects, and their behavior cannot be adequately described only based on the information derived from X-ray structure and without considering their dynamic character<sup>106</sup>. Structural studies by NMR technique suffer from challenges in data interpretation, sensitivity, and slow data acquisition/collection rate.<sup>107, 108</sup>

Advances in modern MS techniques and instrumentation have increased the ability to study conformations of proteins/peptides in a solvent-free gas-phase environment. Hydrogen/deuterium exchange (HDX) reactions and ion mobility-mass spectrometry (IM-MS) are two powerful approaches for detailed conformational analysis of proteins/peptides. Principles of these two gas-phase conformational analysis probes are described in the following sections.

#### *1.4.1. Gas Phase Hydrogen/Deuterium Exchange (HDX) Reaction*

Gas-phase HDX reaction is a type of ion-molecule reaction that has been extensively used for studying proteins' folding/unfolding.<sup>109-112</sup> In HDX reactions, labile hydrogens (*e.g.*, hydrogen atoms bound to N, O, and S atoms) of protein/peptide ions are replaced with deuterium (D) atoms of HDX neutral reagent. Generally, gas-phase accessibilities of labile hydrogens in analytes are reagent type, structure, and conformation dependent. Thus, the degree of deuterium incorporation, HDX pattern, and exchange reaction rate are a reflection of an ion's willingness to exchange its hydrogens with a reagent molecule. The gas-phase HDX reaction rates are conveniently measured in

the ICR cells of FT-ICR mass spectrometers in which ions can be trapped for extended periods of time.<sup>113-118</sup> Accurate HDX rate constant measurements require controlled introduction of neutral deuterating reagent into the FT-ICR vacuum chamber.

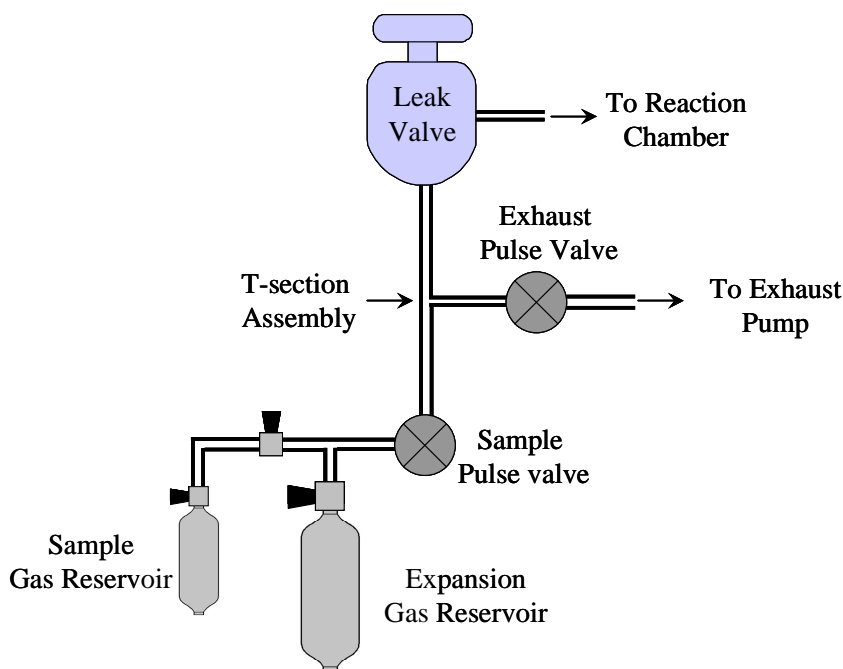


Figure 1.6. Schematic representation of a home-built pulsed-leak valve setup for controlled release of deuterium reagent into the ICR cell. Sample pulse valve is used to introduce the reagent gas into the “T-section” assembly behind a leak valve. Then, the neutral reagent molecules are leaked into the vacuum chamber under a precise control and using the leak valve. The exhaust pulse valve is connected to a mechanical pump and used to pump the residual gas in T-section space at the end of the ion-molecule reaction event.

Different designs have been used in MS trapping instruments for release of deuterating reagent into trap cells. For example, pulsed<sup>119</sup> and leak<sup>120</sup> valve setups are available in commercial trapping MS instruments for HDX reagent introduction. In our laboratory, we use a home-built pulsed-leak valve setup,<sup>116-118, 121</sup> which was originally introduced by Freiser *et al.*<sup>122</sup> For all FT-ICR MS gas-phase kinetic data reported here,

the pulsed-leak valve setup was used for deuterium reagent introductions into the ICR cell.<sup>116, 118, 123-125</sup>

Figure 1.6 shows the configuration of a home-built pulsed-leak valve setup installed on our ESI/FT-ICR mass spectrometers. This pulsed-leak valve system consisted of a sample gas reservoir, an expansion gas reservoir, T-section assembly (internal volume of  $\sim 10 \mu\text{L}$ ), two pulse valves (“Sample” and “Exhaust” pulse valves in Figure 1.6), and one leak valve for controlled release of neutral reagents into the vacuum chamber. Popular deuterium reagents that are used for gas-phase HDX reaction include (in the order of increasing gas-phase proton affinity [PA])  $\text{D}_2\text{O}$ ,  $\text{CD}_3\text{OD}$ , and  $\text{ND}_3$ . Factors such as vapor pressure and corrosivity of deuterating reagents may influence the choice of deuterating reagents for a particular HDX reaction. However, generally the decision for the selection of a deuterating reagent is based on gas-phase PA/or basicity of a reagent relative to the analyte ion of interest.<sup>126</sup> The success of a gas-phase HDX reaction depends on closeness of gas-phase basicity (GB) of deuterating reagent to the GB of analyte ion of interest.<sup>127</sup> Generally, as the GB difference between deuterating reagent and analyte ion of interest decreases the HDX reaction rate constant increases.

The mechanisms of HDX reactions with different deuterating reagents have been extensively studied.<sup>127</sup> For the studies presented here,  $\text{ND}_3$  was used as the HDX reagent. In the following section, details of HDX mechanism in the gas phase and for  $\text{ND}_3$  reagent are provided. Beauchamp and coworkers reported that HDX reaction of glycine oligomer ions ( $[\text{Gly}_n + \text{H}]^+$ ,  $n = 1-5$ ) with  $\text{ND}_3$  proceeds *via* an “onium” ion mechanism.<sup>127</sup> Figure 1.7 shows the onium ion mechanism for HDX reaction of a protonated peptide with  $\text{ND}_3$ .

In onium ion mechanism, first,  $\text{ND}_3$  captures a proton from a protonated peptide ion to form an ammonium ion.

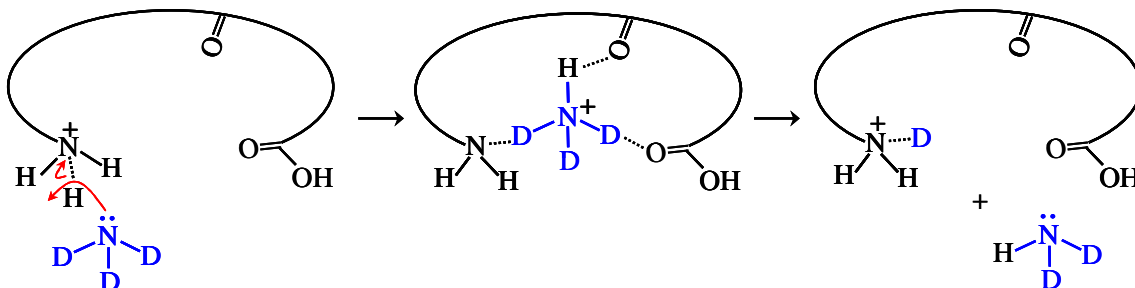


Figure 1.7. Onium ion mechanism for gas-phase HDX reactions of peptides.

The ammonium ion is then solvated by the peptide to form a stable gas-phase complex. Here, hydrogen-bonding to the carboxyl and amine groups of analyte ion anchor the ammonium ion and provide additional internal energy for the intermediate complex ion to overcome the energy barrier for deuterium transfer from  $\text{ND}_3\text{H}^+$  to the peptide.<sup>128, 129</sup> A research paper by Beauchamp and coworkers provides additional details about the HDX mechanisms involving various deuterating reagent.<sup>127</sup>

#### 1.4.2. Ion Mobility-Mass Spectrometry (IM-MS)

Ion mobility spectrometry (IMS) is a gas-phase separation technique that allows for separation of analytes based on their sizes and shapes/conformations.<sup>130</sup> By coupling IM devices to fast scanning MS instruments (*e.g.*, TOF), IM-MS systems have become important and powerful tools for analysis of complex sample mixtures and structural characterizations of biomolecules.<sup>130, 131</sup>

A typical IM-MS instrument consists of an ionization source, a drift chamber filled with a buffer gas for mobility separation, a mass analyzer, and a detector. Different

types of IM devices including conventional linear drift tube (DT), traveling wave (TW), and field asymmetric waveform ion mobility spectrometry (FAIMS) can be coupled to MS instruments.<sup>130</sup> Each one of these devices provides different level of IM resolving power (arrival time (AT)/ $\Delta$ AT<sub>50%</sub>) and sensitivity for IM-MS measurements.

Linear DT IM devices are composed of a set of closely stacked ring electrodes, which are connected in series through a resistor chain to produce a linear field gradient across the drift tube. In linear drift tubes, ions are separated based on their differences in their drift velocities ( $v_d$ ) in the presence of a drift gas (*e.g.*, N<sub>2</sub>, H<sub>2</sub>, and Ar) and under the influence of an electric field gradient (E).<sup>132</sup> Ions with smaller collision cross sections (CCSs or  $\Omega$ ) or larger mobility experience smaller number of ion-molecule/atom collisions with buffer gas as compared to larger size (*i.e.*, larger CCS) ions.<sup>133</sup> Therefore, ions with smaller CCSs transverse the IM drift tube with larger velocities and reach to the detector faster than the larger CCS ions.

Drift velocity of an ion in the IM drift tube is calculated from equation (1.9)<sup>132</sup>:

$$v_d = d / t_D = K \times E \quad \text{(Equation 1.9)}$$

where “d” and “E” denotes the drift tube length and electric field respectively. “t<sub>D</sub>” and “K” denote the ion’s drift time and the ion’s mobility constant respectively.

In DT IM experiments, the CCS ( $\Omega$ ) of an analyte ion is related to its drift time according to the equation (1.10)<sup>132</sup>:

$$\Omega = 3 \times (q / [16 \times N]) \times (1 / K_0) \times (2\pi / [\mu \times k_B \times T])^{1/2} \quad \text{(Equation 1.10)}$$

where “K<sub>0</sub>” denotes ion’s reduced mobility (K<sub>0</sub>)<sup>132</sup> and it is defined by equation (1.11):

$$K_0 = (d / [t_D \times E]) \times (273 / T) \times (P / 760) \quad \text{(Equation 1.11)}$$

Equation (1.10) is only valid for calculating ions' CCSs in DT IM devices where a constant uniform electric field is applied across the drift tube. A novel IM technique that has recently been developed and introduced commercially is 'traveling wave' IMS (TWIMS.)<sup>134, 135</sup> Figure 1.8 shows the schematic representation of commercially available Waters (Waters Corp., Manchester, UK) Synapt G2 HDMS system that uses TWIMS for mobility separation and TOF as detector. The design of IM cell in TWIMS devices is similar to IM cell design in conventional DT IM devices. However, unlike DT IMS, in which a constant electrical field is applied continuously to the cell, a pulsed electric field is applied to one segment of the TWIM cell and swept sequentially through the cell one segment at a time and in the direction of ion migration to TOF MS detector.

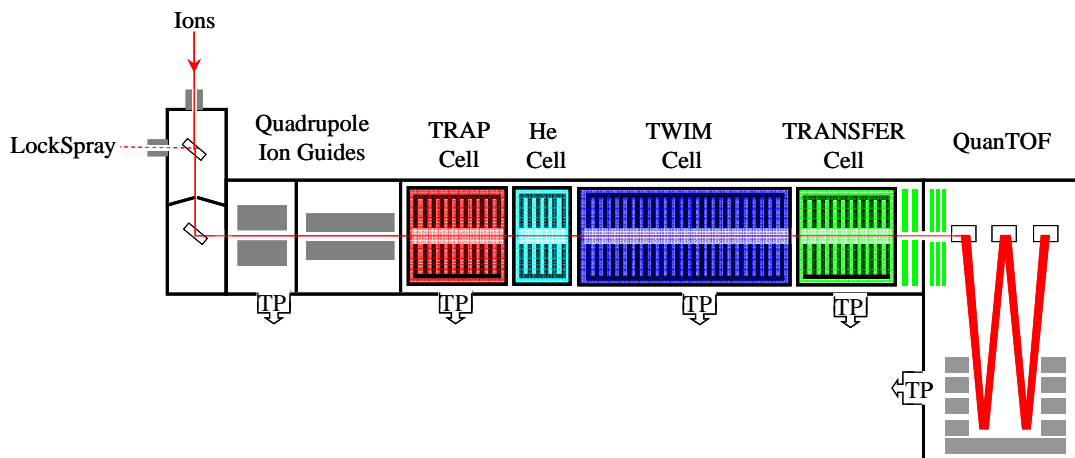


Figure 1.8. Schematic representation of Waters Synpat G2 TWIMS system.

Therefore, ions in TWIMS are moved through the IM cell in pulses as waves of the electrical field passes through the stacked rings (Figure 1.9). Additionally, ions are radially TWIM cell ring by applying a continuous RF voltage on TWIM electrodes. Although TWIMS systems permit higher IM resolution as compared to DT IM systems,

the analytical solution that relates an ion drift time to its CCS in TWIMS is not known. Therefore, obtaining CCS information from TWIMS experiments requires and relies on experimental calibration of IM drift times.<sup>136, 137</sup> The CCSs of unknown analyte ions in TWIMS is determined by calibrating the experimentally measured drift times against those measured for standard ions of known  $\Omega$  values.

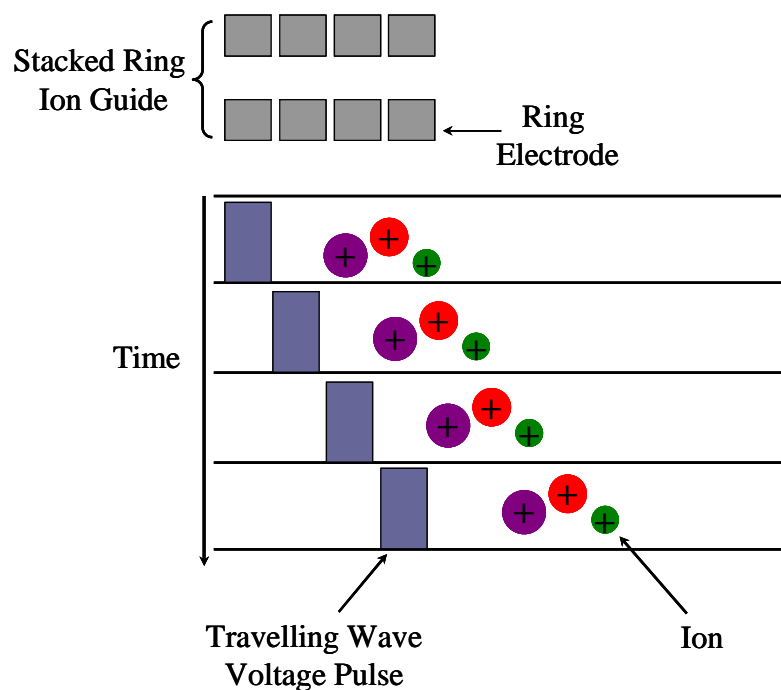


Figure 1.9. Traveling wave voltage pulse propels ions along the stacked ring ion guide (SRIG) and in the presence of background gas.

## CHAPTER TWO

### *Protein and Peptide Amino Acid Sequencing Using Mass Spectrometry*

#### *2.1. Mass Spectrometry-based Proteomics Strategies*

Proteomics is a comprehensive study of specific proteome, related to biological cell processes, involving proteins' and peptides' abundances, post-translational modifications (PTM), and potential molecular or partner interactions.<sup>138, 139</sup> Amino acid sequencing of proteins and peptides plays a vital role in proteomics to establish structure-function relationships, which in turn aids in identifying novel proteins and cascades of cellular processes.<sup>140</sup> Better understanding of cellular processes allows judicious synthesis of novel drugs that can target specific metabolic pathways in biological cells.<sup>141</sup>

Currently, mass spectrometry (MS) is the most commonly used technique for high-throughput protein and peptide amino acid sequence identification.<sup>142</sup> Two of the most commonly used MS-based and tandem-MS (MS<sup>n</sup>)<sup>54</sup> proteomics approaches include “bottom-up” and “top-down” MS (Figure 2.1).<sup>143</sup>

In “bottom-up” proteomics, a mixture of proteins is separated by one- or two-dimensional electrophoresis and individual protein spots or gel slices are subjected to proteolysis (Figure 2.1).<sup>144, 145</sup> Each separated protein is then digested using enzymes such as pepsin or trypsin to produce a pool of peptide fragments.<sup>144, 145</sup> The mixture of peptide fragments is then separated by liquid chromatography (LC) prior to MS analyses. Digested peptides, after separation by LC, are introduced into MS instrument using soft ionization techniques (*e.g.*, ESI<sup>22-24</sup> and MALDI<sup>20, 26, 146</sup>). These digested peptide ions are

identified and their sequences are established by using various gas-phase dissociation or MS fragmentation techniques.<sup>147</sup>

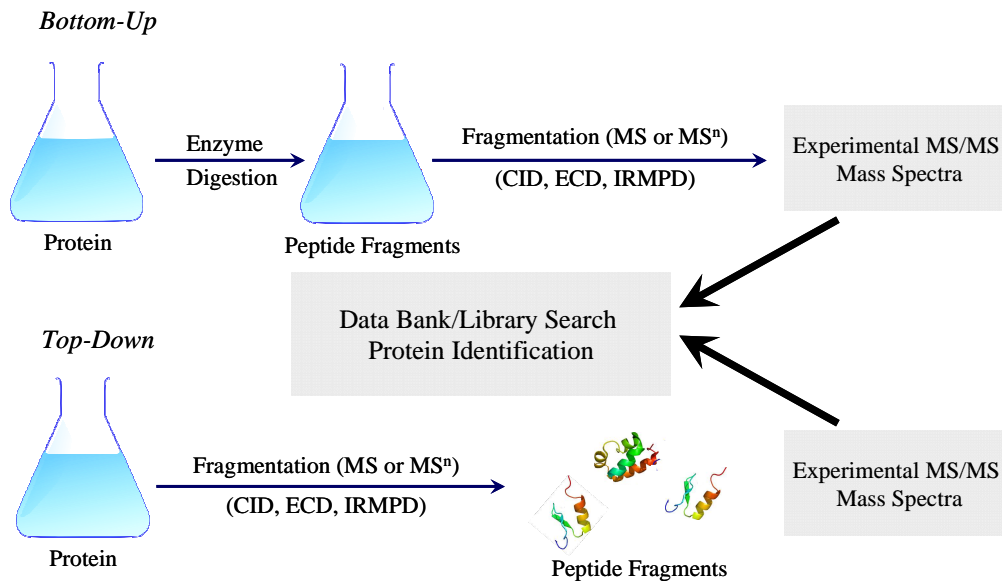


Figure 2.1. Schematic representation of “bottom-up” and “top-down” MS-based protein/peptide amino acid sequence identification.

In “top-down” proteomics a mixture of intact proteins is separated by LC and then MS dissociation methods are used to fragment the ionized intact proteins in the gas phase (Figure 2.1).<sup>148, 149</sup> The most commonly used MS fragmentation techniques in “bottom-up” and “top-down” proteomic approaches are collision-induced dissociation (CID),<sup>150</sup> electron capture dissociation (ECD),<sup>151</sup> electron transfer dissociation (ETD),<sup>89</sup> and infrared multiphoton dissociation (IRMPD).<sup>152</sup> Each one of these gas-phase dissociation techniques has its own pros and cons and, depending on the application type, one may choose one or a combination of two or more fragmentation techniques to increase the sequence coverage.<sup>103, 148, 153, 154</sup>

Moreover, depending on the fragmentation technique employed, different protein and/or peptide backbone bond types can be broken to yield different types of fragment ions. The generated gas-phase fragment ions in “bottom-up” and “top-down” proteomics approaches are then searched against various data bases (*e.g.*, global proteome machine database (GPMDB)<sup>155</sup> and peptide atlas<sup>156</sup>) using bioinformatics software and search engines (*e.g.*, Mascot,<sup>157</sup> OMSSA,<sup>158</sup> SEQUEST,<sup>159</sup> and X!Tandem<sup>160</sup>) to identify amino acid sequences of all peptide and proteins in proteome samples.<sup>161</sup>

## 2.2. Nomenclature for Protein and Peptide Fragments in Mass Spectrometry

Gas-phase fragmentations of proteins and peptides generate different types of product ions and allow for determination of amino acid compositions at a high level of confidence. Fragment ion types from gas-phase dissociation of proteins and peptides are named based on a nomenclature system that was introduced by Roepstorff (Figure 2.2).<sup>162</sup> Roepstorff’s nomenclature system describes the dissociation of the proteins and peptides backbone bonds in a generic manner without relying on adjacent amino acid side-chains.

Generally, protein and peptide backbone cleavages can occur at three different positions depending on the dissociation technique used: (i) between alpha ( $\alpha$ )-carbon and carbonyl carbon (C $\alpha$ -C), (ii) at amide bond (C-N), and (iii) between  $\alpha$ -carbon and amine nitrogen (N-C $\alpha$ ). When the peptide’s charge is retained on the N-terminal side of a cleaved backbone bond, the observed fragment ions are called “a<sub>n</sub>”, “b<sub>n</sub>”, and “c<sub>n</sub>” type fragments, where subscript “n” denotes the number of amino acid(s) in a fragment ion (Figure 2.2). However, when the peptide’s charge is kept by C-terminus of a peptide, the observed fragment ions are called “x<sub>n</sub>”, “y<sub>n</sub>”, and “z<sub>n</sub>” type fragment ions (Figure 2.2).

Generally, dissociations of protein and peptide ions using CID and IRMPD techniques generate  $a_n$ ,  $b_n$ , and  $y_n$  as predominant fragment ions.<sup>163</sup>

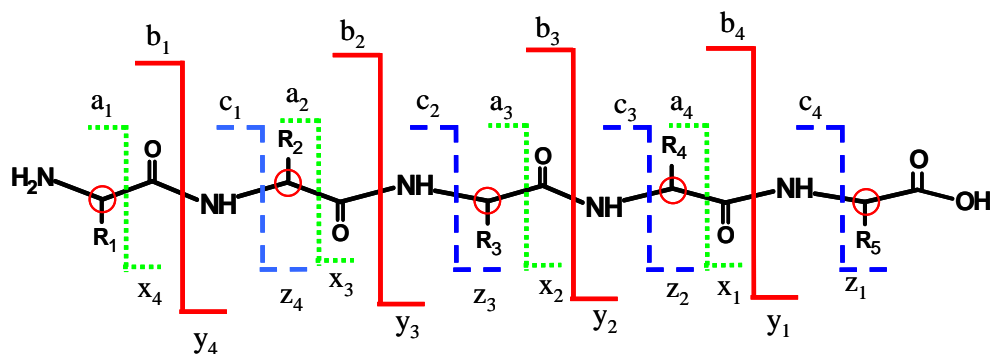


Figure 2.2. Roepstorff' nomenclature system for product ions produced from backbone cleavage of proteins/peptides during gas-phase fragmentation. Red circles indicate positions of all alpha carbons ( $C\alpha$  with respect to carbonyl groups) in the amino acid sequence.

Dissociations of proteins and peptides using ECD and ETD generate  $c_n$ ,  $x_n$ , and  $z_n$  as major fragment ions.<sup>89, 153</sup> In addition to the protein and peptide fragment ions generated from the backbone bond cleavages, fragments resulting from loss of part or all of the side chain of an amino acid at the point of cleavage may also be observed. Fragment ions resulting from loss of amino acid side chains are named based on Johnson's nomenclature system as  $d_n$ ,  $v_n$ , and  $w_n$  type ions.<sup>164</sup>

### 2.3. Challenges Associated with Search Engines and Strategies in Peptide Sequencing

MS-based amino acid sequence identifications are usually deduced from the quality of match (*i.e.*, identification or matching score<sup>165</sup>) between: (i) the observed and predicted sequence-specific MS patterns and/or (ii) the observed and experimentally available MS/MS spectral libraries (*i.e.*, "target-decoy" search).<sup>166</sup> Two of the most

commonly used search engines/algorithms for peptide and protein sequence matching purposes are “sequence search engines” (*e.g.*, SEQUEST, based on the presence or absence of fragment ions)<sup>159</sup> and “spectral search engines” (*e.g.*, SpectraST, based on the global match between the library and query spectra).<sup>167, 168</sup>

Despite successful implementation of the available search engines for protein identification, these searching strategies should be utilized with caution to avoid potential protein misidentifications and false positives (*i.e.*, high matching scores).<sup>169</sup> False positives in proteins’ amino acid sequence identifications generally arise from MS/MS spectral misinterpretations because of: (a) enzymatic digestion at abnormal positions, (b) inaccurate assignment of charge state or mass of the precursor peptide ions, (c) not considering the presence of chemical or post-translational modifications in search engines, (d) absence of the peptide(s) under examination (or interpretation) in the databases being queried, and (e) presence of misleading ions that are attributed to electronic noise, contaminations, and *gas-phase rearrangement reactions*.<sup>170, 171</sup>

Among the above-mentioned reasons for false positive protein identification (or protein misidentification), the presence of misleading ions due to gas-phase fragment ion rearrangements or “sequence scramblings”<sup>172</sup> (more details in section 2.4) are arguably the least straight forward to address.<sup>173-175</sup> Identities of sequence-scrambled fragment ions cannot be assigned to “normal” peptide backbone bond cleavage (*i.e.*, commonly observed fragments of the type a/x, b/y, or c/z, Figure 2.2). For example, our preliminary survey of the national institute of standards and technology (NIST) peptide MS/MS library<sup>176</sup> reveals the presence of high abundant fragment ions assigned as “unknown” in the CID mass spectra of digested peptides. Although the NIST peptide MS/MS library

does not provide the origin of “unknown” fragments, we believe that these (“unknown”) fragments are produced as a result of potential sequence scramblings during the CID processes.

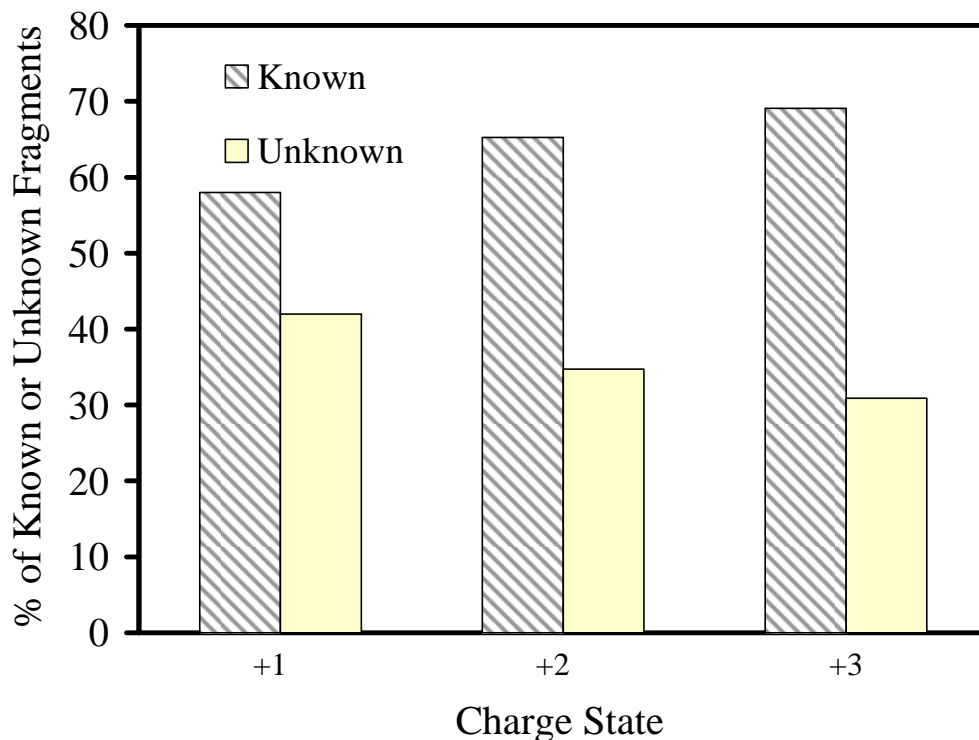


Figure 2.3. Percentages of known (identified) and unknown fragment ions from CID of different charge states (*i.e.*, +1, +2, and +3) of tryptic digested peptides (52 peptides) from bovine serum albumin (BSA). Plots were generated by calculating the percentage of unknown ions from CID MS data taken from NIST peptide tandem MS library.

As an example, we examined the CID mass spectra of 52 tryptic digest peptides from bovine serum albumin (BSA)<sup>176</sup> and noticed that identities of a significant number of fragment ions are unassigned. Figure 2.3 present the summary of our NIST CID survey for tryptic digest peptides of BSA.

Figure 2.3 shows that ~42 %, ~35 %, and ~31 % of the total number of BSA fragment ions generated from singly-, doubly-, and triply-charged peptides, respectively,

are “unknown” ions. The available bioinformatics software and search engines use established gas-phase fragmentation rules and do not account for rearranged or sequence-scrambled fragment ions. Exclusion of the potential sequence scrambling mechanisms within the implemented rules in bioinformatics approaches may result in invalid protein/peptide sequence identifications.<sup>177</sup> Hence, it is important to identify, understand the mechanism(s) of, and (if possible) prevent, the observed sequence scrambling during gas-phase proteins/peptides fragmentation processes.

#### *2.4. Peptides' Amino Acid Sequence Rearrangement during Gas-phase Fragmentation*

The first experimental evidence for gas-phase rearrangement of peptide fragment ions was provided by Tang *et al.* in 1993.<sup>178</sup> Tang *et al.* noticed the presence of high abundant rearranged fragment ions in CID mass spectra of doubly-charged peptide ions. The amino acid sequences of these rearranged fragment ions did match any portion of the original intact amino acid peptide sequence.<sup>178</sup> Subsequent reports also showed further evidences for occurrence of peptide ion gas-phase rearrangement during CID process.<sup>179-181</sup> In 2006, Harrison *et al.* proposed that the gas-phase rearrangements of protonated peptides during CID result in cyclization of b-type ions and subsequent amide bond reopening at different positions in macrocyclic b ions generates sequence-scrambled (non-direct) fragment ions.<sup>172</sup> Based on the hydrogen/deuterium exchange (HDX) reaction results of molecular and fragment ions, potential cyclization of b fragments ions was originally reported by our group in 2001.<sup>117</sup> Harrison's proposed mechanism for peptide sequence scrambling during CID process<sup>172</sup> was later confirmed by various research groups.<sup>182-184</sup> Processes of macrocyclization and generation of sequence-

scrambled fragment ions during a gas-phase ion activation process (*e.g.*, CID) are depicted schematically in Figure 2.4.

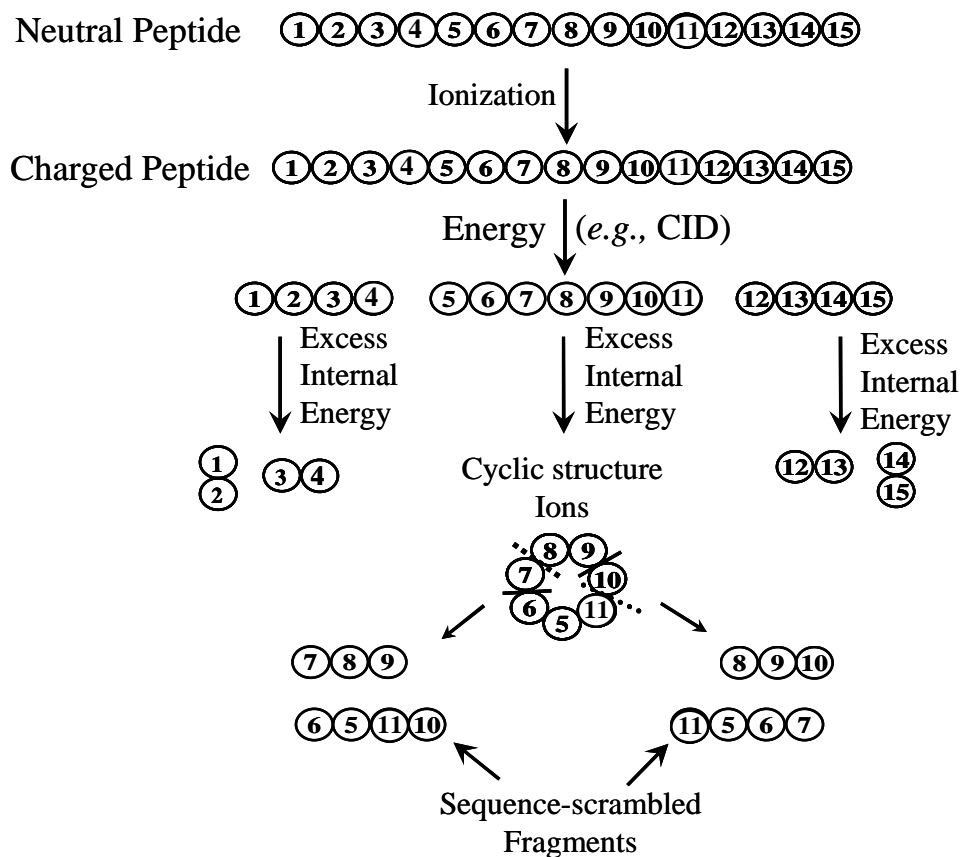


Figure 2.4. Schematic representation of amino acid sequence scrambling during gas-phase fragmentation process of a peptide ion. Each circle denotes an amino acid and each number inside a circle denotes the amino acid residue position in peptide sequence.

During a gas-phase ion activation process (*e.g.*, CID), the linear fragment ions (*e.g.*, b-type ions) can form cyclic structures *via* nucleophilic attack of C-terminus charged group (charged carbonyl group) by the free N-terminus (amine group).<sup>172</sup> Such head-to-tail type macrocyclic-structure fragment ions can reopen at different positions than its originally formed bond and generates sequence-rearranged linear fragment ion(s).

Subsequent losses of amino acid residues from sequence-rearranged linear fragment ion(s) generate sequence-scrambled product ions.<sup>172</sup> Identities of sequence-scrambled fragment ions cannot be assigned to “normal” peptide backbone bond cleavage, and their presence in MS/MS spectra can be misleading. For example, Figure 2.5 shows a CID mass spectrum of a singly-charged peptide ion population with amino acid sequence of GVYVHPV.

A Thermo LTQ/Orbitrap (Thermo Scientific, Waltham, MA) mass spectrometer equipped with an ESI source for ion generation and a quadrupole for ion isolation and collisional activation was used to generate the CID mass spectrum in Figure 2.5. Ion population at  $m/z$  770.4 corresponding to ESI-generated  $[GVYVHPV + H]^+$  were  $m/z$ -isolated in LTQ/Orbitrap MS instrument. Subsequently,  $m/z$ -isolated ions were subjected to CID in the quadrupole in the presence of helium (He) collision gas. The generated fragment ions were then transferred into an Orbitrap cell for high mass-accuracy measurements.

In Figure 2.5, the CID product ions that could be assigned as “normal” fragment ions are labeled in black color with their corresponding identities. However, those fragment ions that could not be assigned according to the peptide’s original amino acid sequence (*i.e.*, GVYVHPV) are labeled with red color. For instance, the fragment ion at  $m/z$  294 in Figure 2.5 is a sequence-scrambled b-type ion with amino acid sequence of GVH. Although we identified three sequence-scrambled fragment ions in CID mass spectrum of  $[GVYVHPV + H]^+$ , there are two “Unknown” fragment ions ( $m/z$  374 and 688) (Figure 2.5) that could not be assigned as products of amide bond cleavages of a linear or a macrocyclic type structure. These “unknown” fragment ions could be

generated through more complex gas-phase rearrangement reactions, which can add to the complexity of CID mass spectra and their interpretations.

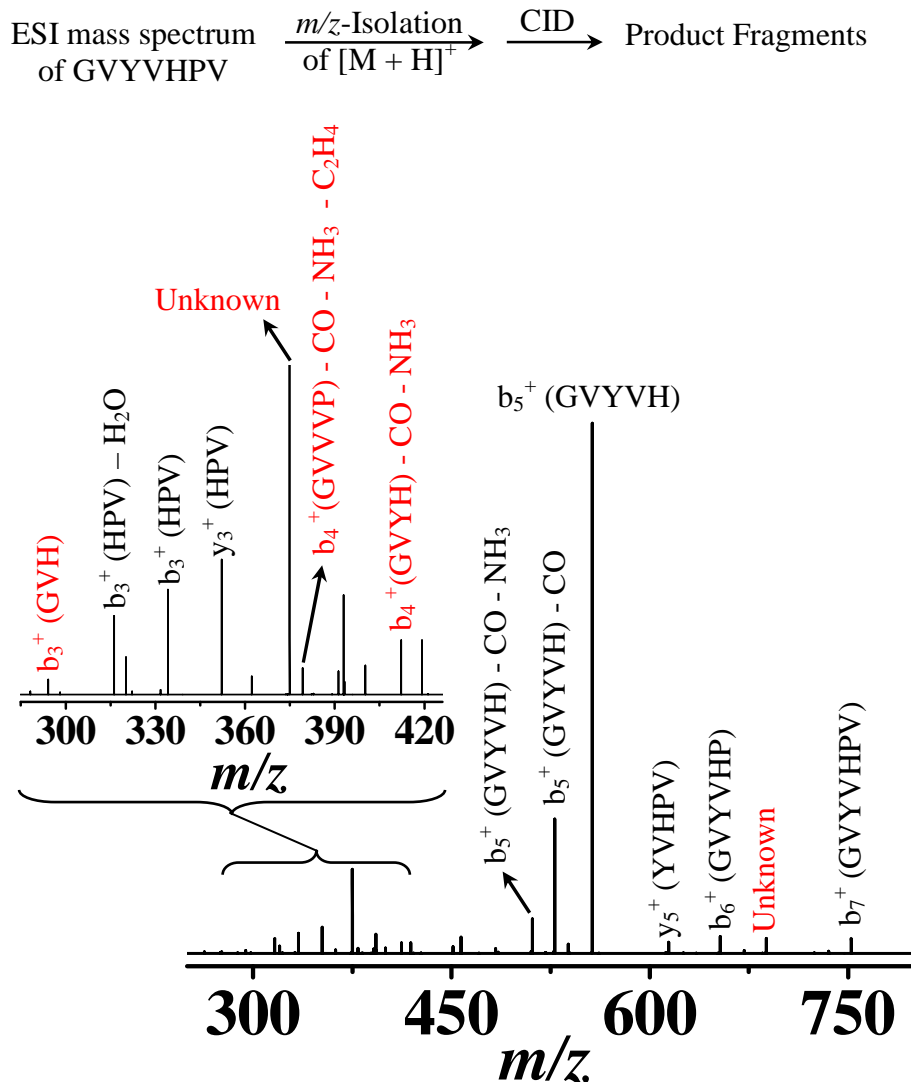


Figure 2.5. CID mass spectrum of a singly-charged protonated peptide (amino acid sequence: GVVYVHPV). Observed b- and y-type fragment ions are labeled. Peaks with red labels denote sequence-scrambled fragment ions.

Better understanding of the mechanisms involved in the generation of sequence-scrambled fragment ions and gas-phase rearrangement reactions requires in-depth characterization of fragment ion structures. Further progress in our understanding of the

gas-phase chemistry involved in peptide fragmentation will have a major impact on future improvements to bioinformatics software and algorithms used for peptide sequencing and identification of proteins' primary structures. In the following section, we introduce commonly used gas-phase probes for studying fragment ion structures/conformations.

### 2.5. Gas-phase Structural Analysis of Peptide Fragment Ions

The occurrence of sequence scrambling could imply the presence of different gas-phase structural isomers for peptides' fragment ions. However, no experimental reports had suggested the possibility for presence of isomeric structures for peptides' fragment ions until the initial observations reported by Solouki *et al.*<sup>117</sup> The original gas-phase HDX report on  $b_4^+$  and  $b_5^+$  fragment ions from WHWLQL peptide by Solouki *et al.* demonstrated the presence of at least two different structural isomers for b-type ions based on both HDX mass spectral patterns and reaction kinetics.<sup>117, 123</sup>

Subsequently, results from various gas-phase structural analysis probes including: (i) gas-phase ion-molecule reactions,<sup>123, 125, 185-188</sup> (ii) molecular modeling,<sup>189, 190</sup> (iii) ion mobility-mass spectrometry (IM-MS),<sup>191-193</sup> and (iv) infrared multiphoton dissociation (IRMPD)<sup>186-188, 194, 195</sup> also suggested that b-type fragment ions exist as a mixture of at least two structure types (*i.e.*, “oxazolone”<sup>196</sup> and “macrocyclic”<sup>172</sup> (see section 2.6 for details)).

In gas-phase ion-molecule reactions, the presence (or absence) of the structurally/conformationally different b fragment ions can be probed by (a) using the appearance of HDX product ion isotopic patterns (*e.g.*, bimodal profiles),<sup>117, 123, 125, 185-188</sup>

(b) measuring the gas-phase HDX reaction rate constants,<sup>117, 123, 125, 185, 186, 188</sup> and (c) measuring the gas-phase proton transfer (PT) reaction rate constants.<sup>121</sup>

In IRMPD studies, the presence (or absence) of oxazolone and macrocyclic b fragment ion structures is probed by comparing the experimentally obtained IRMPD spectra with the theoretically calculated IR spectra.<sup>186-188, 194, 195</sup> For example, presence of the two theoretically calculated IR peaks (*i.e.*,  $\sim 1825\text{ cm}^{-1}$  for C-O stretching of nitrogen-protonated oxazolone and  $\sim 1430\text{ cm}^{-1}$  for CO-H<sup>+</sup> stretching of macrocyclic structures) in the IRMPD spectra of b fragment ions suggest the presence of a mixture of oxazolone and macrocyclic isomers.<sup>186-188, 194, 195</sup>

IM-MS studies offer the possibility of separating the different conformers or isomers of b fragment ions based on their collision cross section variations.<sup>191-193</sup> Mobility separation followed by collision-induced dissociation (CID), or post-IM/CID, can be used to confirm the presence of different b fragment ion structures.<sup>124, 191, 192, 197</sup>

## 2.6. Structures of b-type Fragment Ions

Acylium-type structure (Figure 2.6) was the first proposed structure for b fragment ions reported by Yalcin *et al.*<sup>198</sup> However, further studies suggested that the acylium ion structure is not a stable structure for b fragments and is expected to spontaneously lose carbon monoxide (CO) neutral from its C-terminus (Figure 2.6).<sup>196, 199</sup>

Later, a more stable five-membered ring oxazolone structure was suggested for b fragment ions.<sup>196, 200-202</sup> A five-membered ring oxazolone structure is formed by nucleophilic attack of a backbone carbonyl oxygen atom to C-terminal carbonyl carbon (Figure 2.7).<sup>202, 203</sup> A direct experimental evidence for the existence of oxazolone structure for b-type ions was obtained by IRMPD spectroscopy.<sup>194, 204</sup>

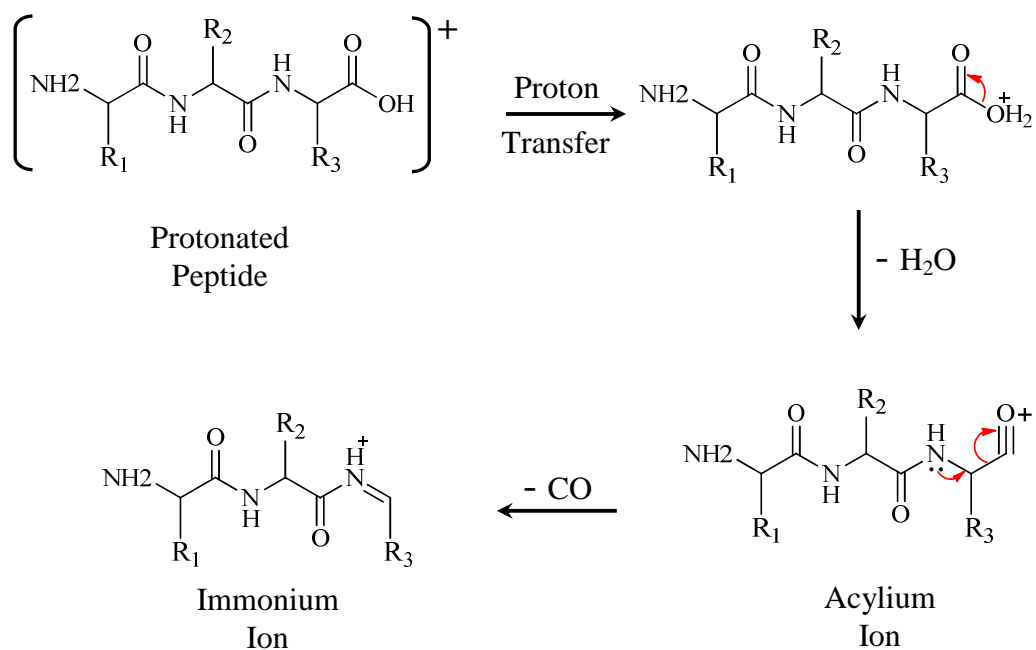


Figure 2.6. Reaction mechanism for the formation of a  $b_2^+$  with acylium -type structure followed by immonium ion formation.

Furthermore, an earlier study by Cordero *et al.* also showed that b fragment ions may adapt a six-membered ring diketopiperazine-type structure (Figure 2.8).<sup>205</sup> Diketopiperazine structures are formed by nucleophilic attack of N-terminal amine nitrogen to the carbonyl carbon of an adjacent amino acid residue (Figure 2.8).

Further studies on b fragment ions using IRMPD spectroscopy and molecular modeling suggested that fragmentation pathways that produce diketopiperazine ions is both energetically and entropically less favorable than oxazolone formation pathway (Figure 2.7).<sup>189, 193, 206</sup>

However, for small size b ions (*e.g.*,  $b_2^+$ ) the presence of a mixture of oxazolone- and diketopiperazine-type structures has been suggested (Figure 2.8).<sup>187, 207, 208</sup>

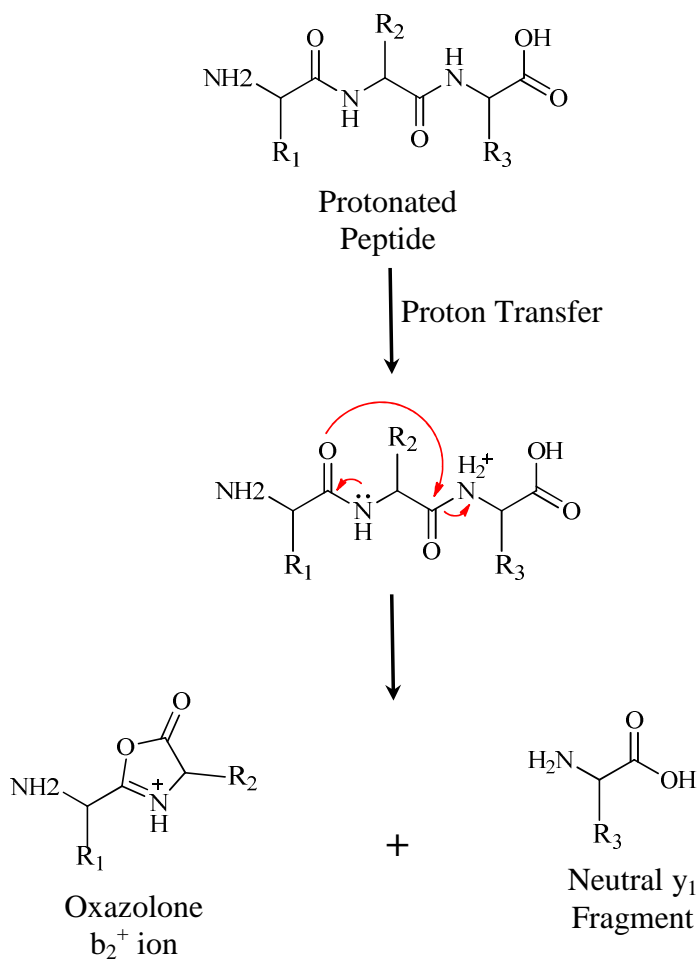


Figure 2.7. Reaction mechanism for the formation of a  $b_2^+$  with oxazolone-type structure.

Harrison and coworkers suggested a macrocyclic-type structure (Figure 2.9) for b fragment ions in order to rationalize the presence of sequence scrambled or non-direct product ions in MS/MS spectra of a model peptide.<sup>172</sup> To test their hypothesis, Harrison and coworkers examined CID fragmentation patterns of  $b_5^+$  from CID of YAGFL-NH<sub>2</sub> and protonated cyclic-(YAGFL) peptide.<sup>172</sup> The CID mass spectra of  $b_5^+$  fragment ion and cyclic-(YAGFL) peptide were similar, suggesting that  $b_5^+$  fragment ion could exist as a macrocyclic structure.<sup>172</sup> Direct experimental evidences for the presence of macrocyclic structure for b ions came from IRMPD spectroscopy<sup>195, 209-211</sup> and IM-MS.<sup>124, 191, 192, 197</sup>

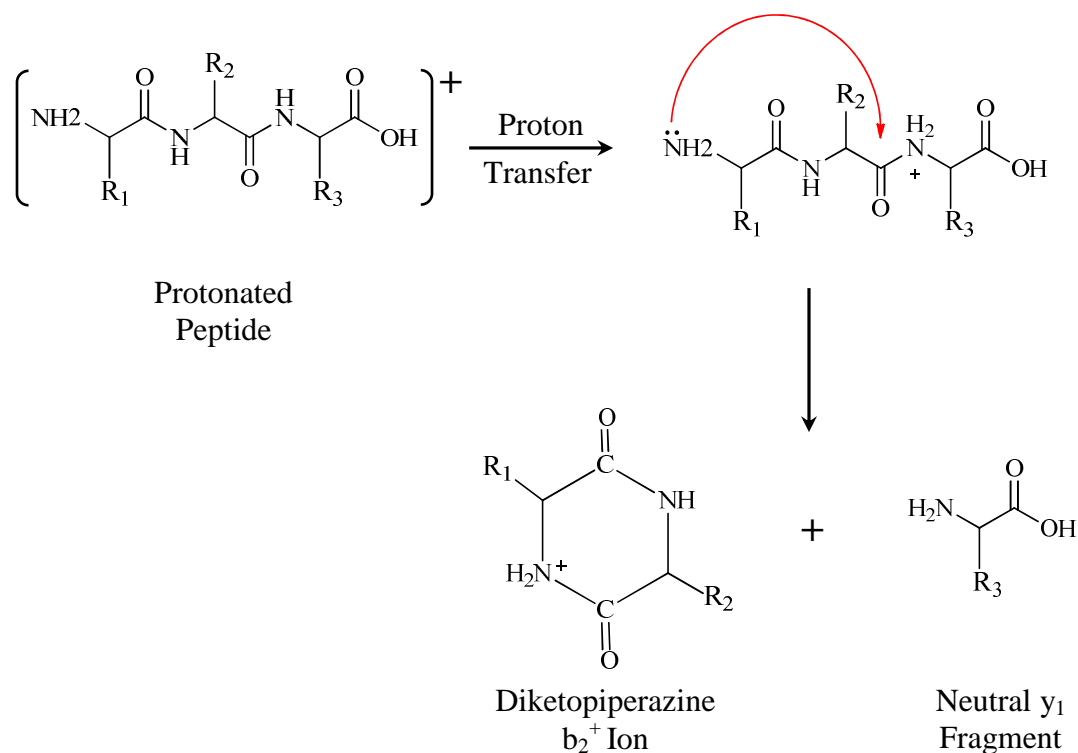


Figure 2.8. Reaction mechanism for the formation of a  $b_2^+$  with diketopiperazine-type structure.

Original IM-MS analysis suggested the presence of smaller collision cross section for macrocyclic b ions as compared to their linear oxazolone structure counterparts.<sup>191, 192</sup> Additionally, our laboratory recently reported on the combined use of post-IM/CID and chemometrics for analysis of structural isomers<sup>212</sup> including b fragments and observed two structurally distinct isomers for selected b fragment ions.<sup>124, 197</sup>

It should be noted that macrocyclization is not limited to b fragment ions and it can also occur in other peptide fragment ion types such as a-type ions.<sup>183, 209, 213</sup> These a-type ions can be formed from direct fragmentation of protonated peptides<sup>214-216</sup> as well as subsequent fragmentation of b-type ions *via* elimination of a neutral CO.<sup>196, 198, 216, 217</sup>

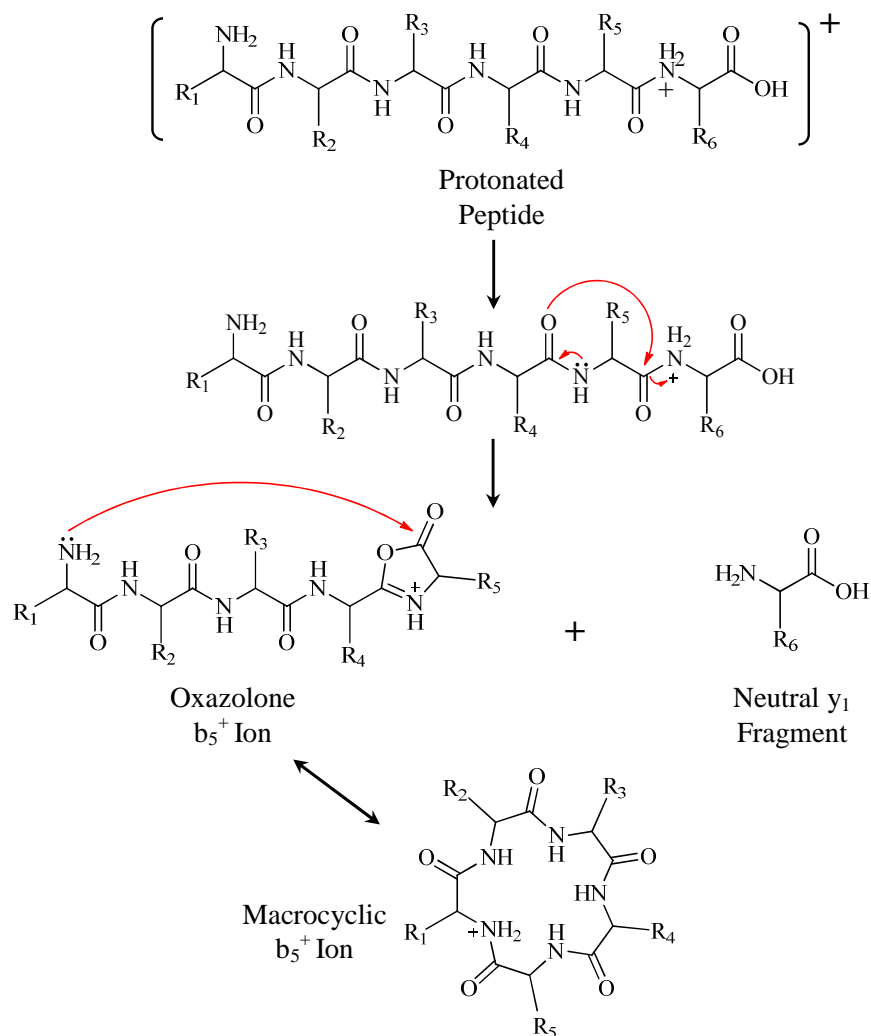


Figure 2.9. Reaction mechanism for the formation of a macrocyclic-type structure for a  $b_5^+$  fragment.

Gas-phase structures of a-type ions have also been studied using IRMPD<sup>193, 209, 213, 218, 219</sup>, IM-MS,<sup>191, 192</sup> and theoretical calculations.<sup>213, 219-221</sup> For example, previous studies on  $a_4^+$  fragment from leu-enkephalin by IRMPD and *ab initio* calculations suggested the presence of both linear immonium (iminium) and macrocyclic structures for a-type ions (Figure 2.10).<sup>209</sup> Furthermore, results from isotope labeling and IM-MS analysis of  $a_4^+$  and  $a_5^+$  fragments, from a set of isomeric peptides (*i.e.*, AYGFL, differing in sequence

location of an isotopically labeled A residue), revealed the presence of two structures (*i.e.*, linear and macrocyclic) for a-type ions.<sup>191, 192</sup>

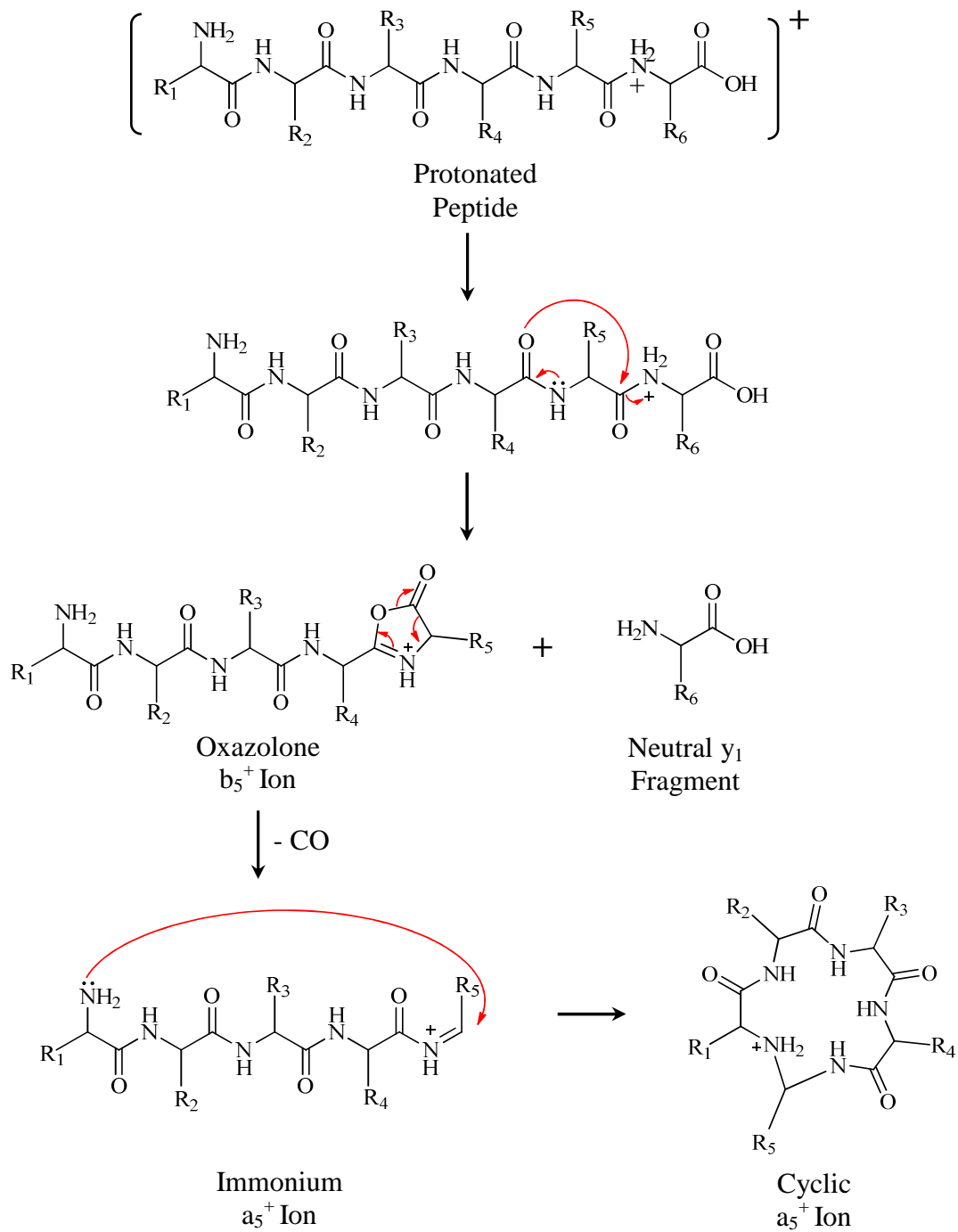


Figure 2.10. Reaction mechanism for the formation of a macrocyclic-type structure for  $a_5^+$  fragment.

## 2.7. Justification for the Research Presented in this Dissertation

Previous studies have shown that several parameters such as peptide fragment ion size,<sup>186, 222</sup> nature of amino acid residue,<sup>181, 223</sup> position of acid/basic amino acid in peptides<sup>190, 224</sup> can play significant roles on directing peptides' fragmentation pathways. For instance, gas-phase dissociation of peptide ions containing acidic (*e.g.*, aspartic acid) and basic (*e.g.*, arginine and histidine) amino acid residues showed that the side chains of these amino acid residues can direct fragmentation pattern and enhance amide bond cleavage near to these residues.<sup>225-227</sup> However, question remains whether the presence/absence of basic or acidic amino acid residues in peptides can influence cyclization of peptide fragment ions.

In Chapter Three of this dissertation, we show the results from combined use of gas-phase HDX and IM-MS to systematically study the structures of histidine (His)-containing  $b_n$  ( $n = 4$  to  $7$ ) ions generated from seven isomeric model heptapeptides including: (His)AAAAAA-NH<sub>2</sub>, A(His)AAAAA-NH<sub>2</sub>, AA(His)AAAANH<sub>2</sub>, AAA(His)AAA-NH<sub>2</sub>, AAAA(His)AA-NH<sub>2</sub>, AAAAA(His)A-NH<sub>2</sub>, and AAAAAA(His)-NH<sub>2</sub>. Data presented in Chapter Three reveals the influence of (i) basic histidine amino acid position and (ii) fragment ion size on the structures of  $b$  ions.

Although previous studies have established the occurrence of sequence scrambling in  $a$ - and  $b$ -type fragment ions,<sup>172, 209</sup> the propensity of  $y$ -type fragment ions from protonated peptides to generate sequence-scrambled product ions has not been studied. In Chapter Four of this dissertation, we present the first experimental evidence for the generation of sequence-scrambled fragment ions from CID of  $y$ -type ions on the

different sizes (4 to 12 amino acids) and charge states (+1 to +3) using tandem MS technique.

Previous studies show that gas-phase HDX is an important chemical probe for conformational analysis of proteins/peptides and their fragment ions.<sup>109, 110, 123, 209, 228, 229</sup> Both HDX patterns and extent of deuterium uptake by protonated proteins/peptides and fragment ions in the gas phase are used for structural elucidation purposes.<sup>123, 186</sup> However, other reaction channels such as gas-phase reagent adduct formation can compete with the intended “normal” HDX reaction and complicate the interpretation of HDX data.<sup>230</sup> Deciphering the mechanisms of these competing reactions will fill an important knowledge gap in gas-phase chemistry and enhance our ability to explore structure-function relationships by avoiding erroneous HDX data interpretations. In Chapter Five of this dissertation, we present the results from the first systematic study by combining *ab initio* calculations, HDX, IM-MS, and isotope labeling to better understand the fundamental chemistry involved in gas-phase reagent adduct formation. Using a simple model peptide, *i.e.*, a benzyloxycarbonyl (*Z*)-capped dipeptide containing glycine (*G*) and proline (*P*) (*i.e.*, *Z-PG*), we present results that address the influence of protonation and alkali metal ion ( $\text{Na}^+$ ,  $\text{K}^+$ , and  $\text{Cs}^+$ ) complexation on gas-phase  $\text{ND}_3$  adduct formation.

## CHAPTER THREE

### A Systematic Study on the Effect of Histidine Position and Fragment Ion Size in the Formation of $b_n$ Ions

This chapter published as: Miladi, M.; Zekavat, B.; Munisamy, S. M.; Solouki, T. A Systematic Study on the Effect of Histidine Position and Fragment Ion Size in the Formation of  $b_n$  Ions. *Int. J. Mass Spectrom.* **2012**, 316-318, 164– 173.

#### *Abstract*

In this study, we utilized gas-phase hydrogen/deuterium (H/D) exchange reactions and ion mobility-mass spectrometry (IM-MS) to examine the effect of: (i) histidine (His) amino acid position and (ii) fragment ion size on the structures of  $b_n$  ( $n = 4-7$ ) ions generated from nozzle-skimmer fragmentation. Both H/D exchange patterns and semi-log temporal plots of histidine-containing  $b_n$  fragment ions generated from seven isobaric model heptapeptides *{i.e., (His)AAAAAA-NH<sub>2</sub>, A(His)AAAAA-NH<sub>2</sub>, AA(His)AAAA-NH<sub>2</sub>, AAA(His)AAA-NH<sub>2</sub>, AAAA(His)AA-NH<sub>2</sub>, AAAAA(His)A-NH<sub>2</sub>, and AAAAAA(His)-NH<sub>2</sub>}* suggested the presence of at least two structures for all  $b$  fragment ions: “fast” and “slow” H/D-exchanging ion populations. The observed H/D exchange rate constants (for disappearance of isolated  $^{12}\text{C}_{\text{all}}$  or  $\text{D}_0$ ) for  $b_4^+$  and  $b_5^+$  fragments were higher than those observed for  $b_7^+$  fragment ions, suggesting more compact and/or stable structures for  $b_7^+$  fragment ions. Among the studied histidine-containing  $b_n^+$  fragments,  $b_4^+$  and  $b_5^+$  showed the most variation in H/D exchange reactivity as a function of histidine position in the original peptide sequence. Ion mobility arrival time distributions (ATDs) for histidine-containing  $b_5^+$  fragments from AA(His)AAAA-NH<sub>2</sub>,

AAA(His)AAA-NH<sub>2</sub>, and AAAA(His)AA-NH<sub>2</sub> showed two ion populations. H/D exchange and ion mobility results both imply the potential presence of a mixture of compact and open structures for b<sub>5</sub><sup>+</sup>. ATDs for b<sub>4</sub><sup>+</sup> fragments generated from A(His)AAAAA-NH<sub>2</sub> and AA(His)AAAA-NH<sub>2</sub> (compared to ATDs of the other model heptapeptides) suggest the appearance or increase in the percentage of a more compact ion population. ATDs of histidine-containing b<sub>6</sub><sup>+</sup> and b<sub>7</sub><sup>+</sup> fragments varied significantly as a function of histidine position in the original heptapeptides.

### 3.1. Introduction

Bottom-up and top-down proteomic methodologies are two widely used tandem mass spectrometry (MS<sup>n</sup>)-based approaches for protein and peptide identification. In these two proteomic approaches, either digested (in bottom-up) or intact (in top-down) proteins are fragmented using activation (*e.g.*, collision-induced dissociation (CID),<sup>150</sup> infrared multiphoton dissociation (IRMPD)<sup>152</sup>) and/or non-activation (*e.g.*, electron capture dissociation (ECD)<sup>88</sup> and electron transfer dissociation (ETD)<sup>89</sup>) dissociation techniques. The product fragment ions are searched against databases or theoretical MS/MS spectra using computer algorithms for protein/peptide sequence identification.<sup>231</sup> Reliability of protein/peptide identification using computer algorithms depends, in part, on the extent and types of protein/peptide dissociation products. Computer-based protein/peptide identification is usually performed without (or with little) insight into the rules that govern peptide dissociation and fragmentation. However, for accurate bioinformatics-based MS<sup>n</sup> sequencing of proteins/peptides, basic knowledge of the chemistry and mechanisms of gas-phase peptide fragmentation is crucial.

There have been many studies addressing mechanism(s) of peptide fragmentation and interested readers are referred to reviews by Paizs<sup>189</sup> and Harrison.<sup>184</sup> Recently, the structures and reactivities of b fragment ions have received special attention, due to the existence of different structures/conformers for b fragment ions. Structural changes during the ion fragmentation may yield “rearranged” b fragment ions.<sup>178, 179</sup> The first experimental evidence for “sequence scrambling”<sup>172</sup> of b fragment ions was reported by Tang *et al.* using tandem MS.<sup>178, 179</sup> Later, gas-phase hydrogen/deuterium (H/D) exchange studies confirmed the presence of different isobaric b fragment ion conformers/structures.<sup>117</sup>

In the original H/D exchange report, using  $b_4^+$  (WHWL) and  $b_5^+$  (WHWLQ) fragment ions from WHWLQL peptide (both in-source and SORI-CID generated b fragments), we proposed that both H/D exchange isotopic patterns and H/D exchange reaction rate constants could be used as tools to explore b fragment ion structural variations.<sup>117</sup> Similar approaches have been used successfully to extend the use of gas-phase H/D exchange reactions to probe conformations/structures of isobaric b fragment ions from several different peptides.<sup>123, 185-188, 229</sup> Follow-up theoretical and experimental studies have shown that the most probable structures for b fragment ions are (i) linear with five-member oxazolone ring(s) at the C-terminal side of the fragment ion<sup>196, 198, 232-235</sup> and (ii) head-to-tail macrocyclic structures.<sup>181, 183, 184, 190, 191, 193, 195, 236</sup>

In the case of macrocyclic structures, b fragment ions can open at different amide bonds to form linear oxazolone structures. Such rearrangements can cause sequence scrambling and loss of the initial amino acid sequence in MS protein sequencing.<sup>172, 182, 183</sup> Therefore, identification and understanding of the parameters that can affect the

sequence scrambling in gas-phase protein/peptide fragmentation will improve MS/MS database search engine/software outcomes. There has been evidence that amino acid type in the peptide sequence<sup>190, 223, 224</sup> and b fragment size<sup>186, 222, 237</sup> can affect the structures of resulting b fragment ions. For instance, we showed that the energetics of fragmentation processes (*e.g.*, in nozzle-skimmer fragmentation) influence the observed relative population of “fast”-to-“slow” H/D-exchanging b fragment ion conformers/isomers.<sup>121</sup>

Recent studies have demonstrated that both acidic<sup>223</sup> and basic<sup>190, 224</sup> amino acid residues in model peptides can influence the extent of b fragment ion sequence scrambling in collision-induced dissociation processes. Bythell *et al.* studied the effect of histidine (His) position on cyclization of b fragment ions {generated from isomeric hexapeptides (His)A<sub>5</sub>} using experimental and theoretical approaches.<sup>190</sup>

CID spectra of histidine-containing b<sub>4</sub><sup>+</sup> and b<sub>5</sub><sup>+</sup> fragment ions from (His)A<sub>5</sub> isomers showed experimental evidence for scrambled ion formation when histidine was near the C-terminus.<sup>190</sup> Molesworth *et al.* studied the effect of arginine (R) amino acid position on the propensity of formation of macrocyclic b fragment ions.<sup>224</sup> In the study by Molesworth *et al.*, the CID spectrum of b<sub>5</sub><sup>+</sup> from YARFLG showed only non-scrambled fragment ions.<sup>224</sup>

It was proposed that the formation of macrocyclic structures was inhibited by the presence of arginine (R) in permuted YARFLG model peptides.<sup>224</sup> Moreover, it has been shown that the size of b fragment ions can affect the tendency of b ions to cyclize and form scrambled ions. For example, recent studies have shown that smaller b<sub>n</sub> (n ≤ 3) ions have a lower tendency for cyclization than larger b<sub>n</sub> (n = 5-10) ions.<sup>222, 237</sup> Evidence for formation of cyclic b fragment structures has also been observed for b<sub>4</sub><sup>+</sup>-b<sub>8</sub><sup>+</sup> of an

octaglycine (*i.e.*,G<sub>8</sub>) peptide.<sup>186</sup> Unlike arginine or lysine (basic amino acid residues) histidine is not found in the C-terminus of resultant digested peptides in bottom-up proteomics. It is helpful to understand the role of these basic histidine residues (which are located in N-termini or internal positions of digested peptide fragments) in directing peptide ion fragmentation pathways.

Recent CID studies have yielded contradictory conclusions about the role of histidine position on b fragment ion macrocyclization and subsequence scrambled ion formation.<sup>190, 238</sup> The theoretical (molecular modeling) and experimental (CID) results by Bythell *at al.* suggested the presence of scrambled fragment ions when histidine is near the C-terminus.<sup>190</sup> On the other hand, in the work reported by Yalçın and Tasoglu sequence scrambling was observed independent of histidine position in peptide sequence.<sup>238</sup>

In this work, we used a combination of H/D exchange reactions and ion mobility-mass spectrometry (IM-MS) for gas-phase structural investigation of histidine-containing b<sub>4</sub><sup>+</sup>-b<sub>7</sub><sup>+</sup> fragment ions generated from seven C-terminal amidated heptapeptides: (His)AAAAAA-NH<sub>2</sub>, A(His)AAAAA-NH<sub>2</sub>, AA(His)AAAA-NH<sub>2</sub>, and AAA(His)AAA-NH<sub>2</sub>, AAAA(His)AA-NH<sub>2</sub>, AAAAA(His)A-NH<sub>2</sub>, and AAAAAA(His)-NH<sub>2</sub>.

## 3.2. Experimental

### 3.2.1. Sample Preparation

All C-terminal amidated isobaric heptapeptides (with one histidine (His) and six alanine (A) residues) *{i.e., (His)AAAAAA-NH<sub>2</sub>, A(His)AAAAA-NH<sub>2</sub>, AA(His)AAAA-NH<sub>2</sub>, and AAA(His)AAA-NH<sub>2</sub>, AAAA(His)AA-NH<sub>2</sub>, AAAAA(His)A-NH<sub>2</sub>, and AAAAAA(His)-NH<sub>2</sub>}*

AAAAAA(His)-NH<sub>2</sub>} were kindly provided by Talat Yalçın from the İzmir Institute of Technology, Turkey. The isotopically labeled AAAA(His)(A<sup>\*</sup>)A-NH<sub>2</sub> heptapeptide (where “A<sup>\*</sup>” denotes the carbon thirteen (<sup>13</sup>C) isotope on alanine side chain) was synthesized in house, using standard solid phase peptide synthesis (SPPS) procedure.<sup>239</sup> The deuterating reagent gas (*i.e.*, ND<sub>3</sub>), all electrospray ionization (ESI) solvents, and pentaalanine (A<sub>5</sub>) were purchased from commercial sources (Sigma-Aldrich, St. Louis, MO) and used without further purification, except for applying conventional freeze-dry cycles as deemed necessary (*e.g.*, for the ND<sub>3</sub> used in gas-phase H/D exchange reactions). Micromolar concentrations of model heptapeptide solutions in methanol: water: acetic acid (49.5: 49.5: 1) were used for ESI/MS experiments.

### 3.2.2. Mass Spectrometry

Mass spectra for the ion-molecule reactions and sustained off resonance irradiation (SORI) CID (data included in the appendix material) were acquired using an FT-ICR mass spectrometer equipped with an open-ended cylindrical Penning trap (former Ion- Spec Corp.- now a division of Agilent Technologies Inc., Santa Clara, CA) and a 9.4 T superconducting magnet (Cryomagnetics Inc., Oak Ridge, TN).

Ions were generated externally using an Analytica electrospray ion source (Analytica of Branford Inc., Branford, CT) equipped with an in-house built spraying setup. The spraying tip was made from fused silica capillary (with polyamide outer coating) {Western Analytical, Wildomar, CA}. The spraying tip was attached to a Teflon tube by a 1/16-inch Swagelok union {Maine/Atlantic Valve & Fitting Co., Hermon, ME}. Electrospray was generated by applying ~4 kV (with respect to ground) on the syringe needle {SGE Inc., Austin, TX}. The flow rate was set at 0.5 μL/min using a Harvard

PHD 2000 syringe pump {Harvard Apparatus, Holliston, MA}. For H/D exchange experiments reported in this study, all  $^{12}\text{C}$  isotopic peaks (abbreviated as “ $^{12}\text{C}_{\text{all}}$ ”) of  $b_n$  fragment and molecular ions were isolated using stored waveform inverse Fourier transform (SWIFT) technique.<sup>240</sup> For gas-phase H/D exchange reactions, peptide fragment ions (*i.e.*, histidine-containing  $b_4^+$ - $b_7^+$ ) were generated via nozzle-skimmer fragmentation technique.<sup>152</sup> The use of  $\sim 1.1$  MHz radiofrequency (RF) in the quadrupole ion guide of our IonSpec ESI/FT-ICR MS imposes a  $m/z$  cut-off of  $\sim 300$  limiting the transfer of low  $m/z$  ions from the external ESI source to the ICR cell.<sup>241</sup>

Therefore, nozzle-skimmer-generated  $b_1^+$ - $b_3^+$  fragments from the studied model heptapeptides could not be transferred into the ICR cell to study their H/D exchange reactions. For the systematic study of H/D exchange ion-molecule reactions, neutral  $\text{ND}_3$  molecules were introduced into the ICR cell using a pulsed-leak valve setup.<sup>122</sup> Supplementary data for qualitative H/D exchange reactions of A5 with  $\text{CD}_3\text{OD}$  were conducted in a Bruker 9.4 T FT-ICR MS. The CID mass spectrum of the isotopically labeled  $\text{AAAA}(\text{His})(\text{A}^*)\text{A-NH}_2$  was acquired using a Thermo LTQ/Orbitrap (Thermo Fisher Scientific, Waltham, MA) instrument operated in positive ion mode. CID was performed in the LTQ by setting the normalized collision energy and activation time at 35 % and 30 ms, respectively. Helium (He) gas was used as collision gas for CID.

### 3.2.3. Ion Mobility-Mass Spectrometry

Ion mobility experiments were performed using a Synapt HDMS ion mobility-time-of-flight mass spectrometer (IM-TOF MS) (Waters, Manchester, UK) equipped with an electrospray ionization source operated in positive ion mode. The IM-MS separations were performed using a traveling wave height of 8.0 V and applied voltages of 6.0 V and

4.0 V, to the trap and transfer cells, respectively.<sup>135</sup> During IM separations, a nitrogen bath gas was introduced into the drift cell at a flow rate of 40 mL/min providing a typical operating pressure of ~0.9 mbar. All arrival time distributions (ATDs) were obtained by integrating the monoisotopic peak of a given analyte in the two-dimensional IM-MS spectra using MassLynx V4.1 SCN714 software (Waters, Manchester, UK). For comparisons, the intensities of the ATD profiles for b fragment and molecular ions were normalized to the highest value in the mobility profile.

#### 3.2.4. Data Analysis

To construct H/D exchange semi-log temporal plots, the natural logarithms of normalized ion intensities were plotted as a function of H/D exchange reaction time (Figures 3.3 and 3.4). Normalized ion intensities ( $I_{D0} / \sum I_{Dm}$ ) were obtained by dividing the  $^{12}\text{C}_{\text{all}}$  (*i.e.*,  $I_{D0}$ ) peak intensity of each ion (*i.e.*, molecular ion or  $b_n$  ( $n = 4-7$ ) fragment ions) by the total peak intensity of all ions ( $\sum I_{Dm}$ ) after H/D exchange events (*i.e.*,  $I_{D0} + I_{D1} + I_{D2} + \dots + I_{Dm}$  where “m” denotes the number of incorporated deuteriums in the b fragment or peptide ion after H/D exchange reaction).

H/D exchange rate constants were calculated using exponential decay time constants ( $\tau$ ) after curve fittings {using Origin software, Origin 7.0 (OriginLab Corporation, MA)} of the temporal plots. Reaction rate constants ( $k$ ) ( $\text{cm}^3 \text{ molecule}^{-1} \text{ s}^{-1}$ ) were calculated using equation 3.1<sup>123</sup>:

$$k = 1 / (\tau \times [N]) \quad \text{(Equation 3.1)}$$

where “ $\tau$ ” is the “combined” time constant {obtained from exponential curve fittings of each reaction temporal plot, assuming a single decay curve rather than double exponential decays} and “N” is the number density (in the ICR cell as  $\text{molecules cm}^{-3}$ ) of

the neutral reagent (*i.e.*, ND<sub>3</sub>) used for the H/D exchange reactions. We chose to use Origin exponential curve fittings (instead of Microsoft Excel calculated linear fittings in semi-log plots) for rate constant calculations because of the higher precision of fitting parameters obtained through iterative computations (*i.e.*, 200 iterations).

Ultrahigh mass measurement accuracy (MMA) and mass resolving power (MRP) of FT-ICR MS allow unambiguous characterization of chemical interferences. For instance, two chemical noise peaks at  $m/z$  564.23749 and 351.09942 were distinguished from <sup>12</sup>C<sub>all</sub> peaks of b<sub>7</sub><sup>+</sup> (at  $m/z$  564.28892 with assigned MMA ~ 0.09 ppm and observed MRP ~ 42,000) and b<sub>4</sub><sup>+</sup> (at  $m/z$  351.17772 with assigned MMA ~ 0.54 ppm and observed MRP ~ 85,000) fragment ions. We were able to resolve/distinguish the  $m/z$  of b fragment ions from chemical noise by maintaining the ICR cell pressure (after ND<sub>3</sub> introduction and H/D exchange reaction) at  $< \sim 2.0 \times 10^{-9}$  Torr during the ion signal detection event.

### 3.3. Results and Discussions

In all subsequent sections and for brevity based on the position of histidine amino acid (His) in the peptide sequence, we designate our seven heptapeptides as P1 to P7 (where numbers designate the position of histidine *viz.*, (His)AAAAAA-NH<sub>2</sub> ≡ P1; A(His)AAAAA-NH<sub>2</sub> ≡ P2; AA(His)AAAA-NH<sub>2</sub> ≡ P3; AAA(His)AAA-NH<sub>2</sub> ≡ P4; AAAA(His)AA-NH<sub>2</sub> ≡ P5; AAAAA(His)A-NH<sub>3</sub> ≡ P6; AAAAAA(His)-NH<sub>2</sub> ≡ P7). The fragmentation patterns of P1-P7 have been studied by Yalçin *et al.*<sup>238</sup> and in here, we do not report on CID of the seven model heptapeptides. Interested readers are referred to the three representative SORI-CID spectra of protonated P2, P4, and P7 (acquired under identical experimental conditions) included in the appendix materials (Figures A.1 to A.3 and Tables A.1 to A.3).

### 3.3.1. Gas-Phase H/D Exchange Reactions

Rates and patterns of H/D exchange reactions can provide valuable information about three dimensional structures of ions.<sup>111, 118, 242</sup> For examples, generally “tight” structures are associated with lower H/D exchange reaction rates;<sup>111</sup> such comparisons have been used to study b fragment ion structures.<sup>123, 185-188</sup> We used similar approaches to investigate b fragment structures from heptapeptides in our study. The nozzle-skimmer fragmentation of all seven model heptapeptides generated only histidine-containing b fragments ions ( $b_4^+$ - $b_7^+$ ) and no b fragment ions without histidine (*i.e.*, alanine-only b fragment ions of the type  $(A)_n$ ,  $n = 4-6$ ) were observed.

We studied H/D exchange reactivities of histidine-containing  $b_4^+$  ( $m/z$  351),  $b_5^+$  ( $m/z$  422),  $b_6^+$  ( $m/z$  493), and  $b_7^+$  ( $m/z$  564) from P1 to P7 heptapeptides. The  $b_4^+$ ,  $b_5^+$ , and  $b_6^+$  ions are assigned based on exact MMA (~1 ppm) and are formed by the cleavage of amide bonds; however, the ion at  $m/z$  corresponding to  $b_7^+$  can be a results of  $NH_3$  loss from any portion of the peptide and hence may not be assigned strictly as a conventional b fragment ion. In other words, the observed fragment ion at  $m/z$  564.28892 can be generated from the amidated heptapeptides through (at least) two pathways: loss of an amino group from either the N-terminus or C-terminus. A recent labeling study on the  $^{15}N$ -FAGFL- $NH_2$  peptide suggests that the source of  $NH_3$  loss (for an amidated peptide) is most likely from the C-terminal amine group.<sup>183</sup>

### 3.3.2. Fragment Ion Scrambling in P1-P7 Peptides

One of the problems associated with b fragment ion rearrangement or cyclization is that subsequent ion fragmentations can lead to formation of new sequence scrambled secondary fragment ions.<sup>172, 179, 183, 222, 243</sup> These rearranged fragment ions which may

include a- or b-type ions, can generally be identified based on accurate mass measurements. However, when the product ions are isobaric, their differentiations based only on the mass differences of fragment ions are not possible.

For example, the histidine-containing  $b_n$  ions from the selected seven P1-P7 peptides can be generated *via* at least two possible fragmentation pathways: (i) molecular ion ( $[M + H]^+$ )  $\rightarrow b_n \rightarrow$  scrambled or non-scrambled b fragment ions and/or (ii)  $[M + H]^+ \rightarrow y_n \rightarrow$  scrambled or non-scrambled b fragments ions. Without isotopic labeling, it is not feasible to identify fragment ion scrambling or pathways leading to b fragment ion scrambling for P1-P7 peptides that contain a single histidine with six neighboring alanine residues. To identify possible sources of ion scrambling, we synthesized and used an isotopically labeled heptapeptide  $\{AAAA(\text{His})(A^*)A\text{-NH}_2$ , where “A\*” denotes the carbon thirteen ( $^{13}\text{C}$ ) isotope on alanine side chain}.

Our preliminary CID results on isotopically labeled P5  $\{AAAA(\text{His})(A^*)A\text{-NH}_2\}$  suggest that scrambled and non-scrambled b fragment ions can originate from the molecular ions (pathway (i)) and/or y fragment ions (pathway (ii)). For example, CID fragmentation patterns of mass isolated  $[M + H]^+$  and  $y_5^+$  from  $AAAA(\text{His})(A^*)A\text{-NH}_2$  show the presence of histidine-containing  $b_4^+$  at  $m/z$  351 (*i.e.*,  $A_3(\text{His})$ ) and 352 (*i.e.*,  $A_2(A^*)(\text{His})$ ). The  $b_4^+$  at  $m/z$  351 (*i.e.*,  $A_3(\text{His})$ ) from CID of  $y_5$  ( $AA(\text{His})(A^*)A\text{-NH}_2$ ) can exclusively be assigned as a scrambled fragment ion. However, due to the presence of multiple (potential) pathways that can generate  $b_4^+$  (*i.e.*, both  $A_3(\text{His})$  and  $A_2(A^*)(\text{His})$ ) from CID process of  $[M + H]^+$ , identities (*i.e.*, scrambled or non-scrambled) of  $b_4^+$  fragments (from  $[M + H]^+$ ) can not be assigned unambiguously.

Therefore, each of the reported histidine-containing  $b_n$  fragment ion populations (*i.e.*,  $b_4^+$ - $b_7^+$  from P1-P7) in this study can be a mixture of scrambled and non-scrambled fragments. We are currently examining various pathways that can lead to  $b_n$  fragment ion (scrambled and non-scrambled) generation and plan to report our findings in future communications.

### 3.3.3. H/D Exchange Reaction Patterns

To minimize the effect of potential experimental variabilities {on the observed H/D exchange patterns and rate constants}, we isolated the  $^{12}\text{C}_{\text{all}}$  peaks of all b fragment and molecular ions for each peptide and followed their H/D exchange reactions simultaneously (a set of five H/D exchange reactions for each model heptapeptide). Figures 3.1a and 3.1b show ESI/FT-ICR mass spectra of the SWIFT-isolated  $^{12}\text{C}_{\text{all}}$  peaks for  $[\text{A}(\text{His})\text{AAAAA-NH}_2 + \text{H}]^+$  and its  $b_7^+$  fragment ion, respectively, after 0 s (top panel), 100 s (middle panel), and 500 s (bottom panel) H/D exchange reaction time with  $\text{ND}_3$  ( $P_{\text{ND}_3} \approx 4.2 \times 10^{-8}$  Torr).

As shown in Figure 3.1a (bottom panel), after ~1500 ion-molecule collisions with  $\text{ND}_3$  (*i.e.*, after 500 s reaction time with  $\text{ND}_3$  ( $P_{\text{ND}_3} \approx 4.2 \times 10^{-8}$  Torr)),  $[\text{M} + \text{H}]^+$  of P2 has exchanged nine out of its twelve (75 %) labile hydrogens and  $\text{D}_0$ ,  $\text{D}_1$ , and  $\text{D}_2$  for  $[\text{M} + \text{H}]^+$  have reacted away. However, after the same number of ion-molecule collisions with  $\text{ND}_3$  (*i.e.*, ~1500 collisions), the  $b_7^+$  fragment ion of P2 exchanged only two out of its nine (22.2 %) labile hydrogens (Figure 3.1b, bottom panel). Figures 3.2a to 3.2c show the H/D exchange patterns of SWIFT-isolated  $^{12}\text{C}_{\text{all}}$  peaks of  $b_4^+$ - $b_6^+$  ions of  $\text{A}(\text{His})\text{AAAAA-NH}_2$  (*i.e.*,  $b_n^+$  fragment ions from the same P2 peptide) under the same experimental conditions (*i.e.*, reactions times and  $\text{ND}_3$  pressure) as in Figure 3.1.

$P(\text{ND}_3) \approx 4.2 \times 10^{-8}$  Torr

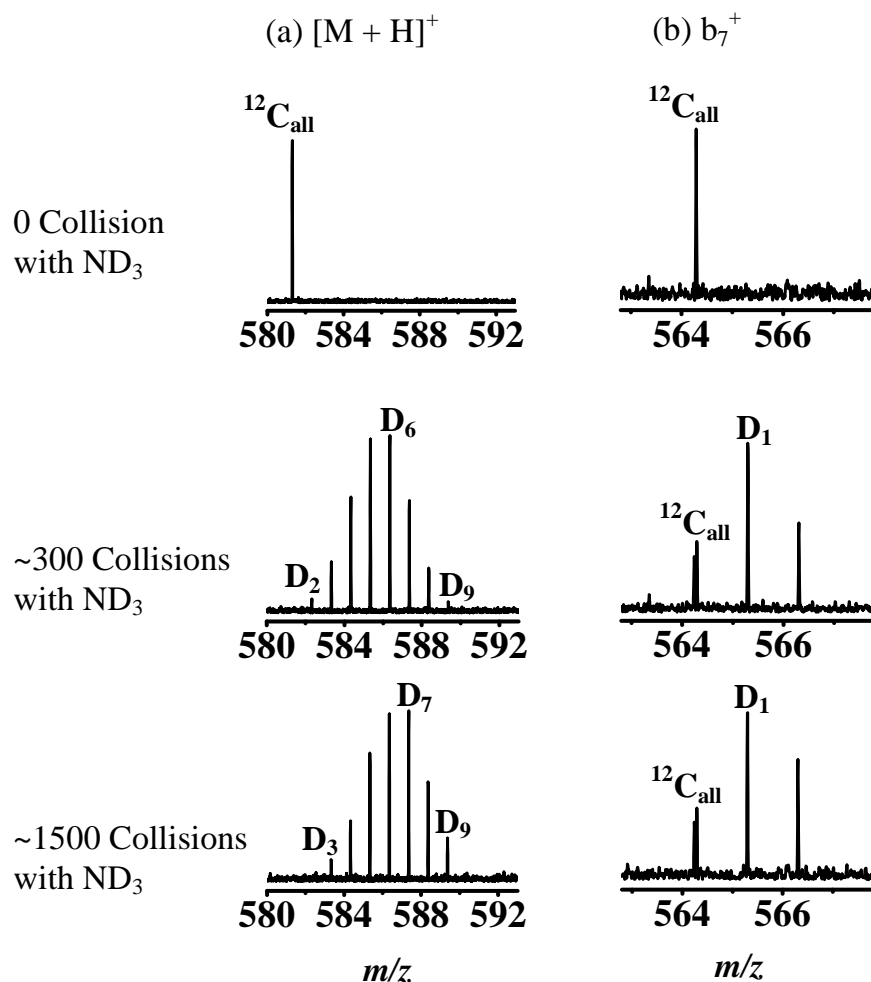


Figure 3.1. ESI/FT-ICR mass spectra of SWIFT-isolated  $^{12}\text{C}_{\text{all}}$  peak at 0 s (top panel), 100 s (middle panel), and 500 s (bottom panel) reaction times with  $\text{ND}_3$  (at  $P(\text{ND}_3) \approx 4.2 \times 10^{-8}$  Torr) for (a) molecular ion (*i.e.*,  $[M + H]^+$ ) and (b)  $b_7^+$  fragment of A(His)AAAAA-NH<sub>2</sub> (P2 peptide).

Under the same H/D exchange reaction conditions (*i.e.*,  $\text{ND}_3$  pressure and ICR cell temperature, as in Figure 3.1),  $b_4^+$  (Figure 3.2a),  $b_5^+$  (Figure 3.2b), and  $b_6^+$  (Figure 3.2c) exchange three, four, and five labile hydrogens, respectively. Similar to  $b_7^+$  (*i.e.*, Figure 3.1b), the  $\text{D}_0$  ion populations of  $b_4^+$ - $b_6^+$  fragment ions do not disappear after  $\sim 1500$  ion-molecule collisions with  $\text{ND}_3$  neutral reagent.

Based on the number of labile hydrogens in  $b_n^+$  fragment ions, one would expect to observe higher number of H/D exchanges for larger b fragment ions. However, experimental results indicated an inverse relationship between the numbers of observed H/D exchanges and b fragment ion size. For example, the H/D exchange reaction patterns in Figures 3.1b and 3.2a to 3.2c show that as  $b_n$  fragment ion size decreases, the percentage of exchanged labile hydrogens increases in the following order:  $b_7^+$  (22.2 %) <  $b_6^+$  (37.5 %) <  $b_5^+$  (57.1 %) <  $b_4^+$  (83.3 %). The H/D exchange reaction patterns for the molecular ion and  $b_n$  ( $n = 4-7$ ) of other heptapeptides (*i.e.*, P1 and P3-P7) were similar to the patterns observed for the molecular ion and  $b_n^+$  ( $n = 4-7$ ) fragment ions of P2 (as in Figures 3.1 and 3.2).

The H/D exchange reaction patterns (*i.e.*, extent of H/D exchange and existence or disappearance of  $D_0$  ion population) for  $[M + H]^+$  and  $b_4^+ - b_7^+$  suggest a drastic structural/conformational change among histidine-containing  $b_n^+$  fragments as compared to their respective molecular ions. The potential  $b_n^+$  structural/conformational changes (compared to  $[M + H]^+$ ) are more pronounced for larger b fragment ions (*e.g.*,  $b_7^+$ ) than smaller b fragment ions (*e.g.*,  $b_4^+$ ). For instance, as shown in Figure 3.1, the H/D exchange mass spectral patterns for  $[M + H]^+$  after  $\sim 300$  and  $\sim 1500$  ion-molecule collisions (with  $ND_3$ ) show disappearance of  $D_0$  and  $D_1$  (Figure 3.1a, middle panel) and  $D_0$ ,  $D_1$ , and  $D_2$  (Figure 3.1a, bottom panel) ion populations, respectively. For the  $b_7^+$  fragment ion, the H/D exchange isotopic pattern does not change significantly between  $\sim 300$  (Figure 3.1b, middle panel) and  $\sim 1500$  (Figure 3.1b, bottom panel) ion-molecule collisions. The gas-phase structural/conformational factors (*e.g.*, hydrogen bonding, salt bridge formation, *etc.*) may play a major role in the observed differences in the extent of

H/D exchange (or multiple H/D exchanges). In addition, proton affinity (PA) variations (between available exchange sites in b fragment or molecular ions) may also influence H/D exchange reaction outcomes. Moreover, occurrence of single versus multiple deuterium uptake during H/D exchange reactions can alter the observed mass spectral patterns. For instance, Gard *et al.* studied the feasibility of exchanging multiple labile hydrogens (by amino acid and peptide ions) during gas-phase H/D exchange reactions<sup>129</sup> and reported that the feasibility of multiple H/D exchanges increases as the  $\Delta$ PA between the two possible exchangeable sites (*i.e.*, most basic sites) on a peptide or amino acid decreases.<sup>129</sup>

Our H/D exchange results suggest that the structural/conformational changes of  $b_n$  fragment ions do not significantly depend on the position of histidine in the original heptapeptide sequence; the extent of H/D exchange (or available hydrogen atoms for deuterium exchange) is the same for each histidine-containing  $b_n^+$  ( $n = 4-7$ ) fragment ion from P1 to P7 and similar to the reported patterns in Figure 3.1. The lower H/D exchange reaction rates (see section below) and a fewer number of deuterium uptake for  $b_7$  ions (among  $b_4$ - $b_7$  fragments) suggest that  $b_7$  ions have more compact structures/conformations than the smaller b fragment ions. Previously, our group<sup>117, 123</sup> and Polfer and co-workers<sup>186</sup> have demonstrated the presence of bimodal H/D exchange patterns for the  $b_4^+$  and  $b_5^+$  fragment ions of WHWLQL and  $b_4^+$ - $b_7^+$  of GGGGGGGG model peptides, respectively. The bimodal H/D exchange patterns are indicative of two (“fast” and “slow”) structurally/conformationally different isobaric b fragment ions. Although the H/D exchange patterns for b fragment ions in Figures 3.1b and 3.2a to 3.2c do not show two resolved ion populations for histidine-containing b fragment ions, the

semi-log plots for H/D exchange reactions of  $b_n^+$  fragment ions (shown in Figure 3.3b inset and Figure 3.4 for P2 or A(His)AAAAA-NH<sub>2</sub>) suggest the presence of at least two ion populations with different reactivities with ND<sub>3</sub> ( $D_0 \rightarrow D_m$ ).

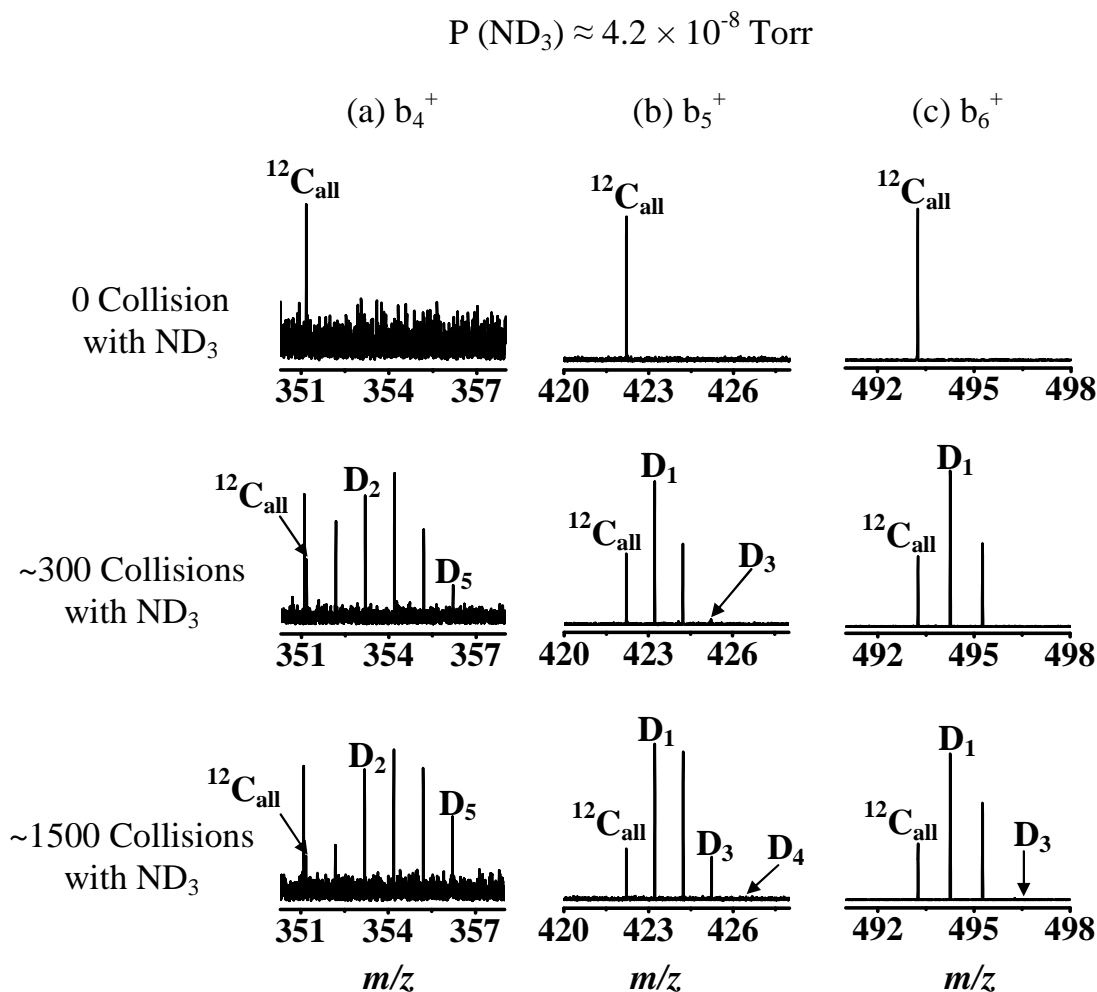


Figure 3.2. ESI/FT-ICR mass spectra of SWIFT-isolated  $^{12}\text{C}_{\text{all}}$  peak at 0 s (top panel), 100 s (middle panel), and 500 s (bottom panel) reaction times with ND<sub>3</sub> (at  $P(\text{ND}_3) \approx 4.2 \times 10^{-8}$  Torr) for (a)  $b_4^+$ , (b)  $b_5^+$ , and (c)  $b_6^+$  fragments of A(His)AAAAA-NH<sub>2</sub> (P2 peptide).

All  $b_n^+$  ( $n = 4-7$ ) fragment ions generated from P1-P7 heptapeptides exhibited semi-log plots similar to Figure 3.3b inset and Figures 3.4a to 3.4c. These results suggest

the presence of at least two ion populations for each b fragment ion, regardless of the position of histidine in the original heptapeptide sequence.

#### 3.3.4. Kinetics of the H/D Exchange Reactions

To further investigate the effect of histidine position on the structure/conformation of the histidine-containing  $b_n$  ( $n = 4-7$ ) fragment ions, the H/D exchange reaction rates of singly-charged b fragment ions of all seven model heptapeptides were studied. To minimize the effect of ion formation and fragmentation energetics in the ESI source on the structure/conformation of generated b fragment ions, the temperature and voltages on the heated metal capillary and skimmer were kept constant at  $\sim 120 \pm 3$  °C,  $\sim +70$  V, and  $\sim +1.0$  V, respectively, for all the H/D exchange reactions reported in this study.

To obtain H/D exchange temporal plots for  $b_n^+$  ( $n = 4-7$ ) fragment ions, the normalized ion intensity (I) for depletion/disappearance of the SWIFT-isolated  $D_0$  peak (*i.e.*,  $I_{D_0} / \sum I_{D_m}$ ) was plotted as a function of H/D exchange reaction time. As an example, the temporal plots for  $[M + H]^+$  and  $b_7^+$  of P2 are shown in Figures 3.3a and 3.3b, respectively. The semi-log plots for H/D exchange reaction of  $[M + H]^+$  and  $b_7^+$  are also shown as insets in Figures 3.3a and 3.3b.

For simplicity, only H/D exchange semi-log plots for  $b_4^+$ ,  $b_5^+$ , and  $b_6^+$  fragments ions (from P2) are shown in Figures 3.4a to 3.4c, respectively. The semi-log plots for b fragment ions (Figure 3.3b inset and Figures 3.4a-c) show two linear segments, indicative of the presence of two H/D-exchanging ion populations.<sup>121, 123, 186</sup> However, the best fits {using Origin 7.0 (OriginLab Corporation, MA)} of the data in the temporal plots of the b fragment ions correspond to single exponential decay equations {*i.e.*,  $Y = A \times \text{Exp}(-t /$

$\tau$ ), where “Y” is normalized ion intensity, “A” is pre-exponential constant, “t” is the reaction time, and “ $\tau$ ” is the time constant for the H/D exchange reaction decay curve}.

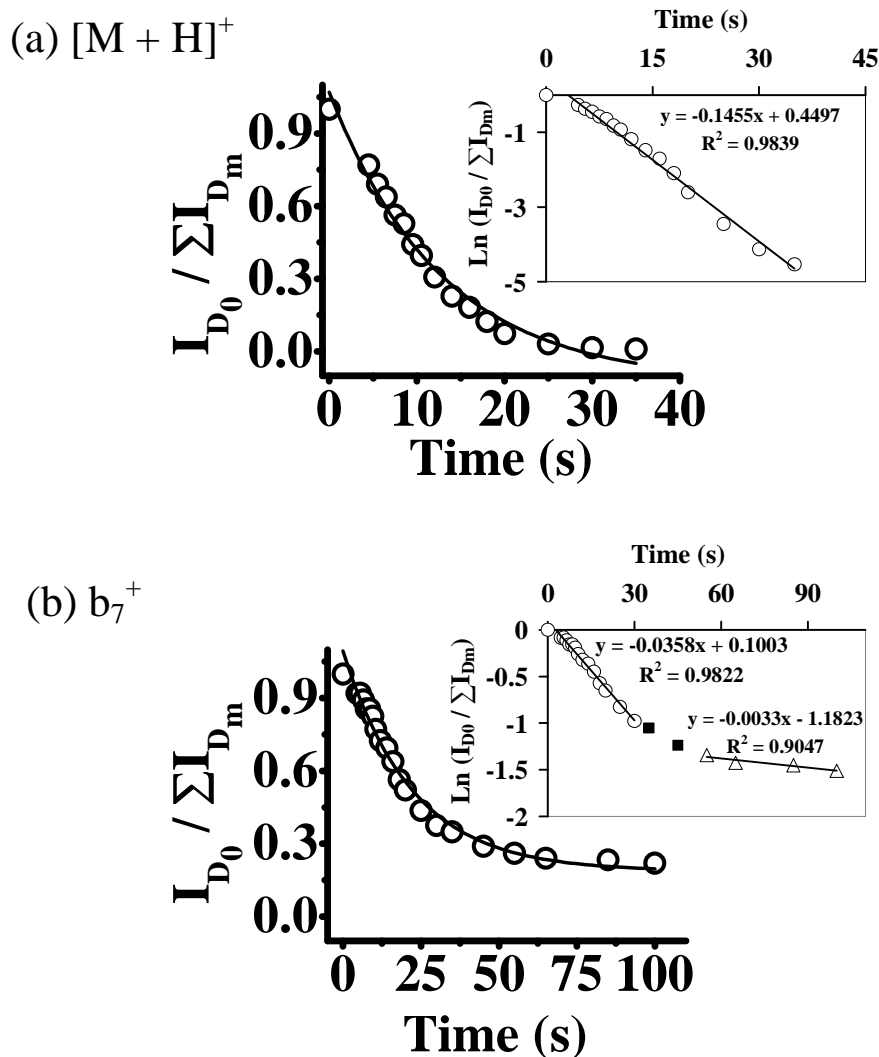


Figure 3.3. Temporal plots of normalized ion abundance versus H/D exchange reaction time for disappearance of the  $^{12}\text{C}_{\text{all}}$  peak (or  $\text{D}_0$ ) for (a)  $[M + H]^+$  and (b)  $b_7^+$  fragment of A(His)AAAAA-NH<sub>2</sub>. The fitted single exponential decay equations for each fragment ions are shown in the corresponding plots. The insets show semi-log plots of  $\ln(I_{\text{D}_0} / \sum I_{\text{D}_m})$  vs. H/D exchange reaction time of each b fragment ion. The empty circles ( $\circ$ ) and triangles ( $\Delta$ ) in the semilog plots show the segments corresponding to “fast” + “slow” and “slow” H/D-exchanging populations, respectively. The fitted linear equations for each segment are shown in the plots. The filled squares ( $\blacksquare$ ) in the semi-log plots correspond to H/D exchange data which were not used for linear fitting.

Attempts to fit the H/D exchange reaction kinetic data for b fragment ions to bi-exponential decay equations  $\{i.e., Y = A_1 \times \text{Exp}(-t / \tau_1) + A_2 \times \text{Exp}(-t / \tau_2)\}$  failed due to high fitting errors. Failure in fitting the data to a bi-exponential equation may be due to the long H/D exchange time constants (*i.e.*,  $> \sim 100$  s) for the “slow” H/D-exchanging b ion populations; for instance, the  $D_0$  normalized intensities for “slow” H/D-exchanging populations of  $b_n^+$  fragment ions of P2 decrease by only  $\sim 3-10$  % when the number of ion-molecule collisions is increased from  $\sim 300$  collisions to  $\sim 1500$  collisions (*i.e.*, compare Figures 3.1b and 3.2a to 3.2c, middle and bottom panels).

The reported average H/D exchange rate constants for  $b_n^+$  fragment ions in Table 3.1 were obtained from single exponential curve fittings. These rate constants (from single exponential curve fittings) have major contributions from the “fast” reacting b fragment ions and only minor contributions from the “slow” reacting b fragment ion populations. Accurate H/D rate constants for “slow” reacting b ion populations can be obtained by acquiring mass spectra at longer reaction times (*i.e.*,  $> 500$  s) and/or higher  $\text{ND}_3$  pressures.

The current version of our Omega software (Omega 8.0.294, former IonSpec Corp. - now a division of Agilent Technologies, Inc., Santa Clara, CA) does not allow running a sequence of events longer than  $\sim 17$  min. This software-imposed restriction and the additional time required to achieve ultrahigh vacuum during ion signal detection limited the dynamic range for ion-molecule reactions (*i.e.*,  $< 500$  s). Table 3.1 shows the H/D exchange rate constants (for disappearance of  $D_0$ ) for histidine-containing  $b_n^+$  ( $n = 4-7$ ) fragment and molecular ions of P1 to P7 heptapeptides.

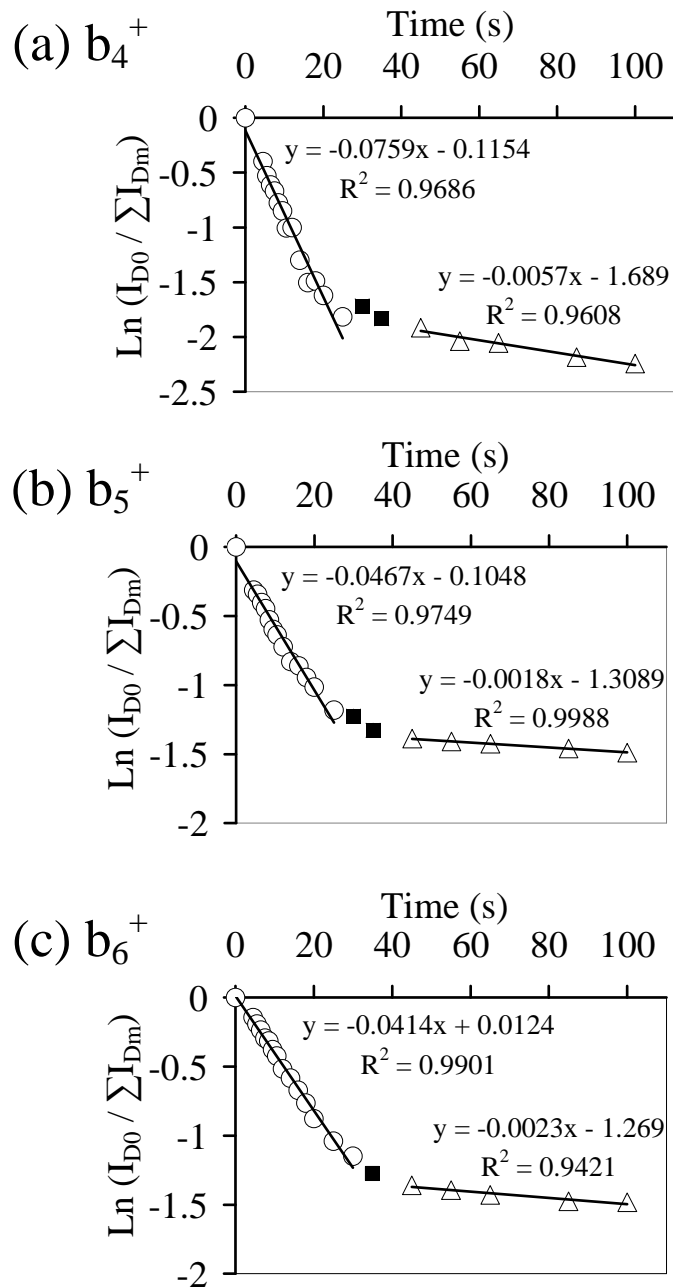


Figure 3.4. Semi-log plots of  $\ln(I_{D0} / I_{Dm})$  vs. H/D exchange reaction time for (a)  $b_4^+$ , (b)  $b_5^+$ , and (c)  $b_6^+$  fragment ions of A(His)AAAAA-NH<sub>2</sub>. The empty circles ( $\circ$ ) and triangles ( $\Delta$ ) in the semi-log plots show the segments corresponding to “fast” + “slow” and “slow” H/D-exchanging populations, respectively. The fitted linear equations for each segment are shown in the plots. The filled squares ( $\blacksquare$ ) in the semi-log plots correspond to H/D exchange data which were not used for linear fitting.

The largest b fragment ion (*i.e.*,  $b_7^+$ ) of all seven peptides, except for P7, showed the lowest H/D exchange rate constant of all the histidine-containing  $b_n^+$  ( $n = 4-7$ ) fragments. The H/D exchange rate constants for  $b_6^+$  and  $b_7^+$  fragment ions of all seven heptapeptides remained approximately constant (*i.e.*,  $\sim 5.0-7.0 \times 10^{-11} \text{ cm}^3 \text{ molecule}^{-1} \text{ s}^{-1}$ ) and did not show dependency on the position of histidine in the original heptapeptide. In other words, the position of histidine in the  $b_6^+$  and  $b_7^+$  fragment ion sequences may not have a significant effect on their gas-phase structures. On the other hand, the  $b_4^+$  and  $b_5^+$  fragment ions showed more H/D exchange reactivity dependence on histidine position (in the original heptapeptide sequence) than  $b_6^+$  and  $b_7^+$ . The observed H/D exchange rate constants decrease as a function of increasing fragment ion size for P1, P2, and P5. In other words, the highest and lowest H/D exchange rate constants correspond to  $b_4^+$  and  $b_7^+$  fragment ions, respectively, of P1, P2, and P5. Alternatively, for P3, P4, and P6 the highest H/D exchange rate constant corresponds to  $b_5^+$ .

On the other hand, the H/D exchange rate constants for  $b_4^+$ - $b_7^+$  fragments of P7 do not show statistically significant (at 95 % confidence interval) dependence on fragment ion size. As we mentioned earlier, without isotope labeling, it is not possible to know if scrambling has occurred for the  $b_4^+$ ,  $b_5^+$ , and  $b_6^+$  fragment ions generated from P1-P7 (due to the presence of isobaric alanine residues in all peptide sequences). The statistically similar (at 95 % confidence interval) H/D exchange rate constants of  $b_6^+$  fragment ions of P7 to the H/D exchange rate constants of  $b_6^+$  from P1-P3 and P5-P6 may imply that these model heptapeptides generate structurally similar  $b_6^+$ , regardless of histidine position in the original peptide sequence. Moreover, the statistically similar (at 95 % confidence interval) H/D exchange rate constants for  $b_7^+$  of all seven heptapeptides

may also suggest similar fragment type for  $b_7^+$  fragment ions, independent of histidine position.

Table 3.1. Experimental rate constants for  $b_4^+$ - $b_7^+$  fragment ions of all seven (His)(A)<sub>6</sub>-NH<sub>2</sub> type model heptapeptides. Rate constants are in  $\times 10^{-11}$  cm<sup>3</sup> molecule<sup>-1</sup> s<sup>-1</sup> and an average of three experimental trials, with standard deviations (n = 3) included within parentheses.

Peptides	Fragment Type				
	$b_4^+$ ( <i>m/z</i> 351)	$b_5^+$ ( <i>m/z</i> 422)	$b_6^+$ ( <i>m/z</i> 493)	$b_7^+$ ( <i>m/z</i> 564)	[M + H] <sup>+</sup> ( <i>m/z</i> 581)
P1	11.30(± 1.37)	09.80(± 1.14)	06.06(± 0.90)	04.57(± 0.71)	02.77(± 0.57)
P2	10.58(± 2.65)	07.37(± 1.88)	05.79(± 0.43)	04.32(± 0.46)	07.42(± 0.99)
P3	06.47(± 0.32)	07.86(± 1.01)	05.77(± 0.55)	04.84(± 0.40)	03.29(± 1.01)
P4	09.78(± 0.55)	12.42(± 2.31)	07.61(± 0.68)	05.00(± 1.71)	03.08(± 0.83)
P5	08.48(± 0.10)	07.96(± 1.12)	04.94(± 1.11)	04.89(± 0.50)	02.26(± 0.50)
P6	06.62(± 0.06)	08.96(± 0.00)	05.50(± 0.63)	05.26(± 0.61)	03.83(± 1.11)
P7	06.58(± 1.43)	05.29(± 0.81)	03.90(± 1.00)	05.85(± 0.52)	05.86(± 0.23)

Previously, two types of structures have been suggested/confirmed for b fragment ions using both experimental (*i.e.*, infrared multiphoton dissociation (IRMPD) spectroscopy<sup>186, 187</sup>) and theoretical (*i.e.*, molecular dynamic simulations<sup>190</sup>) approaches: macrocyclic and oxazolone. Molecular dynamic simulations by Bythell *et al.* suggested a macrocyclic structure (protonated at the histidine side-chain) for histidine-containing  $b_4^+$  {A<sub>3</sub>(His)} and  $b_5^+$  {A<sub>4</sub>(His)} fragments as more energetically stable than an oxazolone structure.<sup>190</sup>

In another study, IRMPD spectroscopy results by Chen *et al.*<sup>186</sup> suggested oxazolone and macrocyclic structures for the “fast” and “slow” H/D-exchanging ion

populations of  $b_4^+$ - $b_7^+$  fragments of the GGGGGGGG peptide, respectively. Our H/D exchange reaction kinetics observations (*i.e.*, presence of two linear segments in the semi-log plots in Figure 3.3b inset, and Figure 3.4) are consistent with Bythell's<sup>190</sup> and Chen's data,<sup>186</sup> suggesting the existence of two structures for histidine-containing  $b_4^+$ - $b_7^+$  fragment ions.

As shown in Table 3.1, the H/D exchange rate constants of  $b_n^+$  ( $n = 4-7$ ) fragment ions of P1-P7 were similar to or higher than the H/D exchange rate constants of their corresponding molecular ions (*i.e.*,  $[M + H]^+$ ), except for  $b_6^+$  and  $b_7^+$  of P2 and  $b_6^+$  of P7. In other words, the calculated  $k_{b_n^+} / k_{[M + H]^+}$  ratios for all the studied model heptapeptides are between  $\sim 1.0$  and  $\sim 4.0$  with the exception of  $b_6^+$  ( $k_{b_6^+} / k_{[M + H]^+} \approx 0.8$ ) and  $b_7^+$  ( $k_{b_7^+} / k_{[M + H]^+} \approx 0.6$ ) of P2 and  $b_6^+$  ( $k_{b_6^+} / k_{[M + H]^+} \approx 0.7$ ) of P7. The higher H/D exchange rate constants for b fragment ions of P1 and P3-P6 (as compared to their corresponding molecular ions) may be due to lower gas-phase basicities and/or less compact structures/conformations for  $b_n^+$  fragment ions (compared to  $[M + H]^+$ ).

It is interesting to note that H/D exchange reactions of  $b_4^+$  and  $b_5^+$  fragment ions from Ala<sub>5</sub> (*i.e.*, a pentapeptide with no histidine) also yield bimodal temporal (and semilog) plots and divergent H/D exchange patterns (for  $b_5^+$ ) (data included in the appendix materials, Figure A.4). The observation of the two  $b_n$  ( $n = 4$  and  $5$ ) fragment ion populations from Ala<sub>5</sub> is similar to previously reported results for  $b_n$  fragment ions ( $n = 4$  to  $7$ ) from Gly<sub>n</sub> species.<sup>186</sup> For similar size  $b_n$  fragment ions (*e.g.*,  $n = 4$  and  $5$ ) from Ala<sub>5</sub> or HisAla<sub>6</sub> (P1 to P7) peptides, both “fast” and “slow” H/D exchanging fragment ion populations are formed.

### 3.3.5. Ion Mobility (IM) Profiles

The focus of our ion mobility experiments was to study the structural variations of histidine-containing  $b_n^+$  ( $n = 4-7$ ) fragment ions as a function of histidine position in the original heptapeptide sequence(s). We only compare the mobility profiles in terms of arrival times and peak shapes of the P1-P7 fragment ions. To minimize possible structural variations of fragment ion as a result of experimental disparities, we used similar experimental parameters (*e.g.*, electrospray and ion generation conditions) for the ESI/IM-MS and ESI/FT-ICR MS studies.

Figures A5a to A5c show the mobility arrival time distributions (ATDs) acquired for molecular ions (*i.e.*,  $[M + H]^+$ ) and nozzle-skimmer generated histidine-containing  $b_4^+$ - $b_7^+$  fragment ions of P3, P4, and P7. The ion intensities (*i.e.*, Y-axes) in Figures A.5a to A.5c were normalized for easier comparison of the mobility profiles of fragment ions with different intensities. The observed ATDs for molecular ions and  $b_4^+$ ,  $b_6^+$ , and  $b_7^+$  fragment ions of P1-P7 show “Gaussian-like” peak shapes. However, the ATDs corresponding to  $b_5^+$  fragments from P3 (Figures A.5a), P4 (Figure A5b), and P5 (not shown) show two ion populations (*i.e.*, mobility profiles can be fitted to bi-Gaussian distributions).

In contrast, ATDs for  $b_5^+$  fragment ions generated from P1 to P2 (not shown), P6 (not shown), and P7 (Figure A.5c) reveal “Gaussian-like” distributions (similar to molecular ions and  $b_4^+$  and  $b_6^+$ - $b_7^+$  fragments). The  $b_5^+$  fragment ion populations with shorter peak arrival times (or smaller collision cross sections) are indicative of more compact structures than the longer arrival time (or larger collision cross section)  $b_5^+$  ion populations. Our preliminary post-IM/CID results (data not shown) on histidine-

containing  $b_5^+$  suggests a more stable structure (*i.e.*, highly resistant to fragmentation) for the shorter arrival time ion population compared to the ion population with a longer arrival time.

To further investigate the effect of histidine position on the structure of  $b_n^+$  fragment ions, we systematically compared the IM peak arrival times and full-width half-heights (FWHHs) of the acquired ATDs (*e.g.*, ATDs shown in Figure A.5). To obtain the mobility peak centroids and FWHHs, we utilized Gaussian curve fitting using Origin software {Origin 7.0 (OriginLab Corporation, MA)}. The mobility arrival time distributions were fitted to  $Y = \{Y_0 + A / (w \times \sqrt{\pi / 2})\} \times \text{Exp}\{-2 ((t - t_A) / w)^2\}$ . The included parameters for the Gaussian curve fitting are as follow: “Y” is the normalized intensity in the mobility profile, “ $Y_0$ ” is the offset in Y value, “A” is a constant, “w” is related to FWHH {using  $\text{FWHH} = w \times \sqrt{\ln(4)}$ }, “t” is the arrival time, and “ $t_A$ ” is the peak arrival time (*i.e.*, central time value in the fitted Gaussian equation).

The ion mobility data (*i.e.*, peak arrival times and FWHHs obtained from Gaussian curve fittings) for all P1-P7 heptapeptides, including molecular ions and their histidine-containing  $b_4^+$ - $b_7^+$  fragment ions, are summarized in Table 3.2. In Table 3.2, columns 1 and 2 indicate identities of the studied ions and their corresponding heptapeptides (P1-P7); columns 3-5 contain ion mobility peak arrival times, FWHH of the mobility profiles, and  $R^2$  values obtained from the Gaussian curve fitting for each fragment ion of each model heptapeptide.

The  $R^2$  values listed in column 5 of Table 3.2 indicate good fits to a Gaussian equation for the fragment and molecular ions of the studied model heptapeptides {except for  $b_7^+$  ( $R^2 = 0.84$ ) and molecular ion ( $R^2 = 0.78$ ) of P1 due to poor signal-to-noise ratio}.

Table 3.2. Ion mobility peak arrival time, full width at half height (FWHH), and  $R^2$  obtained from Gaussian curve fitting for  $[M + H]^+$  and histidine- containing  $b_4^+$ - $b_7^+$  fragment ions of seven (P1-P7) studied heptapeptides.

Fragment ( $m/z$ )	Peptide #	Peak Arrival Time (ms)	FWHH* (ms)	$R^2$
$b_4^+$ ( $m/z$ 351)	P1	7.23	1.07	0.99
	P2	7.48	1.60	0.99
	P3	7.61	1.66	0.99
	P4	7.30	1.08	0.99
	P5	7.31	1.24	0.99
	P6	7.35	1.28	0.98
	P7	7.25	1.09	0.99
Average ( $\pm$ STD)		7.36 ( $\pm$ 0.14)	1.29 ( $\pm$ 0.25)	
$b_5^+$ ( $m/z$ 422)	P1	8.64	1.47	0.99
	P2	8.70	2.00	0.98
	P3	9.25	2.37	0.98
	P4	9.21	2.24	0.98
	P5	9.27	2.26	0.98
	P6	9.09	1.95	0.94
	P7	8.99	1.78	0.99
Average ( $\pm$ STD)		9.02 ( $\pm$ 0.26)	2.01 ( $\pm$ 0.31)	
$b_6^+$ ( $m/z$ 493)	P1	10.65	1.68	0.97
	P2	10.54	2.32	0.99
	P3	11.04	2.30	0.99
	P4	11.06	2.35	0.99
	P5	11.10	2.12	0.99
	P6	10.69	2.03	0.99
	P7	10.79	1.92	0.99
Average ( $\pm$ STD)		10.84 ( $\pm$ 0.23)	2.10 ( $\pm$ 0.25)	
$b_7^+$ ( $m/z$ 564)	P1	12.16	2.54	0.84**
	P2	12.43	2.18	0.99
	P3	12.85	2.19	0.99
	P4	12.63	2.23	0.99
	P5	11.68	2.04	0.99
	P6	12.98	2.76	0.99
	P7	12.99	2.35	0.99
Average ( $\pm$ STD)		12.53 ( $\pm$ 0.48)	2.33 ( $\pm$ 0.25)	
$[M + H]^+$ ( $m/z$ 581)	P1	12.61	1.77	0.78**
	P2	13.33	2.51	0.99
	P3	13.00	2.19	0.99
	P4	13.16	1.98	0.99
	P5	14.12	2.44	0.99
	P6	14.10	2.40	0.99
	P7	13.89	2.61	0.99
Average ( $\pm$ STD)		13.46 ( $\pm$ 0.59)	2.27 ( $\pm$ 0.31)	

\* Experimentally estimated standard deviation (three trials) for FWHH is  $<\pm 0.02$  ms.

\*\* The fitting errors for  $b_7^+$  and  $[M + H]^+$  of P1 were high due to poor S/N.

Also, notice that  $R^2$  values for all  $b_5^+$  ions are lower than the values listed for other fragment ions, consistent with the visual inspection of  $b_5^+$  ATD in Figure A.5 suggesting the presence of different  $b_5^+$  conformers or structures. The peak arrival time values increase linearly as a function of  $m/z$  for studied b fragment and molecular ions. For instance, the best fit to the average peak arrival time- $m/z$  data (shown in Table 3.2) is a linear equation {*i.e.*, peak arrival time (ms) =  $0.03 (\pm 0.00) \times m/z - 1.77 (\pm 0.55)$ ,  $R^2 = 0.99$ }. In general (as it is shown in Table 3.2), the b fragment ions generated from the heptapeptides with histidine at either N- or C-terminus (*i.e.*, positions 1 and 7, respectively) show narrower FWHHs than b fragments from heptapeptides with internal histidine positions. {The FWHH for the  $b_7^+$  fragment ion of P1 is not conclusive due to poor S/N}. This may suggest that the b fragment ions generated from P1 and P7 have less structural variability compared to the b fragment ions from other studied heptapeptides (P2-P6).

In traveling wave ion mobility, peak widths for single-component analytes (*i.e.*, one analyte having one structure) broaden with increasing arrival time.<sup>135</sup> To assess the structural variability based on mobility peak widths (PWs), analyte PWs should ideally be compared to the PWs of compounds with a single structure/component at similar arrival times. We compared the FWHH values of the mobility peaks for a series of standard sodium adduct polypropylene glycol (PPG) ions with the FWHH values of the mobility peaks for  $b_4^+$ - $b_7^+$  from P3. Mobility peaks for sodium adduct PPG ions are expected to reflect only single component (for each species or  $\square$  symbols in Figure 3.5).

Figure 3.5 shows the plot of peak width at half height (FWHH) as a function of the arrival time (AT) values for the sodium adduct PPG species (at  $m/z$  389, 477, 505,

563, and 621) and  $b_n^+$  ( $n = 4-7$ ) and  $[M + H]^+$  of P3. The error bars in Figure 3.5 were calculated using six experimental values for each data point (please note that the error bars for ion arrival times are negligible). As expected,<sup>135</sup> the data for sodium adduct PPG ions (empty squares ( $\square$ )) in Figure 3.5) indicate a linear relationship between the FWHH values and corresponding arrival times (dash-line with  $R^2$  value of  $\sim 0.98$ ).

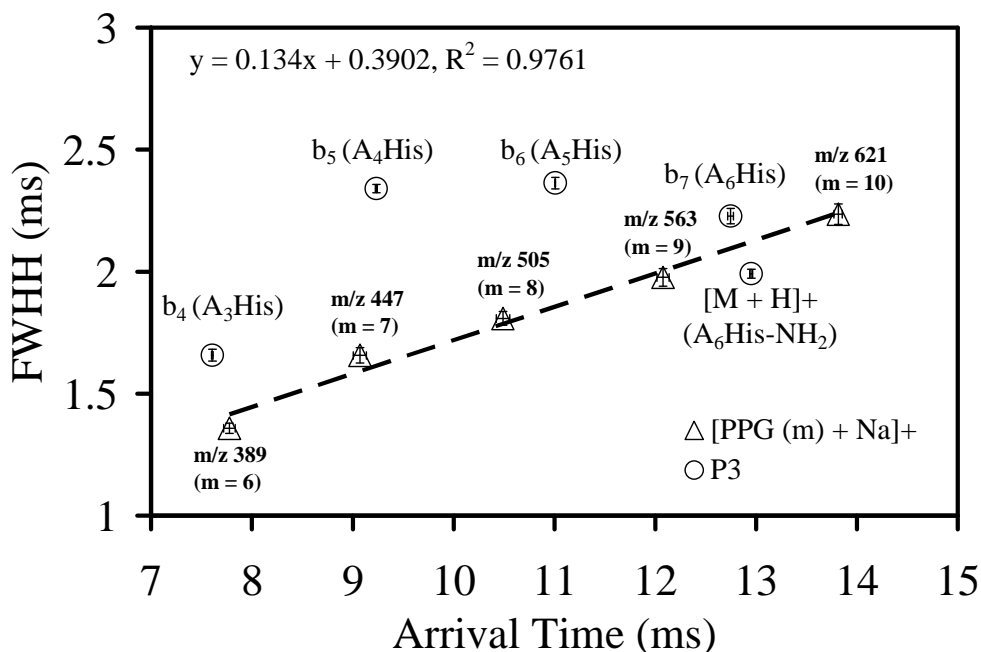


Figure 3.5. Plot of ion mobility peak widths (FWHH) versus arrival time values for standard sodium adduct polypropylene glycol (PPG) ions {empty squares ( $\square$ )} and  $b_n^+$  ( $n = 4-7$ ) and  $[M + H]^+$  of P3 {empty circles ( $\circ$ )}. The  $m/z$ s of the sodium adduct PPG species and the number of propylene glycol units (*i.e.*, “ $m$ ”) in  $[PPG(m) + Na]^+$  ( $m = 6-10$ ) are labeled. The equation obtained from the linear fitting (dash-line) to the sodium adduct PPG ions data is also shown in the top portion of plot. Each data point is the average of six experimental trials performed in two different days and errors (95 % confidence level) for both arrival time ( $<0.7\%$ ) and FWHH ( $<2\%$ ) values are shown as error bars.

The comparisons of the FWHHs for PPG mobility profiles (shown as  $\square$  symbols in Figure 3.5) and  $b$  fragment ions (empty circles ( $\circ$ )) in Figure 3.5) suggest that  $b_4^+$ ,  $b_5^+$ ,  $b_6^+$ , and  $b_7^+$  fragment ions have significantly higher FWHHs than the sodium adduct PPG

ions at similar arrival times. The expected FWHH values for b fragment ions can be calculated by substituting b fragment ions' arrival times in the linear fit equation of Figure 3.5 ( $\text{FWHH} = 0.134 \times \text{AT} + 0.390$ ). For example, the experimentally obtained FWHH values for IM profiles of  $b_4^+$ - $b_7^+$  from P3 are all higher than their calculated FWHH values (*viz.*, ~18 %, ~44 %, ~27 %, and 6 %, respectively). Deviation of the experimentally observed FWHH values for b fragment ions of P3 from the expected linear relationship (as shown in Figure 3.5) is consistent with the presence of more than a single histidine-containing b fragment ion structures.

Also note that  $b_5^+$  from P3 exhibits the highest FWHH value (or 44 % above the expected value obtained from the linear equation in Figure 3.5); these results are in harmony with the H/D exchange (*e.g.*, Figure A.6) and IM profiles (*e.g.*, Figure A.5a) results for  $b_5^+$  of P3 that indicate the presences of at least two populations. Conversely, the experimentally observed (narrower than the predicted value) FWHH for  $[M + H]^+$  of P3 suggests that this molecular ion has less structural variability (as compared to other species such as the b fragments).

Although the presence of two (or more) ion mobility resolved populations and the two “fast” and “slow” H/D exchanging populations could have different chemical reasons, it is interesting to note that relative percentages of the two populations from HDX and IM-MS experiments for  $b_5$  fragments ions are in qualitative agreement. For instance, both HDX semi-log plots and IM-MS results suggest that the majority of  $b_5^+$  fragment ions for P3-P6 have “open” structures (*i.e.*, “fast” H/D exchanging ion populations have higher relative percentages which qualitatively agree with the observed higher abundances of the b fragment ion populations with larger collision cross sections in IM-MS). Again, it

should be noted that HDX and IM-MS comparisons may or may not correlate as each of the  $b_n^+$  fragment populations could contain several sub-populations or multiple structures with unique H/D exchange properties and varying collision cross sections.

### 3.4. Conclusions

Both H/D exchange reaction kinetics (*i.e.*, temporal semi-log plots) and the degree of deuterium incorporation suggest the presence of at least two structures for all histidine-containing  $b_n^+$  ( $n = 4-7$ ) fragment ions, regardless of histidine position in the original P1-P7 heptapeptides. These results are consistent with the previously reported theoretical calculations on the cyclization of b fragment ions from histidine containing hexapeptides by Bythell *et al.*<sup>190</sup> Among the histidine-containing  $b_n^+$  ( $n = 4-7$ ) investigated in our study, the  $b_4^+$  and  $b_5^+$  fragment ions showed higher H/D exchange reactivity dependence on histidine position. Under our low resolving power ion mobility conditions (*i.e.*, peak arrival time/FWHH  $\approx 4-8$ ), the ATDs of histidine-containing  $b_4^+$ ,  $b_6^+$ , and  $b_7^+$  fragments from none of the seven model heptapeptides show mobility resolved ion populations. However, the observed ATDs for  $b_5^+$  fragments show the existence of different  $b_5^+$  isomers or conformers for P3–P5.

Our FWHH comparisons between standard sodium adduct PPG ions with histidine containing  $b_4^+$ - $b_7^+$  of P3 show that these b fragment ions have significantly wider ion mobility peak widths than the standard PPG ions with similar arrival times. The ion mobility results suggest that  $b_4^+$ - $b_7^+$  fragments may exist as several different isomers or conformers. For example, the deviation of the experimental FWHH value for  $b_5^+$  fragment of P3 from the expected linear relationship (Figure 3.5) is consistent with the H/D exchange and IM profiles (for  $b_5^+$  of P3) that indicate the presence of at least two ion

populations. A higher number of ion–molecule collisions (and the use of different deuterium reagents) may provide additional insight to probe various components of the “slow” H/D-exchanging isomers or conformers. We plan to explore the combined use of ion mobility and H/D exchange reactions with post ion mobility CID to resolve different b fragment isomers or conformers.

#### *Acknowledgement*

The authors would like to thank the financial supports from the Institute for Therapeutic Discovery, Department of Defense (DOD) (Grant No. CDMRP-OC060322), and Baylor University. We would like to thank Dr. Christopher Becker for helpful discussions on ion mobility results, Dr. Talat Yalçın for valuable discussions providing P1-P7 peptides used in this study. We are indebted to Dr. Vicki Wysocki and Dr. Arpad Somogyi for their kind assistance with the supplementary H/D exchange reaction data for  $b_4^+$  and  $b_5^+$  of  $A_5$  with their 9.4 Bruker FT-ICR MS instrument.<sup>244</sup>

## CHAPTER FOUR

### Evidence for Sequence Scrambling in Collision-Induced Dissociation of y-Type Fragment Ions

This chapter published as: Miladi, M.; Harper, B.; Solouki, T., Evidence for sequence scrambling in collision-induced dissociation of y-type fragment ions. *J. Am. Soc. Mass. Spectrom.* **2013**, 24, 1755-1766.

#### *Abstract*

Sequence scrambling from y-type fragment ions has not been previously reported. In a study designed to probe structural variations among b type fragment ions, it was noted that y fragment ions might also yield sequence-scrambled ions. In this study, we examined the possibility and extent of sequence-scrambled fragment ion generation from collision-induced dissociation (CID) of y-type ions from four peptides (all containing basic residues near the C-terminus) including: AAAAHAA-NH<sub>2</sub> (where “A” denotes carbon thirteen (<sup>13</sup>C<sub>1</sub>) isotope on the alanine carbonyl group), des-acetylated- $\alpha$ -melanocyte (SYSMEHFRWGKPV-NH<sub>2</sub>), angiotensin II antipeptide (EGVYVHPV), and glu-fibrinopeptide b (EGVNDNEEGFFSAR).

We investigated fragmentation patterns of 32 y-type fragment ions, including y fragment ions with different charge states (+1 to +3) and sizes (3 to 12 amino acids). Sequence-scrambled fragment ions were observed from ~50 % (16 out of 32) of the studied y-type ions. However, observed sequence-scrambled ions had low relative intensities from ~0.1 % to a maximum of ~12 %. We present and discuss potential mechanisms for generation of sequence-scrambled fragment ions. To the best of our

knowledge, results on y fragment dissociation presented here provide the first experimental evidence for generation of sequence-scrambled fragments from CID of y ions through intermediate cyclic “b-type” ions.

#### 4.1. Introduction

Amino acid sequence determination of peptides and proteins is generally performed by sequencing digested peptides and/or intact proteins using tandem mass spectrometry ( $MS^n$ ) and gas-phase ion fragmentation techniques (*e.g.*, collision-induced dissociation (CID),<sup>150</sup> infrared multiphoton dissociation (IRMPD),<sup>152</sup> electron capture dissociation (ECD),<sup>88</sup> and electron transfer dissociation (ETD)<sup>89</sup>). Subsequently, product fragment ions (*e.g.*, a-, b-, c-, x-, y-, and z-type, Roepstorff and Fohlman’s nomenclature<sup>162</sup>) can be searched against protein libraries/databases using search engines<sup>245-247</sup> to identify matching peptide/protein sequences.

Observed degree of match between the experimentally obtained  $MS^n$  protein/peptide mass spectra and available mass spectra from a library or database is expressed as a “matching score”.<sup>170, 181</sup> Matching scores for protein/peptide sequencing can be influenced by the presence of background contaminations<sup>248</sup> and/or unusual fragment ions.<sup>171</sup> Previous studies have suggested that a potential source for generation of unusual fragment ions in  $MS^n$  experiments is fragment ion “rearrangement”<sup>178, 179, 243</sup> or “sequence scrambling”.<sup>172</sup> Unlike “normal” or direct fragment ions (*i.e.*, fragment ions originating from the sequential loss of C- or N-terminus amino acids<sup>189</sup>), scrambled (or non-direct) fragment ions are not sequence-informative and can result in protein/peptide sequence misidentification.<sup>249</sup> The extent of non-direct ion fragmentations’ impact on protein/peptide sequencing has been debated,<sup>250, 251</sup> but clearly, incorporation of ion

fragmentation rules into available search engines should improve protein sequence identification.

The first evidence for generation of rearranged fragment ions from CID of b-type fragment ions was reported by Tang *et al.*<sup>178, 179, 243</sup> Subsequently, evidences from different gas-phase structural probes (*e.g.*, hydrogen/deuterium exchange (HDX),<sup>117, 123, 185, 186, 188</sup> molecular modeling,<sup>189, 190, 229, 252</sup> ion mobility-mass spectrometry (IM-MS),<sup>191-193</sup> IRMPD,<sup>186-188, 194, 195</sup> and gas-phase proton transfer (PT) reactions<sup>121</sup>) suggested the presence of two isobaric structures (*i.e.*, “oxazolone” and “macrocyclic” type) for b fragment ions. Tandem MS results from a number of b fragment ions suggested that scrambled fragment ions were generate *via* fragmentation of macrocyclic type b ions at different amide bond positions.<sup>188, 194, 196, 198, 204, 232, 235, 253, 254</sup>

There are a growing number of experimental and theoretical evidences confirming the existence of structurally different b fragments ions; however, possibility for the presence of rearranged structures from other types of peptide fragment ions (*e.g.*, a-, c-, x-, y-, and z-type<sup>162</sup>) should not be ignored. For instance, results from an IM-MS study by Badman *et al.* revealed the presence of multiple structures/conformations for  $y_{44}^{4+}$  and  $y_n^{5+}$  ( $n = 58-64$ ) fragments of ubiquitin.<sup>255</sup> The study by Riba Garcia *et al.* showed the presence of different structures for  $a_n^+$  ( $n = 4$  and  $5$ ) fragment ions generated from YAGFL-NH<sub>2</sub> peptide.<sup>191</sup> Thus, other types of fragment ions may also yield sequence scrambling. In this study, we examine the possibility of sequence scrambling in CID of y-type fragment ions.

Recently, we reported on HDX reactions of histidine-containing  $b_4^+$  to  $b_7^+$  from seven model heptapeptides (*i.e.*, containing six alanine (A) residues and one histidine (H)

residue, with varied His positions).<sup>125</sup> The HDX reaction kinetics indicated that two ion populations may be present for each of  $b_4^+$  to  $b_7^+$  type fragments from seven model heptapeptides.<sup>125</sup> Due to the presence of isobaric alanine residues in b fragments from these seven heptapeptides, identification of potential b fragment ion scrambling was not possible.<sup>125</sup> To investigate possible pathways for generation of histidine containing b fragments, we conducted CID on an isotopically labeled peptide with an amino acid sequence of AAAAHA-NH<sub>2</sub> (where “A” denotes the presence of a labeled carbon thirteen (<sup>13</sup>C<sub>1</sub>) isotope on the alanine carbonyl group. Our aim was to distinguish between the following two (i and ii) possible reaction pathways that could yield histidine-containing b fragment ions: namely, (i)  $[M + H]^+ \rightarrow b_n \rightarrow$  scrambled or non-scrambled b-type fragments and/or (ii)  $[M + H]^+ \rightarrow y_n \rightarrow$  scrambled or non-scrambled isobaric b-type fragments. Our multistage (MS<sup>n</sup>) CID results indicated that sequence scrambling could occur from both b- and y- type fragment ions (pathways i and ii).

In addition to CID results from the isotopically labeled AAAAHA-NH<sub>2</sub> hexapeptide, here we report MS<sup>n</sup> CID results from angiotensin II antipeptide (EGVYVHPV), des-acetylated- $\alpha$ -melanocyte (SYSMEHFRWGKPV-NH<sub>2</sub>), and glu-fibrinopeptide (EGVNDNEEGFFSAR) to evaluate the propensity of y-type fragment ions to generate sequence-scrambled species.

Our criterion for selection of the examined peptides was the presence of basic amino acid residues near the C-terminal side of the peptide (which is a favorable condition for the generation of abundant y-type fragment ions). We demonstrate that scrambled fragment ions can form from different size (*i.e.*, 3 to 12 amino acid residues) and charge state (*i.e.*, +1 to +3) y fragment ions.

## 4.2. Experimental

### 4.2.1. Sample Preparation

Des-acetylated- $\alpha$ -melanocyte, glu-fibrinopeptide b, electrospray ionization (ESI) solvents, and pentaalanine (or A<sub>5</sub> used as internal calibrant) were purchased from Sigma (Sigma–Aldrich, St. Louis, MO, USA). Angiotensin II antipeptide was purchased from AnaSpec Inc. (AnaSpec Inc., Fremont, CA, USA) and the isotopically labeled (<sup>13</sup>C<sub>1</sub>) peptide AAAAHAA-NH<sub>2</sub> was purchased from CPC Scientific (CPC Scientific Inc., Sunnyvale, CA).

Because we used a gas-phase ion isolation technique<sup>72</sup> to carryout all of our CID experiments, minor contaminations were tolerable and no additional sample purification was necessary. The use of internal mass calibration allowed us to utilize high mass measurement accuracy to confirm analyte identities. Micromolar concentration of each peptide solution was prepared in a methanol: water: acetic acid (~49.5 %: ~49.5 %: ~1 %) mixture and used for ESI/MS experiments.

### 4.2.2. Instrumentation

The MS<sup>n</sup> mass spectra were acquired using a linear trap quadrupole (LTQ)-Orbitrap mass spectrometer (Thermo Fisher Scientific, Waltham, MA, USA) operated in the positive-ion mode ESI. Mass resolving power ( $M/\Delta M_{50\%}$ ) of the Orbitrap was set at 30,000. The ESI source voltage was set at +3 kV. The metal capillary temperature and voltage were set at 260 °C and +50 V, respectively. The tube lens voltage was set at +105 V. For y fragment ions generated from angiotensin II antipeptide, des-acetylated- $\alpha$ -melanocyte, and glu-fibrinopeptide b, LTQ isolation parameters were optimized to

maximize the number of isolated ions within the isotopic envelopes of singly-, doubly-, and triply-charged ions. For y fragment ions generated from AAAAHAA-NH<sub>2</sub>, LTQ isolation parameters were optimized for a narrower window and isolation of the first isotope (<sup>13</sup>C<sub>1</sub> labeled mono isotope) peak.

Collision-induced dissociation of each mass isolated y ion was performed in the LTQ with an optimized collision energy value (corresponding to the “normalized” collision energy) in the range of 15 % to 30 %. For all of the CID experiments, helium (He) was used as the collision gas (at He partial pressure ~ 1 x 10<sup>-5</sup> Torr) and the activation “q” parameter of the LTQ was set at 0.25. The protonated pentaalanine (*m/z* 374) was used as the “lock mass” for acquisition of all mass spectra reported here. The maximum error between experimentally acquired and theoretically calculated *m/z* values was <4.5 ppm. In Figures 4.1-4.3, CID product ions with relative abundance >5 % are labeled.

#### 4.2.3. Nomenclature for Labeling CID Products from y-Type Ions

Gas-phase fragment ion products from protonated peptides are labeled using Roepstorff and Fohlman nomenclature.<sup>162</sup> The y-type ions are assumed to be truncated protonated peptides and, hence, CID products of y-type ions can be isobaric to a, b, or other types of normal CID fragments. To eliminate confusion with CID fragments from protonated molecular ions of peptides (*i.e.*, [M + nH]<sup>n+</sup>), CID products of y fragment ions were assigned based on neutral losses from the isolated “parent” y ion (*i.e.*, loss of NH<sub>3</sub>, H<sub>2</sub>O, CO, and/or amino acid(s)). For example, the loss of a neutral water from the C-terminus of [y<sub>7</sub>]<sup>+</sup> fragment ion from EGVYVHPV peptide (*i.e.*, EGVYVHPV [M + H]<sup>+</sup>, *m/z* 899 → G<sup>+</sup>VYVHPV ([y<sub>7</sub>]<sup>+</sup>, *m/z* 770) → G<sup>+</sup>VYVHPV – H<sub>2</sub>O ([y<sub>7</sub> – (H<sub>2</sub>O)]<sup>+</sup>, *m/z* (752))

yields a fragment which is isobaric to a  $b_7$  fragment ion at  $m/z$  752 generated from a protonated GVVYVHPV peptide. To indicate specific origins of different CID products, all of the observed CID fragment ions from isolated  $y$  fragments were labeled based on neutral losses from the originally isolated  $y$  fragments (*i.e.*,  $[y_n - (\text{NH}_3, \text{H}_2\text{O}, \text{and/or amino acid(s)})]^{m+}$  where  $n = 3$  to 12, and  $m = 1$  to 3).

### 4.3. Results and Discussion

In the following section, we provide conclusive experimental evidence for generation of sequence-scrambled fragment ions from  $y$ -type ions. First, we present results from CID of  $[y_6]^+$  from an isotopically labeled AAAAHAA-NH<sub>2</sub> heptapeptide. Second, we provide additional evidence for sequence-scrambling of singly-, doubly-, and triply-charged  $y$  fragment ions from angiotensin II antipeptide (EGVVYVHPV), des-acetylated- $\alpha$ -melanocyte (SYSMEHFRWGKPV-NH<sub>2</sub>), and glu-fibrinopeptide b (EGVNDNEEGFFSAR).

#### 4.3.1. CID of $y_6^+$ from AAAAHAA

Figure 4.1a shows CID pattern of the mono-isotopically isolated  $[y_6]^+$  fragment, generated from in-source fragmentation of an isotopically labeled C-terminus amidated heptapeptide AAAAHAA-NH<sub>2</sub>. Please note that the underlined amino acid, in position 6 from the N-terminus (or second amino acid from the c-terminus, identified as A), denotes the alanine with isotopically labeled <sup>13</sup>C<sub>1</sub> on the carbonyl group. Under our experimental conditions, the two most abundant fragment ions in CID of  $[y_6]^+$  (Figure 4.1a) correspond to  $[y_6 - (\text{NH}_3)]^+$  ( $m/z$  494) and  $[y_6 - (\text{NH}_3 + \text{A})]^+$  ( $m/z$  423) (Figure 4.1a inset).

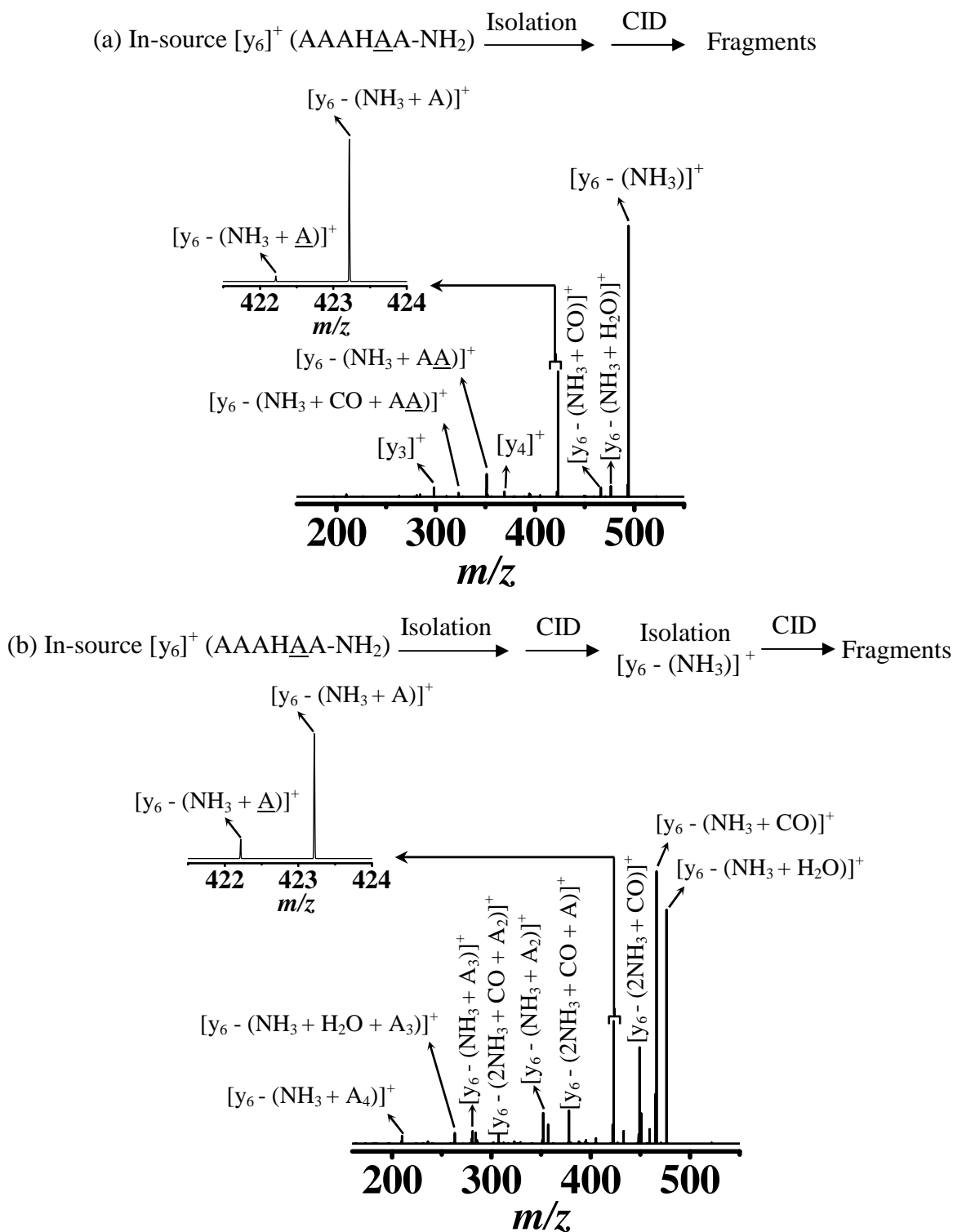


Figure 4.1. Collision-induced dissociation (CID) mass spectra of  $m/z$ -isolated (a)  $[y_6]^+$  ( $m/z$  511) (generated from in-source fragmentation of AAAHAA-NH<sub>2</sub>) and (b)  $[y_6 - (\text{NH}_3)]^+$  ( $m/z$  494) (generated from CID of  $[y_6]^+$ ) at 20 % normalized collision energy. Insets in panels (a) and (b) show the expanded views of  $m/z$  range of 421 to 424 corresponding to  $[y_6 - (\text{NH}_3 + \text{A})]^+$  and  $[y_6 - (\text{NH}_3 + \text{A})]^+$  fragment ions.

The two peaks at  $m/z$  values of 422 and 423 (Figure 4.1a inset) can be assigned as  $[y_6 - (\text{NH}_3 + \underline{\text{A}})]^+$  and  $[y_6 - (\text{NH}_3 + \text{A})]^+$ , with mass measurement error of 0.12 ppm and 0.14 ppm, respectively. The fragment ion at  $m/z$  422 (*i.e.*,  $[y_6 - (\text{NH}_3 + \underline{\text{A}})]^+$ ) corresponds to a loss of an isotopically labeled ( $^{13}\text{C}_1$ ) alanine from internal portion of the peptide and thus can exclusively be assigned as a sequence-scrambled CID product ion from  $[y_6]^+$ . However, the fragment ion at  $m/z$  423 (*i.e.*,  $[y_6 - (\text{NH}_3 + \text{A})]^+$ ) could not be assigned as a “sequence-scrambled” fragment ion, due to the presence of multiple isobaric alanine residues in the original amino acid sequence.

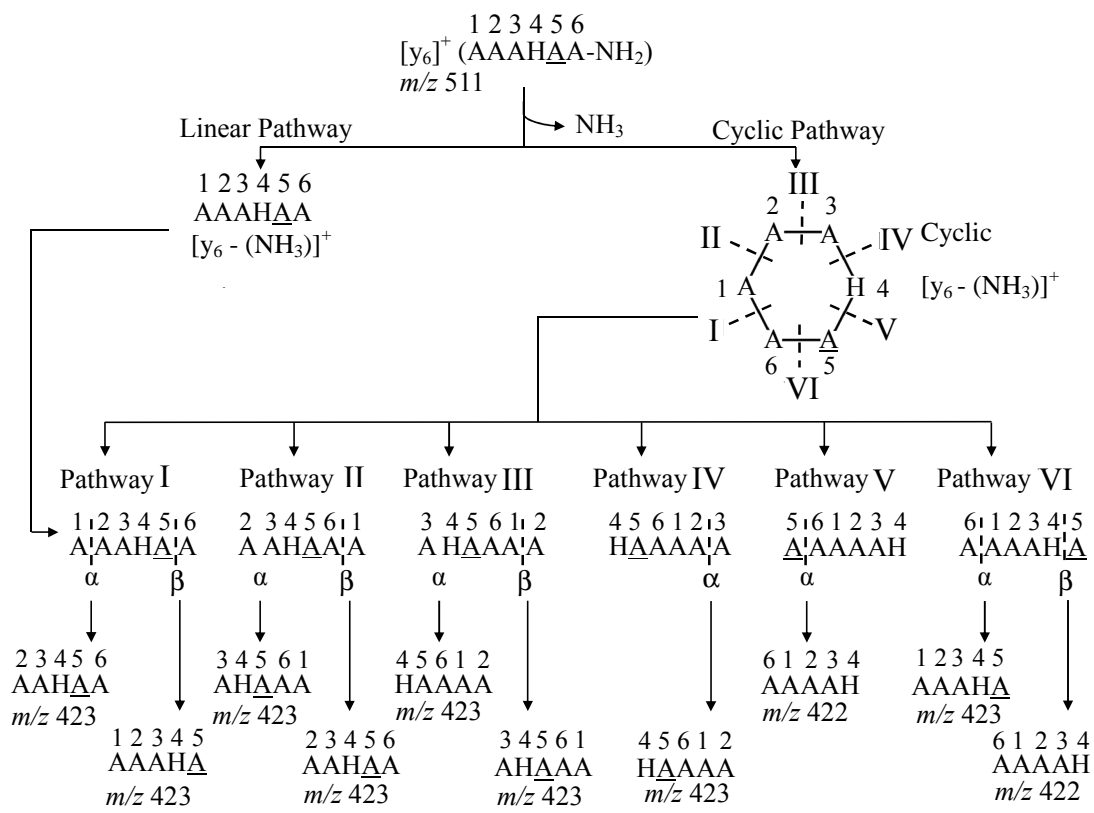
Presence of the scrambled fragment ion at  $m/z$  422 (*i.e.*,  $[y_6 - (\text{NH}_3 + \underline{\text{A}})]^+$ ) suggests that macrocyclic fragment ions can also be generated in subsequent CID of  $y$ -type ions (*e.g.*,  $[y_6]^+$ ). Scheme 4.1 shows possible pathways for formation of sequence-scrambled fragment ions in CID of  $[y_6]^+$ . For example, an ion at  $m/z$  422 could form *via* the following sequence of events:  $[y_6]^+ \rightarrow$  cyclic ( $[y_6 - (\text{NH}_3)]^+$  or  $[\text{A}_3\text{H}\underline{\text{A}}\text{A}]^+$  at  $m/z$  494)  $\rightarrow$  scrambled fragment ion ( $[y_6 - (\text{NH}_3 + \underline{\text{A}})]^+$ ,  $m/z$  422) indicated as  $[y_6]^+ \rightarrow$  cyclic pathway  $\rightarrow$  VI( $\beta$ ) route in scheme 4.1.

To further investigate pathways involved in formation of re-arranged species from CID of  $y$  fragment ions, we conducted several  $\text{MS}^n$  experiments on the isotopically labeled AAAAHAA-NH<sub>2</sub> peptide. For example, to examine the validity of scheme 4.1 type hypothesis for formation of a sequence scrambled ion at  $m/z$  422, fragment ions at  $m/z$  494 (*i.e.*,  $[y_6 - (\text{NH}_3)]^+$  or  $[\text{A}_3\text{H}\underline{\text{A}}\text{A}]^+$ ) were mass isolated and subjected to CID. Figure 4.1b shows the  $\text{MS}^4$  CID mass spectrum of  $m/z$ -isolated  $[y_6 - (\text{NH}_3)]^+$  ( $m/z$  494), generated from subsequent fragmentation of CID product from  $[y_6]^+$  ( $m/z$  511 or AAAHAA-NH<sub>2</sub>) (*i.e.*, isolate  $[y_6]^+$  ( $m/z$  511) from wide mass range ESI mass spectrum

→ perform CID on  $[y_6]^+$  ( $m/z$  511) → isolate  $[y_6 - (\text{NH}_3)]^+$  ( $m/z$  494) → perform CID to yield mass spectrum in Figure 4.1b). The expanded mass spectral view for  $m/z$  range of 421 to 424 is shown in Figure 4.1b inset; when the observed two fragment ions were assigned as  $[y_6 - (\text{NH}_3 + \underline{\text{A}})]^+$  and  $[y_6 - (\text{NH}_3 + \text{A})]^+$ , resulting mass measurement errors were 0.14 ppm and 0.33 ppm, respectively. Observation of the scrambled fragment ion at  $m/z$  422 ( $[y_6 - (\text{NH}_3 + \underline{\text{A}})]^+$ ) in CID mass spectrum of  $[y_6 - (\text{NH}_3)]^+$  (Figure 4.1b) is consistent with the generation of scrambled  $[y_6 - (\text{NH}_3 + \underline{\text{A}})]^+$  through subsequent fragmentation of  $[y_6 - (\text{NH}_3)]^+$  in CID of  $[y_6]^+$  (Figure 4.1a).

Possible pathways for generation of fragment ions at  $m/z$  422 and  $m/z$  423 in CID of  $[y_6]^+$  ( $m/z$  511) and  $[y_6 - (\text{NH}_3)]^+$  ( $m/z$  494) are shown in Scheme 4.1. Positions of the amino acids in peptide fragments are indicated above each species (1 to 6). The loss of ammonia from  $[y_6]^+$ , upon CID, could lead to the formation of both linear and macrocyclic  $[y_6 - (\text{NH}_3)]^+$  species (Scheme 4.1). Subsequent fragmentation of the linear  $[y_6 - (\text{NH}_3)]^+$  ( $m/z$  494) through pathway I (Scheme 4.1) produces the non-scrambled fragment ions at  $m/z$  423 (*i.e.*, cleavage at amide bond position denoted as “ $\alpha$ ” or “ $\beta$ ” in pathway I, Scheme 4.1). However, subsequent dissociation of cyclic  $[y_6 - (\text{NH}_3)]^+$  ( $m/z$  494) can generate scrambled fragment ions through pathways II, III, IV, V, and VI in Scheme 4.1.

As shown in Scheme 4.1, the fragment ion at  $m/z$  423 could also be produced as a scrambled fragment ion in pathways II to IV and VI; however, the exclusive assignment of the fragment ion at  $m/z$  423 as a scrambled ion is not possible due to the presence of multiple alanine (A) residues in the fragment ion sequence.



Scheme 4.1. Possible pathways for formation of fragment ions at  $m/z$  422 and 423 generated from CID of  $[y_6]^+$  from AAAAHAA $\underline{\text{A}}$ NH<sub>2</sub>.

The scrambled fragment ion at  $m/z$  422 can be generated through pathways V (cleavage at amide bond denoted as “α” in Scheme 4.1) and VI (cleavage at amide bond denoted as “β” in Scheme 4.1). Please note that because of potential differences in ion fragmentation energetics and dissociation pathways, relative intensities of the scrambled fragment ion at  $m/z$  422 ( $[y_6 - (\text{NH}_3 + \underline{\text{A}})]^+$ ) and the fragment ion at  $m/z$  423 are different in CID mass spectra of  $[y_6]^+$  (Figure 4.1a inset) and  $[y_6 - (\text{NH}_3)]^+$  (Figure 4.1b inset). For example, fragment ions at  $m/z$  422 and 423 in Figure 4.1a were generated from CID of isolated  $[y_6]^+$  that could potentially be formed *via*  $[y_6]^+ \rightarrow [y_6 - (\text{NH}_3)]^+ \rightarrow m/z$  422 (or 423) indirect pathway. However, the fragment ions observed at  $m/z$  422 and 423 (in

Figure 4.1b) were generated from the direct fragmentation of  $m/z$ -isolated linear and/or cyclic  $[y_6 - (\text{NH}_3)]^+$  (in the LTQ).

In summary, using complementary CID experiments performed on  $[y_6]^+$  and  $[y_6 - (\text{NH}_3)]^+$  fragment ions of AAAAHAA-NH<sub>2</sub>, we show that sequence-scrambling can occur in CID of y ions (similar to reported rearrangements observed for CID of b ions). Additionally, we performed CID on  $m/z$ -isolated  $[y_4]^+$ ,  $[y_5]^+$ , and  $[y_6]^+$  generated from CID of  $m/z$ -isolated doubly charged AAAAHAA-NH<sub>2</sub> (*i.e.*, isolate  $[M + 2H]^{2+}$  from wide mass range ESI mass spectrum  $\rightarrow$  perform CID on  $[M + 2H]^{2+}$   $\rightarrow$  isolate y fragment ion  $\rightarrow$  perform CID on y fragment ion, Supplementary Figures B.1 to B.3). These additional CID data also showed the presence of scrambled fragment ions (similar to CID of  $[y_6]^+$ ) generated from in-source fragmentation of AAAAHAA-NH<sub>2</sub> (Figure 4.1 and Scheme 4.1). In the following sections, we show additional CID results and demonstrate that sequence-scrambling can occur in different size and charge-state y fragment ions.

#### 4.3.2. CID of y Fragment Ions from Des-Acetylated- $\alpha$ -Melanocyte

Most abundant observed ions in ESI mass spectrum of des-acetylated- $\alpha$ -melanocyte were  $[M + 3H]^{3+}$  and  $[M + 4H]^{4+}$ . In separate experiments, we established that CID of triply-charged molecular ions of des-acetylated- $\alpha$ -melanocyte ( $[M + 3H]^{3+}$ ) yielded  $[y_n]^{2+}$  ( $n = 6$  to  $11$ ) whereas  $[M + 4H]^{4+}$  species yielded  $[y_n]^{3+}$  ( $n = 8$  and  $10$  to  $12$ ) and  $[y_n]^+$  ( $n = 4$  to  $7$ ). We utilized all fourteen observed y fragment ions and performed MS<sup>n</sup> on each y-type ion in fourteen separate experiments.

For brevity, we only present/discuss CID mass spectral pattern of  $[y_7]^{2+}$  generated from des-acetylated- $\alpha$ -melanocyte. A summary of the total number of observed y fragment ions and total number of scrambled product ions from CID of various y ions

(with different sizes and charge states) from des-acetylated- $\alpha$ -melanocyte is included in Table 4.1. In Table 4.1, columns #1 to #6 correspond to observed/isolated y fragment ions (sorted in ascending order for y fragment ion sizes), charge states, total numbers of observed secondary fragment ions ( $y_n \rightarrow$  fragments), numbers of observed scrambled secondary fragment ions, percentages of scrambling for each y ion (column four divided by column three), and identities of observed sequence scrambled fragments.

For example, under our experimental conditions, results from CID mass spectra of  $m/z$ -isolated  $[y_n]^+$  ( $n = 4$  to  $7$ ) (generated from CID of  $[M + 4H]^{4+}$ ) and  $[y_9]^{2+}$  and  $[y_{10}]^{2+}$  (generated from CID of  $[M + 3H]^{3+}$ ) did not reveal generation of any sequence-scrambled fragment ions. However, CID mass spectra of  $[y_n]^{2+}$  ( $n = 6$  to  $8$  and  $11$ ) and  $[y_n]^{3+}$  ( $n = 8$  and  $10$  to  $12$ ) produced sequence-scrambled fragment ions that corresponded to  $\sim 1\%$  to  $\sim 18\%$  of the total number of observed fragment ions (from CID of its parent y fragment).

Figure 4.2a shows a CID mass spectrum of  $m/z$ -isolated  $[y_7]^{2+}$  ( $m/z$  444) generated from CID of  $[M + 3H]^{3+}$  of des-acetylated- $\alpha$ -melanocyte. Fragment ions at  $m/z$  774 ( $[y_7 - (NH_3 + P)]^+$ ) and  $m/z$  387 ( $[y_7 - (NH_3 + P)]^{2+}$ ) could exclusively be assigned as scrambled fragment ions (with mass measurement errors of 0.52 ppm and 1.81 ppm, respectively). Presence of sequence-scrambled fragment ions in CID mass spectrum shown in Figure 4.2a suggests that CID of  $[y_7]^{2+}$  ions produces macrocyclic fragment ion intermediate(s).

For example, intermediate macrocyclic fragment ion(s) subsequently can re-open to generate the observed scrambled ions through the following suggested pathway:  $[y_7]^{2+} \rightarrow$  cyclic  $[y_7 - (NH_3)]^{2+} \rightarrow$  scrambled fragment ions ( $[y_7 - (NH_3 + P)]^+$  and  $[y_7 - (NH_3 + P)]^{2+}$ ).

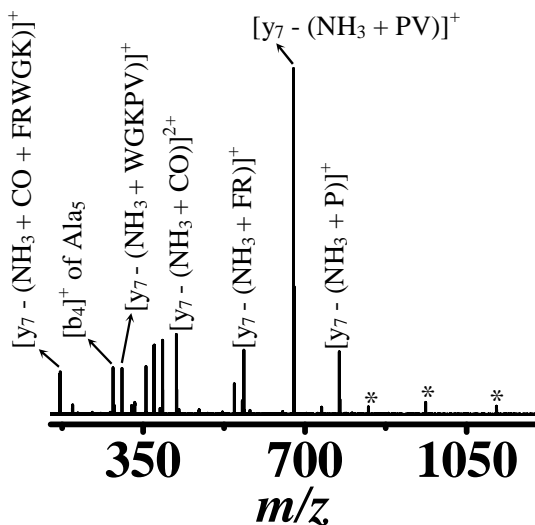
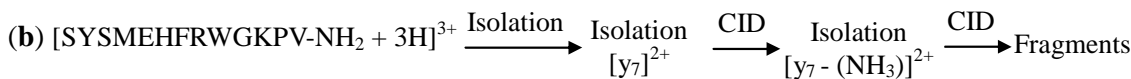
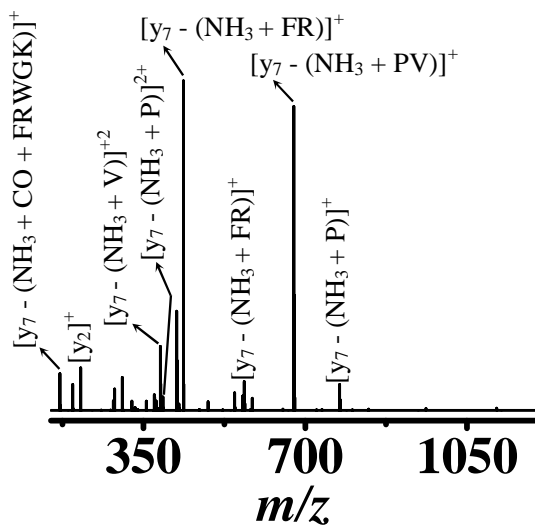
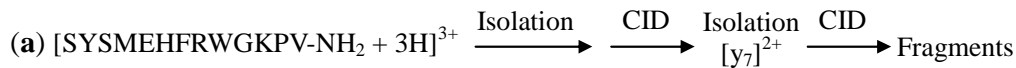


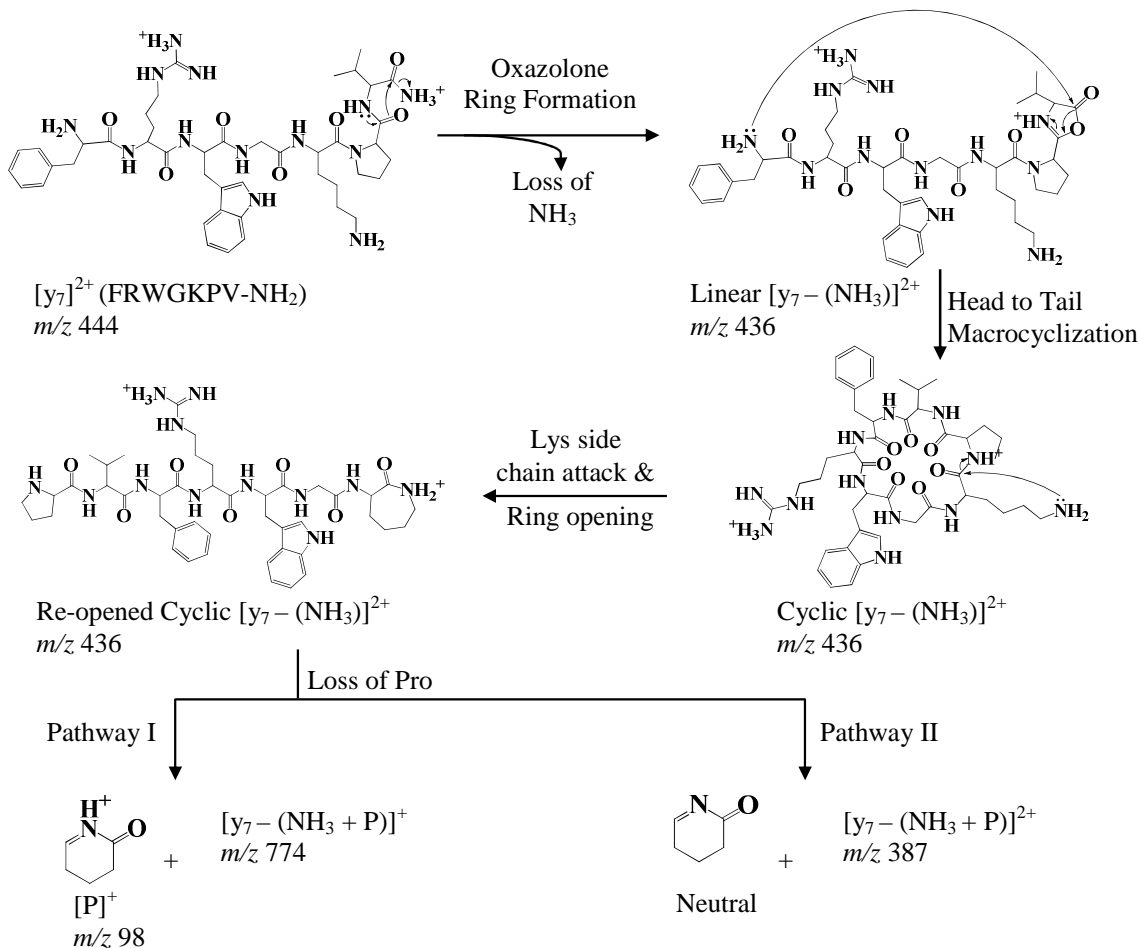
Figure 4.2. Collision induced dissociation (CID) mass spectra of  $m/z$ -isolated (a)  $[\text{y}_7]^{2+}$  ( $m/z$  444) (generated from CID of  $[\text{M} + 3\text{H}]^{3+}$  of des-acetylated- $\alpha$ -melanocyte  $[\text{SYSMEHFRWGKPV-NH}_2]$ ) and (b)  $[\text{y}_7 - (\text{NH}_3)]^{2+}$  ( $m/z$  436) (generated from CID of  $[\text{y}_7]^{2+}$ ) at 15 % normalized collision energy. A list of assigned fragments is included in the appendix materials (Tables B.1 and B.2). Peaks corresponding to electronic noise are marked with asterisk (\*) symbols.

To further investigate the possibility of scrambled fragment ion generation *via* NH<sub>3</sub> loss from [y<sub>7</sub>]<sup>2+</sup> (generated from des-acetylated- $\alpha$ -melanocyte), we performed CID on [y<sub>7</sub> - (NH<sub>3</sub>)]<sup>2+</sup> fragment ion (*m/z* 436). Figure 4.2b shows the CID mass spectrum of *m/z*-isolated [y<sub>7</sub> - (NH<sub>3</sub>)]<sup>2+</sup> species (*i.e.*, isolate [M + 3H]<sup>3+</sup> from wide mass range ESI mass spectrum → perform CID on [M + 3H]<sup>3+</sup> → isolate [y<sub>7</sub>]<sup>2+</sup> (*m/z* 444) → perform CID on [y<sub>7</sub>]<sup>2+</sup> → isolate [y<sub>7</sub> - (NH<sub>3</sub>)]<sup>2+</sup> (*m/z* ~436) → perform CID on [y<sub>7</sub> - (NH<sub>3</sub>)]<sup>2+</sup> to yield the mass spectrum in Figure 4.2b). In CID mass spectrum of [y<sub>7</sub> - (NH<sub>3</sub>)]<sup>2+</sup>, signals at 774.4404 and 387.7242 can be assigned to amino acid scrambled [y<sub>7</sub> - (NH<sub>3</sub> + P)]<sup>+</sup> and [y<sub>7</sub> - (NH<sub>3</sub> + P)]<sup>2+</sup> species (with mass measurement errors of 0.77 ppm and 0.36 ppm, respectively).

Observation of similar scrambled fragments ions in CID mass spectra of [y<sub>7</sub> - (NH<sub>3</sub>)]<sup>2+</sup> and [y<sub>7</sub>]<sup>2+</sup> is consistent with the suggested pathway for production of sequence-scrambled fragment ions (*i.e.*, [y<sub>7</sub>]<sup>2+</sup> → cyclic [y<sub>7</sub> - (NH<sub>3</sub>)]<sup>2+</sup> → scrambled fragment ions ([y<sub>7</sub> - (NH<sub>3</sub> + P)]<sup>+</sup> and [y<sub>7</sub> - (NH<sub>3</sub> + P)]<sup>2+</sup>). CID of [y<sub>7</sub>]<sup>2+</sup> and [y<sub>7</sub> - (NH<sub>3</sub>)]<sup>2+</sup> from des-acetylated- $\alpha$ -melanocyte show similar fragmentation patterns and list of CID products from these two precursors are included in Tables B.1 and B.2, respectively.

Scheme 4.2 shows the proposed mechanism for generation of sequence-scrambled fragment ions in CID of [y<sub>7</sub>]<sup>2+</sup>, generated from des-acetylated- $\alpha$ -melanocyte. Observed loss of ammonia from (C-terminus) [y<sub>7</sub>]<sup>2+</sup> (upon CID) could be initiated by the formation of an oxazolone structure at the C-terminus side of [y<sub>7</sub>]<sup>2+</sup> (Scheme 4.2). The [y<sub>7</sub> - (NH<sub>3</sub>)]<sup>2+</sup> oxazolone structure fragment ion might then undergo macrocyclization and form a cyclic structure (isobaric to a cyclic “b-type” ion).<sup>172, 182, 186</sup> The subsequent

fragmentation and re-opening of the cyclic  $[y_7 - (\text{NH}_3)]^{2+}$  may result in losses of internal amino acid residues.



Scheme 4.2. Proposed mechanism for generation of sequence-scrambled fragment ions from CID of  $[y_7]^{2+}$  from des-acetylated- $\alpha$ -melanocyte.

For example, in the cyclic  $[y_7 - (\text{NH}_3)]^{2+}$  the nitrogen on side chain of lysine (K) can initiate the K-P amide bond cleavage through a nucleophilic attack on carbon center of the carbonyl group from lysine residue. The K-P amide bond cleavage of  $[y_7 - (\text{NH}_3)]^{2+}$  may form a caprolactam-like structure.<sup>199</sup> After re-opening, the rearranged  $[y_7 - (\text{NH}_3)]^{2+}$  can undergo further dissociation *via* pathways I or II (Scheme 4.2) to lose the

proline (P) residue and generate the sequence-scrambled fragment ions at  $m/z$  774 ( $[y_7 - (\text{NH}_3 + \text{P})]^+$ ) or  $m/z$  387 ( $[y_7 - (\text{NH}_3 + \text{P})]^{2+}$ ), respectively.

The proposed K-P amide bond cleavage in Scheme 4.2 is consistent with the results reported by Brechi *et al.*<sup>256</sup> and Kish and Wesdemiotis<sup>257</sup> on the observed enhanced cleavage of amide bonds adjacent to lysine. Furthermore, Brechi *et al.*<sup>256</sup> and Kish and Wesdemiotis<sup>257</sup> observed selective amide bond cleavages on the N-terminus side of proline residue in the presence of basic amino acid residues (*e.g.*, K and H) adjacent to proline. Thus the reported enhanced amide bond cleavage adjacent to lysine and the “proline effect”<sup>256, 257</sup> are consistent with our observations.

#### 4.3.3. CID of $y$ Fragment Ions from Angiotensin II Antipeptide

The  $[y_n]^+$  ( $n = 3$  to  $5$ ) and  $[y_n]^{2+}$  ( $n = 5$  and  $6$ ) fragment ions of angiotensin II antipeptide (EGVYVHPV) were generated by CID of  $m/z$ -isolated  $[M + 2H]^{2+}$  species. The  $[y_6]^+$  and  $[y_7]^+$  fragments of angiotensin II antipeptide were generated by in-source CID. A summary of the total number of  $y$  fragment ions and total number of sequence-scrambled fragments, generated from the CID of the selected  $y$  fragment ions from angiotensin II antipeptide, is included in Table 4.1. As indicated in Table 4.1 (middle section), we did not observe sequence-scrambled fragment ions from CID of  $[y_n]^+$  ( $n = 3$  to  $5$ ) and  $[y_5]^{2+}$ . However, sequence-scrambled fragment ions were observed in CID mass spectra of  $m/z$ -isolated  $[y_6]^+$  (4 %),  $[y_7]^+$  (16 %), and  $[y_6]^{2+}$  (17 %). For brevity, we only present the results from CID of  $[y_7]^+$  and suggest a potential mechanism for generation of its respective sequence-scrambled product ions. Figure 4.3a shows a CID mass spectrum of the  $m/z$ -isolated  $[y_7]^+$  of angiotensin II antipeptide at  $m/z$  770.

Table 4.1. Summary of the total number of observed fragments, number of scrambled fragments, and the identities of the scrambled fragment ions generated from cid of y fragment ions from des-acetylated- $\alpha$ -melanocyte, angiotensin ii anti-peptide, and glu-fibrinopeptide b.

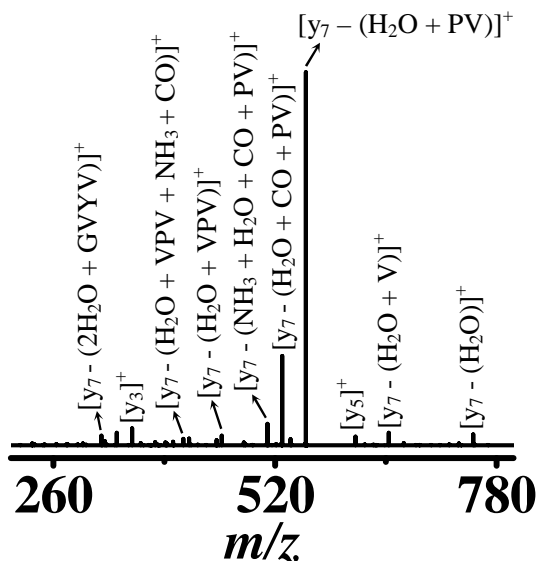
Identity of y fragment	Charge state	Total # of fragments	# of Scrambled fragments	% of Scrambling	Identity of scrambled ions
<i>Des-acetylated-<math>\alpha</math>-melanocyte (SYSMEHFRWGKPV-amidated)</i>					
y <sub>4</sub> (GKPV)	1	4	0	0	NA
y <sub>5</sub> (WGKPV)	1	7	0	0	NA
y <sub>6</sub> (RWGKPV)	1	6	0	0	NA
y <sub>7</sub> (FRWGKPV)	1	2	0	0	NA
y <sub>6</sub> (RWGKPV)	2	11	2	18	[y <sub>6</sub> - (NH <sub>3</sub> + P)] <sup>+</sup> [y <sub>6</sub> - (NH <sub>3</sub> + P)] <sup>+2</sup>
y <sub>7</sub> (FRWGKPV)	2	18	2	11	[y <sub>7</sub> - (NH <sub>3</sub> + P)] <sup>+2</sup> [y <sub>7</sub> - (NH <sub>3</sub> + P)] <sup>+</sup>
y <sub>8</sub> (HFRWGKPV)	2	27	1	4	[y <sub>8</sub> - (NH <sub>3</sub> + P)] <sup>+2</sup>
y <sub>9</sub> (EHFRWGKPV)	2	31	0	0	NA
y <sub>10</sub> (MEHFRWGKPV)	2	52	0	0	NA
y <sub>11</sub> (SMEHFRWGKPV)	2	85	1	1	[y <sub>11</sub> - (NH <sub>3</sub> + E)] <sup>+2</sup>
y <sub>8</sub> (HFRWGKPV)	3	8	1	13	[y <sub>8</sub> - (NH <sub>3</sub> + P)] <sup>+2</sup>
y <sub>10</sub> (MEHFRWGKPV)	3	17	1	6	[y <sub>10</sub> - (NH <sub>3</sub> + P)] <sup>+2</sup>
y <sub>11</sub> (SMEHFRWGKPV)	3	70	3	4	[y <sub>11</sub> - (NH <sub>3</sub> + SMEHP)] <sup>+</sup> [y <sub>11</sub> - (NH <sub>3</sub> + P)] <sup>+2</sup> [y <sub>11</sub> - (NH <sub>3</sub> + P)] <sup>+3</sup>
y <sub>12</sub> (YSMEHFRWGKPV)	3	36	1	3	[y <sub>12</sub> - (NH <sub>3</sub> + P)] <sup>+2</sup>
<i>Angiotensin II (EGVYVHPV)</i>					
y <sub>3</sub> (HPV)	1	4	0	0	NA
y <sub>4</sub> (VHPV)	1	4	0	0	NA
y <sub>5</sub> (YVHPV)	1	11	0	0	NA
y <sub>6</sub> (VYVHPV)	1	23	1	4	[y <sub>6</sub> - (H <sub>2</sub> O + PVY)] <sup>+</sup> [y <sub>7</sub> - (H <sub>2</sub> O + NH <sub>3</sub> + CO + VYPV)] <sup>+</sup> [y <sub>7</sub> - (2H <sub>2</sub> O + VYPV)] <sup>+</sup> [y <sub>7</sub> - (H <sub>2</sub> O + VYPV)] <sup>+</sup>
y <sub>7</sub> (GVYVHPV)	1	43	7	16	[y <sub>7</sub> - (H <sub>2</sub> O + CO + YPV)] <sup>+</sup> [y <sub>7</sub> - (H <sub>2</sub> O + YPV)] <sup>+</sup> [y <sub>7</sub> - (H <sub>2</sub> O + NH <sub>3</sub> + CO + VPV)] <sup>+</sup> [y <sub>7</sub> - (H <sub>2</sub> O + VPV)] <sup>+</sup>
y <sub>5</sub> (YVHPV)	2	22	0	0	NA
y <sub>6</sub> (VYVHPV)	2	6	1	17	[y <sub>6</sub> - (H <sub>2</sub> O + NH <sub>3</sub> + P)] <sup>+</sup>
<i>Glu-Fibrinopeptide b (EGVNDNEEGFFSAR)</i>					
y <sub>4</sub> (FSAR)	1	32	2	6	[y <sub>4</sub> - (NH <sub>3</sub> + SA)] <sup>+</sup> [y <sub>4</sub> - (2NH <sub>3</sub> + A)] <sup>+</sup>
y <sub>5</sub> (FFSAR)	1	30	1	3	[y <sub>5</sub> - (NH <sub>3</sub> + FSA)] <sup>+</sup> [y <sub>6</sub> - (NH <sub>3</sub> + FFSA)] <sup>+</sup> [y <sub>6</sub> - (NH <sub>3</sub> + FFS)] <sup>+</sup> [y <sub>6</sub> - (NH <sub>3</sub> + GFS)] <sup>+</sup> [y <sub>6</sub> - (H <sub>2</sub> O + 2NH <sub>3</sub> + FF)] <sup>+</sup>
y <sub>6</sub> (GFFSAR)	1	57	10	18	[y <sub>6</sub> - (2NH <sub>3</sub> + FSA)] <sup>+</sup> [y <sub>6</sub> - (H <sub>2</sub> O + NH <sub>3</sub> + FF)] <sup>+</sup> [y <sub>6</sub> - (NH <sub>3</sub> + FF)] <sup>+</sup> [y <sub>6</sub> - (H <sub>2</sub> O + NH <sub>3</sub> + F)] <sup>+</sup> [y <sub>6</sub> - (2NH <sub>3</sub> + F)] <sup>+</sup> [y <sub>6</sub> - (NH <sub>3</sub> + F)] <sup>+</sup>
y <sub>7</sub> (EGFFSAR)	1	27	1	4	[y <sub>7</sub> - (2NH <sub>3</sub> + FSA)] <sup>+</sup>
y <sub>8</sub> (EEGFFSAR)	1	12	0	0	NA
y <sub>9</sub> (NEEGFFSAR)	1	14	0	0	NA
y <sub>10</sub> (DNEEGFFSAR)	1	12	0	0	NA
y <sub>11</sub> (NDNEEGFFSAR)	1	35	0	0	NA
y <sub>10</sub> (DNEEGFFSAR)	2	14	0	0	NA
y <sub>11</sub> (NDNEEGFFSAR)	2	32	0	0	NA

The list of all assigned fragment ions from CID of  $[y_7]^+$  (generated from angiotensin II antipeptide) is included in Supplementary Table B.3. The most intense signal in CID mass spectrum of angiotensin II antipeptide  $[y_7]^+$  (Figure 4.3a) corresponds to a fragment ion at  $m/z$  556 assigned as  $[y_7 - (H_2O + PV)]^+$ . Observation of an abundant  $[y_7 - (H_2O + PV)]^+$  fragment (in Figure 4.3a) is consistent with previously reported enhanced selective cleavage of an amide bond located on C-terminus side of a histidine adjacent to proline.<sup>258</sup>

The observed scrambled fragment ions in CID of  $[y_7]^+$  from angiotensin II antipeptide included  $[y_7 - (H_2O + NH_3 + CO + VYPV)]^+$  ( $m/z$  249),  $[y_7 - (2H_2O + VYPV)]^+$  ( $m/z$  276),  $[y_7 - (H_2O + VYPV)]^+$  ( $m/z$  294),  $[y_7 - (H_2O + CO + YPV)]^+$  ( $m/z$  365),  $[y_7 - (H_2O + YPV)]^+$  ( $m/z$  393),  $[y_7 - (H_2O + NH_3 + CO + VPV)]^+$  ( $m/z$  412), and  $[y_7 - (H_2O + VPV)]^+$  ( $m/z$  457). Similar to the y ions from AAAAHAA-NH<sub>2</sub> and des-acetylated- $\alpha$ -melanocyte, the generation of the sequence-scrambled fragment ions from y ions of angiotensin II antipeptide can be explained by re-opening of a macrocyclic structure intermediate (Scheme 4.3).

As depicted in Scheme 4.3, presence of a basic histidine residue, N-terminus to proline, can direct fragmentation (in CID of  $[y_7]^+$  from angiotensin II antipeptide), to generate  $[y_7 - (H_2O + PV)]^+$  with a bicyclic structure at the C-terminus (consistent with the proposed fragmentation mechanism of histidine-containing peptides reported by Tsaprailis<sup>258</sup>). Following the loss of PV from the C-terminus of  $[y_7]^+$  (in scheme 4.3), the intermediate  $[y_7 - (H_2O + PV)]^+$  can form a cyclic structure similar to head to tail macrocyclization in b fragment ions. The cyclic  $[y_7 - (H_2O + PV)]^+$  ( $m/z$  556) can re-open at different amide bonds and generate subsequent fragments.

(a) In-source  $[y_7]^+$  (GVYVHPV)  $\xrightarrow{\text{Isolation}}$   $\xrightarrow{\text{CID}}$  Fragments



(b) In-source  $[y_7]^+$  (GVYVHPV)  $\xrightarrow{\text{Isolation}}$   $\xrightarrow{\text{CID}}$   $[y_7 - (\text{H}_2\text{O} + \text{PV})]^+$   $\xrightarrow{\text{Isolation}}$   $\xrightarrow{\text{CID}}$  Fragments

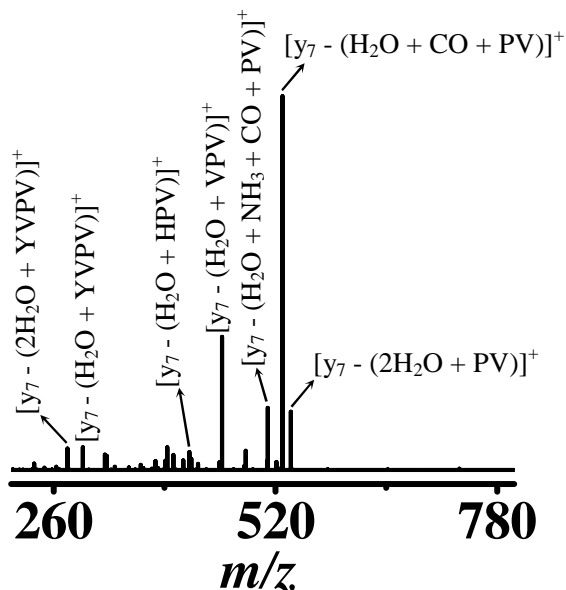
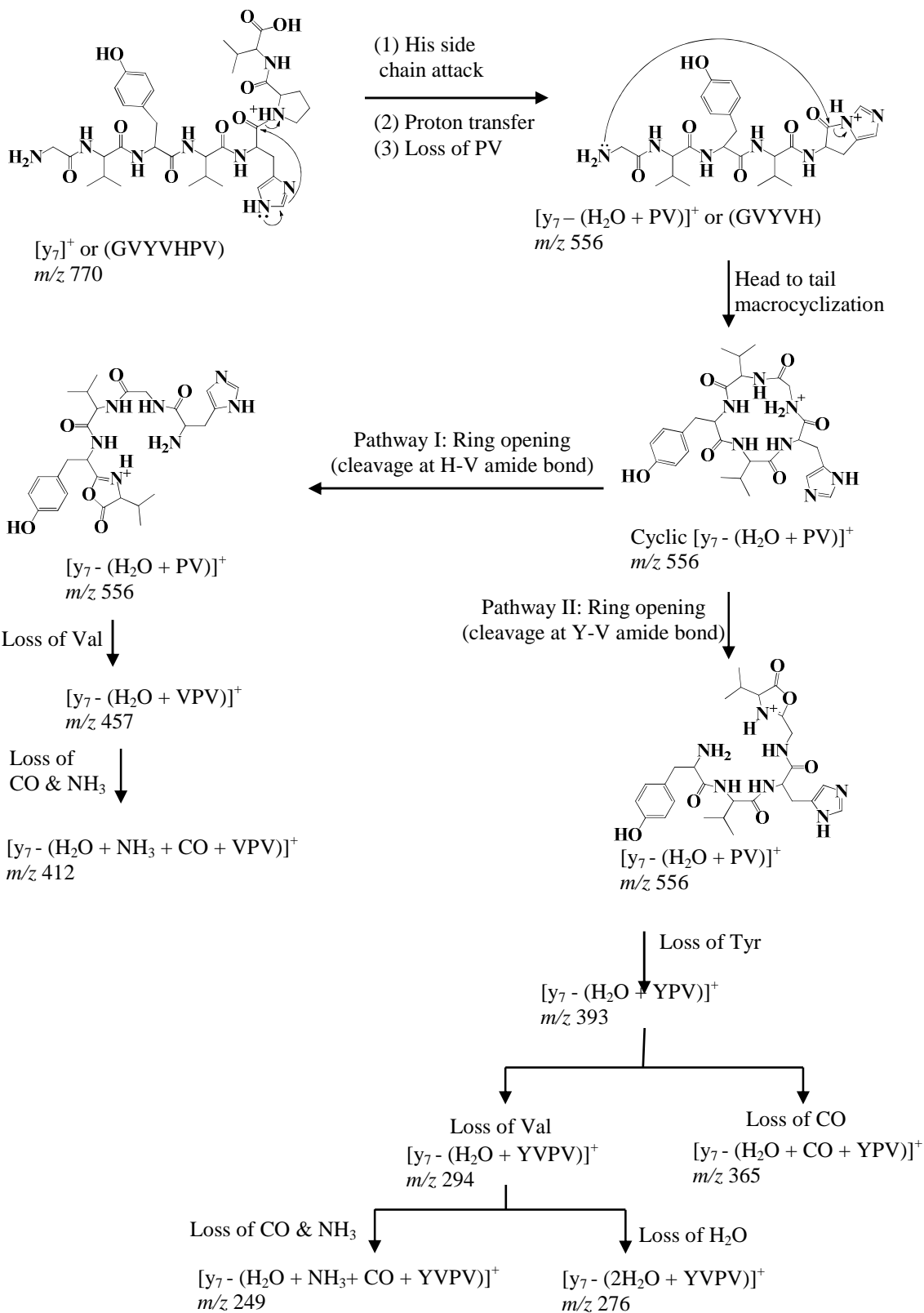


Figure 4.3. Collision induced dissociation (CID) mass spectra of  $m/z$ -isolated (a)  $[y_7]^+$  ( $m/z$  770) (generated from in-source fragmentation of angiotensin II antipeptide (EGVYVHPV)) and (b)  $[y_7 - (\text{H}_2\text{O} + \text{PV})]^+$  ( $m/z$  556) (generated from CID of  $[y_7]^+$ ) at 30 % normalized collision energy. A list of the assigned fragments is included in the appendix materials (Tables B.3 and B.4).

For example, in Scheme 4.3 two possible pathways for re-opening of the cyclic  $[y_7 - (\text{H}_2\text{O} + \text{PV})]^+$  are shown (*i.e.*, pathways I and II, Scheme 4.3). Subsequent fragmentation of the re-opened cyclic  $[y_7 - (\text{H}_2\text{O} + \text{PV})]^+$  (pathway I) can generate the observed scrambled fragment ions at  $m/z$  457 ( $[y_7 - (\text{H}_2\text{O} + \text{VPV})]^+$ ) and  $m/z$  412 ( $[y_7 - (\text{H}_2\text{O} + \text{NH}_3 + \text{CO} + \text{VPV})]^+$ ). Likewise, subsequent fragmentation through pathway II can produce the scrambled fragment ions  $[y_7 - (\text{H}_2\text{O} + \text{YPV})]^+$  ( $m/z$  393),  $[y_7 - (\text{H}_2\text{O} + \text{CO} + \text{YPV})]^+$  ( $m/z$  365),  $[y_7 - (\text{H}_2\text{O} + \text{VYPV})]^+$  ( $m/z$  294),  $[y_7 - (2\text{H}_2\text{O} + \text{VYPV})]^+$  ( $m/z$  276), and  $[y_7 - (\text{H}_2\text{O} + \text{NH}_3 + \text{CO} + \text{VYPV})]^+$  ( $m/z$  249).

To check the plausibility of the suggested pathways in Scheme 4.3 for the generation of scrambled fragments from CID of  $[y_7]^+$ , we performed CID on  $m/z$ -isolated  $[y_7 - (\text{H}_2\text{O} + \text{PV})]^+$  ( $m/z$  556) generated from CID of  $[y_7]^+$  from angiotensin II antipeptide (Figure 4.3b). The CID mass spectrum of  $[y_7 - (\text{H}_2\text{O} + \text{PV})]^+$  showed the presence of similar scrambled fragment ions (Figure 4.3b, Table B.4) as observed in the CID mass spectrum of  $[y_7]^+$  generated from angiotensin II antipeptide (Figure 4.3a, Supplementary Table B.3).

The observation of similar sequence-scrambled fragment ions in the CID of  $[y_7]^+$  and  $[y_7 - (\text{H}_2\text{O} + \text{PV})]^+$  supports our suggested pathway in Scheme 4.3 for production of sequence scrambling from CID of  $[y_7]^+$  in angiotensin II antipeptide (*i.e.*, through a macrocyclized fragment ion intermediate).



Scheme 4.3. Proposed mechanism for generation of sequence-scrambled fragment ions from CID of  $[y_7]^+$  from angiotensin II antipeptide.

#### 4.3.4. CID of $y$ Fragment Ions from Glu-fibrinopeptide b

The CID mass spectra of 10  $y$  fragment ions from glu-fibrinopeptide b (EGVNDNEEGFFSAR) were investigated for the presence or absence of sequence-scrambled fragment ion(s). The  $[y_n]^+$  ( $n = 7$  to  $9$ ) fragments of glu-fibrinopeptide b were generated by CID of  $[M + 2H]^{2+}$  species. The  $[y_n]^+$  ( $n = 4$  to  $6$ ,  $10$ , and  $11$ ), and  $[y_n]^{2+}$  ( $n = 10$  and  $11$ ) fragments were generated by in-source CID of protonated glu-fibrinopeptide b. Among the studied  $y$  fragment ions from glu-fibrinopeptide b, only the CID mass spectra of  $[y_n]^+$  ( $n = 4$  to  $7$ ) fragments showed the presence of sequence-scrambled fragment ions (Table 4.1).

Similar to CID of  $y$  fragment ion discussed in previous sections, generation of sequence scrambled fragment ions in CID of  $[y_n]^+$  ( $n = 4$  to  $7$ ) from glu-fibrinopeptide b can be explained by considering subsequent dissociation of intermediate macrocyclic structure fragment ion(s). For instance, one of the possible pathways for generation of scrambled ions in CID of  $[y_6]^+$  ( $[GFFSAR]^+$ ,  $m/z$  684) is through the following pathway:  $[y_6]^+ \rightarrow \text{cyclic } [y_6 - (\text{NH}_3)]^+ \rightarrow \text{sequence scrambled fragment ions}$ .

Possibility for the generation of sequence-scrambled fragment ions through a macrocyclic structure fragment ion intermediate in CID of  $[y_6]^+$  (from glu-fibrinopeptide b) was further examined by conducting CID experiments on  $m/z$ -isolated  $[y_6 - (\text{NH}_3)]^+$  ( $m/z$  667) from CID of  $[y_6]^+$  (data not shown). The CID mass spectrum of  $m/z$ -isolated  $[y_6 - (\text{NH}_3)]^+$  showed the presence of similar scrambled fragment ions that are observed in the CID of  $m/z$ -isolated  $[y_6]^+$ . The observation of similar scrambled fragment ions in CID of  $[y_6]^+$  and  $[y_6 - (\text{NH}_3)]^+$  (from glu-fibrinopeptide b) supports the suggested “macro ring-opening” pathway for scrambled fragment ion generation in CID of  $[y_6]^+$ .

Our data from a limited number of peptides suggest that sequence scrambling occurs in CID of both free acid-terminated peptides and their amide-terminated counterparts. Future studies, focused on systematic and quantitative evaluation of fragmentation branching ratios for amide- and acid-terminated peptides, should provide additional clues about exact mechanism(s) involved in sequence scramblings.

#### 4.4. Conclusions

We aimed to investigate the possibility of sequence scrambling in CID of y-type fragment ions. We examined ion fragmentation results from CID mass spectra of thirty two y fragment ions, generated from four selected peptides (i.e., AAAAHAA-NH<sub>2</sub>, des-acetylated- $\alpha$ -melanocyte, angiotensin II antipeptide, and glu-fibrinopeptide b) that contained basic amino acid residues near their C-termini. To the best our knowledge, results presented here provide the first experimental evidence for generation of sequence-scrambled fragment ions in CID of y-type ions.

Reported occurrence of “y” fragment sequence scrambling in this work is in line with previous observations on sequence scrambling in b- and a-type fragment ions<sup>172, 213</sup> since neutral loss fragments from y ions may exhibit b-type ion fragmentation chemistry.

Complementary CID experiments on  $[y - (\text{NH}_3/\text{or H}_2\text{O})]^{m+}$  ( $m = 1$  to  $3$ ) species (generated from CID of selected y ions) suggest that sequence scrambling in y ions may occur *via* subsequent fragmentation of intermediate macrocyclic ion(s) (isobaric to “b-type” ions). With a limited number of y fragment ions examined in this report, it is not possible to report on potential or specific trends for sequence scrambling as a function of the fragment ion size, charge state, and/or amino acid composition. However, preliminary results suggest optimal size preference and we plan to conduct additional systematic

studies on the effect of different experimental parameters on generation of sequence-scrambled ions from y fragments. We anticipate that in the near future protein sequencing programs will be improved by full characterization of all potential sequence-scrambling mechanisms including y-fragment ion rearrangements.

#### *Acknowledgment*

The Authors thank Baylor University for financial support. They thank Dr. Behrooz Zekvat for helpful discussions on CID data. The authors express their gratitude to reviewers of a previous paper<sup>125</sup> for their thoughtful comments and questions that led us to explore y-fragment ion scramblings.

## CHAPTER FIVE

### Structural Dependent Competition between Gas-Phase H/D Ex-change and Adduct Formation Reactions

#### *Abstract*

Competition between forming “normal” gas-phase hydrogen/deuterium exchange (HDX) reaction products and “unusual” reagent adducts is a poorly understood phenomenon. Here, we present a systematic study by combining ab initio calculations, HDX studies, ion mobility-mass spectrometry, and isotope labeling to better understand the fundamental chemistry involved in gas-phase adduct formation. We studied the influence of protonation and alkali metal ion ( $\text{Na}^+$ ,  $\text{K}^+$ , and  $\text{Cs}^+$ ) complexation on gas-phase  $\text{ND}_3$  adduct formation of a benzyloxycarbonyl (Z)-capped dipeptide containing glycine (G) and proline (P) (*i.e.*, Z-PG). Gas-phase HDX mass spectra of m/z-isolated Z-PG species showed the presence of  $\text{ND}_3$  adduct; however, adduct formation was absent when  $\text{ND}_3$  reacted with  $[\text{Z-PG} + \text{metal}]^+$  and  $[\text{Z-PG} + \text{H} - \text{CO}_2]^+$  species.

To identify the structural features responsible for divergent reactions of Z-PG species with  $\text{ND}_3$ , we used isotope labeling mass spectrometry (MS) and ab initio calculations. Furthermore, the experimental collision cross sections of Z-PG species were correlated with candidate structures from ab initio calculations. Isotope labeling MS revealed that  $\text{CO}_2$  is lost from the Z carboxylic group of  $[\text{Z-PG} + \text{H}]^+$  to form  $[\text{Z-PG} + \text{H} - \text{CO}_2]^+$ . Comparisons of optimized geometries for protonated and metal-complexed Z-PG species revealed drastically altered structures for  $[\text{Z-PG} + \text{metal}]^+$  as compared to  $[\text{Z-PG} + \text{H}]^+$ . Both experimental observations and theoretical calculations indicate that

simultaneous availability/accessibility of carbonyl groups from glycine, proline, and Z group are necessary for formation of ND<sub>3</sub> adducts with Z-PG species. Supporting evidence from HDX reactions between protonated and metal-complexed species of Z-PG-OCH<sub>3</sub> (a Z-PG analogue containing C-terminal methoxy instead of hydroxyl group) and ND<sub>3</sub> are also presented.

### 5.1. Introduction

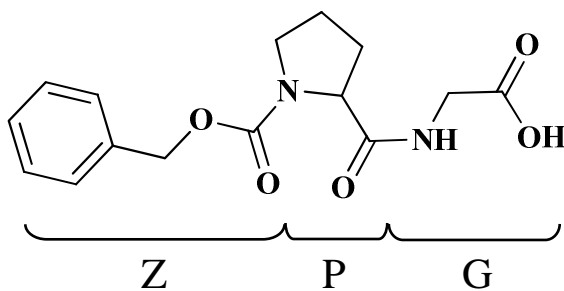
There is an immense interest in understanding the effects of non-covalent interactions such as hydrogen bonding and metal ion complexation on the structures/conformations of proteins and peptides.<sup>259-263</sup> Gas-phase hydrogen/deuterium exchange (HDX) mass spectrometry (MS) has been used extensively for structural/conformational studies of proteins/peptides<sup>113, 127, 264, 265</sup> and their metal-complexed counterparts.<sup>118, 228</sup>

Both HDX patterns and extent of deuterium uptake by protonated and metal-complexed proteins/peptides in the gas phase are used for structural elucidation purposes.<sup>117, 118, 123, 125</sup> However, other reaction channels such as gas-phase reagent adduct formation<sup>230</sup> can compete with the intended “normal” HDX reaction and complicate the interpretation of HDX data. Despite the extensive studies and reports on HDX mechanism<sup>113, 127, 266-268</sup>, mechanism of gas-phase reagent adduct formation during HDX has not been explored. For instance, it is not clear when and how the formation of a reagent adduct (*e.g.*, [peptide + nH + ND<sub>3</sub>]<sup>n+</sup>, where “n” is the number of protons) competes with the intended HDX reactions.

Deciphering the mechanisms of these competing reactions will fill an important knowledge gap in gas-phase chemistry, uncover a new area of study, and enhance our

ability to explore structure-function relationships by avoiding erroneous HDX data interpretations. The present study was inspired by our previous unpublished and puzzling results on  $\text{ND}_3$  adduct formation (of a  $\text{Ca}^{2+}$ -complexed tripeptide) and a recent HDX report hypothesizing that a “guest-host” type of interaction can yield stable ammonia adducts with “macrocyclic” peptide fragment ions.<sup>230</sup> Thorough inspection of the reported mass spectra from several other HDX reaction studies<sup>123-125, 185, 229</sup> reveal that (a) not all “macrocyclic”-type structures may form adducts with deuterated neutral ammonia ( $\text{ND}_3$ ), and (b) non-cyclic structures can also lead to adduct formation.

Our initial observation of  $\text{ND}_3$  adduct formation with a  $\text{Ca}^{2+}$ -complexed tripeptide suggested that metal ions may play an important role in altering available HDX reaction channels. Hence, to uncover the important structural parameters responsible for gas-phase HDX adduct formation in peptides, we chose to study HDX reactions of protonated and alkali metal ( $\text{Na}^+$ ,  $\text{K}^+$ , and  $\text{Cs}^+$ )-complexed species with a model dipeptide. Our model dipeptide contained a glycine (*G*) and a proline (*P*) with N-terminal benzyloxycarbonyl (*Z*) group (*i.e.*, *Z-PG*, Scheme 5.1).



Scheme 5.1. Benzyloxycarbonyl (*Z*)-proline (*P*) glycine (*G*).

We selected *Z-PG* because: (a) its *G* residue lacks a side chain and is conformationally least restricted;<sup>269</sup> hence, its flexibility can allow formation of different

metal complexes<sup>118</sup> and (b) it is small enough to perform high-level *ab initio* calculations and accurately estimate experimental and theoretical collision cross sections (CCSs) of  $[Z-PG + H]^+$  and  $[Z-PG + metal]^+$ , (c) we have observed formation of ND<sub>3</sub> adducts and HDX reaction products for Z-PG species. Additionally, the Z group in Z-PG serves two purposes, namely the Z group (i) protects the N-terminus of Z-PG peptide for “cyclic”-type structure formation, and (ii) increases the molecular weight of PG to 306 Da which is above the low mass cut-off limit of our 9.4 tesla electrospray ionization/Fourier transform-ion cyclotron resonance (ESI/FT-ICR) mass spectrometer.<sup>270</sup>

Detailed experimental results from gas-phase HDX reactions and ion mobility-mass spectrometry (IM-MS) measurements of  $[Z-PG + H]^+$ ,  $[Z-PG + metal]^+$ , and  $[Z-PG + H - CO_2]^+$  are presented to support proposed mechanism for ND<sub>3</sub> adduct formation. We also discuss complementary supporting evidence from molecular modeling of protonated and metal-complexed counterparts of Z-PG. The theoretical observations are correlated with the experimentally observed gas-phase HDX adduct formation behavior of Z-PG species. We show MS results from collision-induced dissociation (CID) of isotopically labeled  $[Z-PG]^{(13C_2, 15N) + H}^+$  (where “G” denotes an isotopically labeled glycine residue with two <sup>13</sup>C and one <sup>15</sup>N) pointing to the importance of N-terminal Z carboxylic group in  $[Z-PG + H]^+$  for ND<sub>3</sub> adduct formation. We use experimental and theoretical findings to predict which peptide structures can support stable ND<sub>3</sub> adduct formation.

## 5.2. Experimental and Theoretical

### 5.2.1. Sample Preparation

Benzyloxycarbonyl-proline glycine (Z-PG), cesium chloride (CsCl), HDX reagent (ND<sub>3</sub>), polypropylene glycol (PPG), and potassium chloride (KCl), were

purchased from Sigma (Sigma-Aldrich, St. Louis, MO, USA). *Z-PG-OCH<sub>3</sub>* was synthesized by Peptide 2.0 (Peptide 2.0 Inc., Chantilly, VA, USA). Isotopically labeled *Z-PG* (where "G" denotes the glycine residue with two <sup>13</sup>C and one <sup>15</sup>N) was synthesized by Pierce Biotechnology (part of Thermo Fisher Scientific Inc., Waltham, MA, USA). Optima grade acetic acid, methanol, and water were purchased from Fisher Scientific (part of Thermo Fisher Scientific Inc., Waltham, MA, USA).

All chemical reagents were used without further purification. Micromolar concentrations of peptide samples in electrospray solvent (methanol:water:acetic acid {49.95:49.95:0.1}) were used for ESI-MS experiments. The original peptide sample contained sodium (Na<sup>+</sup>) and calcium (Ca<sup>2+</sup>) ions and there was no need for addition of NaCl to *Z-PG* solutions to form sodium-complexed species of the dipeptides. However, micromolar concentrations of CsCl and KCl solutions were added to micromolar solutions of *Z-PG* to form potassium- and cesium-complexed species. Appropriate sample volumes were used to keep the final molar ratio of *Z-PG* to salt at 1:10.

[*Z-PG* + K]<sup>+</sup> (*m/z* 345.084) and [*Z-PG* + Ca - H]<sup>+</sup> (*m/z* 345.075) were differentiated based on mass measurement accuracy values better than 2 ppm (which was possible in both FT-ICR MS and IM-MS experiments presented here). Additionally, potassium- and calcium-complexed species of *Z-PG* could be differentiated based on their varied CCSs in IM-MS experiments (Figure C.1).

### 5.2.2. FT-ICR MS

All gas-phase HDX mass spectral data were acquired using an IonSpec (former IonSpec Corp. - now a division of Agilent Technologies, Inc., Santa Clara, CA, USA) Fourier transform-ion cyclotron resonance (FT-ICR) mass spectrometer equipped with an

open-ended cylindrical Penning trap and a 9.4 tesla superconducting magnet (Cryomagnetics Inc., Oak Ridge, TN, USA). An Analytica electrospray ion source (Analytica of Branford Inc., Branford, CT, USA) equipped with an in-house built spraying setup was used for ESI experiments.<sup>118</sup> A Harvard PHD 2000 syringe pump (Harvard Apparatus, Holliston, MA, USA) was used for direct infusion ESI. ESI flow rate was set to 0.3  $\mu\text{L}/\text{min}$ . ESI voltage was set to +3 kV. Sustained off-resonance irradiation-collision induced dissociation (SORI-CID)<sup>81</sup> was used for ion fragmentation in the ICR cell. Nitrogen gas was used as the collision gas in SORI-CID experiments.

Prior to gas-phase HDX reactions, first isotopic peaks (abbreviated as “D<sub>0</sub>”) of protonated and metal-complexed *Z-PG* species were isolated in ICR cell using a stored waveform inverse Fourier transform (SWIFT) technique.<sup>240</sup> In order to keep all the experimental conditions (*e.g.*, ND<sub>3</sub> pressure and ICR cell temperature) identical, we simultaneously isolated the protonated and metal-complexed species of *Z-PG* and conducted HDX reactions. A pulsed-leak valve setup was used for ND<sub>3</sub> introduction.<sup>122</sup> ND<sub>3</sub> pressure was measured by direct readout of a Granville-Phillips (Helix Technology Corp., Longmont, CO, USA) dual ion gauge controller and series 274 Bayard-Alpert type ionization gauge tube outputs. All reported pressures were corrected for (a) geometry factor,<sup>271</sup> (b) magnetic field effect,<sup>124</sup> and, (c) sensitivity factor<sup>272</sup> according to a previously reported procedure.<sup>124</sup>

### 5.2.3. *IM-MS*

Ion mobility (IM)-MS experiments were conducted using a Waters Synapt G2-S HDMS (Waters Corp. Manchester, UK) system equipped with an orthogonal acceleration time-of-flight (oa-TOF) mass spectrometer operated in “high resolution” mode

(MassLynx 4.0, Waters Corp. Manchester, UK). For experiments presented here, it was important to use “high resolution” ( $m/\Delta m_{50\%} \approx 40,000$  at  $m/z$  300) mode of Synapt G2-S to differentiate between  $[Z-PG + K]^+$  and  $[Z-PG + Ca - H]^+$ . The ESI flow rate and voltage were set to 0.3  $\mu\text{L}/\text{min}$  and +3 kV, respectively. Both sampling cone and source offset voltages were set to +25 V.  $\text{N}_2$  ( $\sim 2.84$  Torr) and argon (Ar) ( $\sim 1.36 \times 10^{-2}$  Torr) gases were used as buffer and collision gases, respectively. Helium (He) cell pressure was  $\sim 1.0 \times 10^3$  Torr. For experiments involving CID, ion populations of interest were isolated in the quadrupole mass filter prior to IM separation. Subsequently  $m/z$ -isolated species were fragmented in either trap (pre-IM/CID) or transfer (post-IM/CID) cells.

We used a previously reported procedure by Ruotolo<sup>137</sup> to obtain the experimental CCS values of protonated and metal-complexed species of *Z-PG*. Sodium adduct species of PPG<sup>273</sup> were used as calibrants for CCS calculations. To obtain the CCS values of protonated and metal-complex *Z-PG* species, the peak arrival times of both calibrants and unknown species (*i.e.*,  $[Z-PG + H]^+$  and  $[Z-PG + \text{metal}]^+$ ) were recorded at a constant wave height of +35 V and a wide range of wave velocities (*i.e.*, 800 m/s, 900 m/s, 1000 m/s, 1100 m/s, 1200 m/s). All IM measurements were repeated in triplicate and the reported CCSs are averages of 15 trials (3 trials for each wave velocity) included at the 95 % confidence interval.

#### 5.2.4. Molecular Modeling

Molecular mechanics MMX force field in PCModel 9.3 package (Serena Software, Bloomington, IN, USA) was used to search the conformational spaces of the protonated *Z-PG* dipeptide. The 105 most stable structures (within 3 kcal/mol of the lowest energy structure) were selected for further optimization using MMX force field

and stimulated annealing at 298 K. The resulting low energy conformer was further optimized using B3LYP density functional theory (DFT) method.<sup>274</sup>  $[Z-PG + H]^+$  structure was subsequently optimized at B3LYP/3-21G level and then at B3LYP/6-31+G(d,p) level using Gaussian 09 software (Gaussian Inc., Wallingford, CT, USA).<sup>275</sup> All DFT calculations were scaled by a scaling factor of 0.98.<sup>276</sup>

Previous studies have suggested that B3LYP/3-21G and B3LYP/6-31+G(d,p) levels of theory provide excellent predictions for geometry optimizations and single-point energy calculations of peptides.<sup>252, 262, 277, 278</sup> To optimize the geometries of metal ( $Na^+$ ,  $K^+$ , and  $Cs^+$ )-complexed *Z-PG* species, the proton in the PCModel optimized geometry of protonated *Z-PG* was first replaced with metal cations.<sup>118</sup> Subsequently, the structures of  $[Z-PG + Na]^+$  and  $[Z-PG + K]^+$  were first optimized at B3LYP/3-21G level and then at the B3LYP/6-31+G(d,p) level. The geometry of  $[Z-PG + Cs]^+$  was optimized using SDD pseudo potential basis set.<sup>279</sup> No imaginary frequencies were found for the optimized structures indicating that the optimized structures are not at their transition states (*i.e.*, absence of a saddle point in the energy diagram).

#### 5.2.5. Theoretical CCS Calculations

CCSs of the optimized geometries of protonated and metal-complexed species of *Z-PG* (obtained from *ab initio* calculations) were calculated using Sigma package.<sup>280, 281</sup> Ion-size scaled Lennard-Jones (LJ) model implemented in Sigma was used for CCS calculations.<sup>280, 281</sup> Temperature and CCS calculation accuracy in Sigma were set to 298 K and 2 % percent, respectively.

### 5.3. Results and Discussion

#### 5.3.1. HDX of $[Z-PG + H]^+$ and $[Z-PG + metal]^+$

In this section, we present the results from HDX reactions of protonated *Z-PG* and its alkali metal ion ( $Na^+$ ,  $K^+$ , and  $Cs^+$ )-complexed counterparts with  $ND_3$ . Figure 5.1, top panel shows the ESI/FT-ICR mass spectrum of a *Z-PG* sample containing  $Na^+$ ,  $K^+$ , and  $Cs^+$  after SWIFT isolation of  $D_0$  ion populations corresponding to  $[Z-PG + H]^+$  ( $m/z$  307),  $[Z-PG + Na]^+$  ( $m/z$  329),  $[Z-PG + K]^+$  ( $m/z$  345), and  $[Z-PG + Cs]^+$  ( $m/z$  439). Expanded mass spectral views corresponding to  $m/z$  ranges of 304 to 334 (a), 328.5 to 331 (b), 343 to 368 (c), and 436 to 464 (d) from ESI/FT-ICR mass spectra of SWIFT-isolated *Z-PG* species after 5 s and 600 s HDX reaction times with  $ND_3$  (pressure  $\sim 4.4 \times 10^{-8}$  Torr) are shown in Figure 5.1 middle and bottom panels, respectively.

Expanded mass spectral views in Figure 5.1 middle and bottom panels correspond to expected deuterium uptake (a to d) and  $ND_3$  adducts (a, c, and d) of  $[Z-PG + H]^+$ ,  $[Z-PG + Na]^+$ ,  $[Z-PG + K]^+$ , and  $[Z-PG + Cs]^+$ . After 5 s HDX reaction time with  $ND_3$ , the ESI/FT-ICR mass spectrum of  $[Z-PG + H]^+$  (Figure 5.1a, middle) shows the presence of both deuterium uptake and stable  $ND_3$  adduct (peak cluster labeled with roman numbers in Figure 5.1a). Surprisingly, under an identical number of gas-phase ion-molecule collisions, metal-complexed ( $Na^+$ ,  $K^+$ , or  $Cs^+$ ) species of *Z-PG* did not form  $ND_3$  adduct (Figures 5.1c and 5.1d) and only showed deuterium uptake (Figures 5.1b to 5.1d). For instance, as shown in Figure 5.1a (middle), the peak cluster at  $m/z$  range of 327 to 330 contains signals for  $ND_3$  adduct of  $[Z-PG + H]^+$  as well as  $[Z-PG + H + ND_3]^+$  with up to three deuterium atom (D) uptakes (out of three available labile hydrogens in  $[Z-PG + H]^+$ ) (peak “V” at  $m/z$  330 and labeled as  $[D_3 + ND_2H]^+$  in Figure 5.1a).

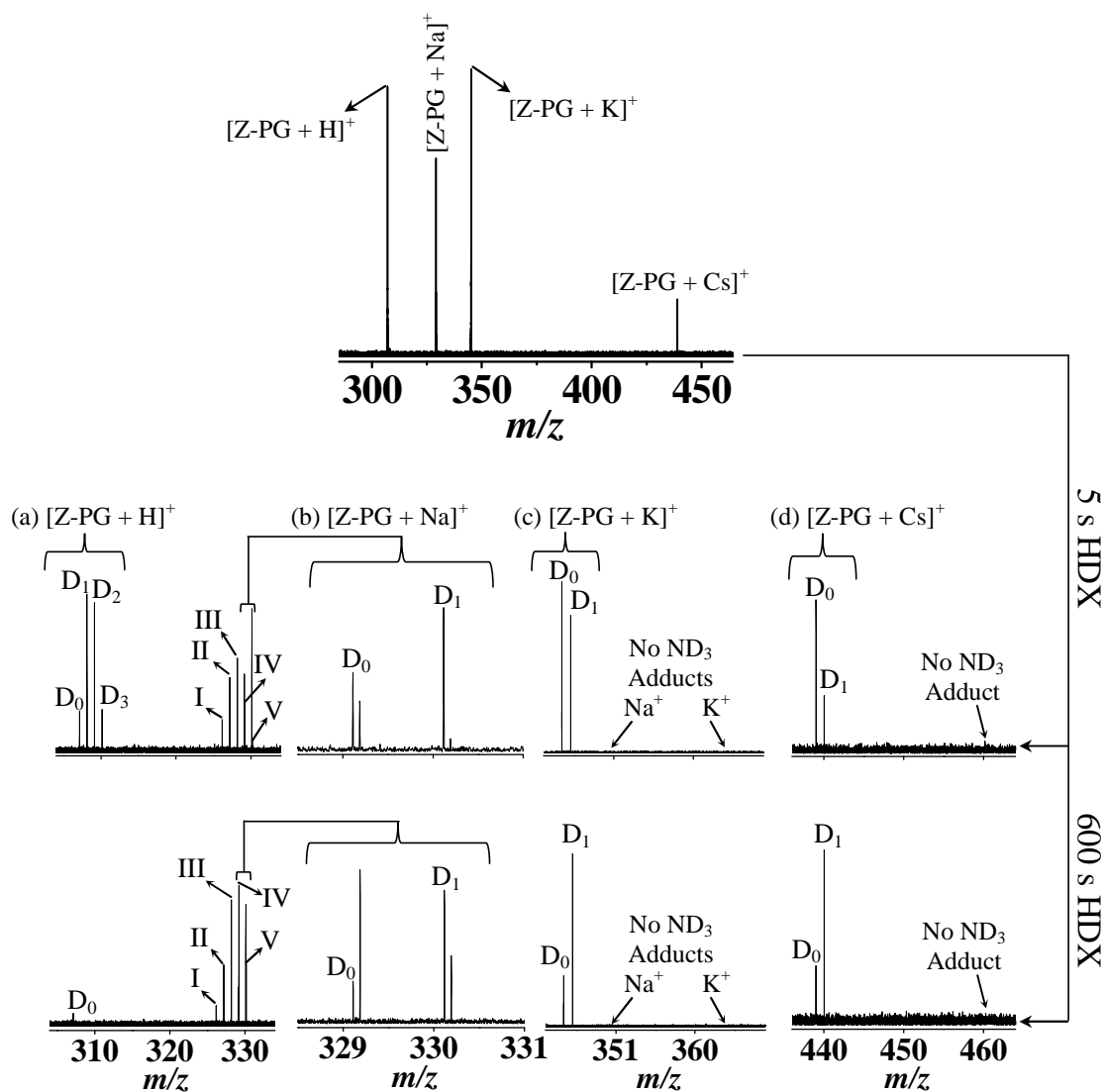


Figure 5.1. (Top) ESI/FT-ICR mass spectrum of a Z-PG sample containing Na<sup>+</sup>, K<sup>+</sup>, and Cs<sup>+</sup> after SWIFT-isolation ( $D_0$ ) of  $[Z-PG + H]^+$ ,  $[Z-PG + Na]^+$ ,  $[Z-PG + K]^+$ , and  $[Z-PG + Cs]^+$ . Expanded view ESI/FT-ICR mass spectra of  $m/z$ -isolated Z-PG species after (middle) 5 s and (bottom) 600 s HDX reaction time with ND<sub>3</sub> (at  $P(\text{ND}_3) \approx 4.4 \times 10^{-8}$  Torr).  $D_n$  ( $n = 0$  to 3) denotes the number of deuterium atom(s) incorporated in each of the Z-PG species. Roman numbers on top of the peaks in panel a designate the identities of ND<sub>3</sub> adduct species of  $[Z-PG + H]^+$ : I  $\equiv [D_0 + \text{ND}_2\text{H}]^+$  ( $m/z$  326); II  $\equiv [D_0 + \text{ND}_3]^+$  ( $m/z$  327); III  $\equiv [D_1 + \text{ND}_3]^+$  ( $m/z$  328); IV  $\equiv [D_2 + \text{ND}_3]^+$  ( $m/z$  329); V  $\equiv [D_3 + \text{ND}_3]^+$  ( $m/z$  330). Arrow heads pointing down in (c) and (d) point to the expected  $m/z$  values of ND<sub>3</sub> adducts of  $[Z-PG + \text{Na}]^+$  (panel c),  $[Z-PG + \text{K}]^+$  (panel c), and  $[Z-PG + \text{Cs}]^+$  (panel d).

In contrast, each one of the  $[Z-PG + Na]^+$ ,  $[Z-PG + K]^+$ , and  $[Z-PG + Cs]^+$  species show one deuterium uptake out of two available labile hydrogens. Formation of  $ND_3$  adduct in  $[Z-PG + H]^+$  does not depend on the reaction time and we have observed  $[Z-PG + H + ND_3]^+$  species at shorter (*e.g.*,  $\sim 1$  s at  $P(ND_3) \approx 4.4 \times 10^{-8}$  Torr) (data not shown) and longer (*e.g.*, 600 s at  $P(ND_3) \approx 4.4 \times 10^{-8}$  Torr, Figure 5.1, bottom) reaction times, suggesting that “collisional cooling” is not responsible for stable  $ND_3$  adduct formation with  $[Z-PG + H]^+$ .

$ND_3$  adduct of  $[Z-PG + H]^+$  ion population in Figure 5.1a shows the presence of one deuterium “back exchange” (*i.e.*, peak “I” at  $m/z$  326 and labeled as  $[D_0 + ND_2H]^+$  in Figure 5.1a). Under similar experimental conditions, no evidence of deuterium back exchange was noticed for  $[Z-PG + H]^+$  or  $[Z-PG + metal]^+$ . The absence of deuterium back exchange in protonated and metal-complexed  $Z-PG$  species suggests that ion at  $m/z$  326 in Figure 5.1a is an  $ND_2H$  adduct (present as impurity in  $ND_3$  neutral reagent).

Previously, Green-Church *et al.* observed stable gas-phase adduct formation during HDX reaction of protonated thymidine-5'-monophosphate (dpT) with  $ND_3$ .<sup>282</sup> Green-Church *et al.* noted that the formation of reagent adduct could indicate similar gas-phase basicity (GB) for  $ND_3$  and dpT.<sup>282</sup> Similar explanation may hold for the formation of gas-phase reagent adduct between  $Z-PG$  and  $ND_3$ . However, previous reports on the observation of  $ND_3$  adduct formation with b fragment ions with varied GB and sizes ( $b_n$ ,  $n \geq 5$ )<sup>230</sup> suggest that GB similarity is not the key determining factor for reagent adduct formation. Observation of neutral reagent adduct formation in HDX reaction of  $[Z-PG + H]^+$  with  $ND_3$  suggests that gas-phase adduct formation is not a suitable chemical probe to differentiate between “linear”- and “macro-cyclic” (compact)-type fragment ion

structures.<sup>230</sup> In fact, smaller number of deuterium uptake for  $[Z-PG + \text{metal}]^+$  (Figure 5.1 middle, panels b to d) as compared to  $[Z-PG + \text{H}]^+$  (Figure 5.1 middle, panel a) suggests the presence of more compact structures for metal-complexed species of *Z-PG* as compared to its protonated counterpart. These observations are consistent with experimentally measured CCS values from IM-MS measurements and molecular modeling (following sections). Therefore, structural compactness is not the determining factor for gas-phase reagent adduct formation and undoubtedly other important structural parameters (*e.g.*, functional group orientation) must be involved.

Formation of gas-phase  $\text{ND}_3$  adduct with the protonated form of the studied *Z*-capped dipeptide does not depend on its amino acid sequence. For instance, HDX reaction of protonated *Z-GP* (*i.e.*,  $[Z-GP + \text{H}]^+$ , *Z*-capped peptide with reverse amino acid sequence as compared to *Z-PG*) with  $\text{ND}_3$  produced  $\text{ND}_3$  adduct and no  $\text{ND}_3$  adduct was observed for  $[Z-GP + \text{alkali metal}]^+$  (data not shown). Experimental data and theoretical calculations presented in the following sections are designed to identify the important functional groups and their potential geometrical orientations for adduct formation in the gas phase.

### 5.3.2. Theoretically Optimized Geometries of $[Z-PG + \text{H}]^+$ and $[Z-PG + \text{metal}]^+$

To better infer the mechanism of neutral reagent adduct formation with  $[Z-PG + \text{H}]^+$  upon HDX reaction, and to interpret the HDX mass spectral patterns in Figure 5.1, we used *ab initio* calculations and optimized the three dimensional (3D) geometries of protonated *Z-PG* and its metal-complexed and  $\text{ND}_3$  adduct counterparts. Figure 5.2 shows the lowest energy 3D geometries of  $[Z-PG + \text{H}]^+$  (panel a),  $[Z-PG + \text{Na}]^+$  (panel b),  $[Z-PG + \text{K}]^+$  (panel c), and  $[Z-PG + \text{Cs}]^+$  (panel d). Total energies for optimized

structures are given at the bottom of each panel in Figure 5.2. For all of the *Z-PG* species in Figure 5.2, charge-solvated structure<sup>283</sup> was the most stable (lowest energy) geometry. Figure 5.3 shows the 3D geometry of the most stable candidate structure for  $[Z-PG + H + ND_3]^+$  in which three carbonyl oxygen atoms are involved in hydrogen bonding with deuterium atoms from  $ND_3$ .

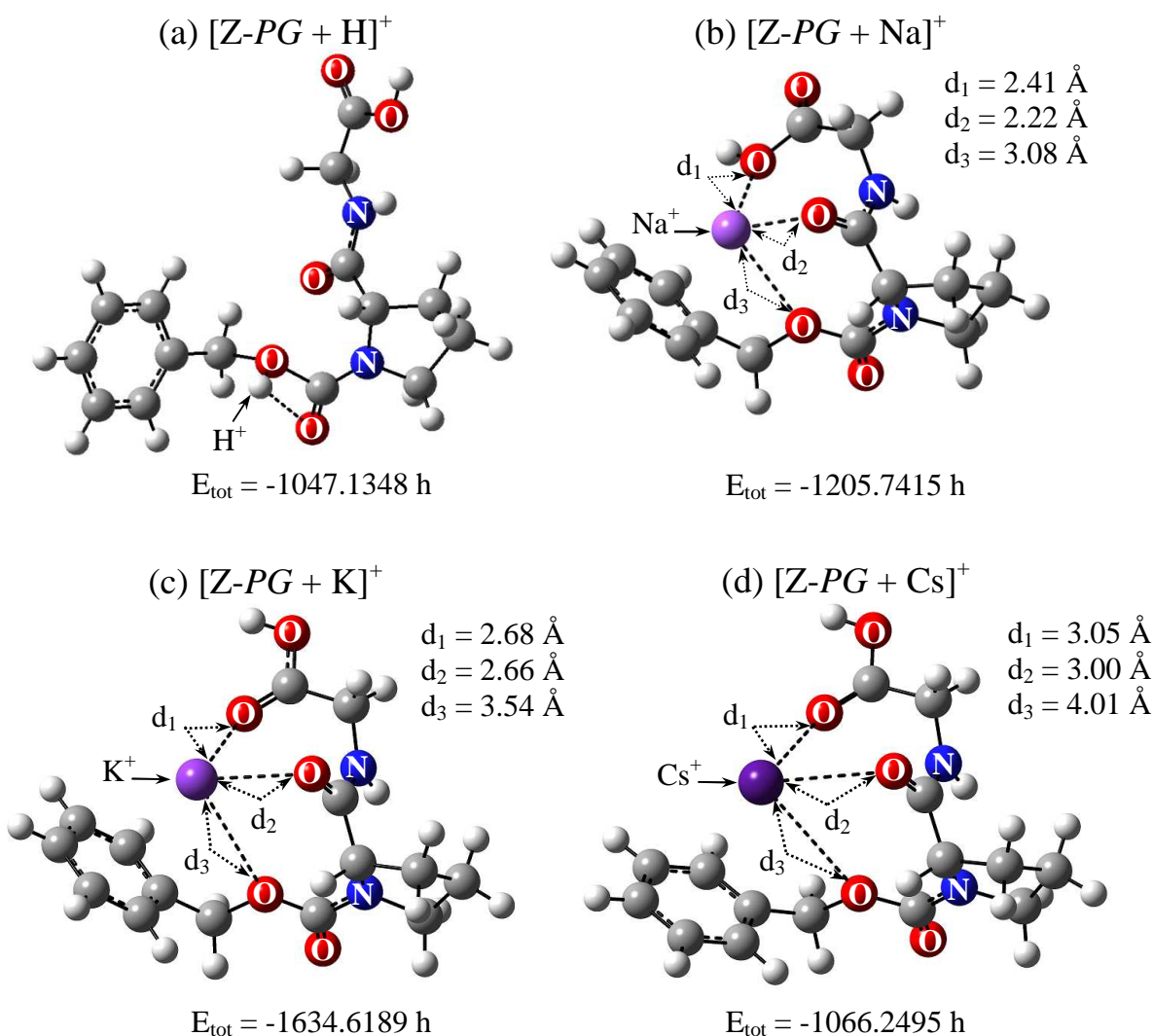


Figure 5.2. Optimized geometries of (a)  $[Z-PG + H]^+$ , (b)  $[Z-PG + Na]^+$ , and (c)  $[Z-PG + K]^+$ , and (d)  $[Z-PG + Cs]^+$ . Carbon and hydrogen atoms are shown in dark gray and light gray colors, respectively. Nitrogen and oxygen atoms are labeled as “N” and “O”, respectively. Total energy ( $E_{tot}$ ) (in Hartree (h)) for each structure is given.

Theoretically optimized geometries in Figure 5.2 show a significantly different conformation for protonated *Z-PG* and its alkali metal-complexed species. For instance, as shown in Figure 5.2a,  $[Z-PG + H]^+$  adopts an open conformation and its C-terminus is not involved in hydrogen bonding. In contrast, metal-complexed species of *Z-PG* adopt compact conformations and carbonyl oxygen (O) atoms of glycine and proline residues and Z group ester-type O atom are involved in metal complexation (Figures 5.2b to 5.2d). These observations are consistent with previous reports suggesting the presence of a multi-dentate interaction<sup>118</sup> between alkali metal ions and peptides.<sup>118, 283-285</sup>

Optimized geometries in Figure 5.2 show the presence of a tighter complexation for  $[Z-PG + Na]^+$  than  $[Z-PG + K]^+$  and  $[Z-PG + Cs]^+$  as it is evident from shorter coordination bond distances between *Z-PG* carbonyl oxygen atoms and  $Na^+$  in  $[Z-PG + Na]^+$  (Figure 5.2b). At the first glance, it seems that the free C-terminal glycine carboxylic group and proline carbonyl oxygen might be responsible for stabilizing  $[Z-PG + H + ND_3]^+$  as these functional groups are involved in metal complexation in  $[Z-PG + metal]^+$ . However, as we discuss later, our experimental results suggest that simultaneous availability of all three carbonyl groups (*i.e.*, carbonyls from Z group, proline, and glycine) are important for formation of stable gas-phase adducts in *Z-PG*. As shown in Figure 5.3, availability of these three carbonyl oxygen atoms maximizes the number of hydrogen bonds with  $ND_3$ . We used IM-MS to measure CCSs of protonated and metal-complexed species of *Z-PG*. The experimental CCSs were correlated with the optimized 3D geometries from molecular modeling (Figure 5.2). Figure 5.4 shows the IM profiles for  $[Z-PG + H]^+$  (panel a),  $[Z-PG + Na]^+$  (panel b),  $[Z-PG + K]^+$  (panel c), and  $[Z-PG + Cs]^+$  (panel d) acquired using a Synapt G2-S HDMS system. IM profiles of all four *Z-PG*

species show a Gaussian-like arrival time distribution suggesting the presence of one conformation for each species.

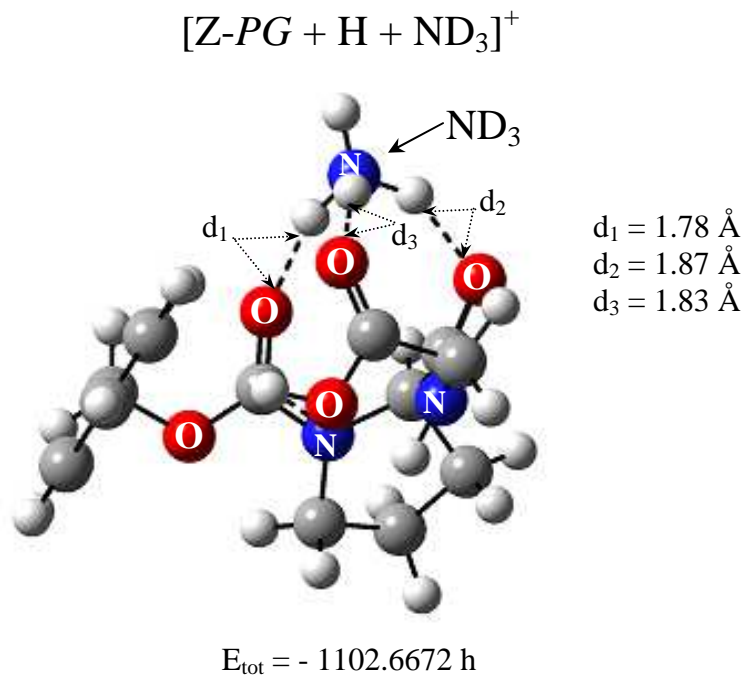


Figure 5.3. Optimized geometry for  $[Z-PG + H + ND_3]^+$  (at B3LYP/6-31+G(d,p) level of theory). Carbon and hydrogen atoms are shown in dark gray and light gray colors, respectively. Nitrogen and oxygen atoms are labeled as “O” and “N”, respectively. Total energy ( $E_{\text{tot}}$ ) (in Hartree (h)) is given.

### 5.3.3. IM-MS of $[Z-PG + H]^+$ and $[Z-PG + metal]^+$

We also used a previously reported post-IM/CID-chemometric approach, which further confirmed the presence of one conformation for each of the *Z-PG* species and absence of IM co-elution.<sup>212</sup> For meaningful comparisons, we converted the measured mobility ATs to CCSs. Table 5.1, second column, contains a summary of the experimentally measured CCS values for protonated and metal-complexed *Z-PG* species.

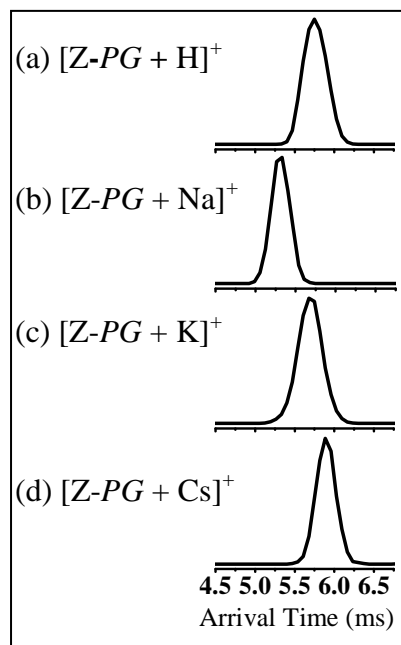


Figure 5.4. IM profiles of (a)  $[Z-PG + H]^+$ , (b)  $[Z-PG + Na]^+$ , (c)  $[Z-PG + K]^+$ , and (d)  $[Z-PG + Cs]^+$ .

Based on the ion mobility data, the following increasing order was observed for CCSs of *Z-PG* species:  $[Z-PG + Na]^+ < [Z-PG + K]^+ < [Z-PG + Cs]^+ \approx [Z-PG + H]^+$ . These IM-MS results for CCS measurements are consistent with the observed HDX mass spectral patterns in Figure 5.1 and suggest the presence of more compact structures for metal-complexed species of *Z-PG* than its protonated counterpart. Experimentally measured CCSs in Table 5.1 suggest that smaller size alkali metal ions bind tighter to *Z-PG* than larger size alkali metal ions. For instance, addition of  $Na^+$  ( $r_{ion} = 0.97 \text{ \AA}^{286}$ ) to *Z-PG* reduces CCS of  $[Z-PG + Na]^+$  by 6 % as compared to  $[Z-PG + H]^+$ . In contrast, addition of  $Cs^+$  ( $r_{ion} = 1.67 \text{ \AA}^{286}$ ) to *Z-PG* does not change CCS of  $[Z-PG + Cs]^+$  significantly (at the 95 % confidence level and using case II t-test for  $n_1 = n_2 = 15$ ) as compared to  $[Z-PG + H]^+$ .

Table 5.1. Experimental and theoretical collision cross sections ( $\Omega$ ) of *Z-PG* and *Z-GP* species. Errors at 95 % confidence level ( $n = 15$  for experimental and  $n = 40$  for theoretical) are included in parentheses.

<i>Z-PG</i> Species	Experimental $\Omega_{\text{He}} (\text{\AA}^2)$	Theoretical $\Omega_{\text{He}} (\text{\AA}^2)$
[ <i>Z-PG</i> + H] <sup>+</sup>	120.84 ( $\pm 0.73$ )	116.99 ( $\pm 0.26$ )
[ <i>Z-PG</i> + Na] <sup>+</sup>	113.23 ( $\pm 0.48$ )	110.06 ( $\pm 0.20$ )
[ <i>Z-PG</i> + K] <sup>+</sup>	117.18 ( $\pm 0.81$ )	112.92 ( $\pm 0.17$ )
[ <i>Z-PG</i> + Cs] <sup>+</sup>	120.72 ( $\pm 0.48$ )	116.48 ( $\pm 0.31$ )

We also compared the CCS values of protonated and metal-complexed *Z-PG* species obtained from IM-MS measurements with those calculated from theoretically optimized candidate structures using *ab initio* calculations. Table 5.1, third column, contains the theoretically calculated CCS values for *Z-PG* species. Average values from forty lowest energy optimized structures for each *Z-PG* species were used to calculate the theoretical CCS values in Table 5.1 (column 3) (*i.e.*, average of 40 CCS values for each *Z-PG* species).

The theoretical (Table 5.1, column 3) and experimental (Table 5.1, column 2) CCSs of *Z-PG* species qualitatively agree with relative difference of <4 %, consistent with the previously reported criterion for assigning structural geometries using IM.<sup>280</sup> Theoretical calculations suggest similar (at the 95 % confidence level) CCSs for [*Z-PG* + H]<sup>+</sup> and [*Z-PG* + Cs]<sup>+</sup>. Experimental measurements and theoretical calculations of CCS are consistent and support the view that the addition of alkali metal introduces multi-dentate type biddings between alkali metals (*viz.*, Na<sup>+</sup>, K<sup>+</sup>, and Cs<sup>+</sup>) and the *Z-PG* peptide.

#### 5.3.4. HDX and IM-MS of $[Z-PG + H - CO_2]^+$

Detailed inspection of the optimized structures in Figure 5.2 suggests that stable gas-phase  $ND_3$  adduct formation with  $Z-PG$  species depends on the availability of backbone carbonyl groups from proline and glycine amino acids and/or ester oxygen (O) atom from the Z group. To test this hypothesis, we conducted HDX reaction on  $[Z-PG + H - CO_2]^+$  ( $m/z$  263) generated from SORI-CID of  $m/z$ -isolated ( $D_0$ )  $[Z-PG + H]^+$  ( $m/z$  307) in the ICR cell.

Figure 5.5a shows the ESI/FT-ICR mass spectrum of  $[Z-PG + H - CO_2]^+$  after  $\sim 600$  s HDX reaction time with  $ND_3$  (pressure  $\sim 4.4 \times 10^{-8}$  Torr). Under an identical number of ion-molecule collisions as in Figure 5.1 bottom,  $ND_3$  adduct was not observed for  $[Z-PG + H - CO_2]^+$  (Figure 5.5a). HDX mass spectrum of  $[Z-PG + H - CO_2]^+$  ion population showed the presence of two deuterium uptakes (out of three available labile hydrogens).

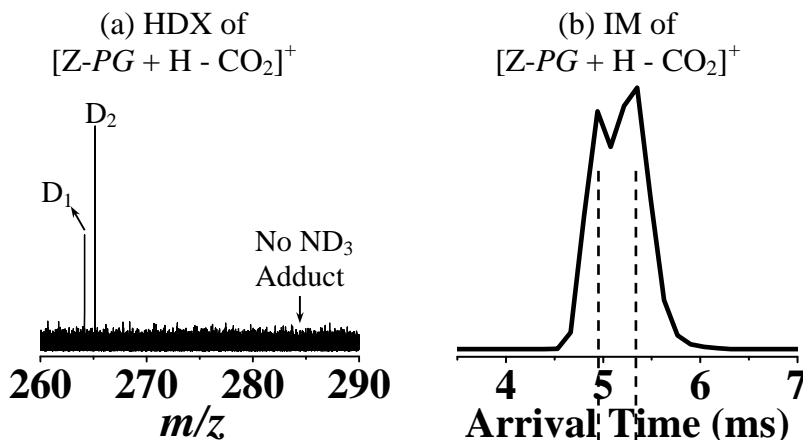


Figure 5.5. (a) ESI/FT-ICR mass spectrum of  $[Z-PG + H - CO_2]^+$  after 600 s HDX reaction time with  $ND_3$  (at  $P(ND_3) \approx 4.4 \times 10^{-8}$  Torr).  $D_n$  ( $n = 1$  and  $2$ ) denotes the number of deuterium atom(s) incorporated in  $[Z-PG + H - CO_2]^+$ . (b) IM profile of  $[Z-PG + H - CO_2]^+$ . The two vertical dash lines in panel b are guides showing the position of peak ATs of the two  $[Z-PG + H - CO_2]^+$  conformers.

Comparison of the HDX mass spectral results in Figures 5.1 bottom (panel a) and 5.5a suggest that loss of carboxylic group from  $[Z-PG + H]^+$  makes the formation of  $ND_3$  adduct with  $[Z-PG + H]^+$  unfavorable. However, there are two sources for loss of  $CO_2$  from  $[Z-PG + H]^+$ : (i) carboxylic group from C-terminal glycine and/or (ii) N-terminal benzyloxycarbonyl (Z) group. The  $CO_2$  loss products from pathways i and ii have identical exact  $m/z$  (263.139) and cannot be distinguished by MS. We used ion mobility and isotope labeling to differentiate between the two  $CO_2$  loss products of  $[Z-PG + H]^+$ .

Figure 5.5b shows the IM profile of  $m/z$ -isolated  $[Z-PG + H - CO_2]^+$  generated from CID of  $[Z-PG + H]^+$  in the Synapt G2-S Z-Spray source. The bi-Gaussian IM profile peak shape in Figure 5.5b may suggest that neutral  $CO_2$  is lost from both glycine and the Z group in  $[Z-PG + H]^+$ . However, it is also possible that  $[Z-PG + H - CO_2]^+$  is the product of  $CO_2$  loss from either glycine or Z group but adapts two different conformations/structures, which can be separated in IM cell. To test this hypothesis, we performed post-IM/CID MS experiments and stable isotope labeling.

Figure 5.6a shows the CID mass spectra of isotopically labeled  $[Z-P\underline{G} + H]^+$  ( $m/z$  310). Underline in “G” is used to depict that the C-terminal glycine contains two  $^{13}C$  and one  $^{15}N$ . To acquire the CID mass spectrum in Figure 5.6a, ion population at  $m/z$  310, corresponding to  $[Z-P\underline{G} + H]^+$ , was mass-isolated in a Synapt G2-S quadrupole assembly and subjected to CID in the trap cell by setting the potential difference between trap cell exit and IM cell entrance to 14 V. If carbon dioxide is lost from both C-terminal glycine and N-terminal Z group of  $[Z-P\underline{G} + H]^+$ , one would expect to observe two peaks at  $m/z$  265 ( $[Z-P\underline{G} + H - ^{13}CO_2]^+$ ) and 266 ( $[Z-P\underline{G} + H - ^{12}CO_2]^+$ ) in the CID mass spectrum of  $[Z-P\underline{G} + H]^+$ . However, as depicted in Figure 5.6a, CID mass spectrum of  $[Z-P\underline{G} + H]^+$

showed the presence of only one peak; only a single peak at ( $m/z$  266), corresponding to loss of  $^{12}\text{CO}_2$ , was observed and no fragment ion was observed at  $m/z$  265 ( $[\text{Z-PG} + \text{H} - ^{13}\text{CO}_2]^+$ ). Figure 5.6b shows the IM profile of  $[\text{Z-PG} + \text{H} - \text{CO}_2]^+$ . Two ion populations were observed for  $[\text{Z-PG} + \text{H} - \text{CO}_2]^+$ , consistent with the results presented in Figure 5.5b for  $[\text{Z-PG} + \text{H} - \text{CO}_2]^+$  and confirming that the observed  $\text{CO}_2$  loss in Z-PG is from the internal carboxylic group of benzyloxycarbonyl (Z) and not the carboxylic end of glycine.

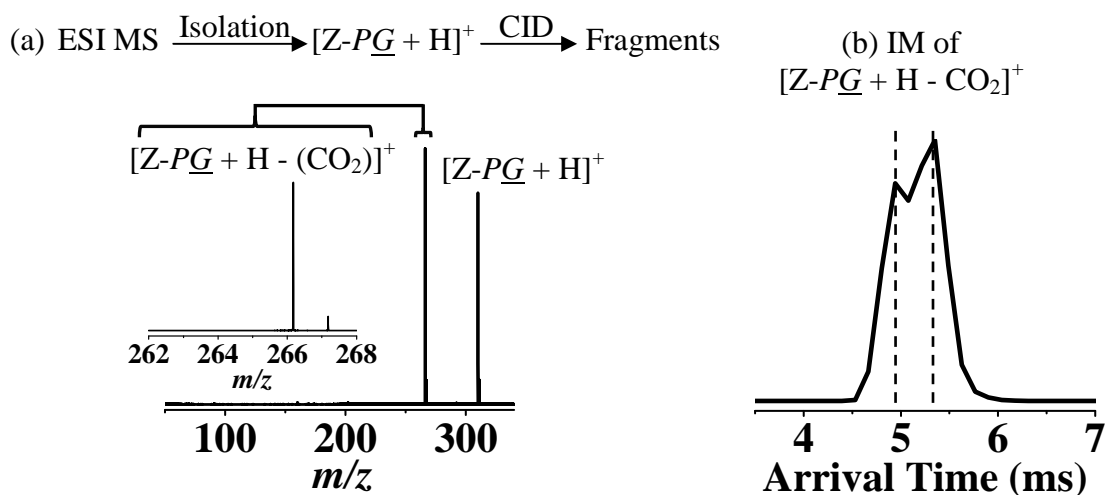


Figure 5.6. (a) CID mass spectrum of  $m/z$ -isolated  $[\text{Z-PG} + \text{H}]^+$  ( $m/z$  310) and (b) profile of  $[\text{Z-PG} + \text{H} - \text{CO}_2]^+$ . “G” in Z-PG contains two labeled carbon thirteen ( $^{13}\text{C}_2$ ) isotopes and one labeled nitrogen fifteen ( $^{15}\text{N}_1$ ) isotope. Inset in panel a shows the expanded view of  $m/z$  range between 262 to 268 corresponding to loss of carbon dioxide from  $[\text{Z-PG} + \text{H}]^+$ .

Again, results from isotope labeling experiment in Figure 5.6 revealed that  $\text{CO}_2$  is lost from N-terminal benzyloxycarbonyl (Z) group of  $[\text{Z-PG} + \text{H}]^+$  to generate  $[\text{Z-PG} + \text{H} - \text{CO}_2]^+$ . The resulting  $[\text{Z-PG} + \text{H} - \text{CO}_2]^+$  ion population adapts two conformations/structures. These two conformationally different  $[\text{Z-PG} + \text{H} - \text{CO}_2]^+$  ion populations show different fragmentation patterns (with similar fragment ion types) when

subjected to CID with an identical collision energy (Figure C.2). Therefore, the absence of stable  $\text{ND}_3$  adduct with  $[\text{Z-PG} + \text{H} - \text{CO}_2]^+$  is explained by lack of interaction between  $\text{ND}_3$  and carbonyl functional group of the benzyloxycarbonyl (Z) group, consistent with the observations from molecular modeling (Figures 5.2 and 5.3).

### 5.3.5. HDX of $[\text{Z-PG-OCH}_3 + \text{H}]^+$

C-terminal glycine amino acid in *Z-PG* contains both carbonyl and hydroxyl oxygen atoms, which may be involved in  $\text{ND}_3$  adduct formation. To determine whether the presence of glycine hydroxyl group is important for *Z-PG* gas-phase adduct formation or not, we conducted HDX reactions on  $m/z$ -isolated species of  $[\text{Z-PG-OCH}_3 + \text{H}]^+$  ( $m/z$  321).

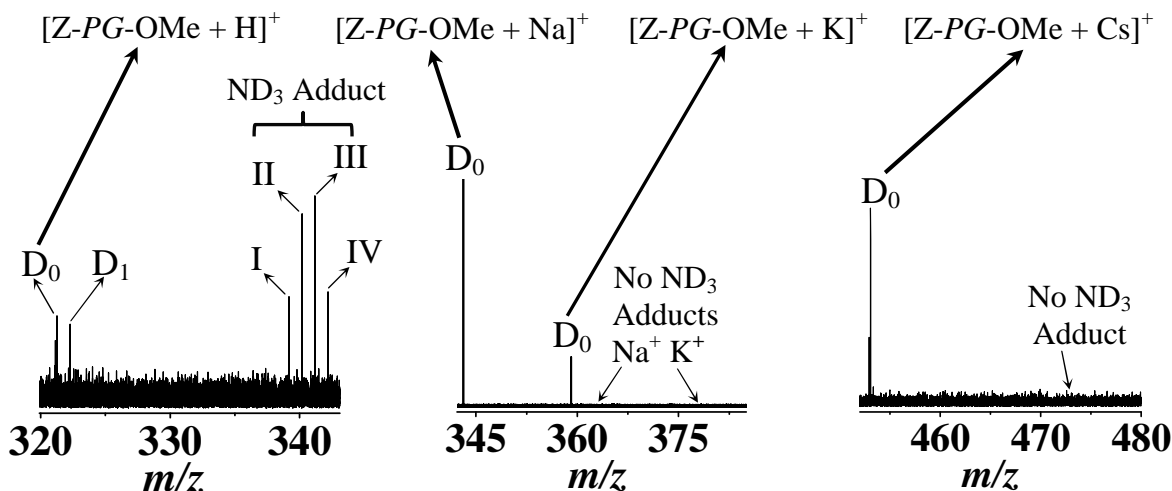


Figure 5.7. ESI/FT-ICR mass spectra of  $m/z$ -isolated ( $\text{D}_0$ ) (left)  $[\text{Z-PG-OMe} + \text{H}]^+$ , (middle)  $[\text{Z-PG-OMe} + \text{Na}]^+$ , (middle)  $[\text{Z-PG-OMe} + \text{K}]^+$ , and (right)  $[\text{Z-PG-OMe} + \text{Cs}]^+$  after 600 s reaction time with  $\text{ND}_3$  (at  $P(\text{ND}_3) \approx 4.4 \times 10^{-8}$  Torr). I  $\equiv [\text{D}_0 + \text{ND}_2\text{H}]^+$  ( $m/z$  340); II  $\equiv [\text{D}_0 + \text{ND}_3]^+$  ( $m/z$  341); III  $\equiv [\text{D}_1 + \text{ND}_3]^+$  ( $m/z$  342); IV  $\equiv [\text{D}_2 + \text{ND}_3]^+$  ( $m/z$  343).

In *Z-PG-OCH<sub>3</sub>*, the hydrogen atom attached to glycine hydroxyl group was

replaced with a CH<sub>3</sub> group, which could interrupt the hydrogen bonding between ND<sub>3</sub> and glycine hydroxyl group in *Z-PG*.

Figure 5.7 shows the ESI/FT-ICR mass spectrum of [*Z-PG-OCH*<sub>3</sub> + H]<sup>+</sup> (left panel), [*Z-PG-OCH*<sub>3</sub> + Na]<sup>+</sup> (middle panel), [*Z-PG-OCH*<sub>3</sub> + K]<sup>+</sup> (middle panel), and [*Z-PG-OCH*<sub>3</sub> + Cs]<sup>+</sup> (right panel) after 600 s HDX reaction time with ND<sub>3</sub> (pressure ~3.0 × 10<sup>-8</sup> Torr). Similar to [*Z-PG* + H]<sup>+</sup> (Figure 5.1 bottom, panel a), HDX mass spectral pattern of [*Z-PG-OCH*<sub>3</sub> + H]<sup>+</sup> showed the presence of both deuterium uptake and ND<sub>3</sub> adduct. The mass spectrum in Figure 5.7 shows the presence of one deuterium uptake in [*Z-PG-OCH*<sub>3</sub> + H]<sup>+</sup> (peak labeled as D<sub>1</sub> in Figure 5.7) and up to two deuterium uptakes in [*Z-PG-OCH*<sub>3</sub> + H + ND<sub>3</sub>]<sup>+</sup> (peak labeled as “IV” in Figure 5.7). No ND<sub>3</sub> adduct was observed for metal (Na<sup>+</sup>, K<sup>+</sup>, and Cs<sup>+</sup>)-complexed species of *Z-PG-OCH*<sub>3</sub> (Figure 5.7 middle and right panels).

Results in Figure 5.7 suggest that C-terminal glycine hydroxyl group is not involved in ND<sub>3</sub> adduct formation in *Z-PG*. HDX results in Figure 5.6 are consistent with the molecular modeling data in Figure 5.3, suggesting that the O atom from glycine’s carbonyl group is engaged in hydrogen bonding with ND<sub>3</sub>.

#### 5.4. Conclusion

We reported on the observation of selective reagent adduct formation in HDX reaction of protonated *Z-PG* with ND<sub>3</sub>. The formation of gas-phase reagent adduct with protonated *Z-PG* was insensitive to model dipeptide amino acid sequence (*i.e.*, *Z-PG* versus *Z-GP*).

To the best of our knowledge, this is the first comprehensive study to examine gas-phase HDX reagent adduct formation by combining experimental MS, IM-MS, and IM-MS/MS and theoretical approaches.

Results presented in here point to the importance of considering all competing gas-phase reaction channels during HDX of peptides, *i.e.*, reagent adduct formation. Although the formation of gas-phase reagent adducts can complicate the interpretation of “normal” HDX uptake and reaction kinetics, it may also reveal important structural information such as orientation of peptides backbone carbonyl groups.

#### *Acknowledgment*

Financial support from Baylor University is greatly acknowledged. Authors would like to thank Dr. Thomas Wytttenbach of University of California, Santa Barbara for providing a copy of Sigma package and Dr. Kevin L. Shuford of Baylor University for his valuable discussion on molecular modeling calculations. We would also like to thank Paul Brown (Dr. Shuford’s graduate student) for helping us with setting up FORTRAN compiler for CCS calculations.

## CHAPTER SIX

### *Conclusions and Future Directions*

Protein identification and characterization using mass spectrometry (MS) techniques relies heavily on bioinformatics algorithms, search engines, and software controlled processes. The available computer software and search engines are generally based on bioinformatics models that relate the experimental tandem MS data to databases and do not account for gas-phase fragment ion rearrangements. Presence of unforeseen post-ionization structural rearrangements and amino acid sequence scrambling can reduce protein/peptide identification reliability and yield “low scores” or even result in misidentification. Therefore, research is needed to better understand the gas-phase chemistry involved in formation of different fragment ion structures during collision induced dissociation (CID) and improve peptide sequencing using MS.

To investigate chemical reactions involved in ion dissociation and address current limitations in gas-phase protein sequencing, we studied structures of model peptides and their fragment ions. In particular, we wanted to: (i) characterize the influence of structural parameters that favored gas-phase fragment ion rearrangements and (ii) identify potential chemical pathways involved in generation of sequence-scrambled product ions. We utilized a variety of analytical techniques such as state-of-the-art MS and ion mobility (IM) devices combined with *ab initio* and theoretical calculations to enhance our fundamental understanding of gas-phase ion physics and ion dissociation processes. In

the following sections, we briefly discuss specific outcomes and future directions of the research presented in each chapter of this dissertation.

### *Dissertation Overview and Future Directions*

*CHAPTER ONE:* Chapter one provided a general overview of the principles of mass spectrometry (MS) and frequently used MS dissociation techniques in protein sequencing. In addition, two analytical techniques (*viz.*, gas-phase hydrogen/deuterium exchange (HDX) reaction and ion mobility (IM) spectrometry) that are commonly used for gas-phase structural characterization of peptides and peptide fragments were introduced in chapter one.

*CHAPTER TWO:* In chapter two, details of commonly used MS-based protein identification approaches and gas-phase peptide fragment ion rearrangements were discussed. Furthermore, a survey of the National Institute of Standards and Technology (NIST) peptide MS/MS library and experimental CID data was presented; the NIST survey and data from a model peptide demonstrated the importance of gas-phase fragment ion rearrangements for peptide sequencing.

Moreover, data presented in chapter two highlighted the essence of (i) understanding of the gas-phase chemistry governing rearrangement reactions in MS fragmentation processes and (ii) characterization of fragment ion structures and pathways leading to fragment ion scrambling for improving the accuracy of bioinformatics software and algorithms used in protein identification.

*CHAPTER THREE:* MS data in chapter three allowed for comprehensive comparisons in a systematic study and ultimate understanding of the effects of basic histidine amino acid positions and fragment ion sizes on structures of b-type fragment

ions (generated during CID). Gas-phase HDX reactions (conducted using a 9.4 teals Fourier transform-ion cyclotron resonance (FT-ICR) MS) and IM-MS were utilized to probe gas-phase structures of 28 histidine (His)-containing  $b_n$  ( $n = 4$  to  $7$ ) ions from seven isomeric heptapeptides of  $A_6(\text{His})\text{-NH}_2$  type. Results from both HDX mass spectral patterns and reaction kinetics were consistent with the presence of at least two structural isomers for the studied histidine-containing  $b_n$  ions, regardless of the histidine position in the original heptapeptide amino acid sequence. The presence of structural isomers in histidine-containing  $b_n$  ( $n = 4$  to  $7$ ) ions was further supported by the experimental data from IM-MS measurements.

IM profiles acquired for  $b_5^+$  from each of  $\text{AA}(\text{His})\text{AAAANH}_2$ ,  $\text{AAA}(\text{His})\text{AAA-NH}_2$ , and  $\text{AAAA}(\text{His})\text{AA-NH}_2$  peptides showed the presence two mobility-overlapped ion populations (*i.e.*, “compact” and “linear” isomers). For IM profiles with un-resolved single-Gaussian peak shapes, we also compared peak profiles for  $b$  ions with standard sodium adduct polypropylene glycol (PPG) ions (peaks’ full widths at half height (FWHH)) that had similar arrival times (ATs). For example, FWHH analyses for  $b_n^+$  ( $n = 4$  to  $7$ ) from  $\text{AA}(\text{His})\text{AAAANH}_2$  (P3) showed the presence of significantly wider IM peak widths for these fragments than standard sodium adduct PPG counter part ions with similar ATs. Results from FWHH analyses suggested the presence of multiple structural isomers for  $b_n^+$  ( $n = 4$  to  $7$ ) of P3, consistent with HDX data.

Future studies might include the use of post-IM/CID MS as a tool to resolve different  $b$  fragment isomers or conformers and obtain the percentages of “compact” and “linear” structural isomers of the histidine-containing  $b$  ions as a function of (i) histidine position in the original heptapeptide amino acid sequence and (ii) experimental

parameters (*e.g.*, ESI capillary voltage and ion transfer kinetic energy). Furthermore, chemical modifications (*e.g.*, peptide N-terminal acetylation) might be used to decrease or even eliminate the possible chances of b fragment ion cyclization and/or confirm the presence or absence of various structural isomers for b ions.

*CHAPTER FOUR:* MS results in chapter four provided the first experimental evidence for occurrence of sequence scrambling in y-type fragment ions. We presented results from CID MS of y fragment ions generated from four model peptides (all containing basic residues near the C-terminus) including: AAAAHAA-NH<sub>2</sub> (where “A” denotes an alanine (A) residue with one carbon thirteen (<sup>13</sup>C) isotope on the alanine carbonyl group), des-acetylated- $\alpha$ -melanocyte (SYSMEHFRWGKPV-NH<sub>2</sub>), angiotensin II antipeptide (EGVYVHPV), and glufibrinopeptide b (EGVNDNEEGFFSAR). A total of thirty two y fragment ions, including fragments of different charge states (+1 to +3) and sizes (4 to 12 amino acids), were investigated.

The presence of sequence-scrambled fragment ions in CID mass spectra of ~50 % of the studied y ions were confirmed. Moreover, results from MS<sup>n</sup> CID MS experiments suggested that sequence scrambling in y ions could occur through subsequent fragmentation of intermediate macrocyclic structure ion(s) (*i.e.*, [y - (NH<sub>3</sub>/orH<sub>2</sub>O)]<sup>m+</sup>, where m = 1 to 3). Based on the MS<sup>n</sup> CID results, potential mechanisms for the occurrence of sequence scrambling in CID of examined y-type ions were proposed.

Future studies in this area could be focused on investigating the effect of (i) peptides' amino acid compositions (*i.e.*, amino acids with different side chains such as polar, non-polar, acidic, and basic) and (ii) peptides' C-terminal amidation (versus acid terminated) on the generation of sequence-scrambled fragment ions during CID of y ions.

*CHAPTER FIVE:* Gas-phase HDX is a powerful chemical probe for structural elucidation of proteins/peptides and their fragment ions and metal-complexed counterparts; however, other reaction channels (*e.g.*, gas-phase reagent adduct formation) can compete with intended “normal” HDX reaction and complicate the interpretation of HDX data. Data in chapter five provided the first comprehensive study on fundamental chemistry involved in gas-phase adduct formation by combining *ab initio* calculations, HDX reactions, IM-MS, isotope labeling, and post-IM/CID MS.

Effects of protonation and alkali metal ion ( $\text{Na}^+$ ,  $\text{K}^+$ , and  $\text{Cs}^+$ ) complexation on gas-phase  $\text{ND}_3$  adduct formation of a benzyloxycarbonyl (*Z*)-capped dipeptide containing glycine (*G*) and proline (*P*) (*i.e.*, *Z-PG*) were studied. We reported on selective reagent adduct formation in HDX reaction of protonated *Z-PG* with  $\text{ND}_3$ . We showed that formation of the gas-phase reagent adduct with protonated *Z-PG* was insensitive to the order of the amino acid sequence of model dipeptide (*i.e.*, *Z-PG* versus *Z-GP*). By combining the results from experimental observations and theoretical calculations we demonstrated that the presence of three carbonyl oxygens from *G*, *P*, and *Z* group are critical for  $\text{ND}_3$  adduct formation in *Z-PG*. Results presented in chapter five point to the importance of considering all competing gas-phase reaction channels (*e.g.*, reagent adduct formation) in HDX studies.

Future studies could explore the influence of (i) alkali (group 1), alkaline earth (group 2), and transition metal ion complexations, (ii) increasing the distance between *P* and *G* residues in *Z-PG* peptide (*e.g.*, using synthetic model peptides of *Z-P(CH<sub>2</sub>)<sub>m</sub>G* type), and (iii) replacing L-glycine and L-proline residues with their corresponding D

stereoisomers on the extent of  $\text{ND}_3$  adduct formation with *Z-PG* and other model peptides.

## APPENDICES

## APPENDIX A

A Systematic Study on the Effect of Histidine Position and Fragment Ion Size in the Formation of  $b_n$  Ions

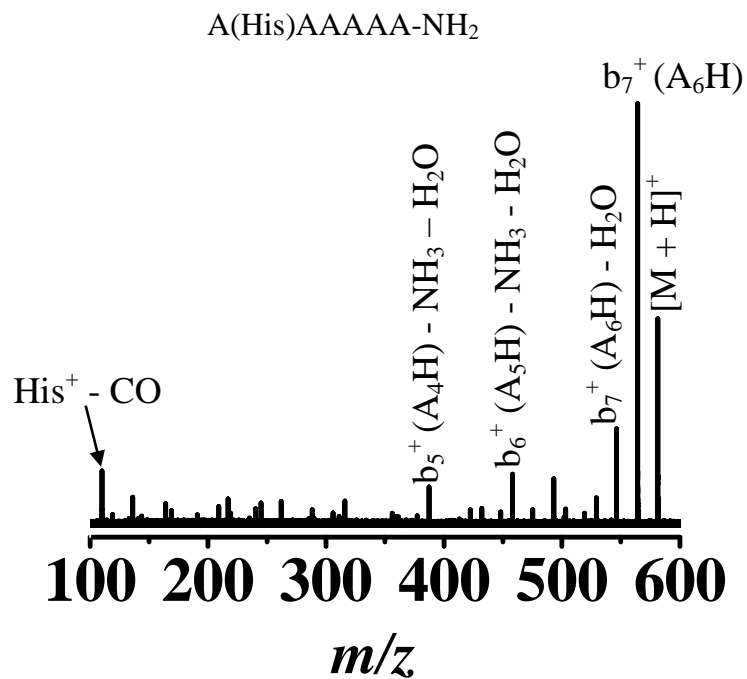


Figure A.1. Sustained off-resonance irradiation-collision induced dissociation (SORI-CID) FT-ICR mass spectrum of protonated AHA(AAA)A-NH<sub>2</sub>. SORI-CID parameters:  $\Delta f = \sim 500$  Hz, RF Amplitude = 12 V<sub>base-to-peak</sub>, duration = 262 ms (N<sub>2</sub> was used as collision gas).

Table A.1. Amino acid composition of the observed SORI-CID fragment ions, their theoretical m/z, experimental m/z, and MMA errors for protonated A(His)AAAAA-NH<sub>2</sub> (signal-to-noise threshold for the assigned fragments is higher than ~4). The fragment ion that could exclusively be assigned as scramble ion is shown in *italic font*.

Fragment	Theoretical m/z	Experimental m/z	Error (ppm)
[M + H] <sup>+</sup> - NH <sub>3</sub>	564.2889	564.2887	0.35
[M + H] <sup>+</sup> - NH <sub>3</sub> - H <sub>2</sub> O	546.2783	546.2781	0.37
[M + H] <sup>+</sup> - NH <sub>3</sub> - CO	536.2940	536.2970	-5.59
[M + H] <sup>+</sup> - NH <sub>3</sub> - NH <sub>3</sub> - H <sub>2</sub> O	529.2518	529.2518	0.00
[M + H] <sup>+</sup> - NH <sub>3</sub> - NH <sub>3</sub> - CO	519.2674	519.2669	0.96
[M + H] <sup>+</sup> - NH <sub>3</sub> - NH <sub>3</sub> - H <sub>2</sub> O - C <sub>2</sub> H <sub>2</sub>	503.2361	503.2355	1.19
[M + H] <sup>+</sup> - NH <sub>3</sub> - NH <sub>3</sub> - H <sub>2</sub> O - CO	501.2568	501.2562	1.20
[A <sub>5</sub> H] <sup>+</sup>	493.2518	493.2516	0.41
[A <sub>5</sub> H] <sup>+</sup> - H <sub>2</sub> O	475.2412	475.2410	0.42
[A <sub>5</sub> H] <sup>+</sup> - H <sub>2</sub> O - NH <sub>3</sub>	458.2146	458.2145	0.22
[A <sub>5</sub> H] <sup>+</sup> - NH <sub>3</sub> - CO	448.2303	448.2302	0.22
[A <sub>5</sub> H] <sup>+</sup> - NH <sub>3</sub> - H <sub>2</sub> O - C <sub>2</sub> H <sub>2</sub>	432.1990	432.1989	0.23
<i>[AAAAAA]<sup>+</sup></i>	<i>427.2300</i>	<i>427.2319</i>	<i>-4.45</i>
[A <sub>4</sub> H] <sup>+</sup>	422.2146	422.2145	0.24
[A <sub>4</sub> H] <sup>+</sup> - H <sub>2</sub> O - NH <sub>3</sub>	387.1775	387.1773	0.52
[A <sub>4</sub> H] <sup>+</sup> - NH <sub>3</sub> - CO	377.1932	377.1934	-0.53
[A <sub>4</sub> H] <sup>+</sup> - H <sub>2</sub> O - NH <sub>3</sub> - C <sub>2</sub> H <sub>2</sub>	361.1619	361.1617	0.55
[A <sub>4</sub> H] <sup>+</sup> - NH <sub>3</sub> - H <sub>2</sub> O - CO	359.1826	359.1828	-0.56
[AAAAA] <sup>+</sup>	356.1929	356.1928	0.28
[A <sub>3</sub> H] <sup>+</sup>	351.1775	351.1776	-0.28
[A <sub>3</sub> H] <sup>+</sup> - NH <sub>3</sub> - H <sub>2</sub> O	316.1404	316.1402	0.63
[AAAAA] - NH <sub>3</sub> - CO	311.1714	311.1713	0.32
[A <sub>3</sub> H] <sup>+</sup> - H <sub>2</sub> O - HCN	306.1561	306.1559	0.65
[A <sub>3</sub> H] <sup>+</sup> - NH <sub>3</sub> - H <sub>2</sub> O - C <sub>2</sub> H <sub>2</sub>	290.1248	290.1246	0.69
[A <sub>3</sub> H] <sup>+</sup> - H <sub>2</sub> O - NH <sub>3</sub> - CO	288.1455	288.1454	0.35
[AAAA] <sup>+</sup>	285.1557	285.1557	0.00
[A <sub>2</sub> H] <sup>+</sup>	280.1404	280.1403	0.36
[A <sub>2</sub> H] <sup>+</sup> - H <sub>2</sub> O	262.1304	262.1297	2.67
[A <sub>2</sub> H] <sup>+</sup> - H <sub>2</sub> O - NH <sub>3</sub>	245.1039	245.1032	2.86
[AAAA] <sup>+</sup> - NH <sub>3</sub> - CO	240.1343	240.1342	0.42
[A <sub>2</sub> H] <sup>+</sup> - NH <sub>3</sub> - CO	235.1190	235.1189	0.43
[A <sub>2</sub> H] <sup>+</sup> - NH <sub>3</sub> - H <sub>2</sub> O - C <sub>2</sub> H <sub>2</sub>	219.0877	219.0876	0.46
[A <sub>2</sub> H] <sup>+</sup> - NH <sub>3</sub> - H <sub>2</sub> O - CO	217.1084	217.1083	0.46
[AH] <sup>+</sup>	209.1033	209.1032	0.48
[AH] <sup>+</sup> - NH <sub>3</sub>	192.0773	192.0766	3.64
[AH] <sup>+</sup> - H <sub>2</sub> O	191.0927	191.0926	0.52
[AAA] <sup>+</sup> - CO - NH <sub>3</sub>	169.0972	169.0971	0.59
[AH] <sup>+</sup> - NH <sub>3</sub> - CO	164.0818	164.0818	0.00
[AAA] <sup>+</sup> - H <sub>2</sub> O - CO - HCN	141.1022	141.1033	-7.80
[AH] <sup>+</sup> - H <sub>2</sub> O - CO - HCN	136.0869	136.0869	0.00
[AH] <sup>+</sup> - NH <sub>3</sub> - H <sub>2</sub> O - CO - HCN	119.0604	119.0604	0.00
[H] <sup>+</sup> - CO	110.0713	110.0713	0.00

AAA(His)AAA-NH<sub>2</sub>

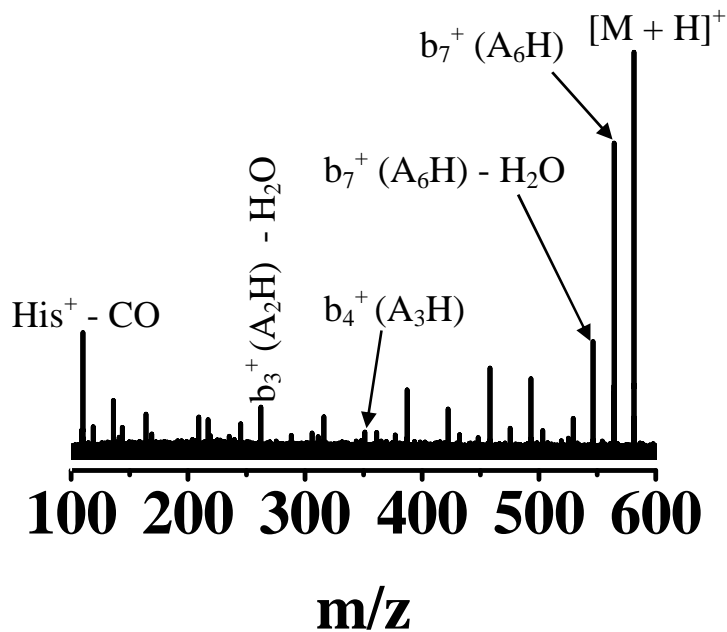


Figure A.2. Sustained off-resonance irradiation-collision induced dissociation (SORI-CID) FT-ICR mass spectrum of protonated AAA(His)AAA-NH<sub>2</sub>. SORI-CID parameters:  $\Delta f = \sim 500$  Hz, RF Amplitude = 12 V<sub>base-to-peak</sub>, duration = 262 ms (N<sub>2</sub> was used as collision gas).

Table A.2. Amino acid composition of the observed SORI-CID fragment ions, their theoretical m/z, experimental m/z, and MMA errors for protonated AAA(His)AAA-NH<sub>2</sub> (signal-to-noise threshold for the assigned fragments is higher than ~4). The two fragment ions that could exclusively be assigned as scramble ions are shown in *italic* font.

Fragment	Theoretical m/z	Experimental m/z	Error (ppm)
[M + H] <sup>+</sup> - NH <sub>3</sub>	564.2889	564.2892	-0.53
[M + H] <sup>+</sup> - NH <sub>3</sub> - H <sub>2</sub> O	546.2783	546.2787	-0.73
[M + H] <sup>+</sup> - NH <sub>3</sub> - NH <sub>3</sub> - H <sub>2</sub> O	529.2518	529.2525	-1.32
[M + H] <sup>+</sup> - NH <sub>3</sub> - NH <sub>3</sub> - CO	519.2674	519.2634	7.70
[M + H] <sup>+</sup> - NH <sub>3</sub> - NH <sub>3</sub> - H <sub>2</sub> O - C <sub>2</sub> H <sub>2</sub>	503.2361	503.2363	-0.40
[A <sub>3</sub> H] <sup>+</sup>	493.2518	493.2518	0.00
[A <sub>3</sub> H] <sup>+</sup> - H <sub>2</sub> O	475.2412	475.2422	-2.10
[A <sub>3</sub> H] <sup>+</sup> - NH <sub>3</sub> - H <sub>2</sub> O	458.2146	458.2147	-0.22
[A <sub>3</sub> H] <sup>+</sup> - NH <sub>3</sub> - CO	448.2303	448.2302	0.22
[A <sub>3</sub> H] <sup>+</sup> - NH <sub>3</sub> - H <sub>2</sub> O - C <sub>2</sub> H <sub>2</sub>	432.1990	432.1993	-0.69
[A <sub>4</sub> H] <sup>+</sup>	422.2146	422.2149	-0.71
[A <sub>4</sub> H] <sup>+</sup> - H <sub>2</sub> O	404.2041	404.2036	1.24
[A <sub>4</sub> H] <sup>+</sup> - H <sub>2</sub> O - NH <sub>3</sub>	387.1775	387.1776	-0.26
[A <sub>4</sub> H] <sup>+</sup> - NH <sub>3</sub> - CO	377.1932	377.1932	0.00
[A <sub>4</sub> H] <sup>+</sup> - H <sub>2</sub> O - NH <sub>3</sub> - C <sub>2</sub> H <sub>2</sub>	361.1619	361.1616	0.83
[A <sub>4</sub> H] <sup>+</sup> - NH <sub>3</sub> - H <sub>2</sub> O - CO	359.1826	359.1829	-0.84
[A <sub>3</sub> H] <sup>+</sup>	351.1775	351.1778	-0.85
[A <sub>3</sub> H] <sup>+</sup> - NH <sub>3</sub> - H <sub>2</sub> O	316.1404	316.1403	0.32
[AAAA] <sup>+</sup> - NH <sub>3</sub> - CO	<i>311.1714</i>	<i>311.1711</i>	<i>0.96</i>
[A <sub>3</sub> H] <sup>+</sup> - H <sub>2</sub> O - HCN	306.1561	306.1558	0.98
[A <sub>3</sub> H] <sup>+</sup> - NH <sub>3</sub> - H <sub>2</sub> O - C <sub>2</sub> H <sub>2</sub>	290.1248	290.1246	0.69
[A <sub>3</sub> H] <sup>+</sup> - H <sub>2</sub> O - NH <sub>3</sub> - CO	288.1455	288.1453	0.69
[AAH] <sup>+</sup> - H <sub>2</sub> O	262.1304	262.1297	2.67
[AAH] <sup>+</sup> - NH <sub>3</sub> - H <sub>2</sub> O	245.1039	245.1033	2.45
[AAAA] <sup>+</sup> - CO - NH <sub>3</sub>	<i>240.1343</i>	<i>240.1343</i>	<i>0.00</i>
[AAH] <sup>+</sup> - NH <sub>3</sub> - CO	235.1190	235.1186	1.70
[AAH] <sup>+</sup> - NH <sub>3</sub> - H <sub>2</sub> O - C <sub>2</sub> H <sub>2</sub>	219.0877	219.0876	0.46
[AAH] <sup>+</sup> - NH <sub>3</sub> - H <sub>2</sub> O - CO	217.1084	217.1083	0.46
[AH] <sup>+</sup>	209.1033	209.1034	-0.48
[AH] <sup>+</sup> - NH <sub>3</sub> - CO	164.0818	164.0818	0.00
[AAA] <sup>+</sup> - H <sub>2</sub> O - HCN - CO	141.1022	141.1022	0.00
[AH] <sup>+</sup> - H <sub>2</sub> O - HCN - CO	136.0869	136.0869	0.00
[AH] <sup>+</sup> - NH <sub>3</sub> - H <sub>2</sub> O - CO - HCN	119.0604	119.0604	0.00
[H] <sup>+</sup> - CO	110.0713	110.0713	0.00

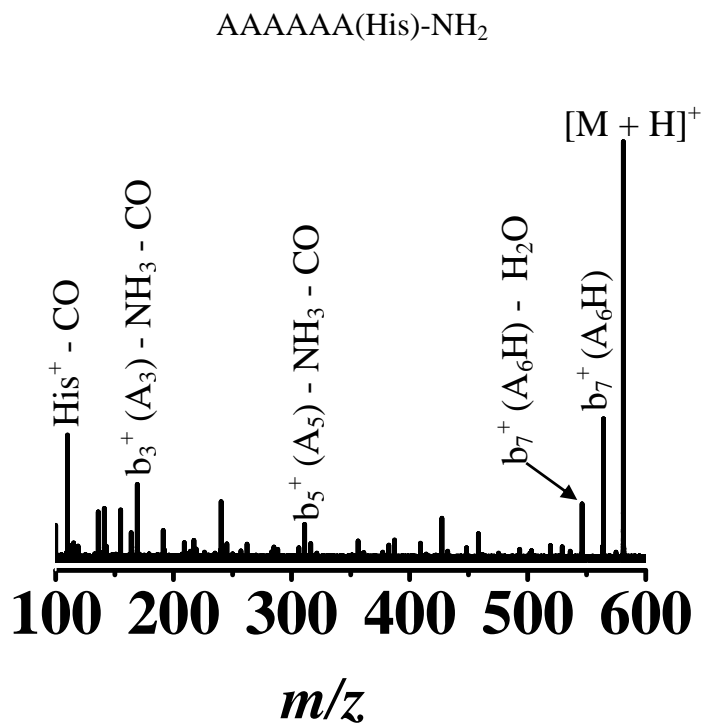


Figure A.3. Sustained off-resonance irradiation-collision induced dissociation (SORI-CID) FT-ICR mass spectrum of protonated AAAAAA(His)-NH<sub>2</sub>. SORI-CID parameters:  $\Delta f = \sim 500$  Hz, RF Amplitude = 12 V<sub>base-to-peak</sub>, duration = 262 ms (N<sub>2</sub> was used as collision gas).

Table A.3. Amino acid composition of the observed SORI-CID fragment ions, their theoretical m/z, experimental m/z, and MMA errors for protonated AAAAAA(His)-NH<sub>2</sub> (signal-to-noise threshold for the assigned fragments is higher than ~4).

Fragment	Theoretical m/z	Experimental m/z	Error (ppm)
[M + H] <sup>+</sup> - NH <sub>3</sub>	564.2889	564.2889	0.00
[M + H] <sup>+</sup> - H <sub>2</sub> O	563.3049	563.3043	1.07
[M + H] <sup>+</sup> - NH <sub>3</sub> - H <sub>2</sub> O	546.2783	546.2784	-0.18
[M + H] <sup>+</sup> - NH <sub>3</sub> - CO	536.2940	536.2935	0.93
[M + H] <sup>+</sup> - NH <sub>3</sub> - NH <sub>3</sub> - H <sub>2</sub> O	529.2518	529.2523	-0.94
[M + H] <sup>+</sup> - NH <sub>3</sub> - NH <sub>3</sub> - CO	519.2674	519.2677	-0.58
[M + H] <sup>+</sup> - NH <sub>3</sub> - NH <sub>3</sub> - H <sub>2</sub> O - C <sub>2</sub> H <sub>2</sub>	503.2361	503.2356	0.99
[A <sub>5</sub> H] <sup>+</sup>	493.2518	493.2515	0.61
[A <sub>5</sub> H] <sup>+</sup> - NH <sub>3</sub> - H <sub>2</sub> O	458.2146	458.2146	0.00
[A <sub>5</sub> H] <sup>+</sup> - NH <sub>3</sub> - CO	448.2303	448.2304	-0.22
[A <sub>5</sub> H] <sup>+</sup> - NH <sub>3</sub> - H <sub>2</sub> O - C <sub>2</sub> H	432.1990	432.1986	0.93
[AAAAAA] <sup>+</sup>	427.2300	427.2299	0.23
[A <sub>4</sub> H] <sup>+</sup>	422.2146	422.2137	2.13
[AAAAAA] <sup>+</sup> - H <sub>2</sub> O	409.2194	409.2196	-0.49
[A <sub>4</sub> H] <sup>+</sup> - H <sub>2</sub> O - NH <sub>3</sub>	387.1775	387.1772	0.77
[AAAAAA] <sup>+</sup> - NH <sub>3</sub> - CO	382.2085	382.2084	0.26
[A <sub>4</sub> H] <sup>+</sup> - NH <sub>3</sub> - CO	377.1932	377.1932	0.00
[A <sub>4</sub> H] <sup>+</sup> - H <sub>2</sub> O - NH <sub>3</sub> - C <sub>2</sub> H <sub>2</sub>	361.1619	361.1614	1.38
[AAAAA] <sup>+</sup>	356.1929	356.1929	0.00
[A <sub>3</sub> H] <sup>+</sup>	351.1775	351.1776	-0.28
[A <sub>3</sub> H] <sup>+</sup> - NH <sub>3</sub> - H <sub>2</sub> O	316.1404	316.1402	0.63
[AAAAA] <sup>+</sup> - NH <sub>3</sub> - CO	311.1714	311.1713	0.32
[A <sub>3</sub> H] <sup>+</sup> - H <sub>2</sub> O - HCN	306.1561	306.1560	0.33
[A <sub>3</sub> H] <sup>+</sup> - H <sub>2</sub> O - NH <sub>3</sub> - CO	288.1455	288.1453	0.69
[AAAA] <sup>+</sup>	285.1557	285.1556	0.35
[AAAAA] <sup>+</sup> - CO - H <sub>2</sub> O - HCN	283.1765	283.1764	0.35
[A <sub>3</sub> H] <sup>+</sup> - H <sub>2</sub> O	262.1304	262.1299	1.91
[AAAA] <sup>+</sup> - CO	257.1608	257.161	-0.78
y <sub>3</sub> [A <sub>2</sub> H] <sup>+</sup> - H <sub>2</sub> O - C <sub>2</sub> H <sub>5</sub>	250.1173	250.1187	-5.60
[A <sub>2</sub> H] <sup>+</sup> - NH <sub>3</sub> - H <sub>2</sub> O	245.1039	245.1033	2.45
[AAAA] <sup>+</sup> - CO - NH <sub>3</sub>	240.1343	240.1342	0.42
[A <sub>2</sub> H] <sup>+</sup> - NH <sub>3</sub> - CO	235.1190	235.1188	0.85
y <sub>2</sub> [AH] <sup>+</sup>	226.1299	226.1298	0.44
[A <sub>2</sub> H] <sup>+</sup> - NH <sub>3</sub> - H <sub>2</sub> O - C <sub>2</sub> H <sub>2</sub>	219.0877	219.0877	0.00
[A <sub>2</sub> H] <sup>+</sup> - NH <sub>3</sub> - H <sub>2</sub> O - CO	217.1084	217.1082	0.92
[AAA] <sup>+</sup>	214.1186	214.1186	0.00
[AH] <sup>+</sup>	209.1033	209.1032	0.48
[AH] <sup>+</sup> - NH <sub>3</sub>	192.0773	192.0768	2.60
[AH] <sup>+</sup> - H <sub>2</sub> O	191.0927	191.0927	0.00
[AAA] <sup>+</sup> - CO - NH <sub>3</sub>	169.0972	169.0971	0.59
[AH] <sup>+</sup> - NH <sub>3</sub> - CO	164.0818	164.0818	0.00
y <sub>1</sub> [His] <sup>+</sup>	155.0927	155.0927	0.00
[AA] <sup>+</sup> - H <sub>2</sub> O - NH <sub>3</sub> - C <sub>2</sub> H <sub>2</sub>	153.0659	153.0659	0.00
[AAA] <sup>+</sup> - H <sub>2</sub> O - HCN - CO	141.1022	141.1023	-0.71
[His] <sup>+</sup>	138.0662	138.0661	0.72
[AH] <sup>+</sup> - H <sub>2</sub> O - HCN - CO	136.0869	136.0869	0.00
[AH] <sup>+</sup> - NH <sub>3</sub> - H <sub>2</sub> O - CO - HCN	119.0604	119.0603	0.84
[AA] <sup>+</sup> - CO	115.0866	115.0866	0.00
[His] <sup>+</sup> - CO	110.0713	110.0713	0.00

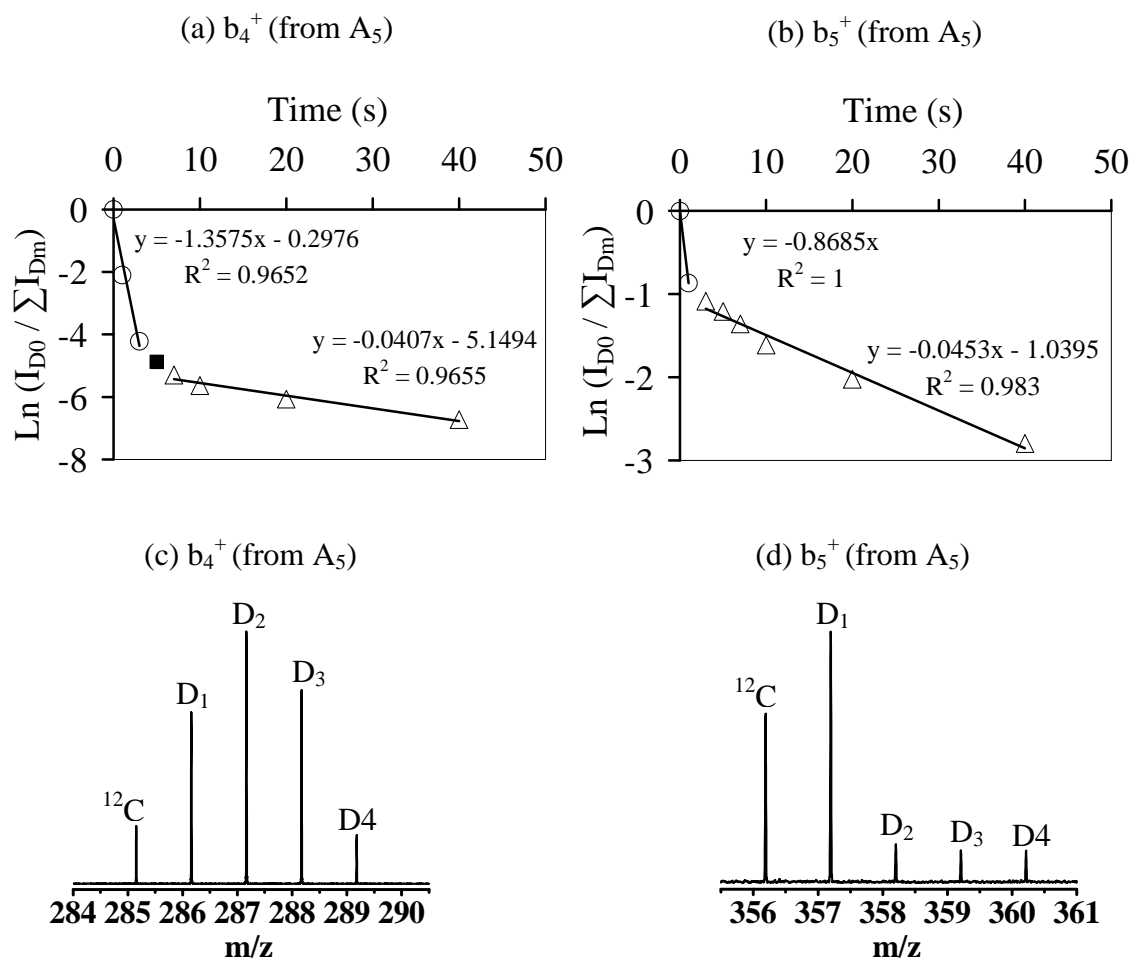


Figure A.4. Semi-log plots of  $\ln(D_0/D_m)$  vs. H/D exchange reaction time for (a)  $b_4^+$ , (b)  $b_5^+$  fragment ions of pentaalanine ( $A_5$ ). The empty circles ( $\circ$ ) and triangles ( $\Delta$ ) in the semi-log plots show the segments corresponding to “fast” + “slow” and “slow” H/D-exchanging populations, respectively. The fitted linear equations for each segment are shown in the plots. The filled square ( $\blacksquare$ ) in the semi-log plot in panel (a) corresponds to H/D exchange data which were not used for linear fitting. The mass spectra in panels (c) and (d) are the H/D exchange isotopic patterns (after 100 ms reaction time) of mass isolated  $^{12}C_{12}$  ion populations of  $b_4^+$  and  $b_5^+$ , respectively.  $CH_3OD$  (at pressure of  $3.5 \times 10^{-5}$  Torr) was used as deuterating reagent.

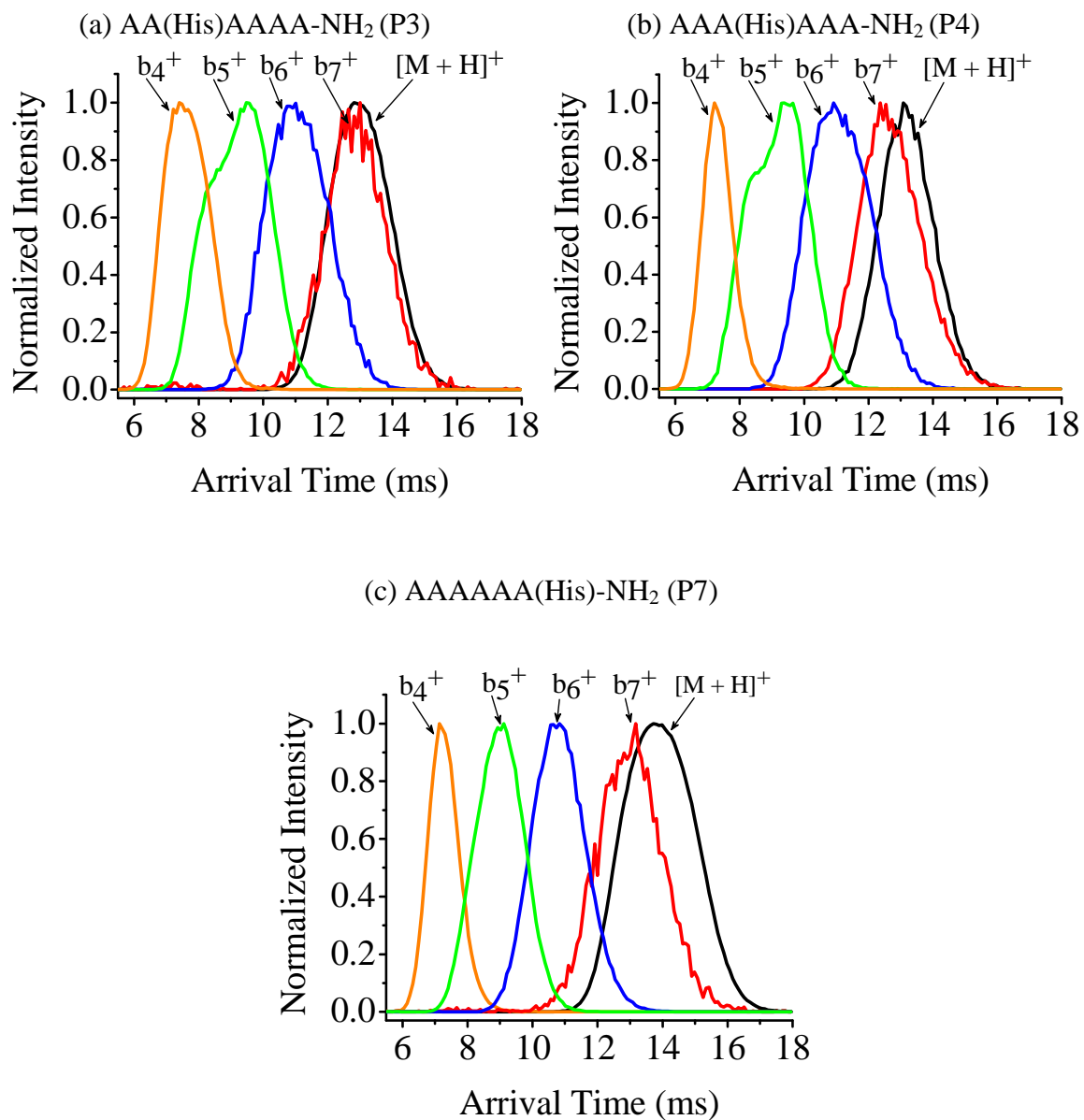


Figure A.5. Ion mobility arrival time distributions (ATDs) acquired for molecular ions (*i.e.*, [M + H]<sup>+</sup>) and the histidine-containing b<sub>n</sub><sup>+</sup> (n = 4-7) fragment ions of (a) AA(His)AAAA-NH<sub>2</sub> (P3), (b) AAA(His)AAA-NH<sub>2</sub> (P4), and (c) AAAAAA(His)-NH<sub>2</sub> (P7).

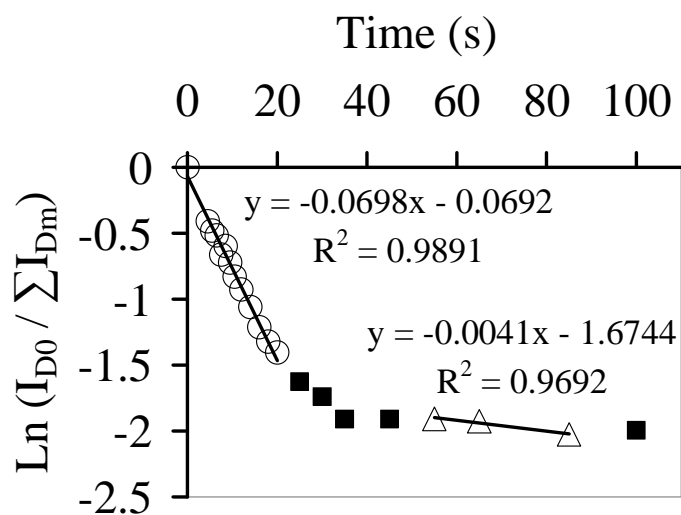


Figure A.6. Semi-log plots of  $\ln(D_0/D_m)$  vs. H/D exchange reaction time for  $b_5^+$  fragment ions of AA(His)AAAA-NH<sub>2</sub>. The empty circles (○) and triangles (Δ) in the semi-log plots show the segments corresponding to “fast” + “slow” and “slow” H/D-exchanging populations, respectively. The fitted linear equations for each segment are shown in the plots. The filled squares (■) in the semi-log plots correspond to H/D exchange data which were not used for linear fitting. ND<sub>3</sub> (at pressure of  $\sim 4.0 \times 10^{-8}$  Torr) was used as deuterating reagent.

## APPENDIX B

### Evidence for Sequence Scrambling in Collision-Induced Dissociation of $\gamma$ -Type Fragment Ions

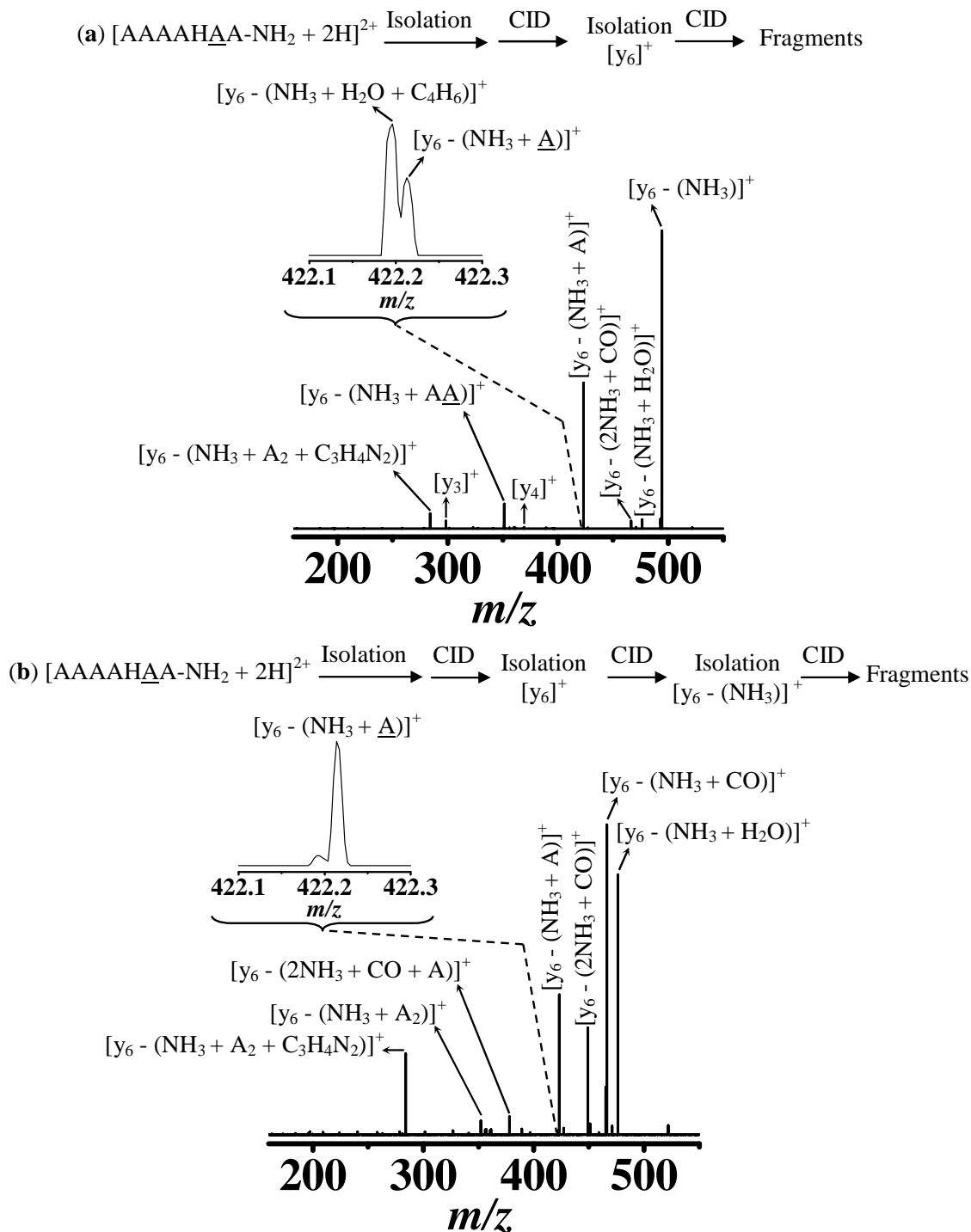


Figure B.1. Collision-induced dissociation (CID) mass spectra of the  $m/z$ -isolated (a)  $[y_6]^+$  ( $m/z$  511) (generated from CID of doubly charged  $AAAAH\underline{A}A-NH_2$ ) and (b)  $[y_6 - (NH_3)]^+$  ( $m/z$  494) (generated from CID of  $[y_6]^+$ ) at 20 % normalized collision energy. Insets in panels (a) and (b) show the expanded views of  $m/z$  range of 422.1 to 422.3 corresponding to identified sequence scrambled fragment ion (*i.e.*,  $[y_6 - (NH_3 + \underline{A})]^+$ ) with mass measurement errors of 4.2 and 0.5 ppm, respectively.

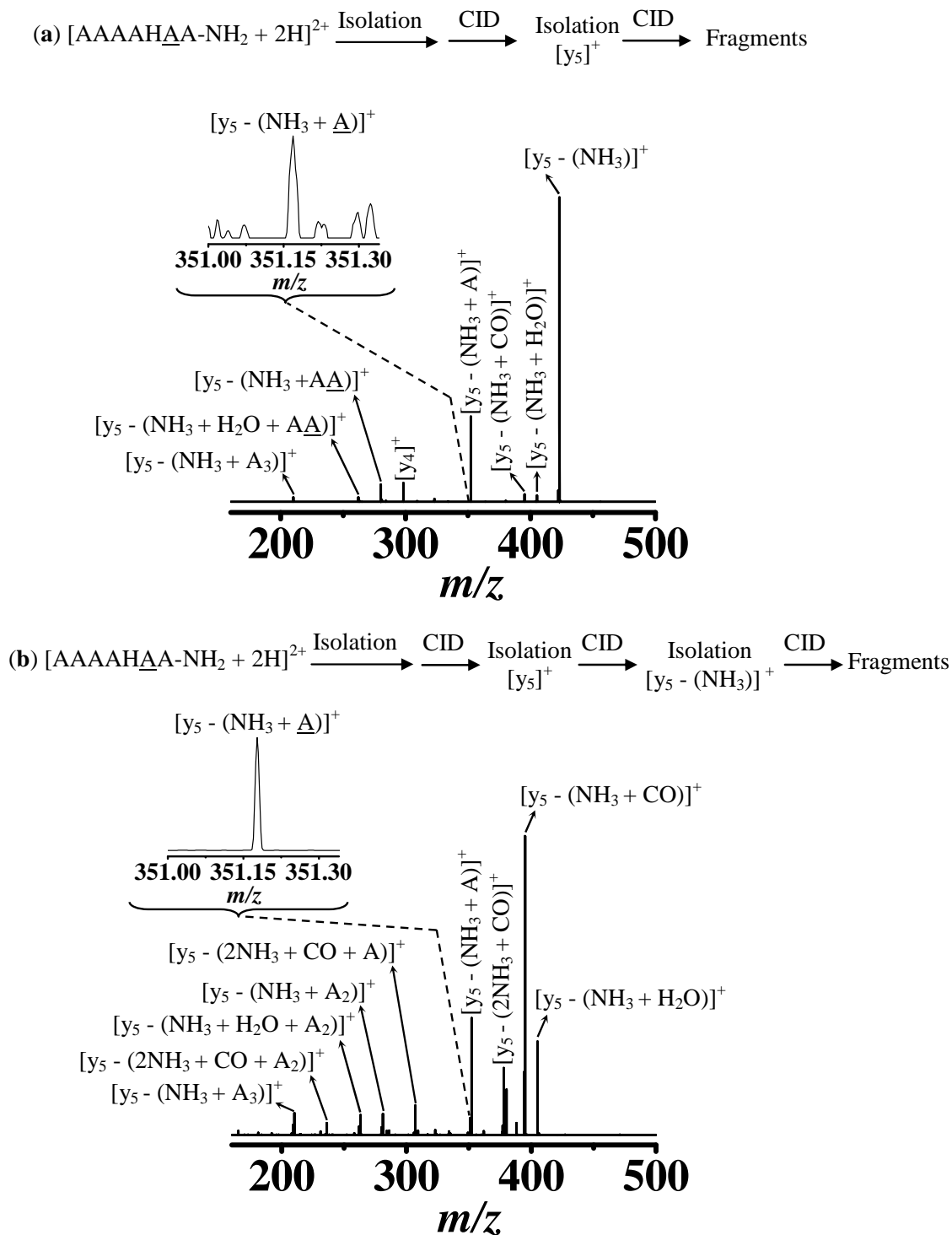


Figure B.2. Collision-induced dissociation (CID) mass spectra of the  $m/z$ -isolated (a)  $[\text{y}_5]^+$  ( $m/z$  440) (generated from CID of doubly charged AAAAHAA-NH<sub>2</sub>) and (b)  $[\text{y}_5 - (\text{NH}_3)]^+$  ( $m/z$  423) (generated from CID of  $[\text{y}_6]^+$ ) at 20 % normalized collision energy. Insets in panels (a) and (b) show the expanded views of  $m/z$  range of 351.0 to 351.3 corresponding to identified sequence scrambled fragment ion (*i.e.*,  $[\text{y}_5 - (\text{NH}_3 + \underline{\text{A}})]^+$ ) with mass measurement errors  $\sim$  3.3 and 0.1 ppm respectively.

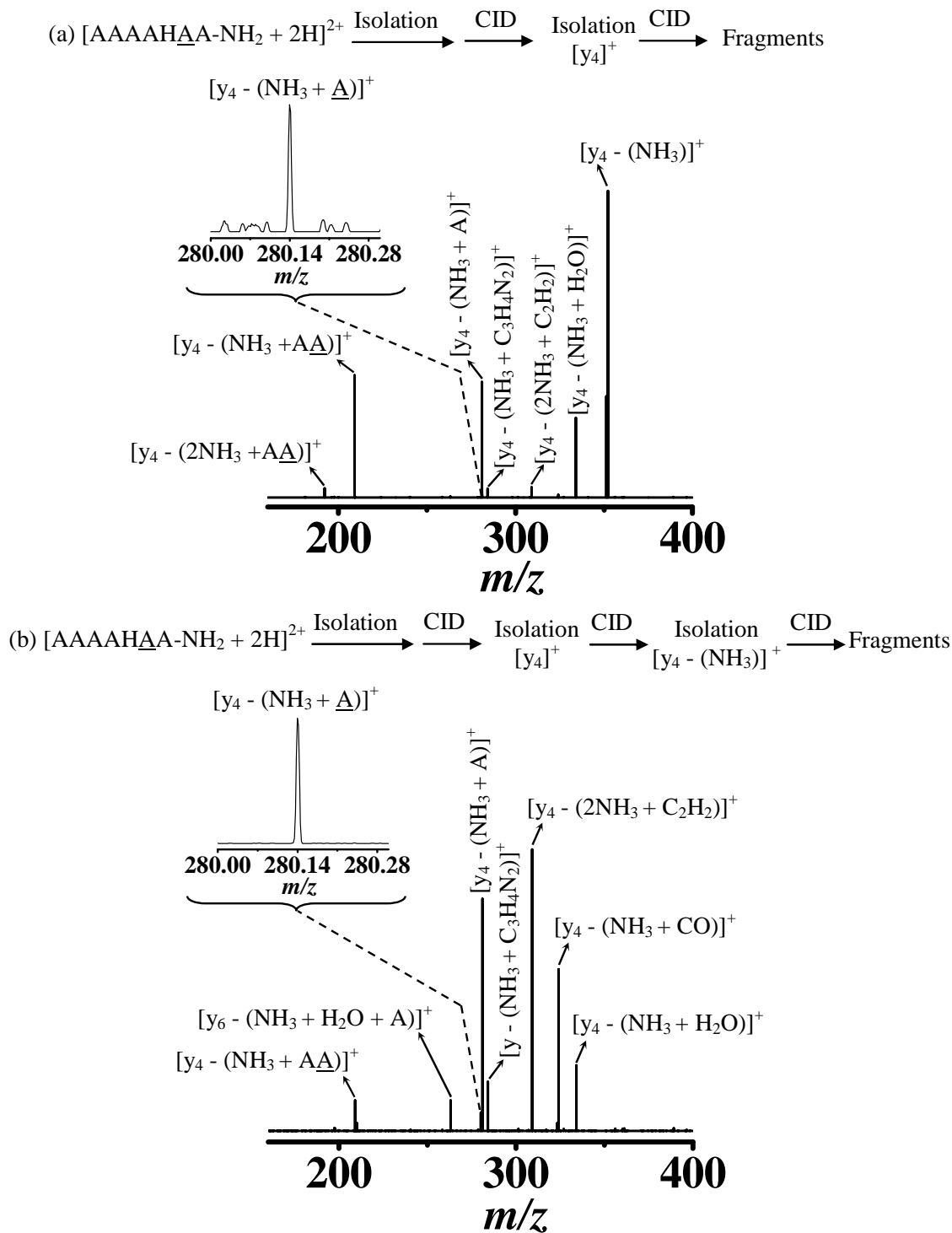


Figure B.3. Collision-induced dissociation (CID) mass spectra of the  $m/z$ -isolated (a)  $[y_4]^+$  ( $m/z$  440) (generated from CID of doubly charged  $AAAAH\underline{AA}-NH_2$ ) and (b)  $[y_4 - (NH_3)]^+$  ( $m/z$  423) (generated from CID of  $[y_4]^+$ ) at 20 % normalized collision energy. Insets in panels (a) and (b) show the expanded views of  $m/z$  range of 351.0 to 351.3 corresponding to identified sequence scrambled fragment ion (*i.e.*,  $[y_4 - (NH_3 + \underline{A})]^+$ ) with mass measurement accuracy of 0.5 and 0.4 ppm respectively.

Table B.1. Fragment ion identity, theoretically calculated  $m/z$  values, experimentally observed  $m/z$  values, and error (ppm) of the assigned fragment ions observed in CID mass spectrum of  $[y_7]^{+2}$  (FRWGKPV-NH<sub>2</sub>) from des-acetylated- $\alpha$ -melanocyte. The sequence-scrambled fragment ions are shown in *italic* font.

Identity of fragment ion	Theoretical $m/z$	Experimental $m/z$	Error (ppm)
$[y_7 - (\text{NH}_3 + \text{CO} + \text{FRWGK})]^+$	169.1335	169.1335	0.00
$[y_7 - (\text{NH}_3 + \text{FRWGK})]^+$	197.1285	197.1284	0.51
$[y_2]^+$	214.1550	214.1550	0.00
$[y_7 - (2\text{NH}_3 + \text{WGKPV})]^+$	287.1503	287.1503	0.00
$[y_7 - (\text{NH}_3 + \text{WGKPV})]^+$	304.1768	304.1769	0.33
$[y_7 - (\text{NH}_3 + \text{FRWG})]^+$	325.2234	325.2235	0.31
$[y_7 - (\text{NH}_3 + \text{PV})]^{+2}$	338.1899	338.1897	0.59
$[y_7 - (\text{NH}_3 + \text{H}_2\text{O} + \text{V})]^{+2}$	377.7110	377.7110	0.00
$[y_7 - (\text{NH}_3 + \text{FRW})]^+$	382.2449	382.2453	1.05
$[y_7 - (\text{NH}_3 + \text{V})]^{+2}$	386.7163	386.7163	0.00
<i><math>[y_7 - (\text{NH}_3 + \text{P})]^{+2}</math></i>	<i>387.7241</i>	<i>387.7248</i>	<i>1.81</i>
$[y_7 - (\text{NH}_3 + \text{CO})]^{+2}$	422.2530	422.2530	0.00
$[y_7 - (\text{NH}_3 + \text{H}_2\text{O})]^{+2}$	427.2452	427.2449	0.70
$[y_7 - (\text{NH}_3)]^{+2}$	436.2505	436.2505	0.00
$[y_7 - (\text{NH}_3 + \text{GKPV})]^+$	490.2561	490.2563	0.41
$[y_7 - (\text{NH}_3 + \text{KPV})]^+$	547.2776	547.2775	0.18
$[y_7 - (\text{KPV})]^+$	564.3041	564.3038	0.53
$[y_7 - (\text{NH}_3 + \text{FR})]^+$	568.3242	568.3240	0.35
$[y_5]^+$	585.3507	585.3503	0.68
$[y_7 - (\text{NH}_3 + \text{PV})]^+$	675.3725	675.3721	0.59
$[y_7 - (\text{NH}_3 + \text{F})]^+$	724.4253	724.4274	2.90
<i><math>[y_7 - (\text{NH}_3 + \text{P})]^+</math></i>	<i>774.4410</i>	<i>774.4406</i>	<i>0.52</i>

Table B.2. Fragment ion identity, theoretically calculated  $m/z$  values, experimentally observed  $m/z$  values, and error (ppm) of the assigned fragment ions observed in CID mass spectrum of  $[y_7 - (\text{NH}_3)]^{+2}$  from des-acetylated- $\alpha$ -melanocyte. The sequence-scrambled fragment ion is shown in *italic* font.

Identity of fragment ion	Theoretical $m/z$	Experimental $m/z$	Error (ppm)
$[y_7 - (\text{NH}_3 + \text{CO} + \text{FRWGK})]^+$	169.1335	169.1335	0.00
$[y_7 - (\text{NH}_3 + \text{FRWGK})]^+$	197.1285	197.1286	0.51
$[y_7 - (2\text{NH}_3 + \text{WGKPV})]^+$	287.1503	287.1505	0.70
$[y_7 - (\text{NH}_3 + \text{WGKPV})]^+$	304.1768	304.1768	0.00
$[y_7 - (\text{NH}_3 + \text{FRWG})]^+$	325.2234	325.2231	0.92
$[y_7 - (\text{NH}_3 + \text{V})]^{+2}$	386.7163	386.7164	0.26
<i><math>[y_7 - (\text{NH}_3 + \text{P})]^{+2}</math></i>	<i>387.7241</i>	<i>387.7242</i>	<i>0.36</i>
$[y_7 - (\text{NH}_3 + \text{CO})]^{+2}$	422.2530	422.2529	0.24
$[y_7 - (\text{NH}_3 + \text{H}_2\text{O})]^{+2}$	427.2452	427.2453	0.23
$[y_7 - (2\text{NH}_3)]^{+2}$	427.7372	427.7380	1.87
$[y_7 - (\text{NH}_3 + \text{GKPV})]^+$	490.2561	490.2561	0.00
$[y_7 - (\text{NH}_3 + \text{KPV})]^+$	547.2776	547.2770	1.10
$[y_7 - (\text{KPV})]^+$	564.3041	564.3041	0.00
$[y_7 - (\text{NH}_3 + \text{FR})]^+$	568.3242	568.3235	1.23
$[y_7 - (\text{NH}_3 + \text{PV})]^+$	675.3725	675.3721	0.59
<i><math>[y_7 - (\text{NH}_3 + \text{P})]^+</math></i>	<i>774.4410</i>	<i>774.4404</i>	<i>0.77</i>

Table B.3. Fragment ion identity, theoretically calculated  $m/z$  values, experimentally observed  $m/z$  values, and error (ppm) of the assigned fragment ions observed in CID mass spectrum of  $[y_7]^+$  [GVYVHPV] from angiotensin II antipeptide. The sequence-scrambled fragment ions are shown in *italic font*.

Identity of fragment ion	Theoretical $m/z$	Experimental $m/z$	Error (ppm)
$[y_7 - (\text{H}_2\text{O} + \text{GVYVV})]^+$	235.1190	235.1190	0.13
$[y_7 - (\text{H}_2\text{O} + \text{CO} + \text{GVHPV})]^+$	235.1441	235.1441	0.00
$[y_7 - (\text{H}_2\text{O} + \text{GVYPV})]^+$	237.1346	237.1346	0.00
<i><math>[y_7 - (\text{H}_2\text{O} + \text{NH}_3 + \text{CO} + \text{VYPV})]^+</math></i>	<i>249.1346</i>	<i>249.1346</i>	<i>0.04</i>
$[y_7 - (\text{H}_2\text{O} + \text{GVHPV})]^+$	263.1390	263.1391	0.11
<i><math>[y_7 - (2\text{H}_2\text{O} + \text{YVPV})]^+</math></i>	<i>276.1455</i>	<i>276.1455</i>	<i>0.07</i>
$[y_7 - (2\text{H}_2\text{O} + \text{CO} + \text{GVYV})]^+$	288.1819	288.1819	0.10
<i><math>[y_7 - (\text{H}_2\text{O} + \text{YVPV})]^+</math></i>	<i>294.1561</i>	<i>294.1561</i>	<i>0.20</i>
$[y_7 - (3\text{H}_2\text{O} + \text{GVYV})]^+$	298.1662	298.1663	0.27
$[y_7 - (2\text{H}_2\text{O} + \text{GVYV})]^+$	316.1768	316.1768	0.13
$[y_7 - (\text{H}_2\text{O} + \text{NH}_3 + \text{CO} + \text{GHPV})]^+$	317.1860	317.1864	1.20
$[y_7 - (\text{H}_2\text{O} + \text{VHPV})]^+$	320.1605	320.1606	0.28
$[y_7 - (\text{H}_2\text{O} + \text{GVYV})]^+$	334.1874	334.1875	0.36
$[y_3]^+$	352.1979	352.1981	0.37
$[y_7 - (\text{H}_2\text{O} + \text{GHPV})]^+$	362.2074	362.2075	0.30
<i><math>[y_7 - (\text{H}_2\text{O} + \text{CO} + \text{YPV})]^+</math></i>	<i>365.2296</i>	<i>365.2295</i>	<i>0.16</i>
$[y_7 - (\text{H}_2\text{O} + \text{C}_2\text{H}_2\text{N}_2 + \text{GVY})]^+$	379.2340	379.2341	0.18
$[y_7 - (2\text{H}_2\text{O} + \text{GVPV})]^+$	382.1874	382.1876	0.58
$[y_7 - (\text{H}_2\text{O} + \text{CO} + \text{HPV})]^+$	391.2340	391.2341	0.23
<i><math>[y_7 - (\text{H}_2\text{O} + \text{YPV})]^+</math></i>	<i>393.2245</i>	<i>393.2245</i>	<i>0.03</i>
$[y_7 - (\text{H}_2\text{O} + \text{GVPV})]^+$	400.1979	400.1979	0.05
<i><math>[y_7 - (\text{H}_2\text{O} + \text{NH}_3 + \text{CO} + \text{VPV})]^+</math></i>	<i>412.1979</i>	<i>412.1980</i>	<i>0.12</i>
$[y_7 - (\text{H}_2\text{O} + \text{HPV})]^+$	419.2289	419.2289	0.07
$[y_7 - (\text{H}_2\text{O} + \text{C}_8\text{H}_9\text{NO} + \text{PV})]^+$	421.2194	421.2193	0.31
$[y_4]^+$	451.2663	451.2663	0.02
<i><math>[y_7 - (\text{H}_2\text{O} + \text{VPV})]^+</math></i>	<i>457.2194</i>	<i>457.2194</i>	<i>0.11</i>
$[y_7 - (2\text{H}_2\text{O} + \text{NH}_3 + \text{CO} + \text{PV})]^+$	493.2558	493.2558	0.12
$[y_7 - (2\text{H}_2\text{O} + \text{CO} + \text{PV})]^+$	510.2823	510.2822	0.27
$[y_7 - (\text{H}_2\text{O} + \text{NH}_3 + \text{CO} + \text{PV})]^+$	511.2663	511.2662	0.23
$[y_7 - (2\text{H}_2\text{O} + \text{NH}_3 + \text{PV})]^+$	521.2507	521.2505	0.35
$[y_7 - (\text{H}_2\text{O} + \text{CH}_2\text{NH} + \text{PV})]^+$	527.2613	527.2613	0.15
$[y_7 - (\text{H}_2\text{O} + \text{CO} + \text{PV})]^+$	528.2929	528.2927	0.42
$[y_7 - (2\text{H}_2\text{O} + \text{PV})]^+$	538.2772	538.2772	0.11
$[y_7 - (\text{H}_2\text{O} + \text{NH}_3 + \text{PV})]^+$	539.2613	539.2612	0.20
$[y_7 - (\text{H}_2\text{O} + \text{PV})]^+$	556.2878	556.2876	0.45
$[y_3]^+$	614.3297	614.3295	0.33
$[y_7 - (\text{H}_2\text{O} + \text{CO} + \text{V})]^+$	625.3457	625.3453	0.51
$[y_7 - (2\text{H}_2\text{O} + \text{V})]^+$	635.3300	635.3298	0.31
$[y_7 - (\text{H}_2\text{O} + \text{V})]^+$	653.3406	653.3404	0.29
$[y_7 - (\text{V})]^+$	671.3511	671.3509	0.34
$[y_7 - (\text{H}_2\text{O} + \text{CO})]^+$	724.4141	724.4137	0.52
$[y_7 - (2\text{H}_2\text{O})]^+$	734.3984	734.3979	0.76
$[y_7 - (\text{H}_2\text{O} + \text{NH}_3)]^+$	735.3824	735.3820	0.60
$[y_7 - (\text{H}_2\text{O})]^+$	752.4090	752.4086	0.56

Table B.4. Fragment identity, theoretically calculated  $m/z$  values, experimentally observed  $m/z$  values, and error (ppm) of assigned fragment ions observed in CID spectrum of  $[y_7 - (H_2O + PV)]^+$  from angiotensin II anti-peptide. The fragment ions that could be assigned as scrambled ions are shown in *italic* font.

Identity of Fragment ion	Theoretical $m/z$	Experimental $m/z$	Error (ppm)
$[y_7 - (H_2O + CO + GVHPV)]^+$	235.1441	235.1441	0.00
$[y_7 - (H_2O + GVYPV)]^+$	237.1346	237.1347	0.42
<i><math>[y_7 - (H_2O + NH_3 + CO + YVPV)]^+</math></i>	<i>249.1346</i>	<i>249.1347</i>	<i>0.40</i>
$[y_7 - (H_2O + GVHPV)]^+$	263.1390	263.1391	0.38
<i><math>[y_7 - (2H_2O + YVPV)]^+</math></i>	<i>276.1455</i>	<i>276.1456</i>	<i>0.36</i>
<i><math>[y_7 - (H_2O + YVPV)]^+</math></i>	<i>294.1561</i>	<i>294.1561</i>	<i>0.00</i>
$[y_7 - (H_2O + VHPV)]^+$	320.1605	320.1606	0.31
$[y_7 - (H_2O + GHPV)]^+$	362.2074	362.2077	0.83
<i><math>[y_7 - (H_2O + CO + YVPV)]^+</math></i>	<i>365.2296</i>	<i>365.2297</i>	<i>0.27</i>
$[y_7 - (2H_2O + GVPV)]^+$	382.1874	382.1875	0.26
$[y_7 - (H_2O + CO + HPV)]^+$	391.2340	391.2340	0.00
<i><math>[y_7 - (H_2O + YPV)]^+</math></i>	<i>393.2245</i>	<i>393.2246</i>	<i>0.25</i>
$[y_7 - (H_2O + GVPV)]^+$	400.1979	400.1981	0.50
<i><math>[y_7 - (H_2O + NH_3 + CO + VPV)]^+</math></i>	<i>412.1979</i>	<i>412.1981</i>	<i>0.49</i>
$[y_7 - (H_2O + HPV)]^+$	419.2289	419.2291	0.48
$[y_7 - (H_2O + C_8H_9NO + PV)]^+$	421.2194	421.2197	0.71
<i><math>[y_7 - (H_2O + VPV)]^+</math></i>	<i>457.2194</i>	<i>457.2195</i>	<i>0.22</i>
$[y_7 - (2H_2O + NH_3 + CO + PV)]^+$	493.2558	493.2559	0.20
$[y_7 - (2H_2O + CO + PV)]^+$	510.2823	510.2824	0.20
$[y_7 - (H_2O + NH_3 + CO + PV)]^+$	511.2663	511.2666	0.59
$[y_7 - (2H_2O + NH_3 + PV)]^+$	521.2507	521.2508	0.19
$[y_7 - (H_2O + CH_2NH + PV)]^+$	527.2613	527.2614	0.19
$[y_7 - (H_2O + CO + PV)]^+$	528.2929	528.2930	0.19
$[y_7 - (2H_2O + PV)]^+$	538.2772	538.2774	0.37
$[y_7 - (H_2O + NH_3 + PV)]^+$	539.2613	539.2615	0.37

## APPENDIX C

### Structural Dependent Competition between Gas-Phase H/D Ex-change and Adduct Formation Reactions

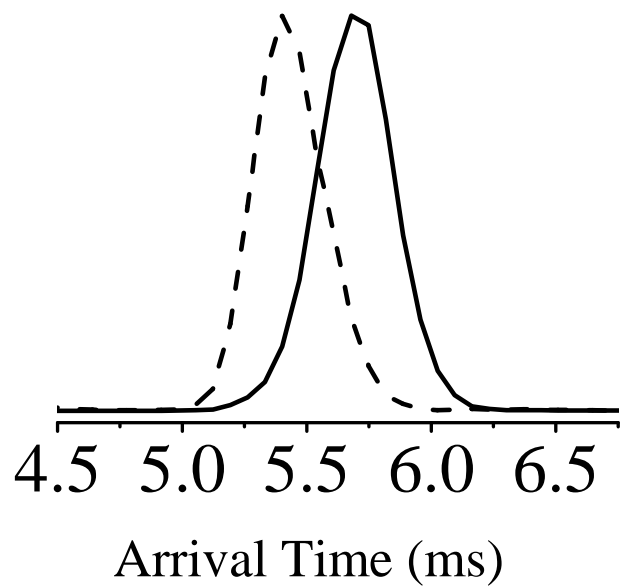


Figure C.1. Overlaid IM profiles of  $[Z-PG + Ca - H]^+$  (dash curve) and  $[Z-PG + K]^+$  (solid curve).

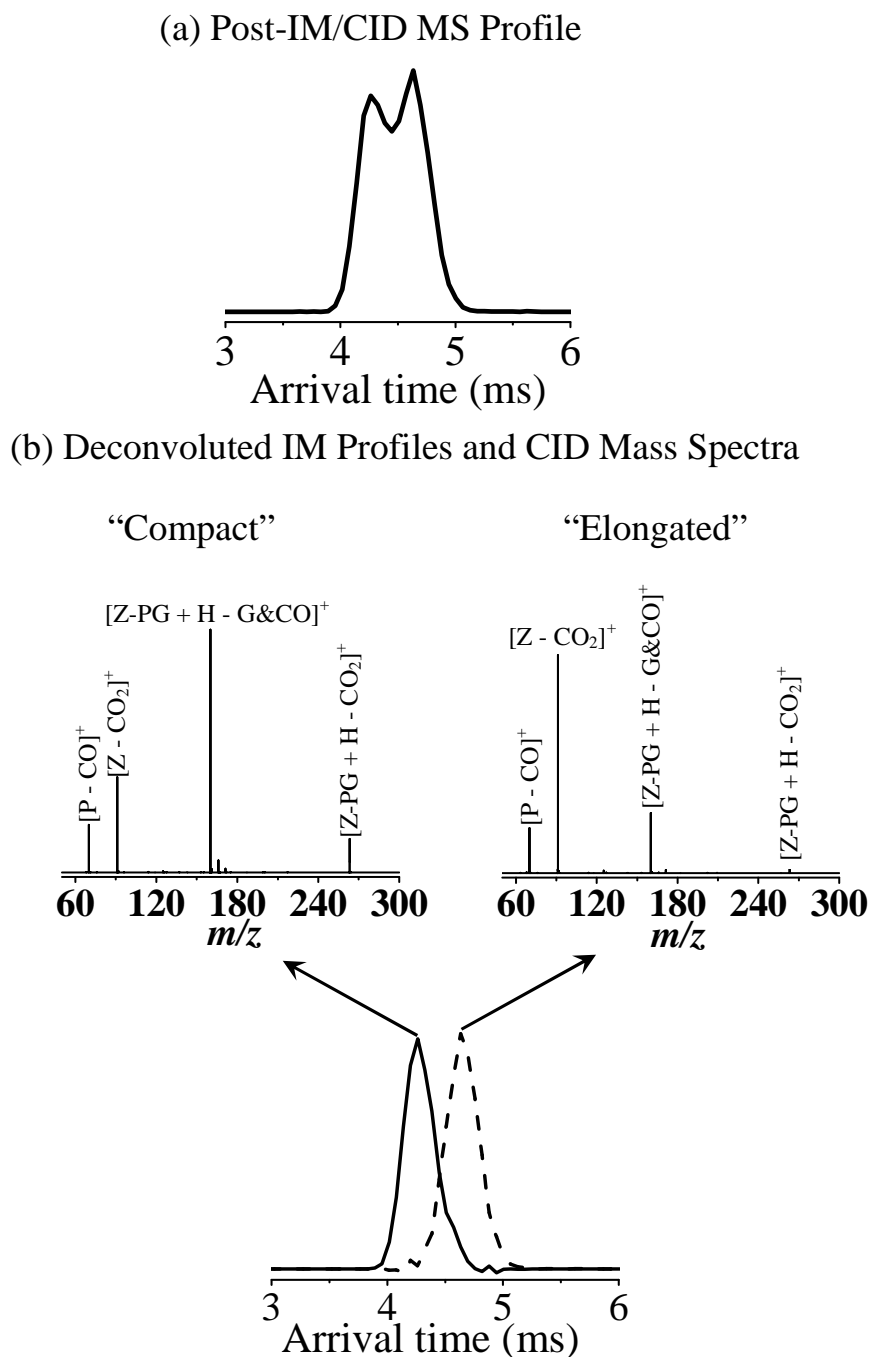


Figure C.2. (a) Post-IM/CID MS profile of  $m/z$ -isolated  $[Z-PG + H - CO_2]^+$ . (b) Deconvoluted IM profiles of “Compact” (solid curve) and “Elongated” (dash curve) conformers of  $[Z-PG + H - CO_2]^+$ . Insets show the deconvoluted CID mass spectra of “Compact” (left) and “Elongated” (right) conformers of  $[Z-PG + H - CO_2]^+$ . A previously reported IM deconvolution technique (*J. Am. Soc. Mass Spectrom.* 2012, 23, 1873-1884) was used to extract pure IM and CID mass spectra of the two  $[Z-PG + H - CO_2]^+$  conformers. Post-IM/CID MS experiment was performed by setting the potential difference between IM cell exit and transfer cell entrance to 28 V. All other parameters are given in experimental section.

## REFERENCES

1. Davidov, E.; Holland, J.; Marple, E.; Naylor, S., Advancing drug discovery through systems biology. *Drug Discov. Today* **2003**, *8*, 175-183.
2. Villoslada, P.; Steinman, L.; Baranzini, S. E., Systems biology and its application to the understanding of neurological diseases. *Ann. Neurol.* **2009**, *65*, 124-139.
3. Kitano, H., Systems biology: A brief overview. *Science* **2002**, *295*, 1662-1664.
4. Weston, A. D.; Hood, L., Systems biology, proteomics, and the future of health care: toward predictive, preventative, and personalized medicine. *J. Proteome Res.* **2004**, *3*, 179-196.
5. Solouki, T.; Miladi, M.; Zekavat, B.; Khalvati, M. A., State-of-the-art chemical analysis of xenobiotics and residues in plant based products: plant proteomics. In *Organic Xenobiotics and Plants: From Mode of Action to Ecophysiology*, Schroeder, P., Ed. Springer-Verlag Berlin Heidelberg: New York, 2010.
6. Lamond, A. I.; Uhlen, M.; Horning, S.; Makarov, A.; Robinson, C. V.; Serrano, L.; Hartl, F. U.; Baumeister, W.; Werenskiold, A. K.; Andersen, J. S.; Vorm, O.; Linial, M.; Aebersold, R.; Mann, M., Advancing cell biology through proteomics in space and time (PROSPECTS). *Mol. Cell. Proteomics* **2012**, *11*, O112 017731-12.
7. Zhang, A.; Sun, H.; Wang, P.; Han, Y.; Wang, X., Modern analytical techniques in metabolomics analysis. *Analyst* **2012**, *137*, 293-300.
8. Andren, P. E.; Emmett, M. R.; Caprioli, R. M., Micro-Electrospray: Zeptomole/attomole per microliter sensitivity for peptides. *J. Am. Soc. Mass Spectrom.* **1994**, *5*, 867-869.
9. Emmett, M. R.; Caprioli, R. M., Micro-electrospray mass spectrometry: Ultra-high-sensitivity analysis of peptides and proteins. *J. Am. Soc. Mass Spectrom.* **1994**, *5*, 605-613.
10. Demirev, P. A.; Fenselau, C., Mass spectrometry for rapid characterization of microorganisms. *Annu. Rev. Anal. Chem.* **2008**, *1*, 71-93.
11. Shevchenko, A.; Chernushevich, I.; Ens, W.; Standing, K. G.; Thomson, B.; Wilm, M.; Mann, M., Rapid 'de novo' peptide sequencing by a combination of nanoelectrospray, isotopic labeling and a quadrupole/time-of-flight mass spectrometer. *Rapid Commun. Mass Spectrom.* **1997**, *11*, 1015-1024.

12. Feng, X.; Liu, X.; Luo, Q.; Liu, B. F., Mass spectrometry in systems biology: an overview. *Mass Spectrom. Rev.* **2008**, *27*, 635-660.
13. Sabido, E.; Selevsek, N.; Aebersold, R., Mass spectrometry-based proteomics for systems biology. *Curr. Opin. Biotechnol.* **2012**, *23*, 591-597.
14. Brodbelt, J. S., Analytical applications of ion-molecule reactions. *Mass Spectrom. Rev.* **1997**, *16*, 91-110.
15. Tasman, H. A.; Boerboom, A. J. H.; Kistemaker, J., Vacuum techniques in conjunction with mass spectrometry. *Vacuum* **1963**, *13*, 33-45.
16. Shukla, A. K.; Futrell, J. H., Tandem mass spectrometry: dissociation of ions by collisional activation. *J. Mass Spectrom.* **2000**, *35*, 1069-1090.
17. Mercer, R. S.; Harrison, A. G., charge inversion and neutralization-reionization mass spectra of some alkoxide ions. *Org. Mass Spectrom.* **1987**, *22*, 710-718.
18. Heiland, W.; Taglauer, E., Low energy ion scattering: Elastic and inelastic effects. *Nucl. Instrum. Methods* **1976**, *132*, 535-545.
19. Yang, S.; Brereton, S. M.; Wheeler, M. D.; Ellis, A. M., Soft or hard ionization of molecules in helium nanodroplets? An electron impact investigation of alcohols and ethers. *Phys. Chem. Chem. Phys.* **2005**, *7*, 4082-4088.
20. Karas, M.; Hillenkamp, F., Laser desorption ionization of proteins with molecular masses exceeding 10,000 daltons. *Anal. Chem.* **1988**, *60*, 2299-2301.
21. Munson, M. S. B.; Field, F. H., Chemical ionization mass spectrometry. I. General introduction. *J. Am. Chem. Soc.* **1966**, *88*, 2621-2630.
22. Dole, M.; Mack, L. L.; Hines, R. L.; Mobley, R. C.; Ferguson, L. D.; Alice, M. B., Molecular beams of macroions. *J. Chem. Phys.* **1968**, *49*, 2240-2249.
23. Whitehouse, C. M.; Dreyer, R. N.; Yamashita, M.; Fenn, J. B., Electrospray interface for liquid chromatographs and mass spectrometers. *Anal. Chem.* **1985**, *57*, 675-679.
24. Fenn, J. B.; Mann, M.; Meng, C. K.; Wong, S. F.; Whitehouse, C. M., Electrospray ionization for mass spectrometry of large biomolecules. *Science* **1989**, *246*, 64-71.
25. Karas, M.; Bachmann, D.; Bahr, U.; Hillenkamp, F., Matrix-assisted ultraviolet laser desorption of non-volatile compounds. *Int. J. Mass Spectrom. Ion Proc.* **1987**, *78*, 53-68.

26. Tanaka, K.; Waki, H.; Ido, Y.; Akita, S.; Yoshida, Y.; Yoshida, T., Protein and polymer analyses up to  $m/z$  100 000 by laser ionization time-of-flight mass spectrometry. *Rapid Commun. Mass Spectrom.* **1988**, 2, 151-153.
27. Macfarlane, R. D.; Torgerson, D. F., Californium-252 plasma desorption mass spectroscopy. *Science* **1976**, 191, 920-925.
28. Barberr, M.; Bordolri, R. S.; Sedgwick, D.; Tyler, A. N., Fast atom bombardment of solids (F.A.B.): a new ion source for mass spectrometry. *J. Chem. Soc., Chem. Commun.* **1981**, 7, 325-327.
29. Benninghoven, A.; Jaspers, D.; Sichtermann, W., Secondary-ion emission of amino acids. *App. Phys.* **1976**, 11, 35-39.
30. [http://www.nobelprize.org/nobel\\_prizes/chemistry/laureates/2002/](http://www.nobelprize.org/nobel_prizes/chemistry/laureates/2002/).
31. Kebarle, P.; Verkerk, U. H., Electrospray: from ions in solution to ions in the gas phase, what we know now. *Mass Spectrom. Rev.* **2009**, 28, 898-917.
32. Beu, S. C.; Senko, M. W.; Quinn, J. P.; Wampler, F. M.; McLafferty, F. W., Fourier-transform electrospray instrumentation for tandem high-resolution mass spectrometry of large molecules. *J. Am. Soc. Mass Spectrom.* **1993**, 4, 557-565.
33. Taflin, D. C.; Ward, T. L.; Davis, E. J., Electrified Droplet Fission and the Rayleigh Limit. *Langmuir* **1989**, 5, 376-384.
34. Wilm, M., Principles of electrospray ionization. *Mol. Cell. Proteomics* **2011**, 10, M111 009407.
35. Emmett, M. R.; White, F. M.; Hendrickson, C. L.; Shi, S. D.; Marshall, A. G., Application of micro-electrospray liquid chromatography techniques to FT-ICR MS to enable high-sensitivity biological analysis. *J. Am. Soc. Mass Spectrom.* **1998**, 9, 333-340.
36. El-Aneed, A.; Cohen, A.; Banoub, J., Mass spectrometry, review of the basics: electrospray, maldi, and commonly used mass analyzers. *Appl. Spectrosc. Rev.* **2009**, 44, 210-230.
37. Stafford, G., Jr., Ion trap mass spectrometry: a personal perspective. *J. Am. Soc. Mass Spectrom.* **2002**, 13, 589-956.
38. McIver, R. T., A trapped ion analyzer cell for ion cyclotron resonance spectroscopy. *Rev. Sci. Instrum.* **1970**, 41, 555-558.
39. Hu, Q.; Noll, R. J.; Li, H.; Makarov, A.; Hardman, M.; Cooks, R. G., The Orbitrap: a new mass spectrometer. *J. Mass Spectrom.* **2005**, 40, 430-443.

40. Douglas, D. J.; Frank, A. J.; Mao, D., Linear ion traps in mass spectrometry. *Mass Spectrom. Rev.* **2005**, 24, 1-29.
41. Guilhaus, M., Principles and instrumentation in time-of-flight mass spectrometry. *J. Mass Spectrom.* **1995**, 30, 1519-1532.
42. Lawrence, E. O.; Edlefsen, N. E., On the production of high speed protons. *Science* **1930**, 72, 372-378.
43. Lawrence, E. O.; Livingston, M. S., The production of high speed light ions without the use of high voltages. *Phys. Rev.* **1932**, 40, 19-37.
44. Hipple, J. A.; Sommer, H.; Thomas, H. A., A Precise Method of Determining the Faraday by Magnetic Resonance. *Phys. Rev.* **1949**, 76, 1877-1878.
45. Anders, L. R.; Beauchamp, J. L.; Dunbar, R. C.; Baldeschwieler, J. D., Ion-cyclotron double resonance. *J. Chem. Phys.* **1966**, 45, 1062-1063.
46. Baldeschwieler, J. D., Ion cyclotron resonance spectroscopy. Cyclotron double resonance provides a new technique for the study of ion-molecule reaction mechanisms. *Science* **1968**, 159, 263-273.
47. Comisarow, M. B.; Marshall, A. G., Fourier transform ion cyclotron resonance spectroscopy. *Chem. Phys. Lett.* **1974**, 25, 282-283.
48. Zhang, L.-K.; Rempel, D.; Pramanik, B. N.; Gross, M. L., Accurate mass measurements by Fourier transform mass spectrometry. *Mass Spectrom. Rev.* **2005**, 24, 286-309.
49. Nikolaev, E. N.; Boldin, I. A.; Jertz, R.; Baykut, G., Initial experimental characterization of a new ultra-high resolution FTICR cell with dynamic harmonization. *J. Am. Soc. Mass Spectrom.* **2011**, 22, 1125-1133.
50. Nikolaev, E. N.; Vladimirov, G. N.; Jertz, R.; Baykut, G., From supercomputer modeling to highest mass resolution in FT-ICR. *Mass Spectrom (Tokyo)*. **2013**, 2.
51. Marshall, A. G., Milestones in Fourier transform ion cyclotron resonance mass spectrometry technique development. *Int. J. Mass Spectrom.* **2000**, 200, 331-356.
52. Guan, S.; Wahl, M. C.; Wood, T. D.; Marshall, A. G., Enhanced mass resolving power, sensitivity, and selectivity in laser desorption Fourier transform ion cyclotron resonance mass spectrometry by ion axialization and cooling. *Anal. Chem.* **1993**, 65, 1753-1757.
53. Quenzer, T. L.; Emmett, M. R.; Hendrickson, C. L.; Kelly, P. H.; Marshall, A. G., High sensitivity Fourier transform ion cyclotron resonance mass spectrometry for biological analysis with nano-LC and microelectrospray ionization. *Anal. Chem.* **2001**, 73, 1721-1725.

54. Solouki, T.; Pasa-Tolic, L.; Jackson, G. S.; Guan, S.; Marshall, A. G., High-resolution multistage MS, MS<sup>2</sup>, and MS<sup>3</sup> matrix-assisted laser desorption/ionization FT-ICR mass spectra of peptides from a single laser shot. *Anal. Chem.* **1996**, 68, 3718-3725.
55. Freitas, M. A.; Hendrickson, C. L.; Emmett, M. R.; Marshall, A. G., High-field Fourier transform ion cyclotron resonance mass spectrometry for simultaneous trapping and gas-phase hydrogen/deuterium exchange of peptide ions. *J. Am. Soc. Mass Spectrom.* **1998**, 9, 1012-1019.
56. Marshall, A. G.; Hendrickson, C. L.; Jackson, G. S., Fourier Transform Ion Cyclotron Resonance Mass Spectrometry: A Primer. *Mass Spectrom. Rev.* **1998**, 17, 1-35.
57. Wanczek, K. P., ICR spectrometry - A review of new developments in theory, instrumentation, and applications. *Int. J. Mass Spectrom. Ion Proc.* **1989**, 95, 1-38.
58. Staneke, P. O.; Nibbering, N. M. M., Matrix-assisted laser desorption ionization and electrospray ionization combined with Fourier transform ion cyclotron resonance mass spectrometry. *Spectrosc. Int. J.* **1997**, 13, 145-150.
59. Fievre, A.; Solouki, T.; Marshall, A. G.; Cooper, W. T., High-resolution Fourier transform ion cyclotron resonance mass spectrometry of humic and fulvic acids by laser desorption/ionization and electrospray ionization. *Energy & Fuels* **1997**, 11, 554-560.
60. McIver, R. T., Trajectory calculations for axial injection of ions into a magnetic field: overcoming the magnetic mirror effect with an r. f. quadrupole lens. *Int. J. Mass Spectrom. Ion Proc.* **1990**, 98, 35-50.
61. Alomary, A.; Solouki, T., Combined external and internal ion accumulation: improved detection limit for electrospray ionization Fourier transform ion cyclotron resonance mass spectrometry. *Proceedings of the 48<sup>th</sup> ASMS Conference on Mass Spectrometry and Allied Topics* **2000**, June 11-15, Long Beach, CA.
62. Boering, K. A.; Rolfe, J.; Brauman, J. I., Control of ion kinetic-energy in ion-cyclotron resonance spectrometry-Very-low-energy collision-induced dissociation. *Rapid Commun. Mass Spectrom.* **1992**, 6, 303-305.
63. Nibbering, N. M. M., Gas-phase ion/molecule reactions as studied by Fourier transform ion cyclotron resonance. *Acc. Chem. Res.* **1990**, 23, 279-285.
64. Comisarow, M. B., Application of rotating electric monopole theory to marginal oscillators. *Int. J. Mass Spectrom. Ion Proc.* **1978**, 26, 369-378.

65. Comisarow, M. B.; Marshall, A. G., Frequency-sweep Fourier transform ion cyclotron resonance spectroscopy. *Chem. Phys. Lett.* **1974**, 26, 489-490.
66. Scigelova, M.; Hornshaw, M.; Giannakopoulos, A.; Makarov, A., Fourier transform mass spectrometry. *Mol. Cell. Proteomics* **2011**, 10, M111.009431.
67. Marshall, A. G.; Schweikhard, L., Fourier-transform ion-cyclotron resonance mass-spectrometry - technique developments. *Int. J. Mass Spectrom. Ion Proc.* **1992**, 118, 37-70.
68. Aarstol, M.; Commisarow, M. B., Apodization of FT-ICR spectra. *Int. J. Mass Spectrom. Ion Proc.* **1987**, 76, 287-297.
69. Perry, R. H.; Cooks, R. G.; Noll, R. J., Orbitrap mass spectrometry: instrumentation, ion motion and applications. *Mass Spectrom. Rev.* **2008**, 27, 661-699.
70. Kingdon, K. H., A method for the neutralization of electron space charge by positive ionization at very low gas pressures. *Phys. Rev.* **1923**, 21, 408-418.
71. Makarov, A., Electrostatic axially harmonic orbital trapping: a high-performance technique of mass analysis. *Anal. Chem.* **2000**, 72, 1156-1162.
72. Makarov, A.; Denisov, E.; Kholomeev, A.; Balschun, W.; Lange, O.; Strupat, K.; Horning, S., Performance evaluation of a hybrid linear ion trap/orbitrap mass spectrometer. *Anal. Chem.* **2006**, 78, 2113-2120.
73. Solouki, T.; Gillig, K. J.; Ruesell, D. H., Detection of high-mass biomolecules in Fourier transform ion cyclotron resonance mass spectrometry: Theoretical and experimental investigations. *Anal. Chem.* **1994**, 66, 1583-1587.
74. Gillig, K. J.; Bluhm, B. K.; Russell, D. H., Ion motion in a Fourier transform ion cyclotron resonance wire ion guide cell. *Int. J. Mass Spectrom. Ion Proc.* **1996**, 157/158, 129-147.
75. Wu, G. X.; Noll, R. J.; Plass, W. R.; Hu, Q. Z.; Perry, R. H.; Cooks, R. G., Ion trajectory simulations of axial ac dipolar excitation in the Orbitrap. *Int. J. Mass Spectrom.* **2006**, 254, 53-62.
76. Stephens, W., Linear time of flight mass spectrometer. In *American Physical Society Meeting*, Phys. Rev.: Cambridge, MA, 1946; Vol. 69, p 691.
77. Wiley, W. C.; McLaren, J. B., Time-of-Flight mass spectrometer with improved resolution. *Rev. Sci. Instrum.* **1955**, 16, 1150-1157.
78. Brown, R. S.; Lennon, J. J., Mass resolution improvement by incorporation of pulsed ion extraction in a matrix-assisted laser desorption/ionization linear time-of-flight mass spectrometer. *Anal. Chem.* **1995**, 67, 1998-2003.

79. Domon, B.; Aebersold, R., Mass spectrometry and protein analysis. *Science* **2006**, 312, 212-217.
80. Fetterolf, D. D.; Yost, R. A., Energy resolved collision-induced dissociation in tandem mass spectrometry. *Int. J. Mass Spectrom. Ion Proc.* **1982**, 44, 37-50.
81. Gauthier, J. W.; Trautman, T. R.; Jacobson, D. B., Sustained off-resonance irradiation for collision-activated dissociation involving Fourier transform mass spectrometry. Collision-activated dissociation technique that emulates infrared multiphoton dissociation. *Anal. Chim. Acta.* **1991**, 246, 211-225.
82. Herrmann, K. A.; Somogyi, A.; Wysocki, V. H.; Drahos, L.; Vekey, K., Combination of sustained off-resonance irradiation and on-resonance excitation in FT-ICR. *Anal. Chem.* **2005**, 77, 7626-7638.
83. Madsen, J. A.; Gardner, M. W.; Smith, S. I.; Ledvina, A. R.; Coon, J. J.; Schwartz, J. C.; Stafford, G. C., Jr.; Brodbelt, J. S., Top-down protein fragmentation by infrared multiphoton dissociation in a dual pressure linear ion trap. *Anal. Chem.* **2009**, 81, 8677-8686.
84. Ledvina, A. R.; Lee, M. V.; McAlister, G. C.; Westphall, M. S.; Coon, J. J., Infrared multiphoton dissociation for quantitative shotgun proteomics. *Anal. Chem.* **2012**, 84, 4513-4519.
85. Fernandez, F. M.; Wysocki, V. H.; Futrell, J. H.; Laskin, J., Protein identification via surface-induced dissociation in an FT-ICR mass spectrometer and a patchwork sequencing approach. *J. Am. Soc. Mass. Spectrom.* **2006**, 17, 700-709.
86. Blackwell, A. E.; Dodds, E. D.; Bandarian, V.; Wysocki, V. H., Revealing the quaternary structure of a heterogeneous noncovalent protein complex through surface-induced dissociation. *Anal. Chem.* **2011**, 83, 2862-2865.
87. Dunbar, R. C., BIRD (blackbody infrared radiative dissociation): evolution, principles, and applications. *Mass Spectrom. Rev.* **2004**, 23, 127-158.
88. Zubarev, R. A.; Kelleher, N. L.; McLafferty, F. W., Electron capture dissociation of multiply charged protein cations. A non-ergodic process. *J. Am. Chem. Soc.* **1998**, 120, 3265-3266.
89. Syka, J. E.; Coon, J. J.; Schroeder, M. J.; Shabanowitz, J.; Hunt, D. F., Peptide and protein sequence analysis by electron transfer dissociation mass spectrometry. *Proc. Natl. Acad. Sci. USA* **2004**, 101, 9528-9533.
90. Wysocki, V. H.; Kenttamaa, H. I.; Cooks, R. G., Internal energy-distributions of isolated ions after activation by various methods. *Int. J. Mass Spectrom. Ion Proc.* **1987**, 75, 181-208.

91. Winters, R. E.; Kiser, R. W., A mass spectrometric investigation of nickel tetracarbonyl and iron pentacarbonyl. *Inorg. Chem.* **1964**, 3.
92. Sleno, L.; Volmer, D. A., Ion activation methods for tandem mass spectrometry. *J. Mass Spectrom.* **2004**, 39, 1091-1112.
93. Rice, O. K.; Ramsperger, H. C., Theories of unimolecular gas reactions at low pressures. *J. Am. Chem. Soc.* **1927**, 49, 1617-1629.
94. Hinshelwood, C. N., On the theory of unimolecular reactions *Proc. R. Soc. Lond. A* **1926**, 113.
95. Turecek, F., N-Cα bond dissociation energies and kinetics in amide and peptide radicals. Is the dissociation a non-ergodic process? *J. Am. Chem. Soc.* **2003**, 125, 5954-5963.
96. Benesch, J. L.; Aquilina, J. A.; Ruotolo, B. T.; Sobott, F.; Robinson, C. V., Tandem mass spectrometry reveals the quaternary organization of macromolecular assemblies. *Chem. Biol.* **2006**, 13, 597-605.
97. Benesch, J. L., Collisional activation of protein complexes: picking up the pieces. *J. Am. Soc. Mass. Spectrom.* **2009**, 20, 341-348.
98. Zhang, H.; Cui, W.; Wen, J.; Blankenship, R. E.; Gross, M. L., Native electrospray and electron-capture dissociation FTICR mass spectrometry for top-down studies of protein assemblies. *Anal. Chem.* **2011**, 83, 5598-5606.
99. Zubarev, R. A., Electron-capture dissociation tandem mass spectrometry. *Curr. Opin. Biotechnol.* **2004**, 15, 12-16.
100. Sobott, F.; Watt, S. J.; Smith, J.; Edelman, M. J.; Kramer, H. B.; Kessler, B. M., Comparison of CID versus ETD based MS/MS fragmentation for the analysis of protein ubiquitination. *J. Am. Soc. Mass Spectrom.* **2009**, 20, 1652-1659.
101. Jones, A. W.; Cooper, H. J., Dissociation techniques in mass spectrometry-based proteomics. *Analyst* **2011**, 136, 3419-3429.
102. Laskin, J.; Futrell, J. H., Activation of large ions in FT-ICR mass spectrometry. *Mass Spectrom. Rev.* **2005**, 24, 135-167.
103. Good, D. M.; Wirtala, M.; McAlister, G. C.; Coon, J. J., Performance characteristics of electron transfer dissociation mass spectrometry. *Mol. Cell. Proteomics* **2007**, 6, 1942-1951.
104. Derrick, J. P.; Wigley, D. B., The third IgG-binding domain from streptococcal protein G. An analysis by X-ray crystallography of the structure alone and in a complex with Fab. *J. Mol. Biol.* **1994**, 243, 906-918.

105. Zahn, R.; Liu, A.; Luhrs, T.; Riek, R.; von Schroetter, C.; Lopez Garcia, F.; Billeter, M.; Calzolari, L.; Wider, G.; Wuthrich, K., NMR solution structure of the human prion protein. *Proc. Natl. Acad. Sci. USA* **2000**, 97, 145-150.
106. Vinson, V. J., Proteins in motion. . *Science* **2009**, 324, 197-197.
107. Pan, Z.; Raftery, D., Comparing and combining NMR spectroscopy and mass spectrometry in metabolomics. *Anal. Bioanal. Chem.* **2007**, 387, 525-527.
108. Scarff, C. A.; Patel, V. J.; Thalassinou, K.; Scrivens, J. H., Probing hemoglobin structure by means of traveling-wave ion mobility mass spectrometry. *J. Am. Soc. Mass Spectrom.* **2009**, 20, 625-631.
109. Suckau, D.; Shi, Y.; Beu, S. C.; Senko, M. W.; Quinn, J. P.; Wampler, F. M., 3rd; McLafferty, F. W., Coexisting stable conformations of gaseous protein ions. *Proc. Natl. Acad. Sci. USA* **1993**, 90, 790-793.
110. Wood, T. D.; Chorush, R. A.; Wampler, F. M., 3rd; Little, D. P.; O'Connor, P. B.; McLafferty, F. W., Gas-phase folding and unfolding of cytochrome c cations. *Proc. Natl. Acad. Sci. USA* **1995**, 92, 2451-2454.
111. McLafferty, F. W.; Guan, Z.; Haupts, U.; Wood, T. D.; Kelleher, N. L., Gaseous conformational structures of Cytochrome c. *J. Am. Chem. Soc.* **1998**, 120, 4732-4740.
112. Mao, D.; Ding, C.; Douglas, D. J., Hydrogen/deuterium exchange of myoglobin ions in a linear quadrupole ion trap. *Rapid Commun. Mass Spectrom.* **2002**, 16, 1941-1945.
113. Green, M. K.; Lebrilla, C. B., Ion-molecule reactions as probes of gas-phase structures of peptides and proteins. *Mass Spectrom. Rev.* **1997**, 16, 53-71.
114. Freitas, M. A.; Marshall, A. G., Rate and extent of gas-phase hydrogen/deuterium exchange of bradykinins: evidence for peptide zwitterions in the gas phase. *Int. J. Mass Spectrom.* **1999**, 182-183, 221-231.
115. Freitas, M. A.; Hendrickson, C. L.; Emmett, M. R.; Marshall, A. G., Gas-phase bovine ubiquitin cation conformations resolved by gas-phase hydrogen/deuterium exchange rate and extent. *Int. J. Mass Spectrom.* **1999**, 185-187, 565-575.
116. Alomary, A.; Solouki, T.; Patterson, H. H.; Cronan, C. S., Elucidation of aluminum-fulvic acid interactions by gas-phase hydrogen/deuterium (H/D) exchange and electrospray fourier transform ion cyclotron resonance mass spectrometry(ESI FT-ICR). *Environ. Sci. Technol.* **2000**, 34, 2830-2838.

117. Fattahi, A.; Solouki, T., Conformational analysis of metal complexed model peptides and their fragment ions using FT-ICR MS and gas-phase H/D exchange reactions. *Proceedings of the 49<sup>th</sup> ASMS Conference on Mass Spectrometry and Allied Topics* **2001**, Chicago, IL.
118. Solouki, T.; Fort, R.; Alomary, A.; Fattahi, A., Gas-phase hydrogen/deuterium exchange reactions of a model peptide: FT-ICR and computational analyses of metal induced conformational mutations. *J. Am. Soc. Mass Spectrom.* **2001**, 12, 1272-1285.
119. Kaltashov, I. A.; Doroshenko, V. M.; Cotter, R. J., Gas phase hydrogen/deuterium exchange reactions of peptide ions in a quadrupole ion trap mass spectrometer. *Proteins* **1997**, 28, 53-58.
120. Zhang, J.; Brodbelt, J. S., Gas-phase hydrogen/deuterium exchange and conformations of deprotonated flavonoids and gas-phase acidities of flavonoids. *J. Am. Chem. Soc.* **2004**, 126, 5906-5919.
121. Solouki, T.; Zekavat, B.; Miladi, M., On the existence of structurally different isobaric  $b_n$  fragment ions. *Proceedings of the 58<sup>th</sup> ASMS Conference on Mass Spectrometry and Allied Topics* **2010**, Salt Lake City, UT.
122. Jiao, C. Q.; Ranatunga, D. R.; Vaughn, W. E.; Freiser, B. S., A pulsed-leak valve for use with ion trapping mass spectrometers. *J. Am. Soc. Mass. Spectrom.* **1996**, 7, 118-122.
123. Fattahi, A.; Zekavat, B.; Solouki, T., H/D exchange kinetics: experimental evidence for formation of different b fragment ion conformers/isomers during the gas-phase peptide sequencing. *J. Am. Soc. Mass. Spectrom.* **2010**, 21, 358-369.
124. Zekavat, B.; Miladi, M.; Al-Fdeilat, A. H.; Somogyi, A.; Solouki, T., Evidence for sequence scrambling and divergent h/d exchange reactions of doubly-charged isobaric b-type fragment ions. *J. Am. Soc. Mass. Spectrom.* **2014**, 25, 226-236.
125. Miladi, M.; Zekavat, B.; Munisamy, S. M.; Solouki, T., A systematic study on the effect of histidine position and fragment ion size on the formation of  $b_n$  ions. *Int. J. Mass Spectrom.* **2012**, 316-318, 164-173.
126. Campbell, S.; Rodgers, M. T.; Marzluff, E. M.; Beauchamp, J. L., Structural and energetic constraints on gas phase hydrogen/deuterium exchange reactions of protonated peptides with  $D_2O$ ,  $CD_3OD$ ,  $CD_3CO_2D$ , and  $ND_3$ . *J. Am. Chem. Soc.* **1994**, 116, 9765-9766.

127. Campbell, S.; Rodgers, M. T.; Marzluff, E. M.; Beauchamp, J. L., Deuterium exchange reactions as a probe of biomolecule structure. fundamental studies of gas phase H/D exchange reactions of protonated glycine oligomers with D<sub>2</sub>O, CD<sub>3</sub>OD, CD<sub>3</sub>CO<sub>2</sub>D, and ND<sub>3</sub>. *J. Am. Chem. Soc.* **1995**, 117, 12840-12854.
128. Cheng, X. H.; Fenselau, C., Hydrogen-deuterium exchange of mass-selected peptide ions with nd<sub>3</sub> in a tandem sector mass-spectrometer. *Int. J. Mass Spectrom. Ion Proc.* **1992**, 122, 109-119.
129. Gard, E.; Green, M. K.; Bregar, J.; Lebrilla, C. B., Gas-phase hydrogen-deuterium exchange as a molecular probe for the interaction of methanol and protonated peptides. *J. Am. Soc. Mass Spectrom.* **1994**, 5, 623-631.
130. Kanu, A. B.; Dwivedi, P.; Tam, M.; Matz, L.; Hill, H. H., Jr., Ion mobility-mass spectrometry. *J. Mass Spectrom.* **2008**, 43, 1-22.
131. Clemmer, D. E.; Jarrold, M. F., Ion mobility measurements and their applications to clusters and biomolecules. *J. Mass Spectrom.* **1997**, 32, 577-592.
132. Uetrecht, C.; Rose, R. J.; Duijn, E. v.; Lorenzen, K.; Heck, A. J. R., Ion mobility mass spectrometry of proteins and protein assemblies. *Chem. Soc. Rev.* **2010**, 39, 1633-1655.
133. Creaser, C. S.; Griffiths, J. R.; Bramwell, C. J.; Sadaf Noreen; Hillb, C. A.; Thomas, C. L. P., Ion mobility spectrometry: a review. Part 1. Structural analysis by mobility measurement. *Analyst* **2004**, 129, 984-994.
134. Giles, K.; Pringle, S. D.; Worthington, K. R.; Little, D.; Wildgoose, J. L.; Bateman, R. H., Applications of a travelling wave-based radio-frequency-only stacked ring ion guide. *Rapid Commun. Mass Spectrom.* **2004**, 18, 2401-2414.
135. Shvartsburg, A. A.; Smith, R. D., Fundamentals of traveling wave ion mobility spectrometry. *Anal. Chem.* **2008**, 80, 9689-9699.
136. Bush, M. F.; Hall, Z.; Giles, K.; Hoyes, J.; Robinson, C. V.; Ruotolo, B. T., Collision cross sections of proteins and their complexes: a calibration framework and database for gas-phase structural biology. *Anal. Chem.* **2010**, 82, 9557-9565.
137. Ruotolo, B. T.; Benesch, J. L.; Sandercock, A. M.; Hyung, S. J.; Robinson, C. V., Ion mobility-mass spectrometry analysis of large protein complexes. *Nat. Protoc.* **2008**, 3, 1139-1152.
138. Banks, R. E.; Dunn, M. J.; Hochstrasser, D. F.; Sanchez, J. C.; Blackstock, W.; Pappin, D. J.; Selby, P. J., Proteomics: new perspectives, new biomedical opportunities. *Lancet* **2000**, 356, 1749-1756.

139. Tyers, M.; Mann, M., From genomics to proteomics. *Nature* **2003**, 422, 193-197.
140. Pandey, A.; Mann, M., Proteomics to study genes and genomes. *Nature* **2000**, 405, 837-46.
141. Fields, S., Proteomics. Proteomics in genomeland. *Science* **2001**, 291, 1221-1224.
142. Aebersold, R.; Mann, M., Mass spectrometry-based proteomics. *Nature* **2003**, 422, 198-207.
143. Chait, B. T., Chemistry. Mass spectrometry: bottom-up or top-down? *Science* **2006**, 314, 65-66.
144. Bogdanov, B.; Smith, R. D., Proteomics by FTICR mass spectrometry: top down and bottom up. *Mass Spectrom. Rev.* **2005**, 24, 168-200.
145. Ferguson, P. L.; Smith, R. D., Proteome analysis by mass spectrometry. *Annu. Rev. Biophys. Biomol. Struct.* **2003**, 32, 399-424.
146. Johnson, R. S.; Martin, S. A.; Biemann, K.; Stults, J. T.; Watson, J. T., Novel fragmentation process of peptides by collision-induced decomposition in a tandem mass spectrometer: differentiation of leucine and isoleucine. *Anal. Chem.* **1987**, 59, 2621-2625.
147. Steen, H.; Mann, M., The ABC's (and XYZ's) of peptide sequencing. *Nat. Rev. Mol. Cell Biol.* **2004**, 5, 699-711.
148. Reid, G. E.; McLuckey, S. A., 'Top down' protein characterization via tandem mass spectrometry. *J. Mass Spectrom.* **2002**, 37, 663-675.
149. McLafferty, F. W.; Breuker, K.; Jin, M.; Han, X.; Infusini, G.; Jiang, H.; Kong, X.; Begley, T. P., Top-down MS, a powerful complement to the high capabilities of proteolysis proteomics. *FEBS J.* **2007**, 274, 6256-6268.
150. McLafferty, F. W., Collisional activation mass spectra. *Phil. Trans. R. Soc. Lond. A* **1979**, 293, 93-102.
151. Zubarev, R. A.; Horn, D. M.; Fridriksson, E. K.; Kelleher, N. L.; Kruger, N. A.; Lewis, M. A.; Carpenter, B. K.; McLafferty, F. W., Electron capture dissociation for structural characterization of multiply charged protein cations. *Anal. Chem.* **2000**, 72, 563-573.
152. Little, D. P.; Speir, J. P.; Senko, M. W.; O'Connor, P. B.; McLafferty, F. W., Infrared multiphoton dissociation of large multiply charged ions for biomolecule sequencing. *Anal. Chem.* **1994**, 66, 2809-2815.

153. Hakansson, K.; Cooper, H. J.; Emmett, M. R.; Costello, C. E.; Marshall, A. G.; Nilsson, C. L., Electron capture dissociation and infrared multiphoton dissociation MS/MS of an N-glycosylated tryptic peptic to yield complementary sequence information. *Anal. Chem.* **2001**, 73, 4530-4536.
154. Frese, C. K.; Altelaar, A. F.; Hennrich, M. L.; Nolting, D.; Zeller, M.; Griep-Raming, J.; Heck, A. J.; Mohammed, S., Improved peptide identification by targeted fragmentation using CID, HCD and ETD on an LTQ-Orbitrap Velos. *J. Proteome Res.* **2011**, 10, 2377-2388.
155. Craig, R.; Cortens, J. P.; Beavis, R. C., Open source system for analyzing, validating, and storing protein identification data. *J. Proteome. Res.* **2004**, 3, 1234-1242.
156. Deutsch, E. W.; Lam, H.; Aebersold, R., PeptideAtlas: a resource for target selection for emerging targeted proteomics workflows. *EMBO Rep.* **2008**, 9, 429-434.
157. Perkins, D. N.; Pappin, D. J.; Creasy, D. M.; Cottrell, J. S., Probability-based protein identification by searching sequence databases using mass spectrometry data. *Electrophoresis* **1999**, 20, 3551-3567.
158. Geer, L. Y.; Markey, S. P.; Kowalak, J. A.; Wagner, L.; Xu, M.; Maynard, D. M.; Yang, X.; Shi, W.; Bryant, S. H., Open mass spectrometry search algorithm. *J. Proteome Res.* **2004**, 3, 958-964.
159. Eng, J. K.; McCormack, A. L.; Yates, J. R., An approach to correlate tandem mass spectral data of peptides with amino acid sequences in a protein database. *J. Am. Soc. Mass Spectrom.* **1994**, 5, 976-989.
160. Craig, R.; Beavis, R. C., TANDEM: matching proteins with tandem mass spectra. *Bioinformatics* **2004**, 20, 1466-1467.
161. Wang, P.; Wilson, S. R., Mass spectrometry-based protein identification by integrating de novo sequencing with database searching. *BMC Bioinformatics* **2013**, 14, 1-9.
162. Roepstorff, P.; Fohlman, J., Proposal for a common nomenclature for sequence ions in mass spectra of peptides. *Biomed. Mass Spectrom.* **1984**, 11, 601-601.
163. Madsen, J. A.; Brodbelt, J. S., Comparison of infrared multiphoton dissociation and collision-induced dissociation of supercharged peptides in ion traps. *J. Am. Soc. Mass. Spectrom.* **2009**, 20, (3), 349-358.
164. Johnson, R. S.; Martin, S. A.; Biemann, K., Collision-induced fragmentation of  $[M + H]^+$  ions of peptides. side chain specific sequence ions *Int. J. Mass Spectrom. Ion Proc.* **1988**, 86, 137-154.

165. Stein, S. E.; Scott, D. R., Optimization and testing of mass spectral library search algorithms for compound identification. *J. Am. Soc. Mass Spectrom.* **1994**, *5*, 859-866.
166. Elias, J. E.; Gygi, S. P., Target-decoy search strategy for increased confidence in large-scale protein identifications by mass spectrometry. *Nat. Methods* **2007**, *4*, 207-214.
167. Lam, H.; Deutsch, E. W.; Eddes, J. S.; Eng, J. K.; King, N.; Stein, S. E.; Aebersold, R., Development and validation of a spectral library searching method for peptide identification from MS/MS. *Proteomics* **2007**, *7*, 655-667.
168. Lam, H.; Deutsch, E. W.; Eddes, J. S.; Eng, J. K.; Stein, S. E.; Aebersold, R., Building consensus spectral libraries for peptide identification in proteomics. *Nat. Methods* **2008**, *5*, 873-875.
169. Taylor, G. K.; Goodlett, D. R., Rules governing protein identification by mass spectrometry *Rapid Commun. Mass Spectrom.* **2005**, *19*, 3420-3420.
170. Nielsen, M. L.; Savitski, M. M.; Zubarev, R. A., Improving protein identification using complementary fragmentation techniques in Fourier transform mass spectrometry. *Mol. Cell. Proteomics* **2005**, *4*, 835-845.
171. Chen, Y.; Zhang, J.; Xing, G.; Zhao, Y., Mascot-derived false positive peptide identifications revealed by manual analysis of tandem mass spectra. *J. Proteome Res.* **2009**, *8*, 3141-3147.
172. Harrison, A. G.; Young, A. B.; Bleiholder, C.; Suhai, S.; Paizs, B., Scrambling of sequence information in collision-induced dissociation of peptides. *J. Am. Chem. Soc.* **2006**, *128*, 10364-10365.
173. Cooper, B., The problem with peptide presumption and low Mascot scoring. *J. Proteome Res.* **2011**, *10*, 1432-1435.
174. Dong, N. P.; Liang, Y. Z.; Yi, L. Z., Investigation of scrambled ions in tandem mass spectra. Part 1. Statistical characterization. *J. Am. Soc. Mass Spectrom.* **2012**, *23*, 1209-1220.
175. Dong, N. P.; Liang, Y. Z.; Yi, L. Z.; Lu, H. M., Investigation of scrambled ions in tandem mass spectra, part 2. On the influence of the ions on peptide identification. *J. Am. Soc. Mass Spectrom.* **2013**, *24*, 857-867.
176. NIST libraries of peptide tandem mass spectra. <http://peptide.nist.gov/>.
177. Nesvizhskii, A. I.; Vitek, O.; Aebersold, R., Analysis and validation of proteomic data generated by tandem mass spectrometry. *Nat. Methods* **2007**, *4*, 787-797.

178. Tang, X. J.; Thibault, P.; Boyd, R. K., Fragmentation reactions of multiply-protonated peptides and implications for sequencing by tandem mass spectrometry with low-energy collision-induced dissociation. *Anal. Chem.* **1993**, *65*, 2824-2834.
179. Tang, X. J.; Boyd, R. K., Rearrangements of doubly charged acylium ions from lysyl and ornithyl peptides. *Rapid Commun. Mass Spectrom.* **1994**, *8*, 678-686.
180. Vachet, R. W.; Bishop, B. M.; Erickson, B. W.; Glish, G. L., Novel peptide dissociation: Gas-phase intramolecular rearrangement of internal amino acid residues. *J. Am. Chem. Soc.* **1997**, *119*, 5481-5488.
181. Yague, J.; Paradela, A.; Ramos, M.; Ogueta, S.; Marina, A.; Barahona, F.; Lopez de Castro, J. A.; Vazquez, J., Peptide rearrangement during quadrupole ion trap fragmentation: added complexity to MS/MS spectra. *Anal. Chem.* **2003**, *75*, 1524-1535.
182. Harrison, A. G., Peptide sequence scrambling through cyclization of  $b_5$  ions. *J. Am. Soc. Mass Spectrom.* **2008**, *19*, 1776-1780.
183. Bleiholder, C.; Osburn, S.; Williams, T. D.; Suhai, S. n.; Van Stipdonk, M.; Harrison, A. G.; Paizs, B., Sequence-scrambling fragmentation pathways of protonated peptides. *J. Am. Chem. Soc.* **2008**, *130*, 17774-17789.
184. Harrison, A. G., To b or not to b: The ongoing saga of peptide b ions. *Mass Spectrom. Rev.* **2009**, *28*, 640-654.
185. Somogyi, A., Probing peptide fragment ion structures by combining sustained off-resonance collision-induced dissociation and gas-phase H/D exchange (SORI-HDX) in Fourier transform ion-cyclotron resonance (FT-ICR) instruments. *J. Am. Soc. Mass Spectrom.* **2008**, *19*, 1771-1775.
186. Chen, X.; Yu, L.; Steill, J. D.; Oomens, J.; Polfer, N. C., Effect of peptide fragment size on the propensity of cyclization in collision-induced dissociation: oligoglycine  $b_2$ - $b_8$ . *J. Am. Chem. Soc.* **2009**, *131*, 18272-18282.
187. Perkins, B. R.; Chamot-Rooke, J.; Yoon, S. H.; Gucinski, A. C.; Somogyi, A.; Wysocki, V. H., Evidence of diketopiperazine and oxazolone structures for HA  $b_2^+$  ion. *J. Am. Chem. Soc.* **2009**, *131*, 17528-17529.
188. Chen, X.; Steill, J. D.; Oomens, J.; Polfer, N. C., Oxazolone versus macrocycle structures for leu-enkephalin  $b_2$ - $b_4$ : Insights from infrared multiple-photon dissociation spectroscopy and gas-phase hydrogen/deuterium exchange. *J. Am. Soc. Mass Spectrom.* **2010**, *21*, 1313-1321.
189. Paizs, B.; Suhai, S., Fragmentation pathways of protonated peptides. *Mass Spectrom. Rev.* **2005**, *24*, 508-548.

190. Bythell, B. J.; Knapp-Mohammady, M.; Paizs, B.; Harrison, A. G., Effect of the His residue on the cyclization of b ions. *J. Am. Soc. Mass Spectrom.* **2010**, *21*, 1352-1363.
191. Riba Garcia, I.; Giles, K.; Bateman, R. H.; Gaskell, S. J., Evidence for structural variants of a- and b-type peptide fragment ions using combined ion mobility/mass spectrometry. *J. Am. Soc. Mass Spectrom.* **2008**, *19*, 609-613.
192. Riba Garcia, I.; Giles, K.; Bateman, R. H.; Gaskell, S. J., Studies of peptide a- and b-type fragment ions using stable isotope labeling and integrated ion mobility/tandem mass spectrometry. *J. Am. Soc. Mass Spectrom.* **2008**, *19*, 1781-1787.
193. Polfer, N. C.; Bohrer, B. C.; Plasencia, M. D.; Paizs, B.; Clemmer, D. E., On the dynamics of fragment isomerization in collision-induced dissociation of peptides. *J. Phys. Chem. A* **2008**, *112*, 1286-1293.
194. Yoon, S. H.; Chamot-Rooke, J.; Perkins, B. R.; Hilderbrand, A. E.; Poutsma, J. C.; Wysocki, V. H., IRMPD spectroscopy shows that AGG forms an oxazolone  $b_2^+$  ion. *J. Am. Chem. Soc.* **2008**, *130*, 17644-14645.
195. Erlekam, U.; Bythell, B. J.; Scuderi, D.; Van Stipdonk, M.; Paizs, B.; Maitre, P., Infrared spectroscopy of fragments of protonated peptides: direct evidence for macrocyclic structures of  $b_5$  ions. *J. Am. Chem. Soc.* **2009**, *131*, 11503-11508.
196. Yalcin, T.; Csizmadia, I. G.; Peterson, M. R.; Harrison, A. G., The structure and fragmentation of  $b_n$  ( $n \geq 3$ ) ions in peptide spectra. *J. Am. Soc. Mass Spectrom.* **1996**, *7*, 233-242.
197. Zekavat, B.; Miladi, M.; Becker, C.; Munisamy, S. M.; Solouki, T., Combined use of post-ion mobility/collision-induced dissociation and chemometrics for b fragment ion analysis. *J. Am. Soc. Mass Spectrom.* **2013**, *24*, 1355-1365.
198. Yalcin, T.; Khouw, C.; Csizmadia, I. G.; Peterson, M. R.; Harrison, A. G., Why are b ions stable species in peptide spectra? *J. Am. Soc. Mass Spectrom.* **1995**, *6*, 1165-1174.
199. Yalcin, T.; Harrison, A. G., Ion chemistry of protonated lysine derivatives. *J. Mass Spectrom.* **1996**, *31*, 1237-1243.
200. Nold, M. J.; Wesdemiotis, C.; Yalcin, T.; Harrison, A. G., Amide bond dissociation in protonated peptides. Structures of the N-terminal ionic and neutral fragments. *Int. J. Mass Spectrom. Ion Proc.* **1997**, *164*, 137-153.
201. Reid, G. E.; Simpson, R.; O'Hair, R. J., A mass spectrometric and ab initio study of the pathways for dehydration of simple glycine and cysteine-containing peptide  $[M+H]^+$  ions. *J. Am. Soc. Mass Spectrom.* **1998**, *9*, 945-956.

202. Paisz, B.; Lendvay, G.; Vekey, K.; Suhai, S., Formation of  $b_2$  ions from protonated peptides: an ab initio study. *Rapid Commun. Mass Spectrom.* **1999**, 13, 525-533.
203. Schlosser, A.; Lehmann, W. D., Five-membered ring formation in unimolecular reactions of peptides: a key structural element controlling low-energy collision-induced dissociation of peptides. *J. Mass Spectrom.* **2000**, 35, 1382-1390.
204. Polfer, N. C.; Oomens, J.; Suhai, S.; Paizs, B., Spectroscopic and theoretical evidence for oxazolone ring formation in collision-induced dissociation of peptides. *J. Am. Chem. Soc.* **2005**, 127, 17154-17155.
205. Cordero, M. M.; Houser, J. J.; Wesdemiotis, C., The neutral products formed during backbone fragmentations of protonated peptides in tandem mass spectrometry. *Anal. Chem.* **1993**, 65, 1594-1601.
206. Paizs, B.; Suhai, S., Combined quantum chemical and RRKM modeling of the main fragmentation pathways of protonated GGG. I. Cis-trans isomerization around protonated amide bonds. *Rapid Commun. Mass Spectrom.* **2001**, 15, 2307-2323.
207. Farrugia, J. M.; Taverner, T.; O'Hair, R. A. J., Side-chain involvement in the fragmentation reactions of the protonated methylesters of histidine and its peptides. *Int. J. Mass Spectrom.* **2001**, 209, 99-112.
208. Gucinski, A. C.; Chamot-Rooke, J.; Nicol, E.; Somogyi, A.; Wysocki, V. H., Structural influences on preferential oxazolone versus diketopiperazine  $b_2^+$  ion formation for histidine analogue-containing peptides. *J. Phys. Chem. A* **2012**, 116, 4296-4304.
209. Polfer, N. C.; Oomens, J.; Suhai, S.; Paizs, B., Infrared spectroscopy and theoretical studies on gas-phase protonated leu-enkephalin and its fragments: direct experimental evidence for the mobile proton. *J. Am. Chem. Soc.* **2007**, 129, 5887-5897.
210. Eyler, J. R., Infrared multiple photon dissociation spectroscopy of ions in Penning traps. *Mass Spectrom. Rev.* **2009**, 28, 448-467.
211. Polfer, N. C.; Oomens, J., Vibrational spectroscopy of bare and solvated ionic complexes of biological relevance. *Mass Spectrom. Rev.* **2009**, 28, 468-494.
212. Zekavat, B.; Solouki, T., Chemometric data analysis for deconvolution of overlapped ion mobility profiles. *J. Am. Soc. Mass Spectrom.* **2012**, 23, 1873-1884.
213. Bythell, B. J.; Maitre, P.; Paizs, B., Cyclization and rearrangement reactions of  $a_n$  fragment ions of protonated peptides. *J. Am. Chem. Soc.* **2010**, 132, 14766-1479.

214. Vachet, R. W.; Ray, K. L.; Glish, G. L., Origin of product ions in the MS/MS spectra of peptides in a quadrupole ion trap. *J. Am. Soc. Mass Spectrom.* **1998**, *9*, 341-344.
215. Paizs, B.; Szlavik, Z.; Lendvay, G.; Vekey, K.; Suhai, S., Formation of  $a_2^+$  ions of protonated peptides. An ab initio study. *Rapid Commun. Mass Spectrom.* **2000**, *14*, 746-755.
216. Cooper, T.; Talaty, E.; Grove, J.; Van Stipdonk, M.; Suhai, S.; Paizs, B., Isotope labeling and theoretical study of the formation of  $a_3^*$  ions from protonated tetraglycine. *J. Am. Soc. Mass Spectrom.* **2006**, *17*, 1654-1664.
217. Allen, J. M.; Racine, A. H.; Berman, A. M.; Johnson, J. S.; Bythell, B. J.; Paizs, B.; Glish, G. L., Why are  $a_3$  ions rarely observed? *J. Am. Soc. Mass Spectrom.* **2008**, *19*, 1764-1770.
218. Verkerk, U. H.; Siu, C. K.; Steill, J. D.; Aribi, H. E.; Zhao, J.; Rodriguez, C. F.; Oomens, J.; Hopkinson, A. C.; Siu, K. W. M.,  $a_2$  Ion derived from triglycine: an N1-protonated 4-imidazolidinone. *J. Phys. Chem. Lett.* **2010**, *1*, 868-872.
219. Paizs, B.; Bythell, B. J.; Maitre, P., Rearrangement pathways of the  $a_4$  ion of protonated YGGFL characterized by IR spectroscopy and modeling. *J. Am. Soc. Mass Spectrom.* **2012**, *23*, 664-675.
220. Bythell, B. J.; Molesworth, S.; Osburn, S.; Cooper, T.; Paizs, B.; Van Stipdonk, M., Structure and reactivity of  $a_n$  and  $a_n^*$  peptide fragments investigated using isotope labeling, tandem mass spectrometry, and density functional theory calculations. *J. Am. Soc. Mass Spectrom.* **2008**, *19*, 1788-1798.
221. Wassermann, T. N.; Boyarkin, O. V.; Paizs, B.; Rizzo, T. R., Conformation-specific spectroscopy of Peptide fragment ions in a low-temperature ion trap. *J. Am. Soc. Mass Spectrom.* **2012**, *23*, 1029-1045.
222. Molesworth, S.; Osburn, S.; Van Stipdonk, M., Influence of size on apparent scrambling of sequence during CID of b-type ions. *J. Am. Soc. Mass Spectrom.* **2009**, *20*, 2174-2181.
223. Atik, A. E.; Yalcin, T., A systematic study of acidic peptides for b-type sequence scrambling. *J. Am. Soc. Mass Spectrom.* **2011**, *22*, 38-48.
224. Molesworth, S. P.; Van Stipdonk, M. J., Apparent inhibition by arginine of macrocyclic b ion formation from singly charged protonated peptides. *J. Am. Soc. Mass Spectrom.* **2010**, *21*, 1322-1328.
225. Dongré, A. R.; Jones, J. L.; Somogyi, Á.; Wysocki, V. H., Influence of peptide composition, gas-phase basicity, and chemical modification on fragmentation efficiency: evidence for the mobile proton model. *J. Am. Chem. Soc.* **1996**, *118*, 8365-8374.

226. Lee, S. W.; Kim, H. S.; Beauchamp, J. L., Salt bridge chemistry applied to gas-phase peptide sequencing: Selective fragmentation of sodiated gas-phase peptide ions adjacent to aspartic acid residues. *J. Am. Chem. Soc.* **1998**, *120*, 3188-3195.
227. Tabb, D. L.; Huang, Y.; Wysocki, V. H.; Yates, J. R., 3rd, Influence of basic residue content on fragment ion peak intensities in low-energy collision-induced dissociation spectra of peptides. *Anal. Chem.* **2004**, *76*, 1243-1248.
228. Reyzer, M. L.; Brodbelt, J. S., Gas-phase H/D exchange reactions of polyamine complexes:  $(M + H)^+$ ,  $(M + \text{alkali metal})^+$ , and  $(M + 2H)^{2+}$ . *J. Am. Soc. Mass Spectrom.* **2000**, *11*, 711-721.
229. Bythell, B. J.; Somogyi, A.; Paizs, B., What is the structure of  $b_2$  ions generated from doubly protonated tryptic peptides? *J. Am. Soc. Mass Spectrom.* **2009**, *20*, 618-624.
230. Somogyi, A.; Harrison, A. G.; Paizs, B., Using gas-phase guest-host chemistry to probe the structures of  $b$  ions of peptides. *J. Am. Soc. Mass Spectrom.* **2012**, *23*, 2055-2058.
231. Mann, M.; Wilm, M., Error-tolerant identification of peptides in sequence databases by peptide sequence tags. *Anal. Chem.* **1994**, *66*, 4390-4399.
232. Paizs, B.; Simonyi, M., Ring inversion barrier of diazepam and derivatives: An ab initio study. *Chirality* **1999**, *11*, 651-658.
233. Paizs, B.; Suhai, S., Combined quantum chemical and RRKM modeling of the main fragmentation pathways of protonated GGG. II. Formation of  $b_2$ ,  $y_1$ , and  $y_2$  ions. *Rapid Commun. Mass Spectrom.* **2002**, *16*, 375-389.
234. Paizs, B.; Suhai, S., Towards understanding the tandem mass spectra of protonated oligopeptides. 1: mechanism of amide bond cleavage. *J. Am. Soc. Mass Spectrom.* **2004**, *15*, 103-113.
235. Bythell, B. J.; Erlekam, U.; Paizs, B.; Maitre, P., Infrared spectroscopy of fragments from doubly protonated tryptic peptides. *Chem. Phys. Chem.* **2009**, *10*, 883-885.
236. Jia, C.; Qi, W.; He, Z., Cyclization reaction of peptide fragment ions during multistage collisionally activated decomposition: an inducement to lose internal amino-acid residues. *J. Am. Soc. Mass Spectrom.* **2007**, *18*, 663-678.
237. Harrison, A. G., Cyclization of Peptide  $b_9$  Ions. *J. Am. Soc. Mass Spectrom.* **2009**, *20*, 2248-2253.
238. Yalcin, T.; Tasoglu, C., Investigation of fragmentation behavior of peptides containing histidine residue. *Proceedings of the 58<sup>th</sup> ASMS Conference on Mass Spectrometry and Allied Topics* **2010**, Salt Lake City, UT.

239. Amblard, M.; Fehrentz, J. A.; Martinez, J.; Subra, G., Methods and protocols of modern solid phase peptide synthesis. *Mol. Biotechnol.* **2006**, 33, 239-354.
240. Wang, T. C.; Ricca, T. L.; Marshall, A. G., Extension of dynamic range in Fourier transform ion cyclotron resonance mass spectrometry via stored waveform inverse Fourier transform excitation. *Anal. Chem.* **1986**, 58, 2935-2938.
241. Zekavat, B.; Solouki, T., Injection of externally-generated low mass ions into high magnetic field in Q/FT-ICR instruments: SIMION simulations and experimental observations. *Proceedings of the 58<sup>th</sup> ASMS Conference on Mass Spectrometry and Allied Topics* **2010**, Salt Lake City, UT.
242. Wyttenbach, T.; Bowers, M. T., Gas-phase conformations of biological molecules: the hydrogen/deuterium exchange mechanism. *J. Am. Soc. Mass Spectrom.* **1999**, 10, 9-14.
243. Tang, X. J.; Boyd, R. K., An investigation of fragmentation mechanisms of doubly protonated tryptic peptides. *Rapid Commun. Mass Spectrom.* **1992**, 6, 651-657.
244. Gucinski, A. C.; Somogyi, A.; Chamot-Rooke, J.; Wysocki, V. H., Separation and identification of structural isomers by quadrupole collision-induced dissociation-hydrogen/deuterium exchange-infrared multiphoton dissociation (QCID-HDX-IRMPD). *J. Am. Soc. Mass Spectrom.* **2010**, 21, 1329-1338.
245. Baldwin, M. A., Protein identification by mass spectrometry: issues to be considered. *Mol. Cell Proteomics* **2004**, 3, 1-9.
246. Lam, H.; Aebersold, R., Building and searching tandem mass (MS/MS) spectral libraries for peptide identification in proteomics. *Methods* **2011**, 54, (4), 424-431.
247. Lubec, G.; Afjehi-Sadat, L., Limitations and pitfalls in protein identification by mass spectrometry. *Chem. Rev.* **2007**, 107, 3568-3584.
248. Mujezinovic, N.; Raidl, G.; Hutchins, J. R.; Peters, J. M.; Mechtler, K.; Eisenhaber, F., Cleaning of raw peptide MS/MS spectra: improved protein identification following deconvolution of multiply charged peaks, isotope clusters, and removal of background noise. *Proteomics* **2006**, 6, 5117-5131.
249. Sadygov, R. G.; Cociorva, D.; Yates, J. R., Large-scale database searching using tandem mass spectra: looking up the answer in the back of the book. *Nat. Methods.* **2004**, 1, 195-202.
250. Saminathan, I. S.; Wang, X. S.; Guo, Y.; Krakovska, O.; Voisin, S.; Hopkinson, A. C.; Siu, K. W., The extent and effects of peptide sequence scrambling via formation of macrocyclic B ions in model proteins. *J. Am. Soc. Mass Spectrom.* **2010**, 21, 2085-2094.

251. Goloborodko, A. A.; Gorshkov, M. V.; Good, D. M.; Zubarev, R. A., Sequence scrambling in shotgun proteomics is negligible. *J. Am. Soc. Mass Spectrom.* **2011**, 22, 1121-1124.
252. Bythell, B. J.; Csonka, I. P.; Suhai, S.; Barofsky, D. F.; Paizs, B., Gas-phase structure and fragmentation pathways of singly protonated peptides with N-terminal arginine. *J. Phys. Chem. B.* **2010**, 114, 15092-15105.
253. Oomens, J.; Young, S.; Molesworth, S.; van Stipdonk, M., Spectroscopic evidence for an oxazolone structure of the b<sub>2</sub> fragment ion from protonated tri-alanine. *J. Am. Soc. Mass Spectrom.* **2009**, 20, 334-339.
254. Tirado, M.; Polfer, N. C., Defying entropy: forming large head-to-tail macrocycles in the gas phase. *Angew. Chem. Int. Ed. Engl.* **2012**, 124, 1-4.
255. Badman, E. R.; Myung, S.; Clemmer, D. E., Gas-phase separations of protein and peptide ion fragments generated by collision-induced dissociation in an ion trap. *Anal. Chem.* **2002**, 74, 4889-4894.
256. Brechi, L. A.; Tabb, D. L.; Yates, J. R.; Wysocki, V. H., Cleavage N-terminal to proline: analysis of a database of peptide tandem mass spectra. *Anal. Chem.* **2003**, 75, 1963-1971.
257. Kish, M. M.; Wesdemiotis, C., Selective cleavage at internal lysine residues in protonated vs. metalated peptides. *Int. J. Mass Spectrom.* **2003**, 227, 191-203.
258. Tsaprailis, G.; Nair, H.; Zhong, W.; Kuppanan, K.; Futrell, J. H.; Wysocki, V. H., A mechanistic investigation of the enhanced cleavage at histidine in the gas-phase dissociation of protonated peptides. *Anal. Chem.* **2004**, 76, 2083-2094.
259. Ryzhov, V.; Dunbar, R. C.; Cerda, B.; Wesdemiotis, C., Cation- $\pi$  effects in the complexation of Na<sup>+</sup> and K<sup>+</sup> with Phe, Tyr, and Trp in the gas phase. *J. Am. Soc. Mass Spectrom.* **2000**, 11, 1037-1046.
260. Zhu, M. M.; Rempel, D. L.; Zhao, J.; Giblin, D. E.; Gross, M. L., Probing Ca<sup>2+</sup>-induced conformational changes in porcine calmodulin by H/D exchange and ESI-MS: effect of cations and ionic strength. *Biochemistry* **2003**, 42, 15388-15397.
261. Rozman, M.; Gaskell, S. J., Non-covalent interactions of alkali metal cations with singly charged tryptic peptides. *J. Mass Spectrom.* **2010**, 45, 1409-1415.
262. Dunbar, R. C.; Steill, J. D.; Polfer, N. C.; Oomens, J., Metal cation binding to gas-phase pentaalanine: divalent ions restructure the complex. *J. Phys. Chem. A* **2013**, 117, 1094-1101.

263. Dunbar, R. C.; Berdenb, G.; Oomens, J., How does a small peptide choose how to bind a metal ion? IRMPD and computational survey of CS versus Iminol binding preferences. *Int. J. Mass Spectrom.* **2013**, 354-355, 356-364.
264. Polfer, N. C.; Dunbar, R. C.; Oomens, J., Observation of Zwitterion Formation in the Gas-Phase H/D-Exchange with CH<sub>3</sub>OD: Solution-Phase Structures in the Gas Phase. *J. Am. Soc. Mass Spectrom.* **2007**, 18, 512-516.
265. Rand, K. D.; Pringle, S. D.; Murphy, J. P., 3rd; Fadgen, K. E.; Brown, J.; Engen, J. R., Gas-phase hydrogen/deuterium exchange in a traveling wave ion guide for the examination of protein conformations. *Anal. Chem.* **2009**, 81, 10019-10028.
266. Cox, H. A.; Julian, R. R.; Lee, S. W.; Beauchamp, J. L., Gas-phase H/D exchange of sodiated glycine oligomers with ND<sub>3</sub>: exchange kinetics do not reflect parent ion structures. *J. Am. Chem. Soc.* **2004**, 126, 6485-6490.
267. Rozman, M., The gas-phase H/D exchange mechanism of protonated amino acids. *J. Am. Soc. Mass Spectrom.* **2005**, 16, 1846-1852.
268. Rozman, M.; Bertosa, B.; Klasinc, L.; Srzic, D., Gas phase H/D exchange of sodiated amino acids: why do we see zwitterions? *J. Am. Soc. Mass Spectrom.* **2006**, 17, 29-36.
269. Ramachandran, G. N.; Ramakrishnan, C.; Sasisekharan, V., Stereochemistry of polypeptide chain configurations. *J. Mol. Biol.* **1963**, 7, 95-99.
270. Zekavat, B.; Szulejko, J. E.; LaBrecque, D.; Olaitan, A. D.; Solouki, T., Efficient injection of low-mass ions into high magnetic field Fourier transform ion cyclotron resonance mass spectrometers. *Rapid Commun. Mass Spectrom.* **2014**, 28, 230-238.
271. Solouki, T.; Szulejko, J. E., Bimolecular and unimolecular contributions to the disparate self-chemical ionizations of alpha-pinene and camphene isomers. *J. Am. Soc. Mass Spectrom.* **2007**, 18, 2026-2039.
272. Bartmess, J. E.; Georgiadis, R. M., Empirical methods for determination of ionization gauge relative sensitivities for different gases. *Vacuum* **1983**, 33, 149-153.
273. Gidden, J.; Wyttenbach, T.; Jackson, A. T.; Scrivens, J. H.; Bowers, M. T., Gas-phase conformations of synthetic polymers: Poly(ethylene glycol), poly(propylene glycol), and poly(tetramethylene glycol). *J. Am. Chem. Soc.* **2000**, 122, 4692-4699.
274. Becke, A. D., Density-functional thermochemistry III. The role of exact exchange. *J. Chem. Phys.* **1993**, 98, 5648-5652.

275. Frisch, M. J.; Trucks, G. W.; Schlegel, H. B.; Scuseria, G. E.; Robb, M. A.; Cheeseman, J. R.; Scalmani, G.; Barone, V.; Mennucci, B.; Petersson, G. A.; Nakatsuji, H.; Caricato, M.; Li, X.; Hratchian, H. P.; Izmaylov, A. F.; Bloino, J.; Zheng, G.; Sonnenberg, J. L.; Hada, M.; Ehara, M.; Toyota, K.; Fukuda, R.; Hasegawa, J.; Ishida, M.; Nakajima, T.; Honda, Y.; Kitao, O.; Nakai, H.; Vreven, T.; Montgomery, J. A., Jr.; Peralta, J. E.; Ogliaro, F.; Bearpark, M.; Heyd, J. J.; Brothers, E.; Kudin, K. N.; Staroverov, V. N.; Kobayashi, R.; Normand, J.; Raghavachari, K.; Rendell, A.; Burant, J. C.; Iyengar, S. S.; Tomasi, J.; Cossi, M.; Rega, N.; Millam, N. J.; Klene, M.; Knox, J. E.; Cross, J. B.; Bakken, V.; Adamo, C.; Jaramillo, J.; Gomperts, R.; Stratmann, R. E.; Yazyev, O.; Austin, A. J.; Cammi, R.; Pomelli, C.; Ochterski, J. W.; Martin, R. L.; Morokuma, K.; Zakrzewski, V. G.; Voth, G. A.; Salvador, P.; Dannenberg, J. J.; Dapprich, S.; Daniels, A. D.; Farkas, Ö.; Foresman, J. B.; Ortiz, J. V.; Cioslowski, J.; Fox, D. J., *Gaussian-09*, **2010**, Revision C.01, Gaussian, Inc., Wallingford, CT.
276. Kapota, C.; Lemaire, J.; Maitre, P.; Ohanessian, G., Vibrational signature of charge solvation vs salt bridge isomers of sodiated amino acids in the gas phase. *J. Am. Chem. Soc.* **2004**, *126*, 1836-1842.
277. El Aribi, H.; Orlova, G.; Rodriguez, C. F.; Almeida, D. R. P.; Hopkinson, A. C.; Siu, K. W. M., Fragmentation mechanisms of product ions from protonated tripeptides. *J. Phys. Chem. B* **2004**, *108*, 18743-18749.
278. Polfer, N. C.; Paizs, B.; Snoek, L. C.; Compagnon, I.; Suhai, S.; Meijer, G.; von Helden, G.; Oomens, J., Infrared fingerprint spectroscopy and theoretical studies of potassium ion tagged amino acids and peptides in the gas phase. *J. Am. Chem. Soc.* **2005**, *127*, 8571-8579.
279. Leininger, T.; Nicklass, A.; Kuchle, W.; Stoll, H.; Dolg, M.; Bergner, A., The accuracy of the pseudopotential approximation: Non-frozen-core effects for spectroscopic constants of alkali fluorides XF (X = K, Rb, Ca). *Chem. Phys. Lett.* **1996**, *255*, 274-280.
280. Helden, G. v.; Hsu, M. T.; Gotts, N.; Bowers, M. T., Carbon cluster cations with up to 84 atoms: structures, formation mechanism, and reactivity. *J. Phys. Chem.* **1993**, *97*, 8182-8192.
281. Wyttenbach, T.; vonHelden, G.; Batka, J. J.; Carlat, D.; Bowers, M. T., Effect of the long-range potential on ion mobility measurements. *J. Am. Soc. Mass Spectrom.* **1997**, *8*, 275-282.
282. Green-Church, K. B.; Limbach, P. A.; Freitas, M. A.; Marshall, A. G., Gas-phase hydrogen/deuterium exchange of positively charged mononucleotides by use of Fourier-transform ion cyclotron resonance mass spectrometry. *J. Am. Soc. Mass Spectrom.* **2001**, *12*, 268-277.

283. Dunbar, R. C.; Steill, J. D.; Polfer, N. C.; Berden, G.; Oomens, J., Peptide bond tautomerization induced by divalent metal ions: characterization of the Iminol configuration. *Angew Chem. Int. Ed. Engl.* **2012**, 51, 4591-4593.
284. Dunbar, R. C.; Oomens, J.; Berden, G.; Lau, J. K.; Verkerk, U. H.; Hopkinson, A. C.; Siu, K. W., Metal ion complexes with HisGly: comparison with PhePhe and PheGly. *J. Phys. Chem. A* **2013**, 117, 5335-5343.
285. Chen, L.; Gao, Y. Q.; Russell, D. H., How alkali metal ion binding alters the conformation preferences of gramicidin A: a molecular dynamics and ion mobility study. *J. Phys. Chem. A* **2012**, 116, 689-696.
286. Frensdorff, H. K., Stability constants of cyclic polyether complexes with univalent cations. *J. Am. Chem. Soc.* **1971**, 93 600-606.